Strojniški vestnik

Journal of Mechanical Engineering

no. 3-4
year 2024
volume 70

Strojniški vestnik – Journal of Mechanical Engineering (SV-JME)

Aim and Scope
The international journal publishes original and (mini)review articles covering the concepts of materials science, mechanics, kinematics, thermodynamics, energy and environment, mechatronics and robotics, fluid mechanics, tribology, cybernetics, industrial engineering and structural analysis.
The journal follows new trends and progress proven practice in the mechanical engineering and also in the closely related sciences as are electrical, civil and process engineering, medicine, microbiology, ecology, agriculture, transport systems, aviation, and others, thus creating a unique forum for interdisciplinary or multidisciplinary dialogue.
The international conferences selected papers are welcome for publishing as a special issue of SV-JME with invited co-editor(s).

Editorial Office
University of Ljubljana, Faculty of Mechanical Engineering
SV-JME, Aškerčeva 6, SI-1000 Ljubljana, Slovenia
Phone: 386 (0)1 4771 137
Fax: 386 (0)1 2518 567
info@sv-jme.eu, http://www.sv-jme.eu

Print: Demat d.o.o., printed in 240 copies

Founders and Publishers
University of Ljubljana, Faculty of Mechanical Engineering, Slovenia
University of Maribor, Faculty of Mechanical Engineering, Slovenia
Association of Mechanical Engineers of Slovenia
Chamber of Commerce and Industry of Slovenia, Metal Processing Industry Association

Cover:
Picture on the cover represents example of sensible seasonal storage technology in Vojens (Denmark) as one of the largest solar heating in the world, with 70 000 m² of solar thermal collectors and one of the largest underground thermal storage pit (200 000 m³). The first article also represents seasonal solar energy storage but with thermo-chemical energy storage (more specifically adsorption storage technology).

Image Courtesy:
Vojens Solar Thermal Plant and Pit Storage, Ramboll.

General information
Strojniški vestnik – Journal of Mechanical Engineering is published in 6 double issues per year.

Institutional prices include print & online access: institutional subscription price and foreign subscription €100,00 (the price of a single issue is €10,00); general public subscription and student subscription €50,00 (the price of a single issue is €5,00). Prices are exclusive of tax. Delivery is included in the price. The recipient is responsible for paying any import duties or taxes. Legal title passes to the customer on dispatch by our distributor. Single issues from current and recent volumes are available at the current single-issue price. To order the journal, please complete the form on our website. For submissions, subscriptions and all other information please visit: *http://www.sv-jme.eu.*

You can advertise on the inner and outer side of the back cover of the journal. The authors of the published papers are invited to send photos or pictures with short explanation for cover content.

We would like to thank the reviewers who have taken part in the peer-review process.

ISSN 0039-2480, ISSN 2536-2948 (online)

The journal is subsidized by Slovenian Research and Inovation Agency.

SV-JME is indexed / abstracted in: SCI-Expanded, Compendex, Inspec, ProQuest-CSA, SCOPUS, TEMA. The list of the remaining bases, in which SV-JME is indexed, is available on the website.

Strojniški vestnik - Journal of Mechanical Engineering is available on *https://www.sv-jme.eu*.

Contents

Strojniški vestnik - Journal of Mechanical Engineering
volume 70, (2024), number 3-4
Ljubljana, March-April 2024
ISSN 0039-2480

Published every two months

Papers

Strojniški vestnik - Journal of Mechanical Engineering 70(2024)3-4, 107-115
DOI:10.5545/sv-jme.2023.788
Original Scientific Paper
Received for review: 2023-09-07
Received revised form: 2024-01-31
Accepted for publication: 2024-02-13

Experimental Testing System for Adsorption Space Heating

Urška Mlakar[1]* – Rok Koželj[1] – Alenka Ristić[2] – Uroš Stritih[1]
[1] University of Ljubljana, Faculty of Mechanical Engineering, Slovenia
[2] National Institute of Chemistry, Slovenia

Approximately 40 % of the final energy is used for heating and cooling of buildings. Of this, as much as 75 % is used in residential buildings. The proportion of energy needed in buildings is relatively high, so it is necessary to start using technologies that have low energy consumption, use it efficiently or provide it from renewable sources. One such technology is thermal energy storage, which allows us to store excess energy for later when we need extra energy. The paper presents two experiments in the field of adsorption space heating. In the first experiment, measurements were carried out on the adsorbents - zeolite 13X and zeolite NaYBFK, which were placed into a duct, through which humid air was transported by means of a centrifugal fan. In the second experiment, water vapour as the working medium was used. With the first experiment we achieved better water uptake on NaYBF, while the second experiment shows the increase of water uptake of zeolite 13X.
Keywords: sorption heat storage, space heating, water vapour, humid air, zeolite 13X, zeolite NaYBFK

Highlights
- *Zeolite NaYBFK achieves lower maximum temperature, but has better water uptake then zeolite 13X, when humid air is used as the working fluid.*
- *Water uptake of zeolite 13X can be improved with higher inlet temperature of water vapour, while reached maximum temperature during adsorption phase is lower.*
- *The maximum temperature during adsorption increased for 24 °C for zeolite NaYBFK with water vapour and the water uptake did not change at the same inlet temperature.*
- *A lower inlet temperature and a smaller amount of NaYBFK reaches a higher maximum temperature, while the heat of adsorption phase lasts longer, when water vapour was used.*

0 INTRODUCTION

If we want to improve the efficiency of systems in the building sector in future generations, the application of storage technologies will be necessary. Storage technologies allow us to store energy during times of excess energy and use it when needs are greater. Energy can be stored in sensible, latent [1], and thermochemical storage technologies (absorption and adsorption) [2]. Such technologies can be applied in both heating and cooling, for different storage periods. The example we discussed in this paper is suitable for building space heating applications.

Based on a review of the literature, it was found that zeolite 13X is used in research of several thermal energy storage (TES) systems. Stritih and Mlakar [3] presented sorption systems, important characteristics of the materials used and some open and closed systems in a chapter, which also include few examples where zeolite 13X was used. It was used in the research by Dawoud and Amer [4], who considered a closed TES system with a working pair of 13X - water. Tatsidjodoung et al. [5] investigated the case of an open system with 13X zeolite and water, the system was intended for use in buildings and obtained energy for storage from solar energy. We also found a case where a working pair of zeolite 13X-water is being tested in industry, as discussed by Schreiber et al. [6] in their research. Zeolite 13X is also used in another combination of working mediums, such as 13X-magnesium sulfate and water, as investigated by Xu et al. [7].

The above research shows that zeolite 13X is suitable for use in building systems. Compared to silica gel, 13X zeolite can provide higher temperature lifts [8]. For binderless zeolite 13X beads the water adsorption isotherms and the adsorption kinetics have been studied in detail by experimental investigation in a sorption analyzer (adsorption isotherms) and fixed bed reactor (adsorption kinetics) by Mette et al. [9]. Experimental investigations have shown that this zeolite is characterized by a high-water uptake and fast reaction kinetics. Both properties are of great importance when using this material for thermochemical energy storage application. A high-water uptake is required for a high energy storage density whereas high sorption kinetics is essential for a high thermal power output during adsorption. Banaei and Zanj [10] focused on different utilization of zeolite 13X and main challenges such as compact system design, charging supply, humidity management, system output power, and system efficiency. Rogala et al. [11] proposed a novel model useful for analyzing the silica gel-water adsorption

*Corr. Author's Address: University of Ljubljana, Faculty of Mechanical Engineering, Slovenia, urska.mlakar@fs.uni-lj.si

and desorption process in air-fluidized systems. Presented model is especially reliable tool for silica gel particle diameters from 1 mm to 3 mm. Model was validated through an extensive experimental study, which was carried out on the laboratory test-stand. Antonellis et al. [12] studied open sorption thermal energy storage system based on zeolite 13X and its integration at system level through an experimental and a numerical approach. The study provides a methodology for determining the efficiency of a complete thermal storage system with an adsorption TES as well as identifying possible engineering applications of such a technology. Through literature review could be observed that zeolite 13X is the most widely researched and obtainable sorption material, that's also why it was used in our comparison with other zeolite material.

In our work we focused on zeolite 13X, which is presented in the literature as a promising medium for sorption energy storage in building systems. At the same time, we wanted to compare the already known zeolite 13X with another sorption material - zeolite NaYBFK.

The paper discusses energy storage in the summer for the purpose of the use in the winter - technology of seasonal storage. With the applications of such technologies, energy can be used more efficiently. Our system is an open adsorption system that uses air to which water vapour is added (e.g. humid air) and water vapor, as working media. The temperature of these working media allows the activation of the adsorbent material to initiate heat release. The heat released during the adsorption phase can then be used as a heating source. The aim of the research was to obtain experimental data for the adsorption phase for zeolite 13X (Silkem, Slovenia) and zeolite NaYBFK (CWK, Germany), which would later be used to verify the results obtained by simulation in the Ansys environment. In the analysis of the results, we focused on the maximum achieved temperature in the adsorption phase, the duration of adsorption phase and the achieved water uptake.

This paper consists of 4 chapters. Chapter 1 presents adsorption heating in all three stages of the process, using a p-T-x diagram. Chapter 2 presents the performed experiments together with their measuring setup and the equipment used. Chapter 3 first presents an explanation of the temperatures measured in the experiments, and then presents the results of each experiment in two subchapters. The paper concludes with a final discussion.

1 ADSORPTION HEATING

The circular process in adsorption storage is the same as the circular process of a heat pump, the difference is only in the interruption of operation between the processes of desorption and adsorption. This interruption represents a time when stored energy is not needed. Fig. 1 shows a p-T-x diagram of an adsorption heat storage process.

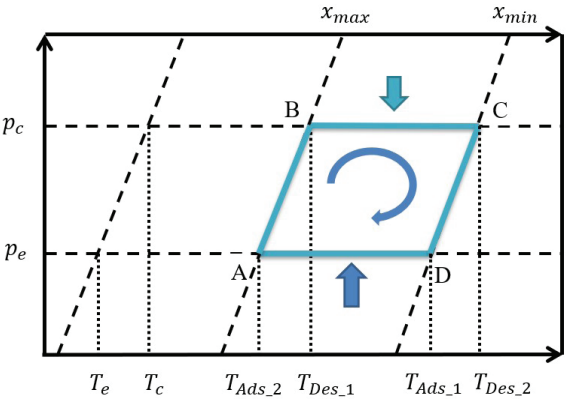

Fig. 1. p-*T-x diagram of an adsorption heat storage process*

The mass of the adsorbate varies between the minimum (line C, D) and the maximum value (line A, B). The adsorption process takes place between points D-A at the evaporation pressure p_e and desorption process takes place at pressure p_c between points B-C. This work cycle consists of the following four steps:

Step 1: The storage of heat in the bulk region - adsorber begins with isosteric (humidity is constant) heating of the adsorbent. The pressure and temperature in the adsorber increase in line from point A to point B until the initial desorption temperature T_{Des_1} is reached. At this temperature, the pressure in the adsorber equals the condensation pressure of the adsorbed working medium (at point B).

Step 2: At point B, the desorption phase will start. The adsorbent is heated until working medium is removed, and the adsorbent becomes dry (the lines between points B and C). This is when the maximum available temperature T_{Des_2} is reached. Meanwhile, the condenser is cooled to maintain the condensation pressure p_c. The heat generated by condensation (Q_c) is discharged to the surroundings as waste heat. This affects the condensation temperature T_c, which must be kept as low as possible to ensure the best desorption possible. At the maximum reached temperature T_{Des_2}, the degree of saturation of the adsorbent with the adsorbate is minimum $x_{\min}$, so the cycle is completed.

Step 3: Depending on the time period of energy storage and ambient temperature, the temperature in the storage region may fall during this period. The drop in temperature and, consequently, the pressure, shows an isostere between C and D. The temperature may decrease to the initial adsorption temperature T_{Ads_1} or even lower.

Step 4: Emptying the stored heat begins by supplying heat to the adsorber. We can supply heat from various sources (solar collectors, earth heat). The working medium is evaporated at the evaporation pressure pe and the temperature T_e. Currently the working medium is adsorbed on the adsorbent and heat is released - Q_{Ads} (the line between points D and A). The released heat is called usable heat that can be used in the heating system.

This paper presents the adsorption phase of the storage process which can be used for heating of the building in the winter.

2 EXPERIMENTAL

Two experiments were conducted on the adsorption process of working fluid on the bulk using the zeolite 13X and zeolite NaYBFK. In the first experiment, the working medium was humid air, e.g. air to which water vapour was added from ultrasonic humidifier, while in the second experiment, water vapour was used as the working medium. Temperatures measurements of adsorption process were performed to validate the numerical model. Fig. 2 shows the scheme of the experimental setup for sorption process.

The system has two key parts of the experimental line, namely the centrifugal fan (1) and the compartment with the adsorption substance bulk. By adjusting the frequency on the frequency regulator (2), the speed of the centrifugal fan that drives air through the duct is controlled. Air velocity into the duct was measured using a vane anemometer (3). After vane anemometer the first thermocouple (4) was positioned to measure temperature of the air in the duct. The vane anemometer, the first thermocouple, hygrometer and the pressure transmitter are connected to the TESTO 400 data logger (5), where the measurement data is collected. A pressure converter (6) was also used to convert the pressure before entering the porous bed and the pressure after the porous bed. The pressure difference meter thus measures a pressure drop through the packed bed of the adsorption material. We also carried out an indirect measurement of air flow

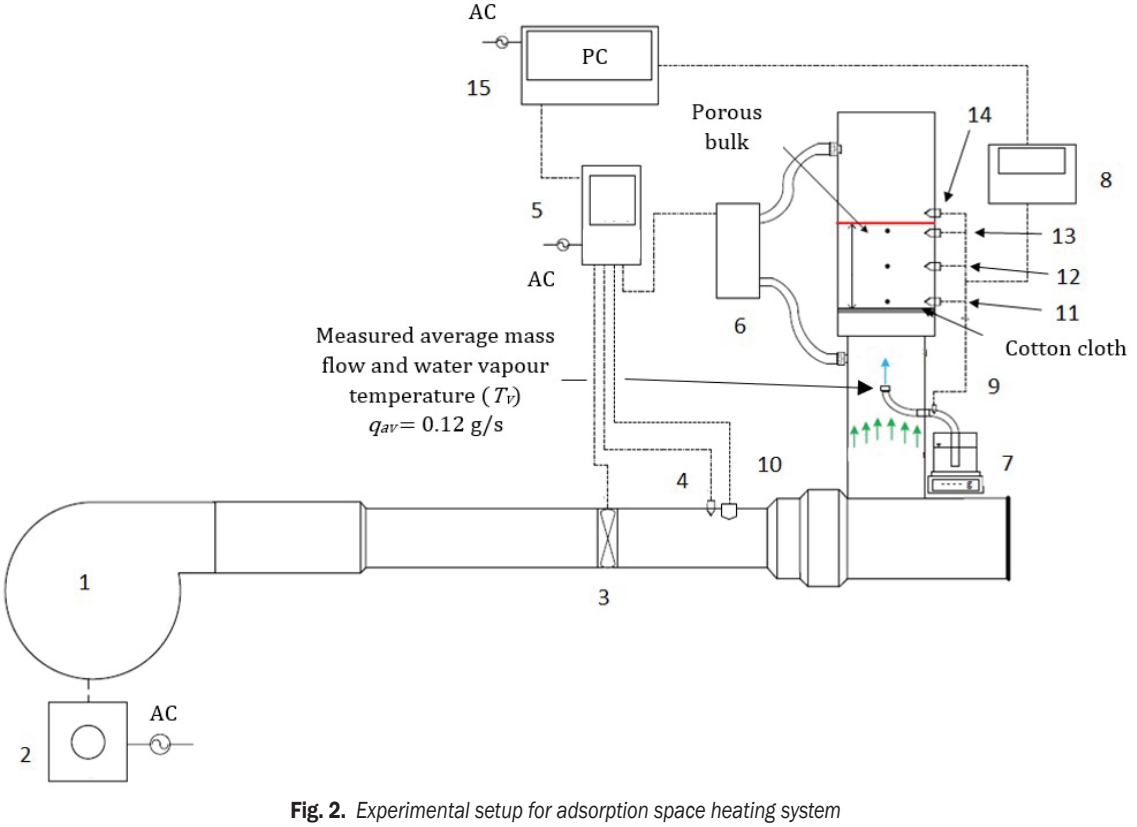

Fig. 2. *Experimental setup for adsorption space heating system*

through the duct as shown with green arrows. Water vapour was added to the working medium - air, thus moistening it. The mass flow of water vapour that was added to the air was determined with difference in weight of water in ultrasonic humidifier (7) and time measurement. The water vapour temperature measurement data and the porosity temperature data measured with thermocouples were linked to Agilent 34970a data logger (8). In addition to the flow that is shown as blue arrow on the experimental setup, we also measured the water vapour temperature (9) that was added to the air flow. After vane anemometer and the first thermocouple, hygrometer (10) was positioned to measure humidity of the air in the duct. When water vapour was added to the air, these two streams were mixed before entering the porous bulk. In the porous bulk the temperatures were measured at different locations or heights. The first temperature (11) was measured immediately behind the cot-ton fabric at the bottom of the porous bulk. The second temperature (12) was measured at medium height of the porous bulk. The next thermocouple (13) was located at the top of the porous packed bed. The last thermocouple (14) measured the air temperature behind the porous packed bed. The measurements of all the meters were collected on a computer (15).

Fig. 3. *Adsorber with bulk of zeolite 13X*

The boundary conditions of the first experiment were as follows: The volume of the porous packed bed was 281 ml (zeolite 13X), 260 ml, 280 ml and 180 ml (zeolite NaYBFK), and the mass of the porous material was 173 g, 192 g, 200 g and 134 g, respectively. The height of the porous bulk was 25.7 mm. The mass flow of water vapour varied in the range from 0.05 to 0.1 g/s. Time interval of measurement reading was 10 seconds. The Zeolite 13X porous bulk (Fig. 3) had a granulation size between 1.6 mm and 2.5 mm.

The experimental setup for the second experiment is part of the experimental setup of the first experiment. The difference is that this time we only use water vapour as a working medium. By supplying water vapour as working medium, we got rid of the problem of efficient mixing of air and water vapour before entering a porous bulk. As in the first experiment, this time we measured the water vapour temperature, the water vapour mass flow, and the temperatures in the porous bulk at different heights. The flow of water vapour is shown in the Fig. 4 with a blue arrow.

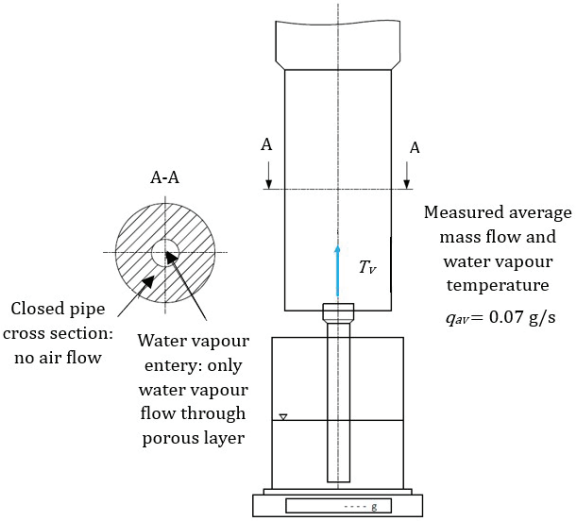

Fig. 4. *Experimental setup for experiment with water vapour as working medium*

Experimental setup is shown in Fig. 5.

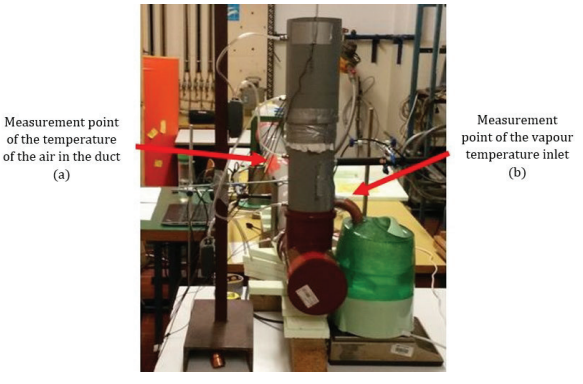

Fig. 5. *Measurement points of water vapour temperature inlet and temperature of the air in the duct*

3 RESULTS

In the following sections, the temperature measurements of each set of experiments are shown in graphs. The results show 7 different temperatures:

- Duct temperature (a) is the temperature of the air in the horizontal duct in the first experimental

setup as shown in the Fig. 2 (measured at number 4).

- Temperature (b) is the temperature of a water vapour inlet in the first and second experiment
- Temperature (c) is the temperature that was measured at the bottom of the packed bed on 1/4 of the cross section of the duct.
- Temperature (d) is the temperature that was measured at the bottom of the zeolite bulk in the middle of the cross section of the duct.
- Temperature (e) is the temperature that was measured at the bottom of the zeolite bulk on 3/4 of the cross section of the duct.
- Temperature (f) is the temperature that was measured at the bottom edge of the zeolite bulk.
- Temperature (g) is the temperature that was measured at the top of the zeolite bulk on 1/4 of the cross section of the duct. On the experimental line in Fig. 2 the thermocouple for measuring this temperature is marked with the number 12.

Fig. 5 shows the measuring point of the temperature of the water vapour entering the duct and the air temperature in the horizontal duct.

Figs. 6 and 7 shows the thermocouples used to measure the temperatures in the zeolite bulk in the adsorber.

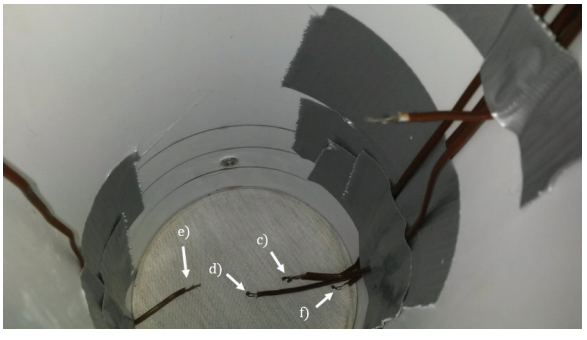

Fig. 6. *Measurement points of the temperatures that were measured at the bottom of zeolite bulk*

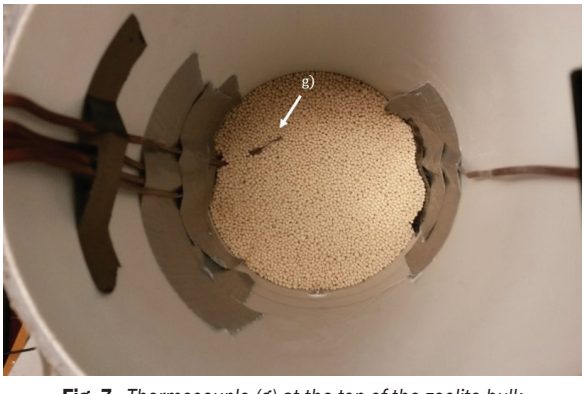

Fig. 7. *Thermocouple (g) at the top of the zeolite bulk*

Several sets of measurements were performed for each experiment. For the first experiment, we performed three sets of measurements:one for zeolite 13X and two for zeolite NaYBFK.

For the second experiment, we performed two sets of measurements:

- one for zeolite 13X,
- one for zeolite NaYBFK.

4.1 First Experiment

The results of the first experiment are shown in the following figures. In the first set of measurements, conditions were as follows: The used adsorbent was zeolite 13X with the amount of 173 g. The average water vapour inlet temperature was 22 °C in the interval from 20 to 91 (time span of 12 minutes). The maximum temperature reached was 128 °C. The water uptake of 0.22 kg_w/kg_a was reached. Fig. 8 shows the measured temperatures in the packed bed at different locations.

In addition to temperatures, Fig. 9 also shows the air velocity through the bulk. We had a water vapour inflow from interval of 20 to 91, with a very slow velocity - performing adsorption. When the water vapour supply stopped at interval 91, the air velocity was increased to remove heat from the adsorbent by blowing air. It can be observed that at interval 91, the air velocity suddenly increases to 0.9 m/s, and consequently a decrease in temperatures occurs. The adsorption phase is completed. Forced heat dissipation occurs, which takes about 16 minutes. Temperatures drop to around 25 °C.

The results of the first measurements for zeolite NaYBFK are shown in the following figures. In the first set of measurement, conditions for zeolite NaYBFK were as follows: The amount was 192 g. The average water vapour inlet temperature was 22 °C in the interval from 73 to 204 (time span of 22 minutes). The maximum temperature reached was 110 °C, the water uptake for zeolite NaYBFK was determined to be 0.25 kg_w/kg_a. Fig. 10 shows temperatures in the zeolite packed bed at different heights.

At interval 180 the air velocity suddenly increases to remove heat from the adsorbent and consequently a decrease in temperatures occurs after the adsorption phase is completed. Temperatures drop to around 25 °C in about 8 minutes after the forced dissipation occurs.

In the second set of measurement conditions for the zeolite NaYBFK were as follows: The quantity of the zeolite was 200 g. The average water vapour

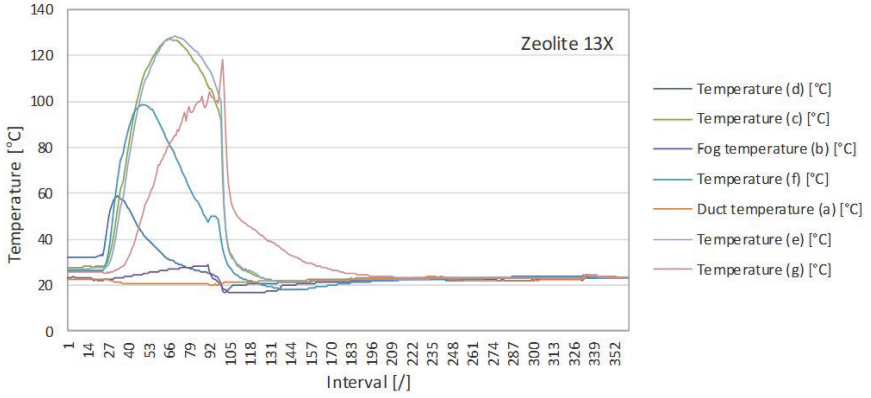

Fig. 8. *Temperatures in packed bed of zeolite 13X during the first set of conditions*

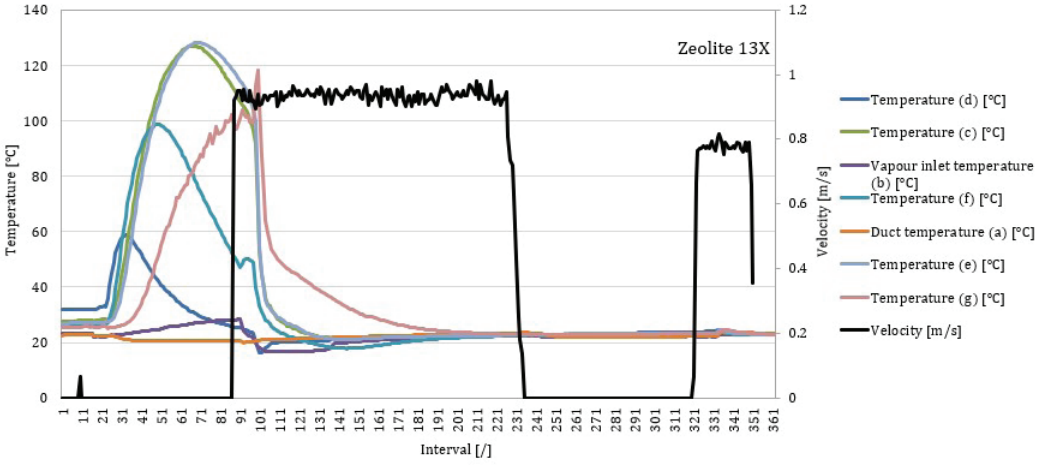

Fig. 9. *Temperatures in zeolite 13X bulk and air velocity during the first set of conditions*

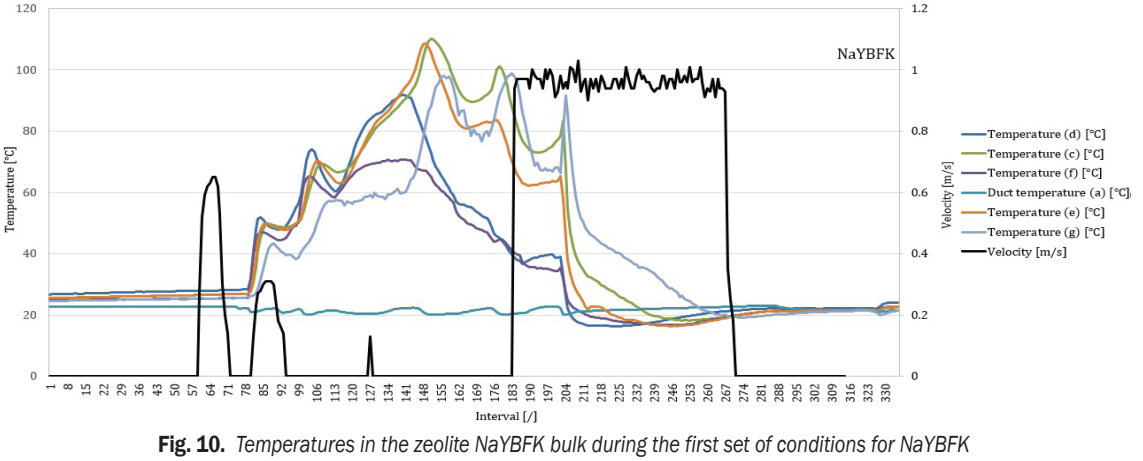

Fig. 10. *Temperatures in the zeolite NaYBFK bulk during the first set of conditions for NaYBFK*

inlet temperature was 22 °C in the interval from 23 to 178 (time span of 26 minutes). The maximum temperature reached was 97 °C. The water uptake of zeolite NaYBFK was 0.26 kg_w/kg_a. Fig. 11 shows temperatures in the packed bed at different heights and air velocity

At interval 178 the air velocity suddenly increases to remove heat from the adsorbent and consequently a decrease in temperatures occurs, after the adsorption phase is completed. Temperatures drop to around 25 °C in about 6 minutes after the forced dissipation occurs.

The inflection of temperature curve is due to the return flow, where inlet of water vapour does not flow through packed bed. When the steadiness of the flow of water vapour and air in the system is restored, the adsorption process in the porous layer starts again. Therefore, the inflection point is due to unsteadiness of the flow of water vapour in the system.

4.2 Second Experiment

Results of measurements of the second experiment are presented below. The difference is that water vapour as a working medium has been used.

The boundary conditions of the last experiment with zeolite 13X were as follows: The volume of the bulk was 281 ml, and the amount was 173 grams. The height of the bulk was 25.7 mm. The mass flow of water vapour was 0.12 g/s. The zeolite 13X bulk had a size of granules between 1.6 mm and 2.5 mm. The average water vapour inlet temperature was 28 °C in the interval from 34 to 228 (time span of 32 minutes). The maximum reached temperature was 120 °C and the water uptake of material was 0.27 kg_w/kg_a.

Fig. 12 shows temperatures at different layers of the porous packed bed in the period before the start of the adsorption phase, during the adsorption

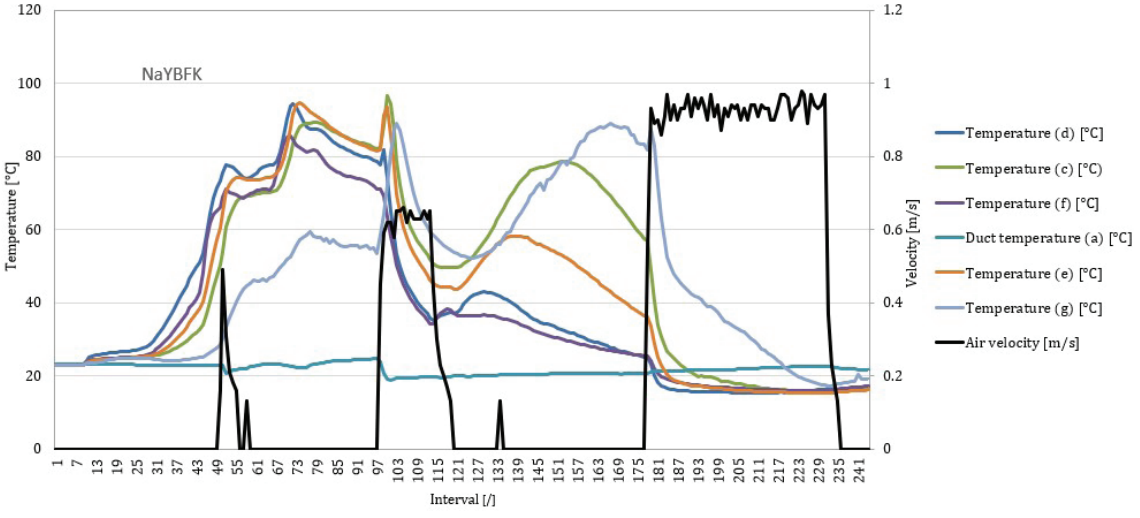

Fig. 11. *Temperatures in the zeolite NaYBFK packed bed and air velocity during the second set of conditions*

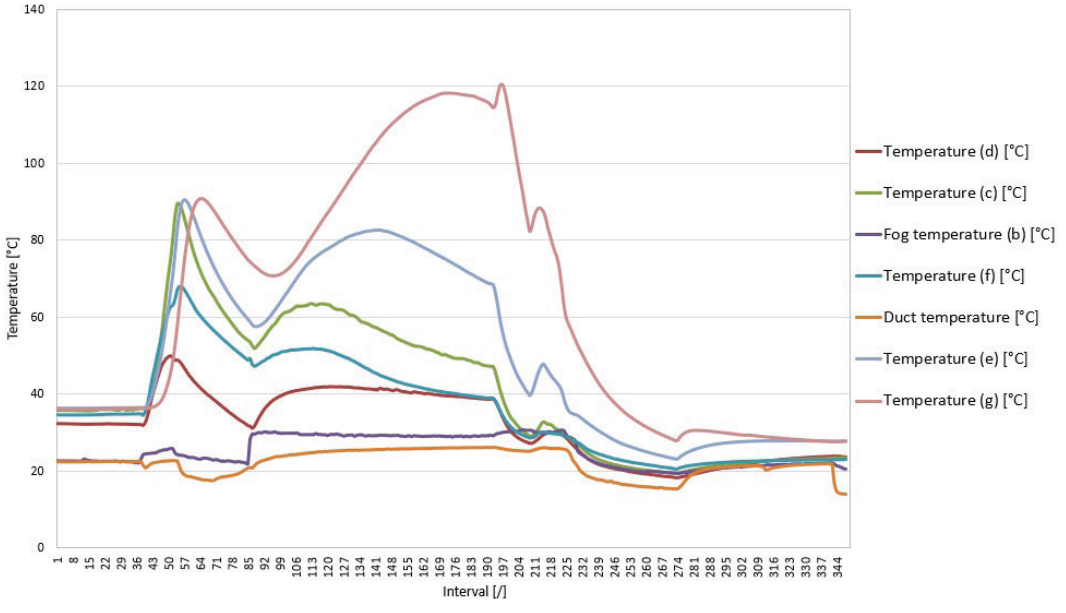

Fig. 12. *Temperatures in bulk during the second set of conditions for zeolite 13X*

phase and after the adsorption phase was completed. Two infection points of temperature distribution can be seen from Fig. 12. This is the consequence of desorption of the packed bed layers that already went through adsorption process. The layers that are going through the adsorption process are emitting heat to the adjacent layers that already went through the adsorption and are now desorbing.

The results of the measurements for zeolite NaYBFK are shown in Fig. 13. At this experiment, measurement conditions for zeolite NaYBFK were as follows: the mass was 134 g. The average water vapour inlet temperature was 22 °C in the interval from 35 to 96 (time span of 10 minutes). The mass flow of steam was 0.07 g/s. The maximum temperature reached was 134 °C. The water uptake was 0.25 kg_w/kg_a.

At time interval of 35 intake of water vapour starts to flow through packed bed and the adsorption process starts. The water vapour flows through the packed bed up to the time interval of 96. After the adsorption process, the air is imposed to the system at time interval of 141 to cool down the material. The reached peak temperature is 130 °C. Temperatures drop to around 25 °C in about 23 minutes after the forced dissipation occurs.

5 CONCLUSIONS

Two experiments were conducted on the adsorption process on the bulks of zeolite 13X and zeolite NaYBFK as the adsorbents. From all the results it can be seen that the temperature distribution in the packed bed changes depending on the cross-section of the packed bed (we have a lower maximum temperature at the edges). Comparing two measurements for zeolite NaYBFK for the first experiment, we see that a larger quantity (8 g more) of the sorption material achieves a maximum temperature that is 13 °C lower, but at the same time has slightly better water uptake.

A comparison of zeolite 13X and NaYBFK for the first experiment shows that zeolite NaYBFK reaches a lower maximum temperature but has better water uptake, and that released heat during adsorption phase lasts longer with zeolite 13X. A comparison of the first and second experiment for zeolite 13X shows that with the same amount of sorption material (173 g), but a few degrees higher inlet temperature of the mist in the second experiment (28 °C), a better water uptake is achieved (1st experiment 0.22 kg_w/kg_a, 2nd experiment 0.27 kg_w/kg_a), but at the same time the maximum temperature reached is 8 °C lower. Comparing the 1st and 2nd test for zeolite NaYBFK shows that the same water adsorption is achieved with a smaller amount of sorption material (58 g less) at the same inlet temperature, but at the same time the maximum temperature reached in the 2nd experiment is 8 °C lower. The results of the second experiment shows that zeolite NaYBFK reaches a higher maximum temperature (14 °C higher) at a lower inlet temperature than zeolite 13 X and a lower amount of the sorption material (39 g less), while the heat during adsorption phase lasts longer (11 minutes longer).

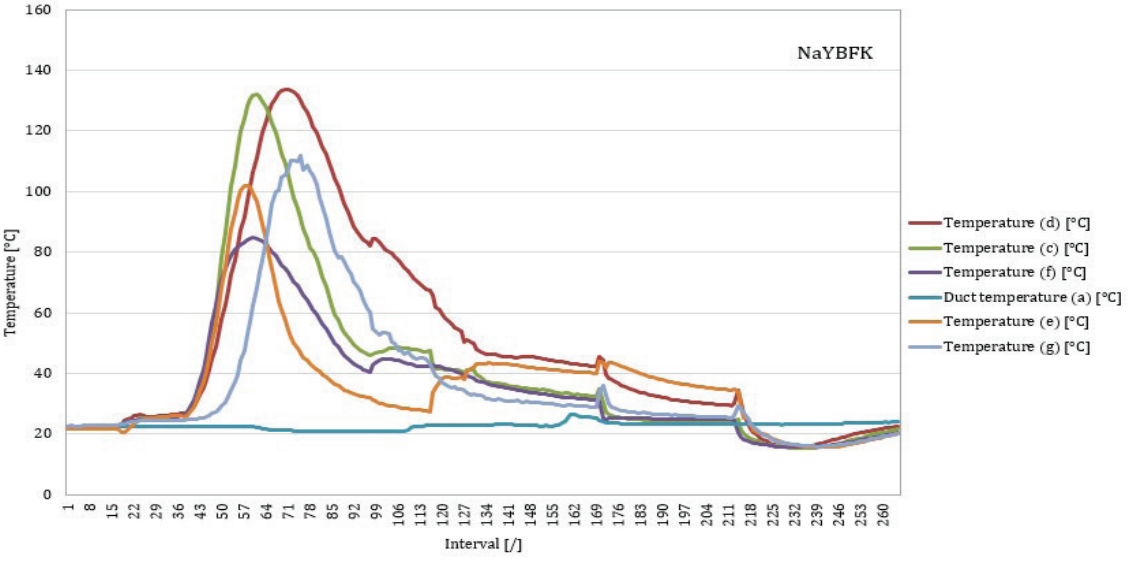

Fig. 13. *Temperatures in packed bed during the set of conditions for zeolite NaYBFK with water vapour as working medium*

6 ACKNOWLEDGEMENTS

This study was financially supported by Slovenian Research Innovation Agency (ARIS) through project number L1-7665.

7 REFERENCES

[1] Kittusamy, R. K., Rajagopal, V., and Felix, P. G. (2022) Preparation and thermal characterization of nanographene-enhanced fatty acid-based solid-liquid organic phase change material composites for thermal energy storage. *Strojniški Vestnik - Journal of Mechanical Engineering*, vol. 68, no. 7-8, p. 461-470, **DOI:10.5545/sv-jme.2022.148**.

[2] Wu, W. (2020). Low-temperature compression-assisted absorption thermal energy storage using ionic liquids. *Energy and Built Environment*, vol. 1, no. 2, p. 139-148, **DOI:10.1016/j.enbenv.2019.11.001**.

[3] Stritih, U., Mlakar, U. (2018). Technologies for seasonal solar energy storage in buildings. *InTech*, p. 51-75, **DOI:10.5772/intechopen.74404**.

[4] Dawoud, B., Amer, E.-H., Gross, D.-M. (2007). Experimental investigation of an adsorptive thermal energy storage. *International Journal of Energy Research*, vol. 31, no. 2, p. 135-147, **DOI:10.1002/er.1235**.

[5] Tatsidjodoung, P., Le Pierrès, N., Heintz, J., Lagre, D., Luo, L., Durier, F. (2016). Experimental and numerical investigations of a zeolite 13X/water reactor for solar heat storage in buildings. *Energy Conversion and Management*, vol. 108, p. 488-500, **DOI:10.1016/j.enconman.2015.11.011**.

[6] Schreiber, H., Graf, S., Lanzerath, F., Bardow, A. (2015). Adsorption thermal energy storage for cogeneration in industrial batch processes: Experiment, dynamic modeling and system analysis. *Applied Thermal Engineering*, vol. 89, p. 485-493, **DOI:10.1016/j.applthermaleng.2015.06.016**.

[7] Xu, S.Z., Lemington, Wang, R.Z., Wang, L.W., Zhu, J. (2018). A zeolite 13X/magnesium sulfate-water sorption thermal energy storage device for domestic heating. *Energy Conversion and Management*, vol. 171, p. 98-109, **DOI:10.1016/j.enconman.2018.05.077**.

[8] Yu, N., Wang, R.Z., Wang, L.W. (2013). Sorption thermal storage for solar energy. *Progress in Energy and Combustion Science*, vol. 39, no. 5, p. 489-514, **DOI:10.1016/j.pecs.2013.05.004**.

[9] Mette, B., Kerskes, H., Drück, H., Müller-Steinhagen, H. (2014). Experimental and numerical investigations on the water vapor adsorption isotherms and kinetics of binderless zeolite 13X. *International Journal of Heat and Mass Transfer*, vol. 71, p. 555-561, **DOI:10.1016/j.ijheatmasstransfer.2013.12.061**.

[10] Banaei, A., Zanj, A. (2021). A review on the challenges of using Zeolite 13X as heat storage systems for the residential sector. *Energies*, vol. 14, no. 23, art. ID 8062, **DOI:10.3390/en14238062**.

[11] Rogala, Z., Kolasiński, P., Gnutek, Z. (2017). Modelling and experimental analyzes on air-fluidised silica gel-water adsorption and desorption, *Applied Thermal Engineering*, vol. 127, p. 950-962, **DOI:10.1016/j.applthermaleng.2017.07.122**.

[12] De Antonellis, S., Colombo, L.P.M., Castellazzi, P., Rossetti, A., Marocco, L. (2024). System integration analysis of a zeolite 13x thermal energy storage. Energy and Built Environment, vol. 5, no. 4, p. 568-579, **DOI:10.1016/j.enbenv.2023.04.006**.

Strojniški vestnik - Journal of Mechanical Engineering 70(2024)3-4, 116-127
DOI:10.5545/sv-jme.2023.662
Original Scientific Paper
Received for review: 2023-05-31
Received revised form: 2023-10-31
Accepted for publication: 2023-11-20

Research on the Adaptability of Packers for Integrated String Fracturing Operations in Low Porosity and Low Permeability Reservoirs

Zhiyong Wan[1,*] – Hao Yu[1] – Yong Xiao[2] – Zhaoyang Zhao[1] – Zhanghua Lian[1] – Fangxin Chen[1]
[1] Southwest Petroleum University, State Key Laboratory of Oil and Gas Reservoir Geology and Exploitation, China
[2] Chengdu North Petroleum Exploration and Development Technology Co, Ltd, China

To study the failure of conventional packers in the fracturing and stimulation of low-porosity and low-permeability reservoirs and reduce the failure accidents of packers in the fracturing process, a suitable integrated string packers was selected in the process of fracturing and stimulation in an oilfield in the Middle East as a case study. Three different well types have been established. The wellbore temperature distribution and the axial force of the string can be calculated under the conditions of various wellhead pressures and different displacement, and it is found that the temperature at the bottom of the well can reach 130 °C, and the maximum axial force at the wellhead is 500 kN. At the same time, the applicability of retrievable tubing testing squeeze (RTTS) and hydraulic-set retrievable (RH) packer in different working conditions was evaluated, and it was found that only RTTS packers can meet the needs of the oil field. According to the calculated temperature field and axial force distribution, the stress on different components of the packer under different working conditions is established during the fracturing-stimulation operation. In the worst working conditions, the maximum stress of the packer occurs at the lower part of the central pipe, reaching 303.83 MPa, which is in a safe state. The contact stress on rubber rings can reach 30 MPa, indicating that the sealing performance can meet the requirements of on-site use. The temperature and axial force data calculated by the model provide a theoretical basis for safe well control. At the same time, through model evaluation, it was found that the RTTS packer can be suitable for the fracturing and stimulation needs of the oilfield. The research methods and achievements in the article provide theoretical guidance for evaluating the applicability of packers in the fracturing and stimulation process of low porosity and low permeability reservoirs.

Keywords: low porosity and low permeability reservoirs, integrated pipe string, packer rubber ring, acid fracturing, finite element simulation

Highlights

- *Established a practical applicability evaluation model for three types of well types used in a Middle Eastern oil field.*
- *Based on the results obtained from the adaptability evaluation model of the packer, combined with the finite element method to calculate the stress distribution of key components on the packer, it is found that the upper central pipe of the packer is a weak structure.*
- *Combined with the contact pressure and contact length obtained by finite element calculation, the sealing performance of the rubber ring under extreme conditions was evaluated, and the adaptability evaluation model of the rubber ring of the packer was established.*

0 INTRODUCTION

In recent years, with the improvement of mining technology, more low-porosity and low-permeability reservoirs have been developed. In order to activate the reservoir and increase production, it is necessary to use acid fracturing technology [1]. However, the reservoir is characterized by high crustal stress, easy leakage, interlayer interaction, strong formation heterogeneity, relatively developed fractures, and great difficulty in oil testing and reservoir reconstruction. The conventional operation of lowering the string multiple times cannot meet the requirements of oil and gas well testing and acidizing stimulation operations [2]. Therefore, in the process of acid fracturing operation, the perforation-fracturing-completion triple integrated string operation is adopted, which has reliable tool function and stable performance, reducing the number of frequently lowered strings and damage to the reservoir [3]. It can also improve construction efficiency, save the cost of exploration and development, avoid the secondary pollution of the formation by the well control fluid to the greatest extent, meet the needs of environmental protection, fracturing displacement and efficient construction [4], and can solve the problem of out-of-control wellhead during the installation of blowout preventers, to reduce well control risks, construction risks and operating costs [5]. To realize the perforation-fracturing-completion operations once, the design of the integrated string is more stringent. There are still defects, such as insufficient understanding in the design, which seriously restricts the development of

*Corr. Author's Address: State Key Laboratory of Oil and Gas Reservoir Geology and Exploitation, Southwest Petroleum University, China, 202122000793@stu.swpu.edu.cn

special reservoir characteristics, such as low porosity and low permeability [6] and [7].

At present, the research on the design of the integrated string mainly focuses on the research on the failure of the thread seal [8] and [9], the construction process of the integrated operation string [10], and the design of the perforation-pressure test dual string. For harsh reservoir conditions, such as low porosity and low permeability, research on the use of perforating-fracturing-completion triple-integrated operation strings is lacking. In conventional production operations, the string is often run in three times, which increases the risk of reservoir damage, and the wellhead needs to be lifted and lowered multiple times, which increases the risk of well control failure. Compared with the integrated operation string, the construction operation time is increased, as are the development costs of oil and gas reservoirs [11]. Therefore, this article focuses on three different well types developed in a Middle Eastern oil field with low porosity and low permeability reservoirs, namely vertical wells, deviated wells, and horizontal wells. Key components in the integrated perforation fracturing completion operation string used for special reservoir development include a numerical simulation model for wellbore string temperature and axial force during perforation and fracturing processes, as well as an evaluation model for the applicability of packers, which was established through software. The simulated temperature and axial force data were then combined with finite element analysis software. Conduct applicability analysis and research on key components of integrated operation string, provide theoretical basis and guidance for the failure research of key components of integrated operation string used in oil fields, and also provide theoretical basis for the design of integrated operation string and various safe construction operations.

1 INTEGRATED PIPE STRING STRUCTURE AND ANALYSIS OF ITS STRESS CONDITIONS

1.1 Structure and Working Principle of Key Components of Integrated Pipe String

At present, in the development process of some oil and gas fields, multiple lowering pipe strings are used [12]. The schematic diagram of the operation process is shown in Fig. 1.

First, the well-cleaning and scraping strings are lowered to clean the debris attached to the inner wall of the strings, and then the perforated strings are lowered for perforation operations, and finally the acid fracturing and well completion operations are performed. During this series of operations, it is necessary to open the wellhead several times to raise and lower the pipe string, increasing the risk of well control failure, but the integrated operation string can prevent it. Therefore, an oilfield in the Middle East actually uses the perforation-fracturing-completion triple integrated operation string, which consists of tubing, rupture disk (RD) cycle valve, rupture disk safety (RDS) valve, OMNI™ valve, packer, tubing conveyed perforation (TCP) gun and other components. The three different wellbore structures and integrated pipe strings used are shown in Fig. 2.

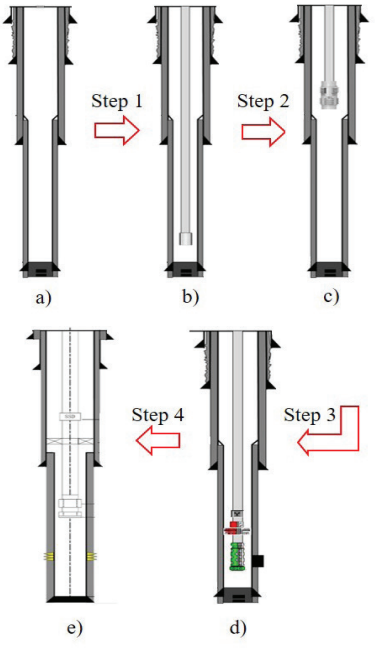

Fig. 1. *Schematic diagram of the operation process of repeatedly lowering the pipe column; a) hole structure, b) wiper string, c) scraper string, d) perforation string, and e) completion string*

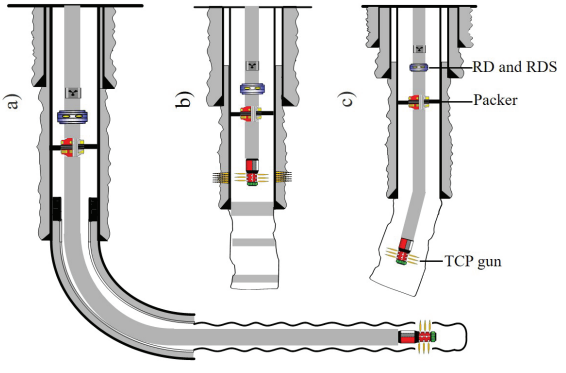

Fig. 2. *Schematic diagram of three types of wellbore structures and integrated pipe string structures; a) horizontal well, b) vertical well, and c) deviated well*

As a key component of the integrated string, the packer determines the sealing performance of the operating string during perforation and acid fracturing; therefore, an in-depth safety analysis is required. There are two packer selection schemes on site: the RTTS packer and the RH packer. The technical parameters and manufacturer of the packer are shown in Table 1 The structural schematic diagrams of the two packers are shown in Fig. 3.

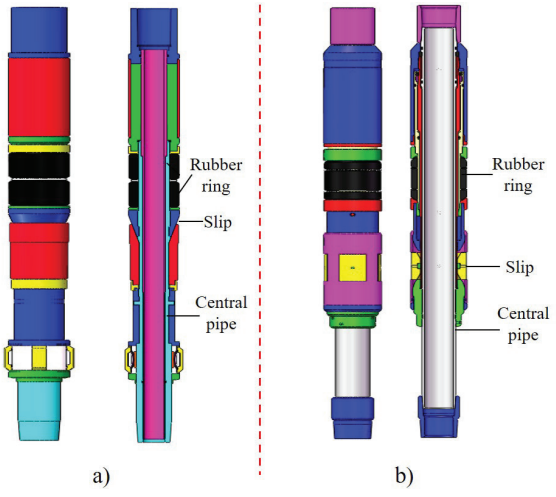

Fig. 3. *Structural schematic diagram of; a) RTTS packer, and b) RH packer*

The RTTS packer is a suspension packer with a large diameter and can seal off two-way pressure. It consists of a slot transposition mechanism, slips, rubber ring and hydraulic anchoring mechanism. The hydraulic anchoring mechanism can prevent the lower part of the packer from being pushed out of the wellbore when the pressure is too high. It is also equipped with friction blocks and an automatic groove sleeve structure. Designed for formation testing, acidizing, and cementing plug well operations, the large diameter is used to pump a large amount of fluid under a small pressure drop and can pass through the tubing perforating gun. Its working principle is that when it is necessary to seal the annular space between the tubing and the production casing, the upper limit groove of the packer is rotated so that the upper structure of the packer can move axially within the allowable range of the limit. When the string applies a part of its own weight and axial displacement to the RTTS packer, the slips are stretched to fix the packer on the inner wall of the production casing, and then continue to apply its own weight and axial displacement until the rubber ring of the packer is fully supported and the annulus between the oil pipe and the production casing is completely sealed.

The other type of packer planned to be selected on site is the hydraulic retrievable packer, which is a compact, sturdy, reliable, convenient to use, single column hydraulic retrievable packer that can be directly lifted up and released. It is suitable for applications such as deviated wells, multi packer completion. The envelope curves for the sealing performance of two types of packers are shown in Fig. 4.

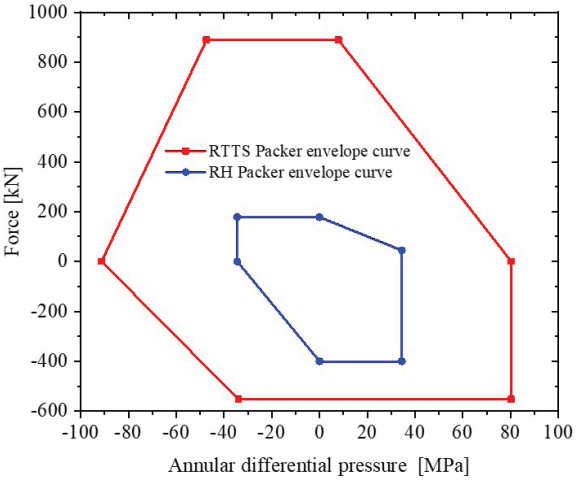

Fig. 4. *Envelope Curve of RTTS Packer and RH Packer*

The packing capacity of the two packers selected on site can be obtained from Fig. 4. The red shape in the figure is the envelope curve of the RTTS packer, while the envelope curve of the RH packer is the blue shape, and the envelope of the RTTS packer completely encompasses the RH packer, indicating that the packing ability of the RTTS packer is better than that of the RH packer.

Table 1. *Manufacturer and technical characteristics of the packers*

Packer type	Maximum outer diameter [mm]	Minimum inner diameter [mm]	Length [mm]	Working pressure [MPa]	Working temperature [°C]	Applicable tubing diameter [mm]	Manufacturer
RTTS	201	124	1450	25 to 100	20 to 150	177.8	GWDC
RH	213	137	1300	10 to 60	20 to 120	177.8	TechWest

1.2 Theoretical Analysis of the Failure of Key Components of Packers

As an important part of ensuring the sealing ability of the packer, the packer rubber ring needs to be analysed thoroughly. The rubber ring is made of rubber, which is a typical hyper-elastic body.[13] and [14] It is often described with the Mooney-Rivlin constitutive model, and its constitutive relation expression is:

$$W = C_{10}(I_1 - 3) + C_{01}(I_2 - 3), \tag{1}$$

where W is the density of strain energy [J/m³], C_{10} and C_{01} are the Mooney-Rivlin coefficients of the material [MPa], and I_1 and I_2 are the first and second strain tensor invariant, [1].

The relationship between shear modulus and elastic modulus is:

$$\begin{cases} E = 6(C_{10} + C_{01}) \\ G = 2(C_{10} + C_{01}) \end{cases}. \tag{2}$$

According to the large deformation properties of rubber, the relationship between its elastic modulus E, shear modulus G and material constants is:

$$\begin{cases} E = 6(C_{10} + C_{01}) \\ G = 2(C_{10} + C_{01}) \end{cases}. \tag{3}$$

According to the rubber compression test, due to E = 11.49 MPa, the simulation results are relatively close to the measured results, resulting in C_{10} = 1.879 MPa and C_{01} = 0.038 MPa.

In acid fracturing operations, the fracturing fluid injected from the wellhead is regarded as a Newtonian fluid, and when it flows to the target layer, the calculation formula for pipe flow friction is:

$$R_e = \frac{\rho v_t d}{\mu}, \tag{4}$$

where R_e is the pipe flow friction; ρ is the fluid density [kg/m³], v_t the fluid velocity, [m/s], d the inner diameter of the pipe column [m], and μ the fluid viscosity, [kg/(s·m)].

When the Reynolds number R_e of the acid fluid in the wellbore is less than 2000, the flow state of the acid fluid in the wellbore is a laminar flow state. At this time, the hydraulic friction coefficient of the fracturing fluid in the wellbore in the pipeline is [15]:

$$f = \frac{64}{R_e}. \tag{5}$$

When the Reynolds number R_e of the acid fluid in the wellbore is greater or equal to 2000, it is in a turbulent state. At this time, the hydraulic friction coefficient of the fracturing fluid in the wellbore in the pipeline is:

$$f = \frac{0.079}{R_e^{0.25}}. \tag{6}$$

However, when the fluid flows to the bottom of the well in the annular space, it will be subjected to friction along the way to reduce the pump pressure. The formula for calculating the friction loss of the fluid along the way is:

$$\Delta P = f \frac{\rho L v_t^2}{2gd}, \tag{7}$$

where ΔP is the frictional loss along the way [kg/m²], L is the length of the pipeline along the route [m], and g is the gravitational acceleration [m/s²].

When the fluid reaches the bottom of the well, since the temperature of the injected fluid at the wellhead is much lower than the temperature of the downhole formation, the temperature of the wellbore will change during the acid fracturing operation, resulting in thermal expansion and contraction.

The temperature effect expression is [16]:

$$\varepsilon_T = a \cdot \Delta T, \tag{8}$$

where ε_T is the thermal expansion elongation per unit length [m/m = 1], the expansion coefficient [m/°C] and ΔT the temperature difference [°C].

In the process of acid fracturing, it is often necessary to suppress the pressure of the wellbore, and the pressure mainly acts on the inner wall of the string, which will cause the axial deformation of the string. At the same time, in order to protect the downhole tools, such as packers, from failure, it is necessary to apply pressure to the annulus by squeezing the string from outside to inside will result in a reduction in the diameter of the string and an axial elongation.

The pressure inside the tubing consists of two parts: pump pressure and the hydrostatic column pressure of the liquid inside the tubing.

$$P_i = P_p + \rho_i g h, \tag{9}$$

where P_i is the pressure inside the tubing [MPa], P_p is the surface pump pressure [MPa], and ρ_i the fluid density inside the casing [kg/m³].

The external pressure of the pipeline is mainly the static liquid column pressure of the annular liquid, which is $P_o = \rho_o g h$, where ρ_o is the density of liquid in the annular space [17] and [18].

The total axial deformation of the oil pipe under the combined action of internal and external pressures is:

$$\Delta l = -\int_0^H \frac{2v}{E} \cdot \frac{P_o R^2 - P_i}{R^2 - 1} dh, \quad (10)$$

where d_o is the outer diameter of the oil pipe [m], d_i the inner diameter of the oil pipe [m] where $R = d_o / d_i$, H the depth of pipe string [m], and v Poisson's ratio.

When the axial load on the string in the wellbore exceeds a certain critical value, the string will lose its stable state and buckle, causing the string to shrink, shorten, bend, and deform, and increase the friction between the string and the wellbore. The axial deformation of the packer will cause the seal failure of the packer and even the plastic failure of the string.

Then the true axial force of the tubing cross section at any well depth is F_a, and the equivalent axial force F_e is:

$$F_e = F_a + P_o A_o - P_i A_i, \quad (11)$$

where A_o is the outer circular area of the column cross-section [mm²], and A_i is the internal circular area of the pipe column cross-section [mm²].

The critical value of helical buckling deformation of the pipe column is **[19]**:

$$F_{hel} = 5.55\sqrt[3]{EIq_m^2}, \quad (12)$$

where F_{hel} is the critical buckling load [kN], q_m is the line floating weight of the oil pipe [kN/m] and EI is the bending stiffness of the oil pipe [kN·m²].

When the pipe column is in a helical buckling state, the bending stress on the pipe column σ_m is:

$$\sigma_m = \frac{M}{W} = \frac{2Fr_{out}^2}{\pi(r_{out}^4 - r_{in}^4)}, \quad (13)$$

where σ_m is the bending stress when the pipe string undergoes helical buckling [MPa], M is the bending moment at the central pipe when the pipe column undergoes helical buckling [N/mm], and W is the bending section coefficient of a circular section [mm³].

By calculating the stress on the string and comparing it with the yield strength of its material, if it is less than the yield strength, it means that the pipe string is still in a safe state. Although the average stress on the integrated pipe string can be evaluated and calculated by Eq. (13), the pipe string is not regular, and it is impossible to accurately calculate the force on the upper part of the packer with an analytical formula, and only the finite element method can be used for simulation.

2 TEMPERATURE AND AXIAL FORCE ANALYSIS OF INTEGRATED PIPE STRING

According to the data provided by the Halfaya Oilfield in Iraq **[20]**, the average porosity of the B1, B2, and B3 sub-member of the Sadi Formation is 17.5 %, 19.3 %, and 13.6 %, respectively, and the average permeability is 0.13 mD, 0.2 9 mD, and 5.11 mD, respectively. It belongs to a low porosity, ultra-low permeability carbonate reservoir, with a wellbore temperature of 25 °C, a fracturing fluid density of 1200 kg/m³, a wellhead injection pressure of 30 MPa to 50 MPa, and a displacement of 3 m³/min to 5 m³/min, The data on the wellbore structure and the integrated string structure used are summarized in Table 2, The geological structure of the Halfaya Oilfield is shown in Fig. 5.

X1 to X3 wells are three typical well types developed in an oil field in Middle East. The obtained data were used to establish an integrated string temperature and axial force analysis model using software, and the temperature, axial force, axial safety factor, and packer applicability were calculated for different layers of the wellbore structure.

2.1 Analysis of Temperature Field Calculation Results for Integrated Pipe String

Since the higher the wellhead pumping pressure and displacement, the larger the volume of the pumped fluid, the more intense the downhole string cooling, so the analysis and calculation of the temperature of the three wellbore structures when the wellhead pumping pressure is 50 MPa and the pumping displacement is 5 m³/min The field distribution diagram is shown in Fig. 6. It is found that during the acid fracturing process, the temperature of the tubing string at all levels in the wellbore increases to varying degrees compared

Table 2. *Summary of well bore structure and integrated pipe string structure data used*

Number	Well type	Well depth [m]	Intermediate casing diameter [mm]	Production casing diameter [mm]	Tubing diameter [mm]	Packer depth [m]
X1	Vertical	4000	381.0	254.0	177.80	2100
X2	Deviated	2500	/	254.0	177.80	2200
X3	Horizontal	3750	342.9	247.65	177.80	1900

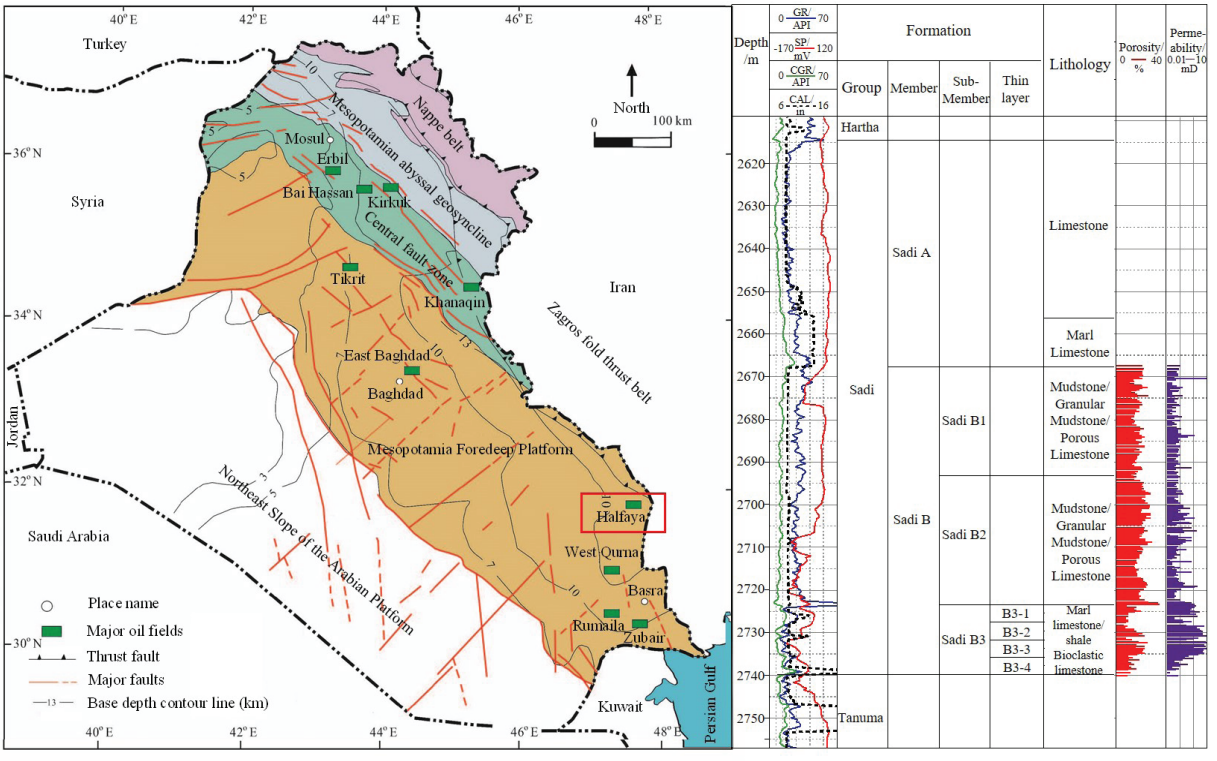

Fig. 5. *Sadi formation information comprehensive histogram*

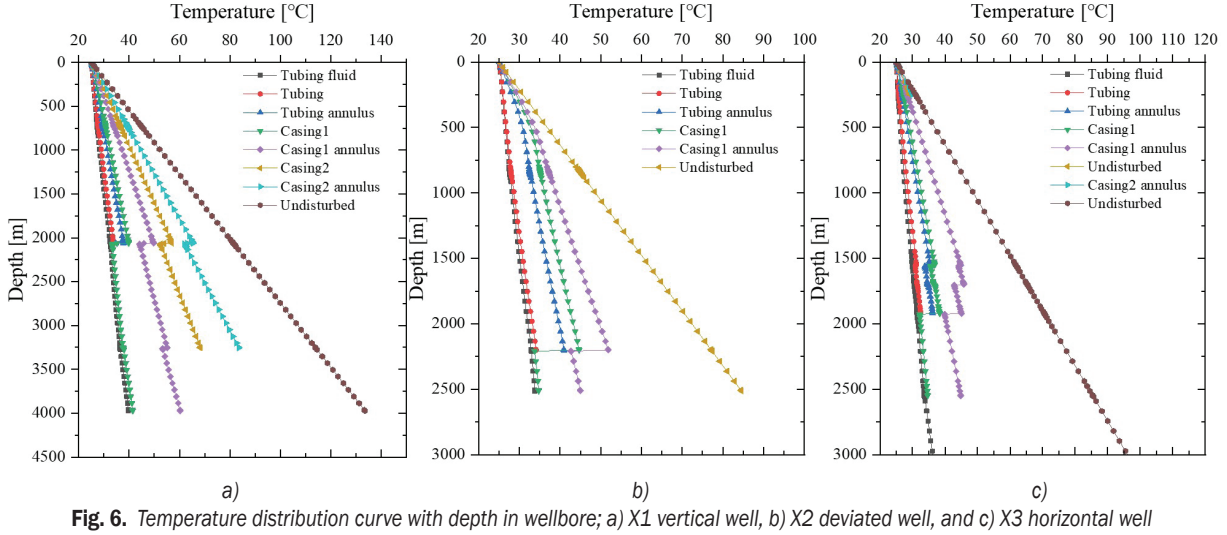

Fig. 6. *Temperature distribution curve with depth in wellbore; a) X1 vertical well, b) X2 deviated well, and c) X3 horizontal well*

with the wellhead. However, due to the injection of fracturing fluid into the wellhead, the temperature near the oil pipe is lower at the same depth, and the farther layers are closer to the formation temperature. Additionally, due to the role of the integrated string packer, temperature faults occur at the packer, as shown in Table 3.

Table 3. *Temperature statistics at the upper and lower packers*

Number	Well type	Packer depth [m]	Upper [°C]	Lower [°C]
X1	Vertical	2100	38.5	27.3
X2	Deviated	2200	33.2	26.7
X3	Horizontal	1900	31.9	25.8

2.2 Analysis of Axial Force Calculation Results for Integrated Pipe String

Because the axial force of the integrated pipe column directly determines the safety status of the pipe column during service, attention needs to be paid to it, so the axial force distribution curve of the integrated string under different displacement and pump pressure conditions is obtained through software simulation calculation, as shown in Fig. 7, it is found that the axial force of the string at the wellhead is axial tension, while the axial compression force is generated at the bottom of the well, and the position where the axial force is 0 appears at the packer. Due

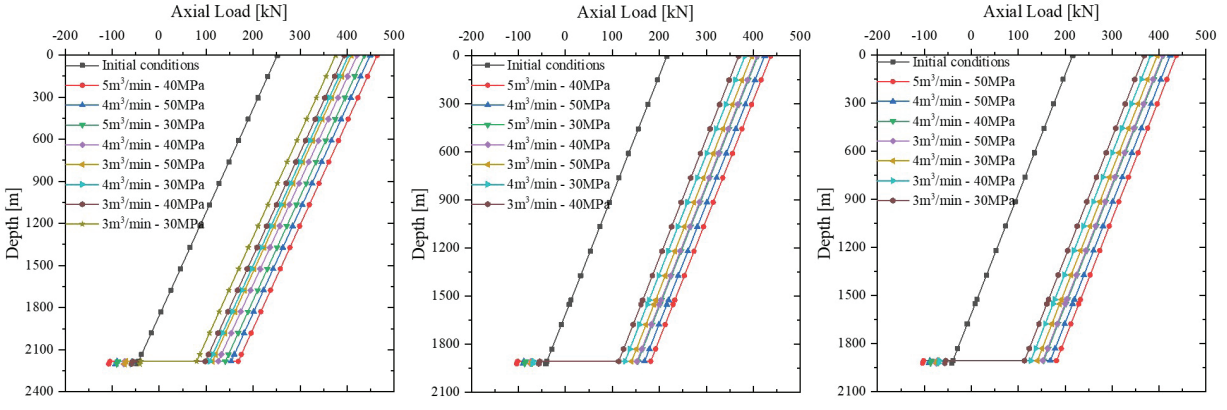

Fig. 7. *Distribution curve of axial force in Wellbore with depth; a) X1 vertical well, b) X2 veviated well, c) X3 horizontal well*

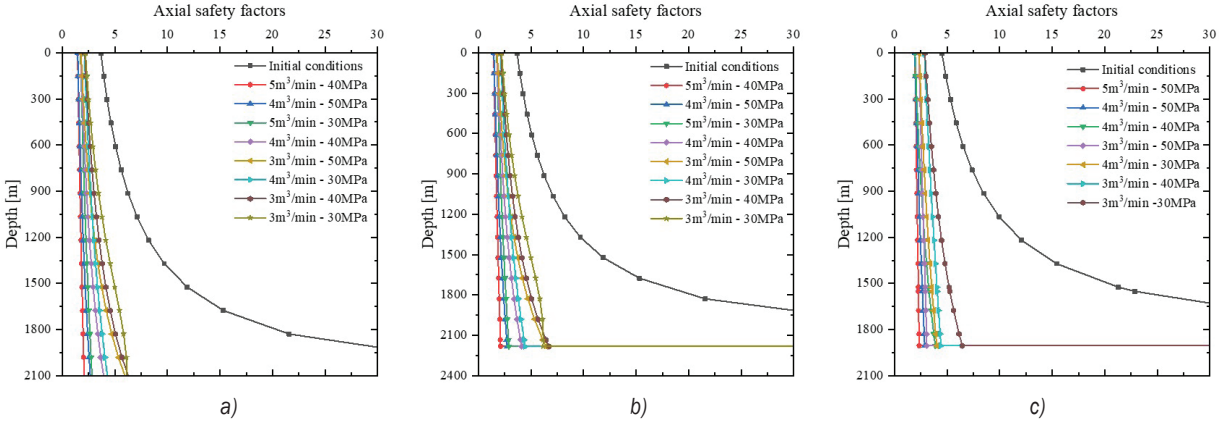

Fig. 8. *Distribution curve of axial safety factor in Wellbore with depth; a) X1 vertical well, b) X2 deviated well, c) X3 horizontal well*

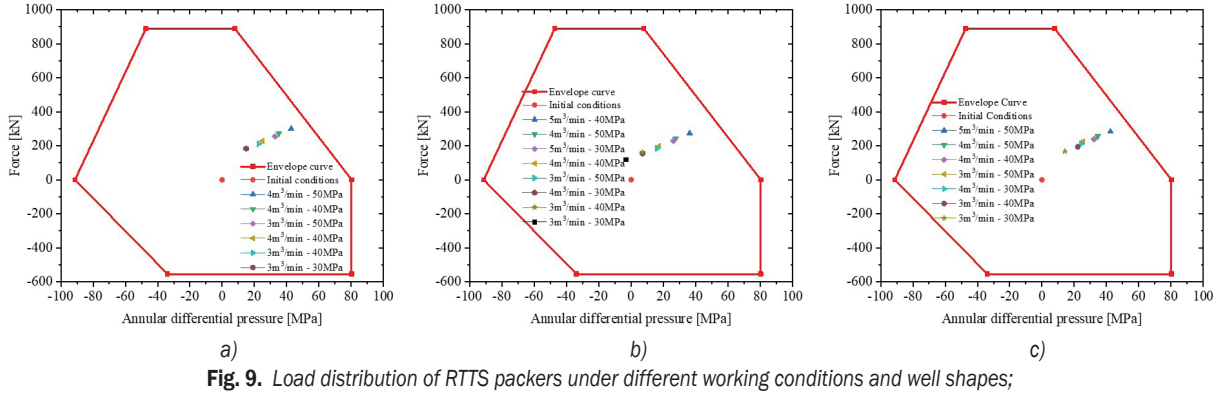

Fig. 9. *Load distribution of RTTS packers under different working conditions and well shapes; a) X1 vertical well, b) X2 deviated well, c) X3 horizontal well*

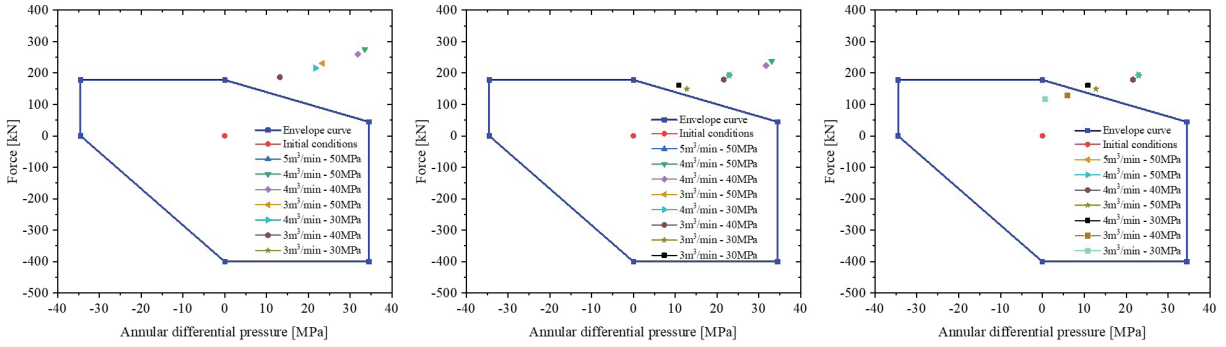

a) b) c)

Fig. 10. *Load distribution of well completion packers under different working conditions and well shapes; a) X1 vertical well, b) X2 deviated well, c) X3 horizontal well*

to the cold contraction of the pipe string during the acid fracturing process, the normal packer prevents the displacement of the string. In order to intuitively judge the safety state of the string, the axial safety factors of each well type are summarized in Fig. 8 It is found that the axial safety factors of all pipe strings are greater than 1, indicating that the pipe strings are in a safe state and there will be no phenomenon of plastic tensile fracture.

Through model calculation, the evaluation diagrams of load and envelope curves of RTTS packer and RH packer are shown in Figs. 9 and 10. It is found that the RTTS packer is applicable in all working conditions, and the RH packer cannot be applied in most cases due to its weak packer capability.

3 STRESS ANALYSIS OF INTEGRATED STRING PACKER

3.1 Establishment of Finite Element Model for RTTS Packer

According to the model established in the second section, the analysis shows that only the RTTS packer is suitable for the use of the integrated string in this oilfield; therefore, based on the actual use of the integrated string structure in an oilfield in Middle East, a static 2D axisymmetric finite element mechanical simulation of the RTTS packer is established using ABAQUS. In the finite element model, the number of finite elements is 17,207, the number of nodes are 18455, including 16.837 quadrilateral finite elements (CAX4R), 370 triangular finite elements (CAX3), the size of the casing finite elements is 10 mm, the size of the centre pipe is 10 mm, and the other components are 1 mm. The model and its finite elements model are shown in Fig. 11. In the figure, the RTTS packer is mainly composed of connectors, rubber ring, spacers, slip cones, slips, and tubing. When the RTTS packer is in normal operation, pressure is applied downwards from the connectors, and squeezed after the slip pressure cone stretches the slips, it bites on the inner wall of the casing to fix the packer and then continues to exert axial pressure on the joint to squeeze and deform the rubber ring to seal the inner wall of the casing, so that the centre pipe and the annulus between the casing can maintain a certain pressure difference between the upper and lower sides, so as to avoid the temperature effect caused by the temperature decrease during the acid fracturing process, which will cause the axial displacement of the integrated pipe string.

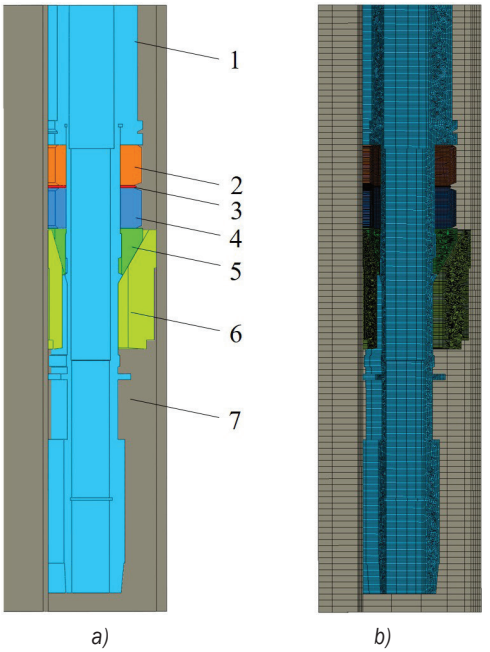

a) b)

Fig. 11. *Finite Element Mechanical Model of RTTS Packer; a) solid model, and b) finite elements model; (1 connector, 2 and 4 rubber ring, 3 spacer ring, 5 slip cone, 6 slip, and 7 casing)*

The RTTS packer mainly uses two materials: steel and rubber. The Poisson's ratio of the steel is 0.3, the elastic modulus is 2.1×10^5 MPa, the yield strength is 758.6 MPa, and the tensile strength is 862 MPa. Comprising propylene-polytetrafluoroethylene material, high temperature resistance, high pressure, reliable sealing performance, compressive strength up to 60 MPa, the rubber ring and the end protection ring are vulcanized into one, prevent shoulder protrusions on the rubber ring, improve the pressure resistance of the rubber ring, and are used for the rubber material of the rubber ring Mooney-Rivlin constitutive model, in which parameters C_{10} = 1.879 MPa, $C_{0\ 1}$= 0.038 MPa, and temperature and axial force data obtained by software simulation are attached to the packer. The force situation of the packer from running into fracturing operation is simplified into four steps: the stage of fixed constraint, the stage of applying gravity, the stage of applying setting force, and the stage of applying internal and external pressure and axial force. The whole load and boundary a summary of the conditions imposed is shown in Fig. 12. In the fixed constraint stage, the slips are in a fixed state during the entire stress process, so fixed constraints are applied to the lower part of the slips, and secondly, in the gravity application stage, after the slips are fixed, the gravity of the entire string is applied to the packer. Then apply the upper axial force on the joint in the stage of applying the setting force, and finally apply the lower axial force and the internal and external pressure in the model in the stage of applying the internal and external pressure and axial force, which were simulated in Section 2 and are affected by the temperature difference; the applied load is shown in Table 4.

3.2 Finite Element Analysis Results of RTTS Packer

Through the finite element calculation of the established model, the stress distribution image of the three wells under different acid fracturing conditions are shown in Fig. 13.

Analysis of the worst acid fracturing conditions in the field, when the wellhead pressure is 50 MPa and the displacement is 5 m³/min, the maximum stress on the packer does not exceed 400 MPa, which is much smaller than the yield strength of the RTTS packer, indicating that at this time it is in the safe state, the maximum stress value appears in the lower part of the

Table 4. *Summary of the stress situation during the setting stage of RTTS packer*

Well number	Axial force F1 [kN]	Axial force F2 [kN]	Internal pressure Pin [MPa]	Upper external pressure Pout1 [MPa]	Lower external pressure Pout2 [MPa]
X1	100	84.28	61.98	19.59	61.98
X2	100	106.87	64.18	27.98	64.14
X3	100	103.77	50.38	18.64	50.34

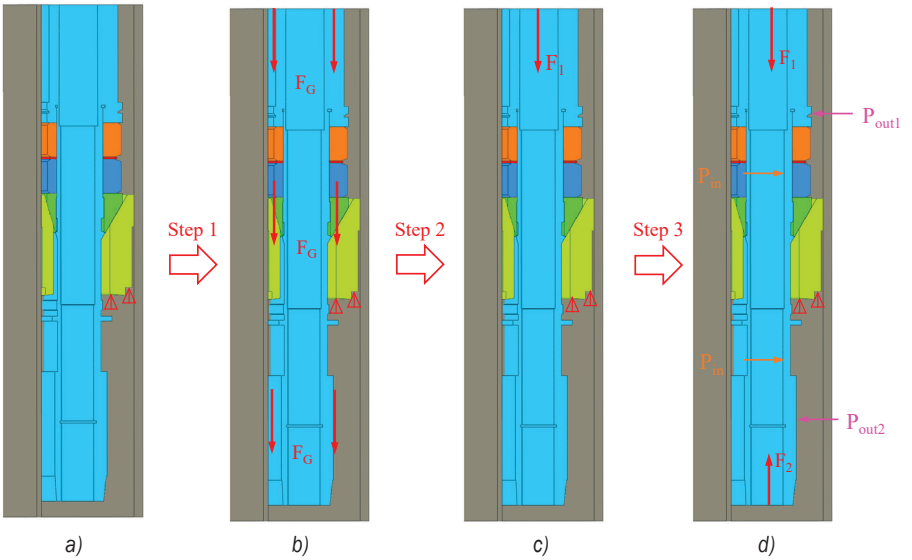

Fig. 12. *Schematic diagram of constraints and forces during the setting stage of RTTS packer; a) fixed constraints, b) apply gravity, c) apply sealing force, and d) apply pressure and axial force*

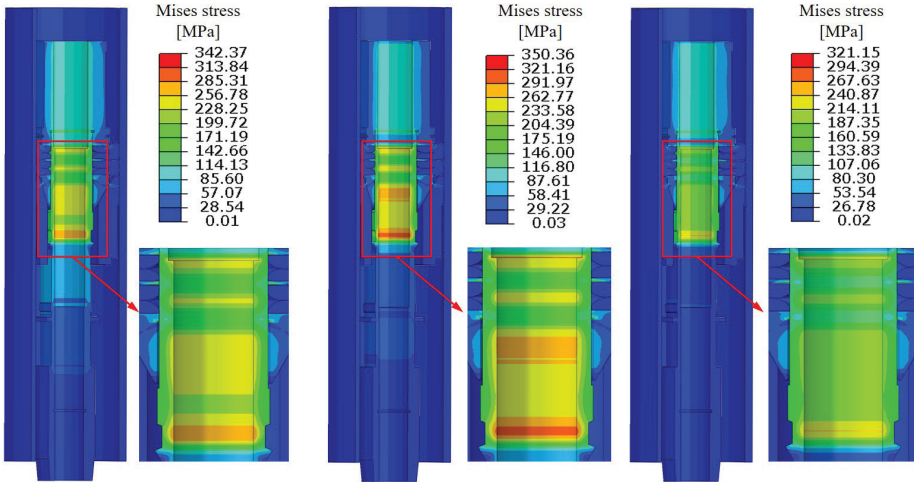

Fig. 13. *Stress distribution image of RTTS packer under acid fracturing conditions; a) X1 vertical well, b) X2 deviated well, and c) X3 horizontal well, (1 central tube, 2 rubber ring, 3 slip, and 4 casing)*

centre pipe, and the rubber ring is greatly deformed, completely sealing the annulus between the pipe strings, and achieving a complete seal, indicating that the RTTS packer can meet the actual requirements of the site. However, in order to achieve the purpose of eliminating potential safety hazards in actual operation, it is recommended to increase the wall thickness of the lower part of the central tube.

As a key component for sealing in the packer, the rubber ring can be evaluated for its sealing performance using the Mises stress and contact pressure on the rubber ring. Therefore, the Mises distribution image and contact pressure distribution image were obtained through a finite analysis model, as shown in Figs 14 and 15, respectively. From the Mises distribution image, it is found that in the worst working conditions of each well, the maximum stress on the rubber ring has reached 60 MPa, but the material of the rubber ring is a special type of rubber, it still does not break under the stress state. The reason for the possible failure of the upper rubber ring is the failure of the seal; the contact pressure of the rubber ring in contact with the outer wall is 0 MPa. As shown in Fig. 16, the distribution shows that the maximum

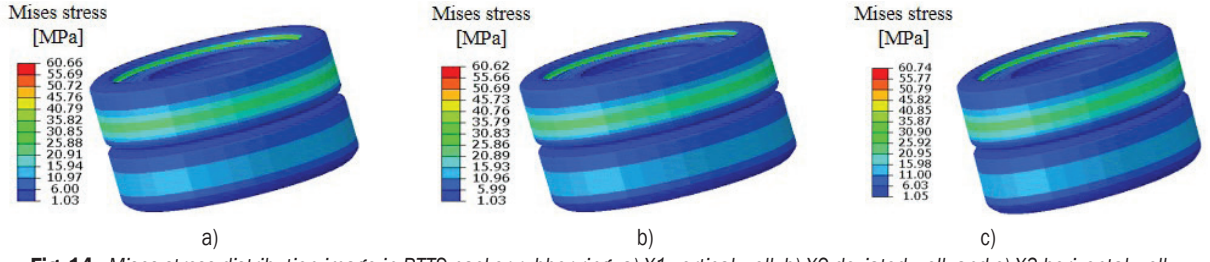

Fig. 14. *Mises stress distribution image in RTTS packer rubber ring; a) X1 vertical well, b) X2 deviated well, and c) X3 horizontal well*

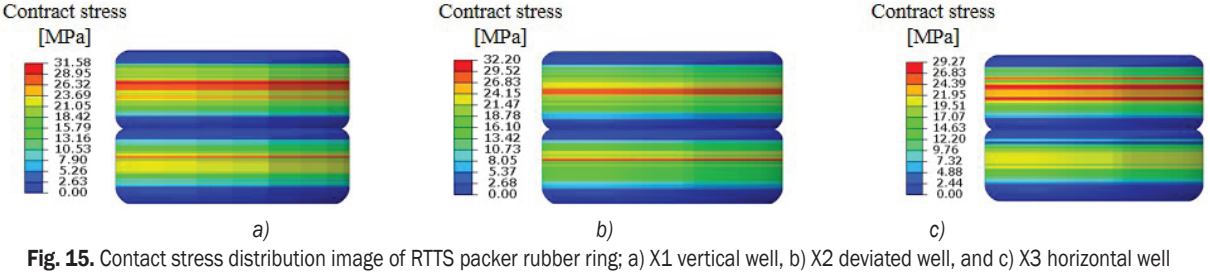

Fig. 15. Contact stress distribution image of RTTS packer rubber ring; a) X1 vertical well, b) X2 deviated well, and c) X3 horizontal well

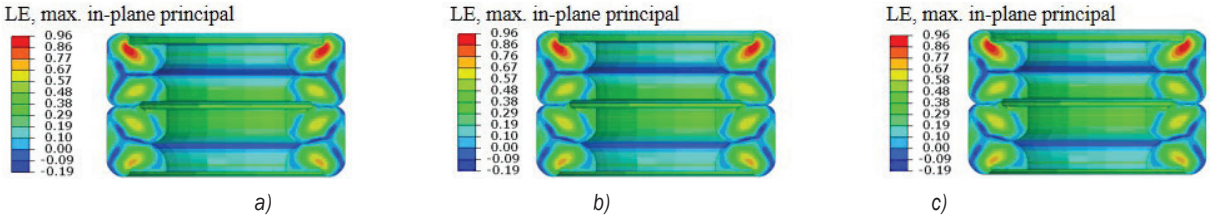

a) b) c)

Fig. 16. *Strain distribution image of RTTS packer rubber ring; a) X1 vertical well, b) X2 deviated well, and c) X3 horizontal well*

principal logarithmic strain of the upper rubber ring is greater than that of the lower rubber ring, but the material of the rubber ring is rubber. In the case of such a large strain, it can still work safely, but the extrusion part of the upper joint can be optimized in the design. The structure makes the deformation of the upper and lower joints similar, unifies the service life of the packer rubber ring, and facilitates the replacement of the rubber ring at the same time.

The contact pressure distribution curve of the contact part between the packer rubber ring and the outer wall casing is extracted, as shown in Fig. 17; the contact pressure on the rubber ring reaches about 30 MPa, indicating that the rubber ring can still maintain good performance under the worst working conditions. The sealing performance is excellent, and the contact pressure of the upper rubber ring is larger than that of the lower rubber ring, but it can fully meet the requirements of the integrated string packer in the oil field.

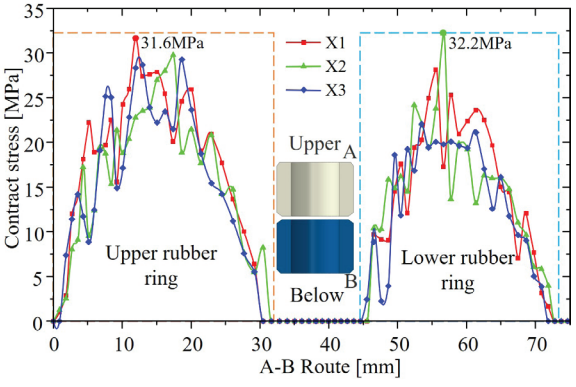

Fig. 17. *Contact pressure distribution curve of the contact part of the rubber ring*

4 CONCLUSIONS

(1) Based on the dimensions and production data of three different wellbore structures provided on site, a multi-factor analysis model for the wellbore was established. The temperature, axial force of the tubing, and safety factor distribution of each part of the wellbore were calculated for three different wellbore types in a middle eastern oilfield. The analysed data provides a theoretical basis for on-site well control.

(2) According to the finite element model of the mechanical distribution of the packer structure during acid fracturing established in this article, this model can simulate the stress distribution of various components in the packer under various working conditions during the acid fracturing process after the packer is set, and then evaluate the adaptability of the packer. It provides a reliable theoretical basis for the safety evaluation of the packer in the safe production of oil and gas fields.

(3) The three types of wells studied in the article can all meet the needs of safety production using RTTS packers. However, the use of completion packers can lead to insufficient sealing capacity and safety production hazards. Therefore, using RTTS packers in integrated pipe strings is recommended.

(4) Through a large number of finite element calculations and analyses, the packer can withstand the wellhead displacement of 5 m^3/min and wellhead pressure of 50 MPa, which is the worst production condition on site. At this time, the maximum stress of the packer appears on the centre pipe of the packer, so special attention should be paid in the production process, and the contact pressure on the rubber ring reaches 30MPa without sealing contact failure.

(5) In the process of fracturing bottom layer stimulation, when the normal temperature fracturing fluid injected at the wellhead reaches the target formation, it causes the downhole string to cool down, causing the axial tension of the string to reach 500 kN due to thermal expansion. In order to reduce the axial tension of wellhead equipment and prevent accidents such as wellhead falling, adding expansion joints in the string is recommended.

5 ACKNOWLEDGEMENTS

This work was supported by the Sichuan Province Science and Technology Program (No. 2023NSFSC0427).

6 REFERENCES

[1] Qi, N., Chen, G.B., Liang, C., Guo, T.K., Liu, G.L., Zhang, K. (2019). Numerical simulation and analysis of the influence of fracture geometry on wormhole propagation in carbonate reservoirs. *Chemical Engineering Science*, vol. 198, no. 1, p. 124-143, **DOI:10.1016/j.ces.2018.12.047**.

[2] Zhu, D., Hu, Y., Cui, M., Chen, Y., Liang, C., He, Y., Wang, X., Wang, D. (2019). Feasibility analysis on the pilot test of acid fracturing for carbonate reservoirs in Halfaya Oilfield, Iraq. *Energy Science & Engineering*, vol. 7, no. 3, p. 721-729, **DOI:10.1002/ese3.290**.

[3] Al-salali, Y, Al-Bader, H, Duggirala, V., Manimaran, A., Packirisamy, S., Al-Ibrahim, A., Rajkhowa, A. (2013). Challenges in testing and completion of highly sour HPHT reservoir in the State of Kuwait. *SPE Kuwait Oil and Gas Show and Conference*, art. ID 164311, **DOI:10.2118/164311-MS**.

[4] Bybee, K. (2006). Continuous improvements in acid fracturing at Lake Maracaibo. *Journal of Petroleum Technology*, vol. 58, no. 7, p. 54-56, **DOI:10.2118/0706-0054-JPT**.

[5] Cohen, C.E., Tardy, P.M.J., Lesko, T.M., Lecerf, B.H., Mchaweh, A. (2010). Understanding Diversion with a Novel Fiber-Laden Acid System for Matrix Acidizing of Carbonate Formations. *SPE annual technical conference and exhibition*, art. ID 134495, **DOI:10.2118/134495-MS**.

[6] Chen, Y., Tan, J., Xiao, G. (2021). Investigation on the depth of slip hanger teeth bite into casing and the mechanical properties of casing under different suspension loads in ultra-deep wells. *Strojniški vestnik-Journal of Mechanical Engineering*, vol. 67, no. 10, p. 516-524, **DOI:10.5545/sv-jme.2021.7251**.

[7] Qi, Y., Wu, Z.F., Bai, X.H. (2013). Fracture design optimization of horizontal wells targeting the Chang 6 formation in the Huaqing Oilfield. SPE Asia Pacific Unconventional Resources Conference and Exhibition, art. ID 167008, **DOI:10.2118/167008-MS**.

[8] Hassani, F., Faisal, N.H., Nish, R., Rothnie, S., Njuguna, J. (2021). The impact of thermal ageing on sealing performance of HNBR packing elements in downhole installations in oilfield wellhead applications. *Journal of Petroleum Science and Engineering*, vol. 208, p. 109200, **DOI:10.1016/j.petrol.2021.109200**.

[9] Zhang, J., Xie, J. (2018). Investigation of static and dynamic seal performances of a rubber O-ring. Journal of Tribology, vol. 140, no. 4, art. ID 042202, **DOI:10.1115/1.4038959**.

[10] Koblar, D., Škofic, J., Boltežar, M. (2014). Evaluation of the young's modulus of rubber-like materials bonded to rigid surfaces with respect to Poisson's ratio. *Strojniški vestnik-Journal of Mechanical Engineering*, vol. 60, no. 7-8, p. 506-511, **DOI:10.5545/sv-jme.2013.1510**.

[11] Polonsky, V. L., Tyurin, A. P. (2015). Design of packers for sealing of the inter-tube space in equipment used for recovery of oil and gas. *Chemical and Petroleum Engineering*, vol. 51, no. 1-2, p. 37-40, **DOI:10.1007/s10556-015-9994-2**.

[12] Lopez, G. J. N., Amaya, M., Mora, J. H., Agudelo, O. (2010). Integrated sand-production management in a heterogeneous and multilayer mature field with water injection. *SPE Latin America and Caribbean Petroleum Engineering Conference*, art. ID. 139378, **DOI:10.2118/139378-MS**.

[13] Liu, Y., Lian, Z.H. (2021). Failure analysis on rubber sealing structure of mandrel hanger and improvement in extreme environments. *Engineering Failure Analysis*, vol. 125, art. ID 105433, **DOI:10.1016/j.engfailanal.2021.105433**.

[14] Liu, Y., Qian, L., Xia, C., Zou, J., Lian, Z.H., Yi, X. (2023). Failure analysis and structural optimization of rubber core and support rib of full-size spherical blowout preventer. *Engineering Failure Analysis*, vol. 143, art. ID 106865, **DOI:10.1016/j.engfailanal.2022.106865**.

[15] Karadžić, U., Bergant, A., Starinac, D., Božović, B. (2019). Water hammer investigation of the shut-down of a high-head hydropower plant at very high Reynolds number flows. *Strojniški vestnik-Journal of Mechanical Engineering*, vol. 65, no. 7-8, p. 430-440, **DOI:10.5545/sv-jme.2019.6092**.

[16] Jin, L., Xue, Z., Wang, Z., Li, R., Liu, J. (2023). Mechanical response of the sealing packer based on two rubber materials at high temperatures. *Polymer Testing*, vol. 124, no. 5, art. ID 108073, **DOI:10.1016/j.polymertesting.2023.108073**.

[17] Hu, G. (2018). Study on sealing performance of packing element in permanent packer under complicated conditions. *Southwest Petroleum University*, **DOI:10.27420/d.cnki.gxsyc.2018.000425**. (in Chinese)

[18] Liu, Y., Qian, L., Zou, J., Xia, C., Lian, Z.H. (2022). Study on failure mechanism and sealing performance optimization of compression packer. *Engineering Failure Analysis*, vol. 136, art. ID 106176, **DOI:10.1016/j.engfailanal.2022.106176**.

[19] Mitchell, R. F. (2012). Buckling of tubing inside casing. *SPE Drilling & Completion*, vol. 27, no. 4, p. 486-492, **DOI:10.2118/150613-MS**.

[20] Wang, Y.X., Zhou W., Guo R., (2017). shoal facies reservoir characteristics and genesis of mishrif formation in Halfaya oilfield, Iraq. Journal of Jilin University, vol. 47, no. 4, p. 1007-1020, **DOI:10.13278/j.cnki.jjuese.201704104**. (in Chinese)

Strojniški vestnik - Journal of Mechanical Engineering 70(2024)3-4, 128-140
DOI:10.5545/sv-jme.2023.673
Original Scientific Paper
Received for review: 2023-06-04
Received revised form: 2023-10-17
Accepted for publication: 2023-11-23

Service Performance Optimization and Experimental Study of a New W-W Type Non-circular Planetary Gear Train

Changbin Dong[1] – Xudong Yang[1] – Dawei Li[1] – Gang Zhao[2] – Yongping Liu[1]
1 Lanzhou University of Technology, School of Mechanical and Electrical Engineering, China
2 Wuhan University of Science and Technology, Hubei Key Laboratory of Mechanical Transmission and Manufacturing Engineering, China

To address the vibration problem in traditional W-W-type non-circular planetary gear trains during operation, this study proposes two new combinations of W-W-type non-circular planetary gear trains. The study focuses on analysing the transmission error and improving service performance. By utilizing the conjugate theory and the coordinate transformation theory, an accurate mathematical model for non-circular gears is derived. The transmission error models for the two combination forms of the non-circular planetary gear train are established using the incremental meshing line method. The analysis also examines the influence of eccentricity on the transmission error. Kinematic analysis of the multi-body dynamics model confirms that the new W-W type non-circular planetary gear train, formed by combining non-circular gears and cylindrical gears, exhibits superior transmission performance. Furthermore, a test analysis is conducted on the roller pumping unit test platform and the indicator diagrams of the pumping unit under various working conditions are obtained. The study concludes that the optimal matching mode for the sucker rod counterweight and motor frequency of the reversing device of the pumping unit is 20 kN and 20 Hz, and the dynamic balance of the pumping unit load can be achieved by adjusting the motor frequency.

Keywords: Non-circular planetary gear train, reversing device, incremental meshing line method, transmission error, indicator diagram

Highlights

- *Two new W-W type non-circular planetary gear train combinations have been proposed to reduce torque fluctuations at the output end.*
- *A new method for establishing the transmission error model of new W-W-type non-circular gear planetary gear trains based on the incremental meshing line method was proposed.*
- *An idealized indoor pumping unit test platform was built, and indicator diagrams of non-circular gear pumping units under different working conditions are obtained.*

0 INTRODUCTION

As a new type of gear transmission, non-circular gear (NCG) is mainly used to realize nonlinear rotation between two transmission shafts [1]. It has the advantages of strong bearing capacity and variable ratio transmission [2] to [4] and is widely used in agriculture, military, aerospace, and other important places. This kind of functional gear device has also evolved in nature [5]. Burrows have found a natural gear structure on the hind legs of the jumping Issus worm. Its distribution type, transmission mode, and functions are consistent with those of NCG, which proves that NCG can also play a functional role in the natural behaviour of jumping insects as a biological gear. With the development of modern machinery towards high speed, heavy load, and high precision, it has been difficult to make a single NCG pair to meet the application requirements. Thanks to the time-varying transmission characteristics of NCG, various transmission forms can be realized by combining different types of NCG into multiple non-circular planetary gear trains (NCPGT), which are applied in hydraulic motors, hydraulic pumps, astronomical clocks, automobile gearboxes, and other fields [6] to [8].

Generally, NCPGT [9] and [10] has four types, namely N-G-W, N-W, W-W, N-N, and each type can achieve different functions and can be applied in different situations. In large-scale agricultural machinery with complex movement tracks, such as automatic seedling picking, hole pricking, fertilization, etc., using an NCG rotating mechanism to replace the traditional crank linkage mechanism can make the improved mechanism have smaller inertia, more compact structure, and maintain high motion accuracy when working at medium and high speeds [11] to [13]. Sun et al. [14] proposed the design method of NCPGT in approximate multi pose transplanting mechanism. Zhao et al. [15] and Ye et al. [16] studied the onion automatic seedling delivery mechanism and vegetable rotary seedling taking mechanism of NCPGT. Yu et al. [17] proposed a planetary gear train formed by the combination of incomplete eccentric circular gear and NCG in order to solve the rigid impact of the seedling picking mechanism of the transmission intermittent

*Corr. Author's Address: Lanzhou University of Technology, Gansu Lanzhou, 730050, China, ldw969968604@163.com and lutdcb@126.com

planetary gear train. Based on the space "8"-shaped transplanting track, Wang et al. [18] designed a wide narrow row rice bowl seedling transfer mechanism driven by the combination of plane NCG and bevel gear. The NCPGT transfer mechanism can complete the actions of clamping, pulling, holding, and pushing seedlings, which is of great significance for improving the efficiency of agricultural machinery. In addition to agricultural applications, as the key core component of hydraulic motors [19], NCPGT is widely used in metallurgy, mines, and other dangerous working environments to achieve low-speed and high-torque transmission. Considering that NCPGT often uses several planetary gears to share the load, which will cause uneven load distribution and lead to impact and vibration, Lin [20] proposed a new type of double-sided internal meshing NCPGT. The gear train has only one planetary gear, which avoids the problem of uneven load that may occur due to multiple planetary gears.

Due to the accurate variable ratio transmission characteristics of NCG, the planetary gear train composed of NCG and other mechanisms plays an irreplaceable role in many occasions with special motion requirements and force requirements. However, it is difficult to improve the transmission performance of NCPGT. The existing transmission accuracy is only applicable to agricultural machinery, which makes it difficult to meet the use requirements of high-precision occasions, thus restricting the industrial application and development of NCPGT. Therefore, based on the original W-W type NCPGT, this paper proposes a comparative analysis of the two combination modes of the new W-W type NCPGT and applies them to the reversing device of the drum pumping unit. Through the idealized rod production indoor test, the optimal load and motor frequency matching data of the NCPGT pumping unit are obtained, which will lay a theoretical foundation for improving the transmission performance of the NCPGT and promote its industrial application.

1 THE GENERATION MOTION OF CONJUGATE TOOTH PROFILE FOR NCG

Fig. 1 shows the basic principle of using gear shaper cutters as gear cutters to produce NCG. The principle of tooth profile envelope is to ensure the pure rolling of the pitch surface of a pair of NCG, while the instantaneous contact between another cylindrical gear and the pitch surface of this pair of pure rolling NCG ensures the pure rolling relationship.

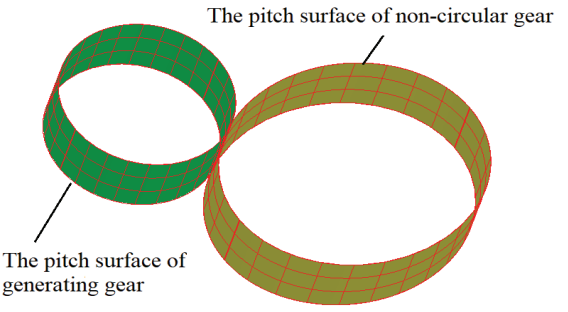

Fig. 1. *Basic principle of using cylindrical gear shaper to produce NCGs*

The tooth profile of NCG is an involute tooth profile. For involute tooth profile gear transmission, the section of the gear shaping cutter is an involute, and the section equation is:

$$\begin{cases} x_g(u) = r_{gb}(\cos u + u \sin u) \\ y_g(u) = r_{gb}(\sin u - u \cos u) \end{cases}, \quad (1)$$

where $r_{gb} = r_{gp} \cos \alpha$. r_{gb} is the base circle radius. r_{gp} is the indexing circle radius of the gear cutter. u is the tooth shape parameter. Specifically, it is the sum of the unfolding angle and pressure angle of the involute at any point. α is the gear transmission pressure angle.

According to the principle of gear meshing, the relationship between the generating wheel and the generated gear satisfies a pure rolling relationship. Specifically, the pitch curve of the gear shaper and the pitch curve of the NCGs are in instantaneous tangent contact, so the coordinate system can be established through the tangent vector and normal vector of the NCG pitch curve to build the kinematic relationship between the coordinate systems. Based on the basic idea of the motion reversal method, if an NCG is fixed, the relationship between the coordinate system of the gear shaper cutter, the coordinate system of the NCG, and the auxiliary coordinate system at the contact point P of the gear shaper cutter can be defined.

Fig. 2 shows the coordinate conversion relationship when producing NCGs, which contains the following three coordinate systems:

(1) Fixed coordinate system $S_0(O_0 - x_0 y_0 z_0)$, which is fixed on an NCG to be produced. The rotation angle of an NCG is expressed as θ, and the pitch curve equation is defined as $r_p(\theta)$.

(2) Auxiliary coordinate system $S_G(O_g - x_G y_G z_G)$, which is determined by the normal and tangential directions of the NCG pitch curve and the contact point P of the generating tool (gear shaper), as well as the center of the generating wheel. The

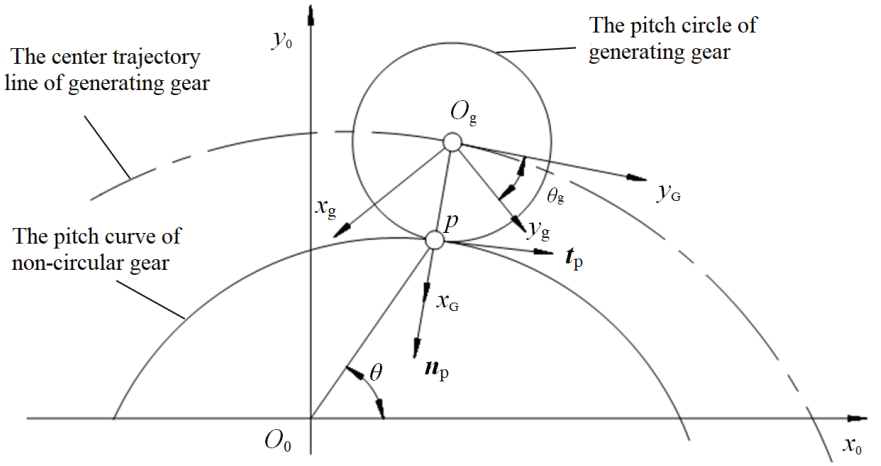

Fig. 2. *Coordinate transformation relationship during the production of NCG*

centre of the generating gear is the point of the radius of the normal gear shaper cutter. Using vector coordinate transformation, the unit vector of the three coordinate axes of the coordinate system S_p can be expressed as:

$$\begin{cases} \mathbf{i}_p(\theta) = \mathbf{n}_p(\theta) \\ \mathbf{j}_p(\theta) = \mathbf{t}_p(\theta) \\ \mathbf{k}_p(\theta) = [0\ 0\ 1]^T \end{cases}. \tag{2}$$

The unit vector of the three axes of coordinate system S_0 can be expressed as:

$$\begin{cases} \mathbf{i_0} = [1\ 0\ 0]^T \\ \mathbf{j_0} = [0\ 1\ 0]^T \\ \mathbf{k_0} = [0\ 0\ 1]^T \end{cases}. \tag{3}$$

The coordinate transformation relationship between coordinate system S_G and coordinate system S_0 is as follows:

$$\mathbf{M}_{0G}(\theta) = \begin{bmatrix} \mathbf{n}_{p0} & \mathbf{t}_{p0} & 0 & \mathbf{r}_{og\,0} \\ \mathbf{n}_{p1} & \mathbf{t}_{p1} & 0 & \mathbf{r}_{og\,1} \\ 0 & 0 & 1 & 0 \\ 0 & 0 & 0 & 1 \end{bmatrix}. \tag{4}$$

(3) Gear shaper cutter coordinate system $S_g(O_g{-}x_g y_g z_g)$. In Fig. 2, the angle at which the relative coordinate system S_p rotates is the angle of rotation of the gear shaping cutter, which can be calculated based on the pure rolling relationship of the pitch curve using the following equation:

$$\theta_g = \frac{S_{pg}(\theta)}{r_{gp}} = \frac{\int_0^{\theta} \left| \mathrm{d}r_p(\theta)/\mathrm{d}(\theta) \right| \mathrm{d}(\theta)}{r_{gp}}, \tag{5}$$

where $S_{pg}(\theta)$ represents the arc length of the NCG pitch curve from the starting position to the current position. The coordinate transformation from the slotting cutter coordinate system S_g to the relative coordinate system S_p can be obtained as:

$$\mathbf{M}_{Gg}(\theta_g) = \begin{bmatrix} \cos\theta_g & \sin\theta_g & 0 & 0 \\ -\sin\theta_g & \cos\theta_g & 0 & 0 \\ 0 & 0 & 1 & 0 \\ 0 & 0 & 0 & 1 \end{bmatrix}. \tag{6}$$

According to Eqs. (4) and (6), the coordinate transformation from the gear shaper cutter coordinate system to the NCG coordinate system can be obtained as follows:

$$\mathbf{M}_{0g}(\theta) = \mathbf{M}_{0G}(\theta)\mathbf{M}_{Gg}(\theta_g). \tag{7}$$

Based on the analysis of gear-cutting tools according to the above generation motion, the tooth profile of NCG can be obtained. By transforming the tooth surface of the generation wheel into the gear coordinate system, the envelope equation of NCG can be obtained as follows:

$$\mathbf{R}_{Eg}(\theta, u, v) = \mathbf{M}_{0g}(\theta)\mathbf{R}_g(u, v). \tag{8}$$

The boundary of Eq. (8) is the tooth profile surface of an NCG, and its meshing equation is usually:

$$\mathbf{M}_{0g}(\theta)\mathbf{n}_{rg}(u, v) \cdot v_g = 0. \tag{9}$$

Due to the fixed gear coordinate system S_0, the relative velocity of the meshing point is the velocity of that point in the production wheel coordinate system. The motion of the auxiliary coordinate system S_G along the NCG pitch curve and the motion of the generative gear can be combined to form the relative velocity at the meshing point, so the relative velocity is:

$$\mathbf{v}_g(\theta,u,v)=\mathbf{t}_p(\theta)+\left[0 \quad 0 \quad \mathrm{d}\theta_g/\mathrm{d}\theta\right]^T\times\mathbf{R}_g(u,v). \quad (10)$$

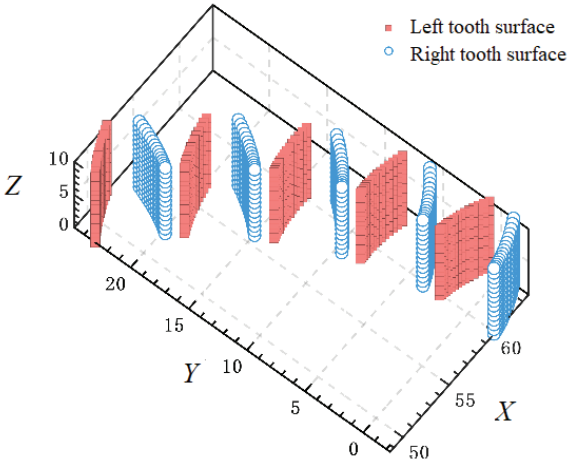

Fig. 3. *The partial digital tooth surface of the NCG*

By substituting Eq. (10) into the meshing Eq. (9), the instantaneous meshing line between the NCG and the generating gear at any time can be solved, thus forming the tooth profile of the NCG. The digital tooth surface of the NCG is established using Eq. (10), as shown in Fig. 3.

2 TRANSMISSION ERROR MODEL OF NEW W-W TYPE NCPGT

3.1 The Transmission Error Model of NCG Based on Meshing Line Increment Method

The transmission error of a gear transmission system is the main factor affecting its transmission performance and accuracy. Transmission errors caused by excitation parameters such as eccentricity error, time-varying backlash, and load are all dynamic transmission errors. The main idea of the incremental meshing method is to equate the centre distance error and eccentricity error to the instantaneous meshing line of the gear, and convert the increment of the meshing line of the driving gear and the driven gear under different turns into the angle of the driven gear, thus obtaining the transmission error of the driving gear under different turns.

In some cases, an NCG pair will be required to achieve reciprocating motion. Because the rotation centre of NCG is not at its geometric centre, there is an eccentricity error. The difference between the various tooth profiles of NCG results in a more pronounced excitation of transmission errors by the backlash between the teeth. There may be some differences in transmission between clockwise and counterclockwise rotation. Therefore, the meshing line increment of the driving and driven gears under different direction of rotation is considered in the analysis.

Figs. 4 and 5 show the transmission error analysis models of NCG pair established by the incremental meshing line method after considering the comprehensive eccentricity error and driving gear direction of rotation. Figs. 4a and b show the driving gear meshing line increment and driven gear meshing line increment when the driving gear

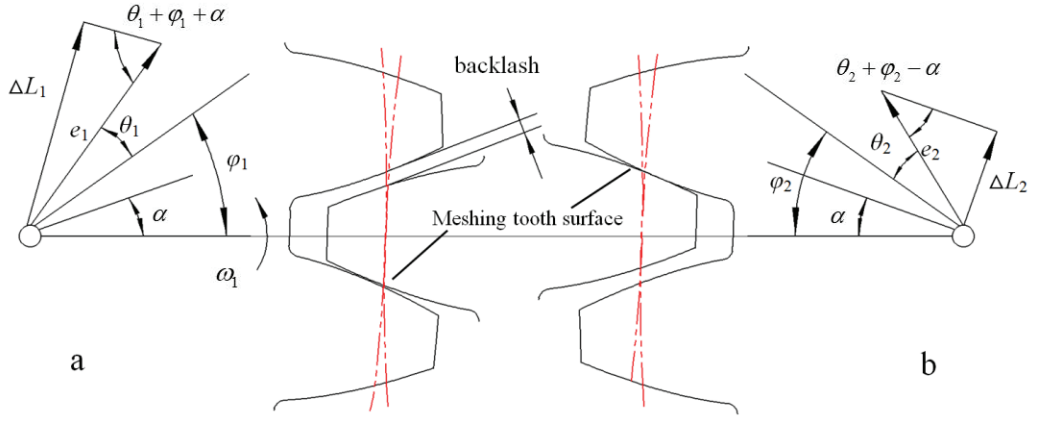

Fig. 4. *Calculation model of meshing line increment when driving gear rotates counterclockwise*

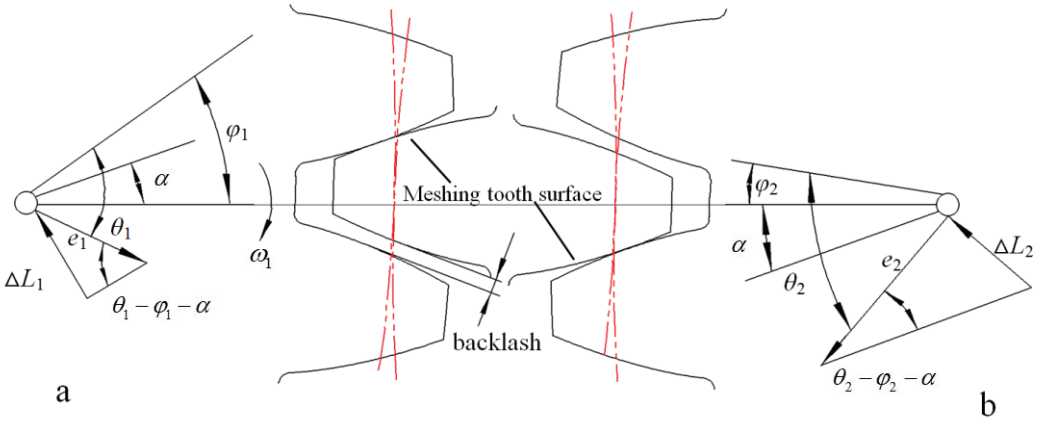

Fig. 5. *Calculation model of meshing line increment when driving gear rotates clockwise*

rotates counterclockwise, and Figs. 5a and b show the driving gear meshing line increment and driven gear meshing line increment when the driving gear rotates clockwise. Combined with Figs. 4 and 5, it can be determined that the increment of meshing line of driving gear and driven gears under two kinds of direction of rotation are:

$$\Delta L_1 = \mathrm{e}_1 \sin(\theta_1 \pm \varphi_1 + \alpha), \tag{11}$$

$$\Delta L_2 = \mathrm{e}_2 \sin(\theta_2 \pm \varphi_2 - \alpha), \tag{12}$$

where e_1 and e_2 are the eccentricity errors of the driving and driven gears, respectively. θ_1 and θ_2 are the rotation angles of the driving and driven gears, respectively. φ_1 and φ_2 are the initial phase angles of the driving and driven gears, respectively. ΔL_1 and ΔL_2 are the meshing line increments of the driving and driven gears, respectively. α is the pressure angle.

At the initial time, the increment of the meshing line of the driving and driven gears caused by the eccentricity error is as follows:

$$\Delta L_{10} = \mathrm{e}_1 \sin(\pm\varphi_1 + \alpha), \tag{13}$$

$$\Delta L_{20} = \mathrm{e}_2 \sin(\pm\varphi_2 - \alpha). \tag{14}$$

According to the meshing line increment method, when the driving gear rotates counterclockwise and clockwise, the theoretical no-load transmission error can be obtained as follows:

$$\begin{aligned}\Delta\varphi_{\mathrm{n}} = \frac{180}{\pi r \cos\alpha} \times [&\mathrm{e}_1 \sin(\theta_1 + \varphi_1 + \alpha) \\ &+ \mathrm{e}_2 \sin(\theta_2 + \varphi_2 - \alpha) \\ &- \mathrm{e}_1 \sin(\varphi_1 + \alpha) \\ &- \mathrm{e}_2 \sin(\varphi_2 - \alpha)],\end{aligned} \tag{15}$$

$$\begin{aligned}\Delta\varphi_{\mathrm{s}} = \frac{180}{\pi r \cos\alpha} \times [&\mathrm{e}_1 \sin(\theta_1 - \varphi_1 + \alpha) \\ &+ \mathrm{e}_2 \sin(\theta_2 - \varphi_2 - \alpha) \\ &- \mathrm{e}_1 \sin(-\varphi_1 + \alpha) \\ &- \mathrm{e}_2 \sin(-\varphi_2 - \alpha)].\end{aligned} \tag{16}$$

3.2 Establishment of Transmission Error Model of New W-W type NCPGT

A W-W type NCPGT consists of two externally engaged NCGs, and its structural principle is shown in Fig. 6, where 1, 2, 3 and 4 are NCGs. The NCG 1 and 4 are fixed, and H is a tie rod. The power is input from I, and the NCG 4 is driven to rotate by the rotation of the tie rod H, and the final power is output from NCG 4.

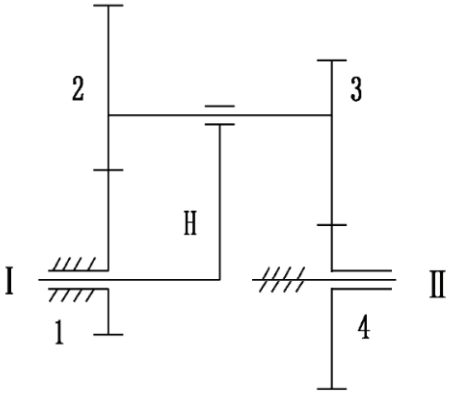

Fig. 6. *Schematic diagram of W-W type NCPGT mechanism*

Practice shows that the difference between the tooth profiles of NCGs leads to a certain vibration

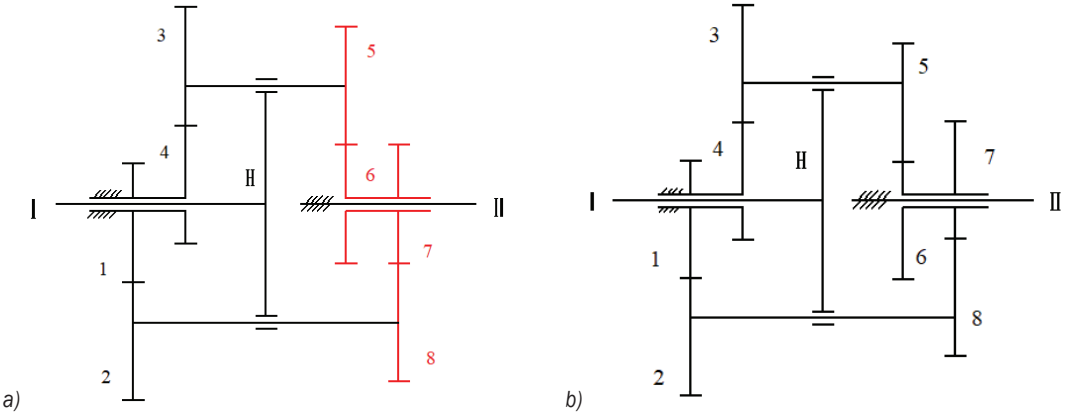

Fig. 7. *Schematic diagram of new W-W type NCPGT mechanism: case A, and b) case B*

of W-W gear train during operation, and there is also a certain fluctuation in the torque at the output end [21], which is not allowed for high-precision gear transmission systems. Therefore, on the basis of the traditional W-W gear train, this paper proposes two new combinations as shown in Fig. 7. Case A is composed of two externally engaged NCGs and two externally engaged cylindrical gears. In Fig.7a, 1, 2, 3 and 4 are NCGs, and 5, 6, 7 and 8 are cylindrical gears. Case B consists of four externally engaged NCGs. The new W-W type NCPGT formed by the above combination can achieve power balance and stable torque at the output end. The design parameters of NCGs are shown in Table 1.

Table 1. *The design parameters of NCGs*

	Cylindrical gear	NCG
Modulus [mm]	3.5	3
Tooth number	42	47
Eccentricity (k)	0	0.3287
Tooth width [mm]	30	30
Center distance [mm]	150	150
Pressure angle [°]	20	20 (Pitch line)
Pitch curve equation		$r(\theta)=\frac{64.667}{1-0.3287\cos\theta}$

To further clarify the engagement between gears, the two gear trains in Fig. 7 are simplified as shown in Fig. 8, where the red line represents Case A. In Fig. 8, the engagement of gears in Cases A and B is as follows: in Case A, the power input drives NCGs 2 and 3 to rotate by the tie rods at the axle holes of NCGs 1 and 4, and NCGs 1 and 4 are fixed. At the same time, the cylindrical gears 5 and 8 mesh with the cylindrical gears 6 and 7 respectively, and then the power is output by the sleeves of the shaft holes of the cylindrical gears 6 and 7. For Case B, only cylindrical gears 5 to 8 are replaced with NCGs, and its transmission mechanism is consistent with Case A.

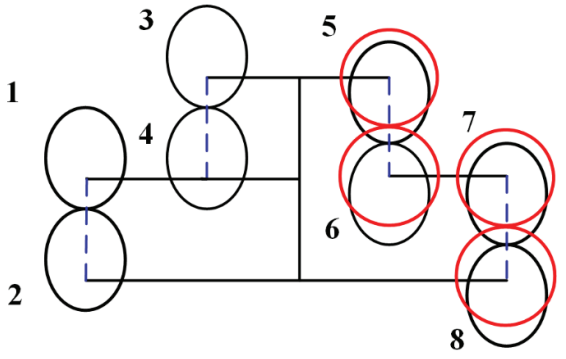

Fig. 8. *Schematic diagram of two types of NCPTG simplification*

The transmission error of a gear transmission system is the main factor affecting its transmission performance. During the meshing process of the NCG pair, due to the different tooth profiles, a certain displacement difference will be generated in the direction of the meshing line of the driving and driven gears [22] and [23], that is, transmission error. Most NCG transmission systems can realize quick return motion; at this time, its rotation centre is not at its geometric centre, thus involving eccentric errors. Therefore, the NCG in Cases A and B proposed in this paper also has eccentric errors. In view of the key role and special requirements of NCPGT in transmission, it is more practical to analyse the transmission error of an NCG transmission system under eccentric error. Based on the incremental meshing line method [23] to [25] and Eqs. (15) and (16), the transmission error models of the two cases proposed in this paper are established respectively. The general formula of

transmission error of each gear pair in Cases A and B is:

$$\Delta_{ij} = \frac{180}{\pi r_{jb} \cos\alpha_j}\left[e_i \sin\left(\theta_i + \varphi_i + \alpha_i\right) + e_j \sin\left(\theta_j + \varphi_j - \alpha_j\right) - e_i \sin\left(\varphi_i + \alpha_i\right) - e_j \sin\left(\varphi_j - \alpha_j\right)\right], \quad (i = 1,3,5,7 \quad j = 2,4,6,8), \tag{17}$$

where e is the eccentricity error. θ is the rotation angle. φ is the initial phase angle.

Therefore, the transmission errors of Case A and Case B are respectively:

$$TE_{\text{CaseA}} = \Delta_{\text{NCG12}} + \Delta_{\text{NCG34}} + \Delta_{\text{NCG56}} + \Delta_{\text{NCG78}}, \tag{18}$$

$$TE_{\text{CaseB}} = \Delta_{\text{NCG12}} + \Delta_{\text{NCG34}} + \Delta_{\text{CG56}} + \Delta_{\text{CG78}}. \tag{19}$$

Through the above mathematical model of transmission error, the transmission error distribution law of Cases A and B can be obtained under different design parameters, and the respective advantages of the two NCPGT can be determined through transmission error.

3.3 Comparative Analysis of Transmission Performance of New W-W-Type NCPGT

As the core component of the pumping unit, the transmission performance of the reversing device directly affects the quality and efficiency of the pumping unit. Therefore, it is necessary to systematically analyse the transmission performance of the reversing device of the proposed two NCPGTs. For the new W-W type NCPGT, this paper mainly compares and analyses the transmission error, output swing angle, angular velocity, kinetic energy and angular momentum to determine the optimal combination form. In Fig. 9, the transmission errors of Case A and Case B show a periodic change trend. As the NCG has eccentricity, the transmission error of the gear teeth under eccentric excitation has a cumulative effect. In contrast, the transmission errors of Case A are smaller, which indicates that the new W-W type NCPTG composed of NCGs and cylindrical gears has more advantages for high-precision transmission.

Figs. 10 and 11 show the variation trend of the transmission error of the NCPGT corresponding to Cases A and B with the eccentricity (k). With the increase of eccentricity, the transmission errors of the cases show an increasing trend. However, the transmission error in Case B increases more significantly. For the reversing device of a pumping unit, the transmission error is directly related to its up and down strokes, and excessive transmission error will lead to increased energy loss during the up and down strokes of the pumping unit. Therefore, Case A has better transmission performance based on transmission error analysis.

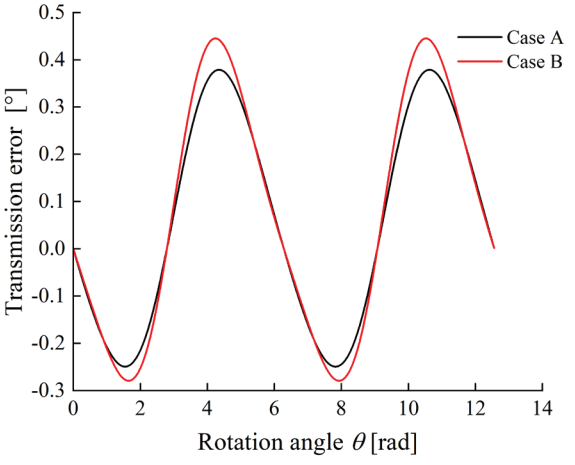

Fig. 9. *Transmission error distribution law of two cases*

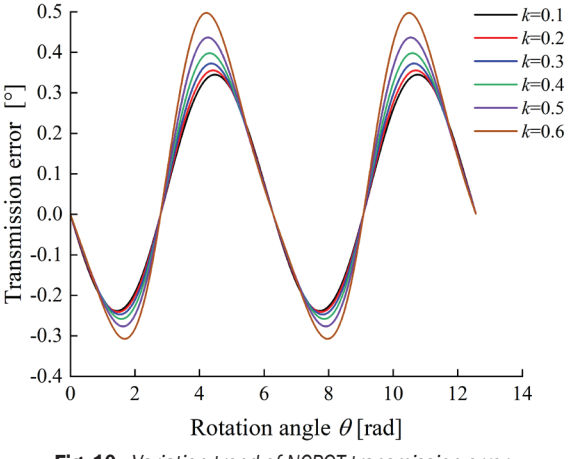

Fig. 10. *Variation trend of NCPGT transmission error corresponding to Case A with eccentricity*

To verify the above conclusions, a virtual prototype model (as shown in Fig. 12) was established for Cases A and B, respectively, and the working condition parameters consistent with the actual working condition of the pumping unit were set. By solving the model, the change laws of the contact force, frequency spectrum, output swing angle, angular velocity, kinetic energy, and angular momentum of the NCPGT corresponding to Cases A and B were obtained, respectively.

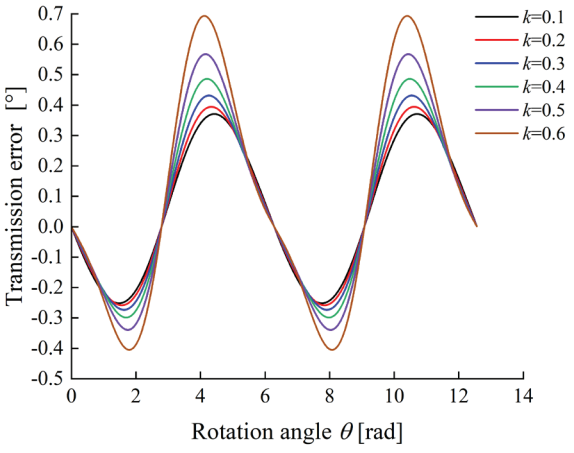

Fig. 11. *Variation trend of NCPGT transmission error corresponding to Case B with eccentricity*

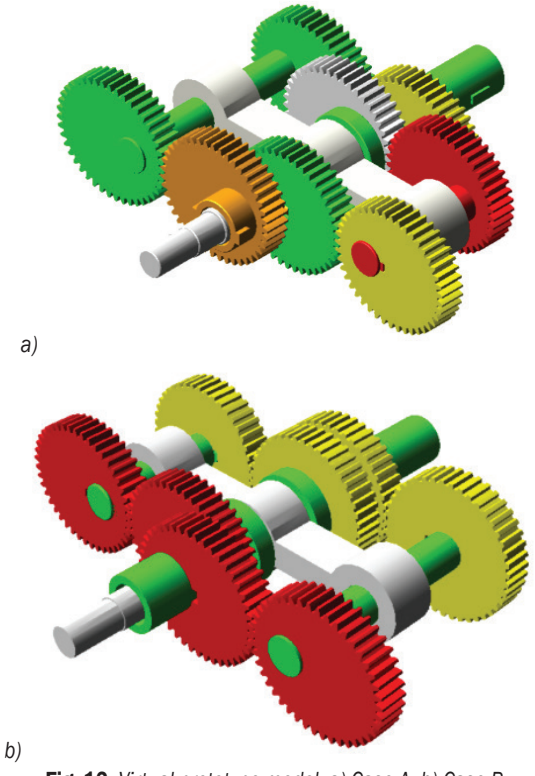

Fig. 12. *Virtual prototype model: a) Case A, b) Case B*

To demonstrate the differences between the original gear group and the added gear group, we conducted model validation to verify the rationality of the model proposed in this article. Fig. 13 shows the dynamic meshing force and frequency spectrum distribution of a) the original gear set (Fig. 6), b) Case B, and c) Case A. The original gear model has multiple peaks in the meshing force amplitude due to power imbalance and inertia force, which will exacerbate the impact and torque fluctuations of the system. In the model corresponding to Case B, the peak meshing force is mainly concentrated at the turning point of the gear train, which is around 0.72 seconds and 1.44 seconds. From a frequency perspective, it is mainly concentrated in the low-frequency range within 200 Hz. Compared to Case B, the model responding to Case A shows a decrease in the peak meshing force from 22 N to 18 N, and the change in meshing force during gear meshing is more uniform. Furthermore, the peak value tens to expand to both sides during the turning of the gear train. The system response frequency has also been wider, expanding from 200 Hz to 400 Hz. In Fig. 13c, there are many sub-harmonics with the same pattern in the distribution of the meshing force spectrum. Due to the addition of cylindrical gear pairs in the gear train, torque fluctuations in the initial stage of system dynamic balance will inevitably cause system vibration, which is necessary to reduce torque fluctuations in the initial stage of the system. To summarize, compared with

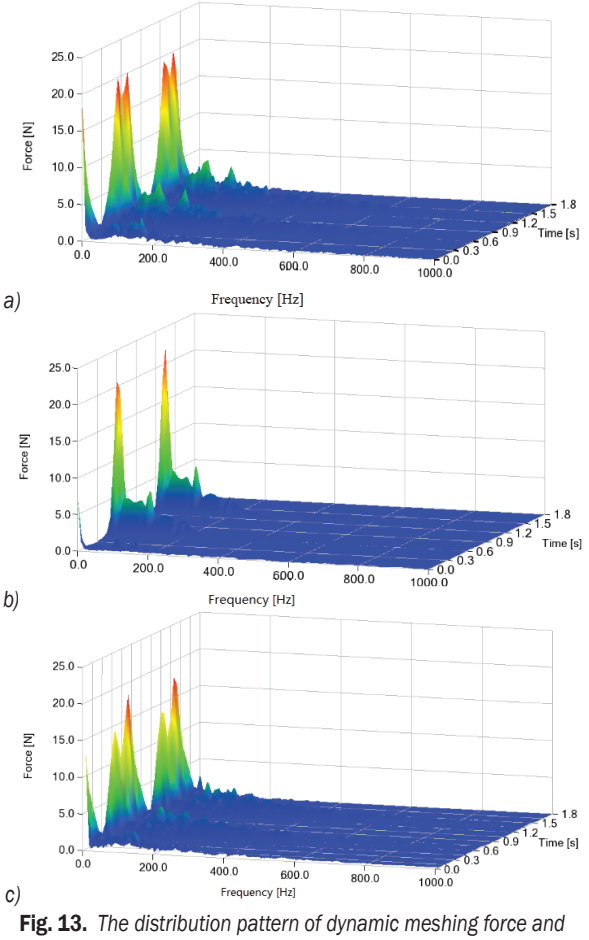

Fig. 13. *The distribution pattern of dynamic meshing force and spectral; a) the original gear set, b) Case B, and c) Case A*

the above two schemes, the dynamic meshing force in Case A is reduced and the distribution is more uniform and gentle, which indicates that Case A has better motion characteristics and spectral distribution patterns.

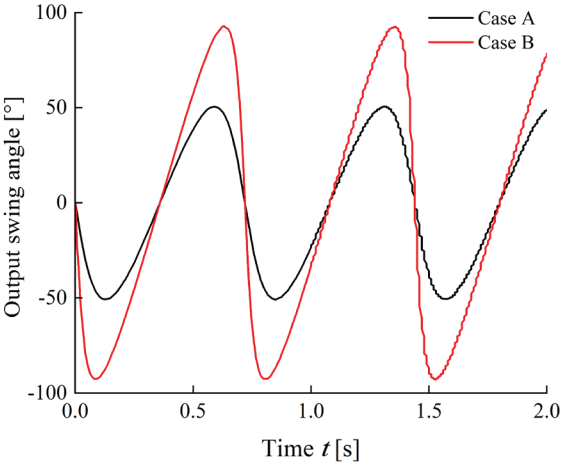

Fig. 14. *Comparison and analysis of output swing angle of two cases*

In Fig. 14, the output swing angle of Cases A and B shows a periodic change trend. The amplitude of the output swing angle corresponding to Case B is larger, but the time interval between the extreme values of the output swing angle is longer. For pumping units, a large output swing angle means that a longer stroke can be achieved, which is expected in the pumping process and is of great significance for improving the working efficiency of pumping units. However, the curve in Case B fluctuates greatly, while Case A can reduce the vibration caused by NCG pair engagement on the basis of achieving stable power because of the introduction of cylindrical gears to participate in planetary gear train engagement. The vibration phenomenon should be avoided as much as possible during the working process of the pumping unit, and the output swing angle can be adjusted by the sprocket system at the output end of the reversing device of the pumping unit. In contrast, the stability of the system is more important.

Figs. 15 to 17 show the angular velocity, kinetic energy and angular momentum curves of Cases A and B respectively. The negative value appears in Fig. 14, which is due to the preset clockwise rotation as a square during multi body dynamics simulation. When the output end of NCPGT rotates counterclockwise, a negative value will appear. In Fig. 15, Case B has great velocity fluctuation and impact during reversing, while Case A's angular velocity curve is

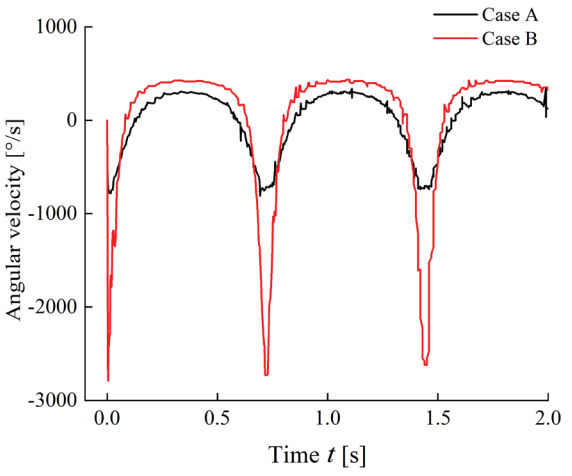

Fig. 15. *Comparison and analysis of angular velocity of two cases*

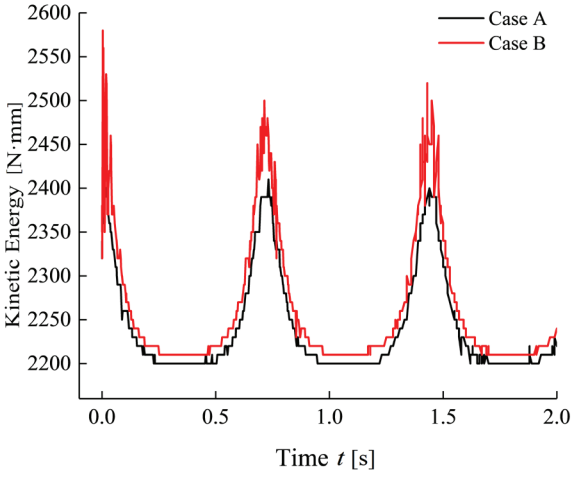

Fig. 16. *Comparison and analysis of kinetic energy of two cases*

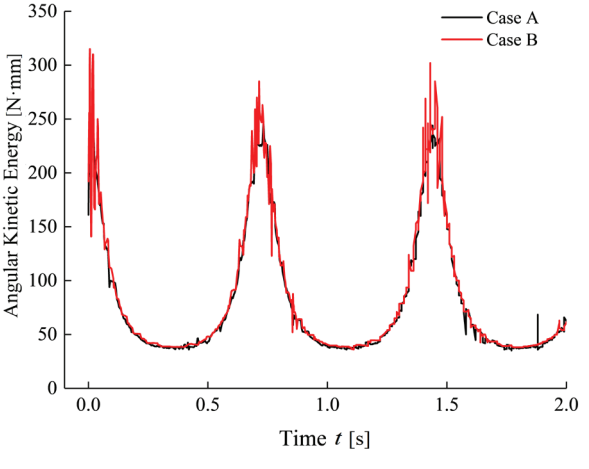

Fig. 17. *Comparison and analysis of angular kinetic energy of two cases*

more periodic. In Figs. 16 and 17, although Cases A and B have the same distribution law, the impact and fluctuation of Case B are larger. It is indicated that within a certain range, the impact of NCG gear pairs on the transmission performance of the system can be reduced by introducing cylindrical gears, thereby reducing the vibration and impact of the system. The above analysis further shows that the NCPGT formed by the combination of NCG and cylindrical gear has better transmission performance, and also verifies the correctness of the transmission error analysis results. Therefore, the Case A scheme is adopted for the subsequent pumping unit reversing device.

3 TRANSMISSION TEST OF PUMPING UNIT REVERSING DEVICE

The idealized indoor test of sucker rod pumping unit is realized by building a test prototype with the same proportion as the actual pumping unit. The test prototype of the pumping unit is shown in Fig. 18. Its working principle is as follows: the motor inputs torque into the NCPGT reversing device of the pumping unit through belt transmission. The output shaft transmits the torque to the drum through the sprocket drive and finally completes the up and down stroke movement of the sucker rod through the connection between the steel wire rope wound on the drum and the simulation loading device. During the experiment, an MPS wire displacement sensor was used to detect the real-time displacement of the suspension point; The DYLY-102 tensile sensor is used to measure the suspension load. Finally, the indicator diagram is drawn based on the dynamic matching relationship between them.

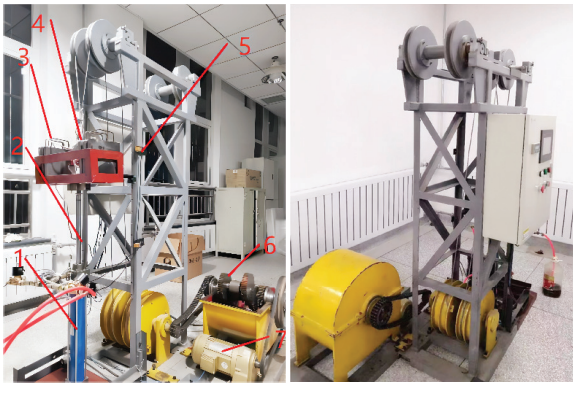

Fig. 18. *NCPGT reversing device pumping unit; 1 hydraulic cylinder, 2 sucker rod, 3 balance weight, 4 DYLY-102 tensile sensor, 5 MPS wire displacement sensor, 6 new w-w type NCPGT, and 7 variable frequency motor*

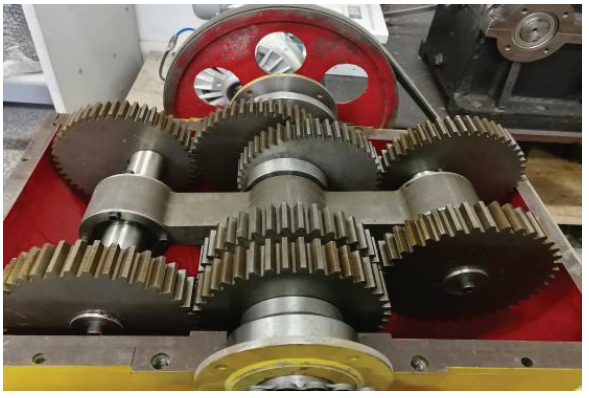

Fig. 19. *New W-W type NCPGT reversing device*

Fig. 19 shows the new W-W type NCPGT reversing device corresponding to Case A. The indicator diagram is an important indicator for evaluating the performance of the pumping unit [26]. A closed parallelogram can be formed by real-time collecting the corresponding data in a cycle of the suspension point load and displacement sensor, and then establishing a two-dimensional coordinate system with suspension point displacement and load as the horizontal axis and vertical axis respectively. However, due to the influence of complex environment, the measured indicator diagram curve often has certain fluctuations.

The balance weight and stroke times of sucker rod will affect the stability of pumping unit operation. During the test, the counterweight of the counterweight box and the motor frequency are given. The indicator diagrams of pumping units under different working conditions are obtained by dynamically adjusting the experimental data, as shown in Figs. 20 and 21.

In Fig. 20, the change of polished rod load during up and down strokes has great fluctuation. The reason is that the impact and vibration of the gear pair in the new W-W type NCPGT reversing device during meshing, and the load mismatch in the up and down strokes under the load frequency mode aggravates this situation.

Fig. 21 shows the indicator diagram of the pumping unit under three working conditions: load is 20 kN, and motor frequencies are 10 Hz, 15 Hz, and 20 Hz, respectively. There are obvious fluctuations at the starting point of the upstroke, which leads to a large impact at the starting point of the pumping unit. The reason is that the inertia of the sucker rod counterweight load is too large, and the pumping unit stroke is not dynamically adjusted. With further increase of the motor frequency, the polished rod load line obviously tends to be stable, showing a stable state, and there is basically no fluctuation. In the

process of the down stroke, the fluctuation amplitude of polished rod load decreases gradually and tends to be stable. It shows that the pumping unit has the best balance weight and pumping stroke, and adjusting the motor frequency is helpful to balance the polished rod load from the up and down strokes of the pumping rod. Therefore, increasing the motor frequency can effectively improve the performance of the pumping unit.

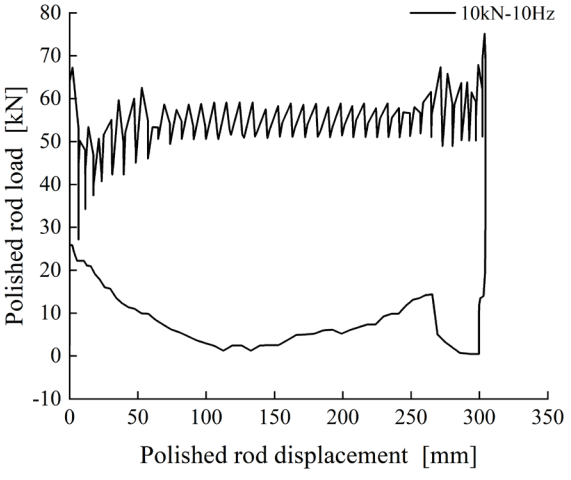

Fig. 20. *Indicator diagram of 10 kN load*

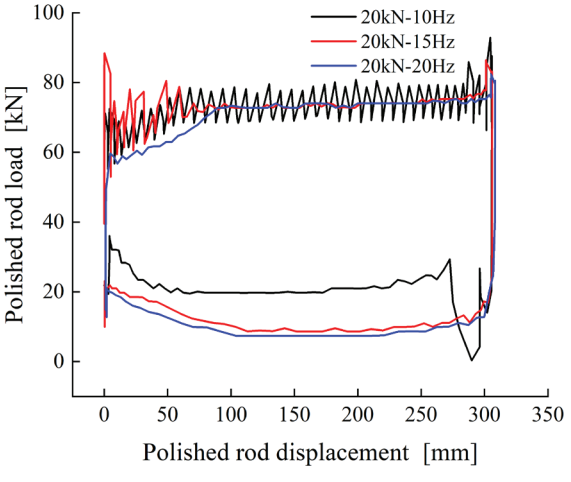

Fig. 21. *Variation trend of indicator diagram of pumping unit with motor frequency under 20 kN load*

Fig. 22 shows the indicator diagram of the pumping unit when the load is 30 kN and the motor frequencies are 15 Hz and 20 Hz, respectively. The polished rod load at the starting point and the end point of the down stroke of the pumping unit fluctuates slightly. The vibration of the polished rod load at the beginning of the upstroke has an obvious decreasing trend with the increase of the motor frequency, which indicates that increasing the motor frequency can significantly reduce the load impact at the upper and lower dead points of the pumping unit.

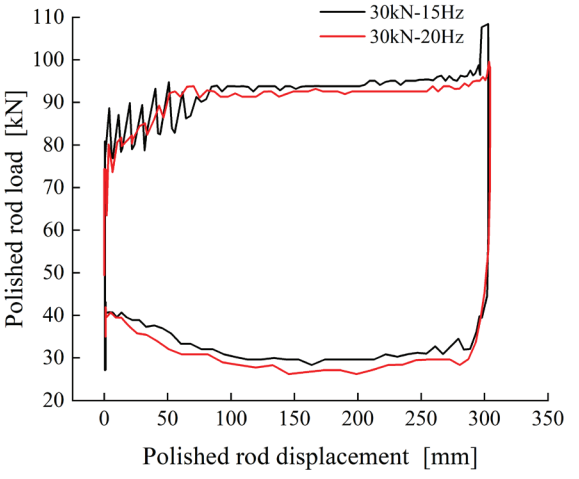

Fig. 22. *Variation trend of indicator diagram of pumping unit with motor frequency under 30 kN load*

Based on the comparison and analysis of indicator diagrams of several groups of different tests from Figs. 20 to 22, it is concluded that the pumping unit is the most stable when the load frequency matching mode of the pumping unit is 20 kN and 20 Hz. At this time, the pumping unit has the optimal balance weight and the optimal pumping unit stroke. Therefore, the above analysis shows that the load imbalance problem during the operation of the pumping unit can be alleviated by adjusting the matching between the load and the motor frequency. It can also reduce the impact and vibration caused by the reversing of the NCPGT reversing device, thereby improving the efficiency of the pumping unit and the service life of the reversing device.

4 CONCLUSIONS

This paper proposes two new combination methods for W-W type NCPGT. Based on the incremental meshing line method, the transmission error models are established respectively. The advantages of the two types of gear trains are judged by the contact force, frequency spectrum, transmission error, output swing angle, angular velocity, kinetic energy, and angular momentum. The correctness of the analysis is verified by the virtual prototype model. The new W-W type NCPGT, which is composed of NCGs and cylindrical gears, has better transmission performance. On this basis, the new W-W type NCPGT is applied to the reversing device of the drum pumping unit,

and the idealized rod production laboratory test is carried out. The indicator diagrams under different load frequency matching modes are obtained, and the optimal load frequency matching mode is 20 kN and 20 Hz. The test results further show that adjusting the motor frequency can effectively achieve the dynamic load balance of the test pumping unit. The research results in this paper can lay a theoretical foundation for the industrial application and improvement of the transmission performance of NCPGT.

5 ACKNOWLEDGMENTS

The research was supported by the National Natural Science Foundation of China (Grant No.52265008), the Gansu Province Youth Science Foundation Project of China (Grant No. 23JRRA751), the Gansu Provincial Department of Education of China: Innovation Fund Project for University Teachers (Grant No. 2023A-021), the Open Fund of Hubei Key Laboratory of Mechanical Transmission and Manufacturing Engineering at Wuhan University of Science and Technology (Grant No. MTMEOF2023B01) and the Key Research and Development Program of Hubei Province of China (Grant No. 2021BAA202).

6 REFERENCES

[1] Dong, C.B., Liu, Y.P., Wei, Y.Q., Yun, B.B., Li, D.W., Dong, Z.Q. (2020). Analysis on meshing characteristics and transmission error of elliptic gears. *Mathematical Problems in Engineering*, vol. 2020, art. ID 2017218, **DOI:10.1155/2020/2017218**.

[2] Niu, R., Wang, G. (2020). Application of non-circular gear system in artillery system. *Fire Control & Command Control*, vol. 45, p. 102-104, **DOI:10.3969/j.issn.1002-0640.2020.02.020**. (in Chinese)

[3] Osiecki, L. (2019). New generation of the satellite hydraulic pumps. *Journal of Mechanical and Energy Engineering*, vol. 3, no. 4, p.309-314, **DOI:10.30464/JMEE.2019.3.4.309**.

[4] Ye, B., Wu, G., Yu, G., Jin, X., Sun, L. (2016). Optimized design and tests on rice potted seedling transplanting mechanism of planetary gear train with non-circular gears. *Transactions of the Chinese Society for Agricultural Machinery*, vol. 47, p. 68-73, **DOI:10.6041/j.issn.1000-1298.2016.11.009**. (in Chinese)

[5] Burrows, M., Sutton, G. (2013). Interacting gears synchronize propulsive leg movements in a jumping insect. *Science*, vol. 341, no. 6151, p. 1254-1256, **DOI:10.1126/science.1240284**.

[6] Addomine, M., Figliolini, G., Pennestri, E. (2018). A landmark in the history of non-circular gears design: The mechanical masterpiece of Dondi's astrarium. *Mechanism and Machine Theory*, vol. 122, p. 219-232, **DOI:10.1016/j.mechmachtheory.2017.12.027**.

[7] Xu, G., Chen, J., Zhao, H. (2018). Numerical calculation and experiment of coupled dynamics of the differential velocity vane pump driven by the hybrid higher-order Fourier non-circular gears. *Journal of Thermal Science*, vol. 27, p. 285-293, **DOI:10.1007/s11630-018-1010-7**.

[8] Zhao, Y., He, C. (2022). Matching between mechanics and thermodynamics among 4 individual strokes in a 4-stroke engine by non-circular gear mechanism. *Journal of Central South University*, vol. 29, p. 2112-2126, **DOI:10.1007/s11771-022-5024-7**.

[9] Yokoyama, Y., Ogawa, K., Kurebayashi, S. (1973). Studies on the noncircular planetary gear mechanisms. *Japan Society of Mechanical Engineers Proceedings*, vol. 39, no. 317, p. 393-403, **DOI:10.1299/kikai1938.39.393**. (in Japanese)

[10] Mundo, D. (2006). Geometric design of a planetary gear train with non-circular gears. *Mechanism and Machine Theory*, vol. 41, no. 4, p. 456-472, **DOI:10.1016/j.mechmachtheory.2005.06.003**.

[11] Ye, B., Yi, W., Yu, G., Gao, Y., Zhao, X. (2017). Optimization design and test of rice plug seedling transplanting mechanism of planetary gear train with incomplete eccentric circular gear and non-circular gears. *International Journal of Agricultural and Biological Engineering*, vol. 10, no. 6, p. 43-55, **DOI:10.25165/j.ijabe.20171006.2712**.

[12] Zhao, X., Chu, M., Ma, X., Dai, L., Ye, B., Chen, J. (2018). Research on design method of non-circular planetary gear train transplanting mechanism based on precise poses and trajectory optimization. *Advances in Mechanical Engineering*, vol. 10, no. 12, p. 1-12, **DOI:10.1177/1687814018814368**.

[13] Sun, L., Shen, J., Zhou, Y., et al. (2019). Design of non-circular gear linkage combination driving type vegetable pot seedling transplanting mechanism. *Transactions of the Chinese Society for Agricultural Machinery*, vol. 35, pp. 26-33, DOI:**10.11975/j.issn.1002-6819.2019.10.004**. (in Chinese)

[14] Sun, L., Hu, Y., Xing, Z. et al. (2020). Motion synthesis of rotary pot seedling transplanting mechanism based on approximate multi-pose. *Transactions of the Chinese Society for Agricultural Machinery*, vol. 51, p.103-111, **DOI:10.6041/jissn.1000-1298.2020.12.011**. (in Chinese)

[15] Zhao, X., Ye, J., Chu, M., Dai, L., Chen, J. (2020). Automatic scallion seedling feeding mechanism with an asymmetrical high-order transmission gear train. *Chinese Journal of Mechanical Engineering*, vol. 33, no. 10, p. 1-14, **DOI:10.1186/s10033-020-0432-9**.

[16] Ye, B., Zeng, G., Deng, B., Yang, C., Liu, J., Yu, G. (2020). Design and tests of a rotary plug seedling pick-up mechanism for vegetable automatic transplanter. *International Journal of Agricultural and Biological Engineering*, vol. 13, no. 3, p.70-78, **DOI:10.25165/j.ijabe.20201303.5647**.

[17] Yu, Y., Liu, J., Ye, B., Jin, X., Sun, L., Tong, J. (2019). Design and experimental research on seedling pick-up mechanism of planetary gear train with combined non-circular gear transmission. *Chinese Journal of Mechanical Engineering*, vol. 32, no. 49, p. 1-13, **DOI:10.1186/s10033-019-0357-3**.

[18] Wang, L., Sun, L., Xu, Y., Yu G.H., Zhang, W., Zheng, J. (2021). Design method of transplanting mechanism of planetary gear train based on spatial trajectory. *Transactions of the Chinese Society of Agricultural Machinery*, vol. 52, p. 51-59, **DOI:10.6041/j.issn.1000-1298.2021.07.005**. (in Chinese)

[19] Y. Liu, X. Fu, Y. Wei, Li, D.W. (2021). Parametric design and motion simulation analysis of Non-circular gear planetary gear

train. *Journal of Mechanical Transmission*, vol. 45, p. 70-75, **DOI:10.16578/j.issn.1004.2539.2021.08.010**. (in Chinese)

[20] Lin, C., Xia, X., Li, P. (2018). Geometric design and kinematics analysis of coplanar double internal meshing non-circular planetary gear train. *Advances in Mechanical Engineering*, vol. 10, no. 12, p. 1-12, **DOI:10.1177/1687814018818910**.

[21] Dong, C., Liu, Y., Zhao, G. (2021). A method for calculating elliptic gear transmission efficiency based on transmission experiment. *Strojniški vestnik - Journal of Mechanical Engineering*, vol. 67, no. 11, p. 557-569, **DOI:10.5545/sv-jme.2021.7318**.

[22] Margielewicz, J., Gąska, D., Litak, G. (2019). Modelling of the gear backlash. *Nonlinear Dynamics*, vol. 97, p.355-368, **DOI:10.1007/s11071-019-04973-z**.

[23] Dong, C., Liu, Y. (2022). Experimental study on transmission error and dynamic backlash of elliptic gear transmission system. *Proceedings of the Institution of Mechanical Engineers, Part K: Journal of Multi-body Dynamics*, vol. 236, no. 1, p. 130-139, **DOI:10.1177/14644193221077494**.

[24] Zou, S., L. Yu, G. Wang, et al. (2017). Research on the dynamic transmission error of a spur gear pair with eccentricities by finite element method. *Mechanism and Machineary Theory*, Vol. 109, pp. 1-13, **DOI:10.1016/j.mechmachtheory.2016.11.006**.

[25] Wang, G., Zhu, D., Zou, S., Jing, Y., Tian, X. (2022). Simulation and experimental research on electrical control anti-backlash based on a novel type of variable tooth thickness involute gear pair. *Strojniški vestnik - Journal of Mechanical Engineering*, vol. 68, no. 2, p. 126-140, **DOI:10.5545/sv-jme.2021.7452**.

[26] Yin, X., Du, Z., Wang, Y., Lu, S., Li, Y., Zhao, T. (2022). Analysis and experimental study of oil well indicator diagram based on electric parameter method. *Energy Reports*, vol. 8, supp. 4, p.732-745, **DOI:10.1016/j.egyr.2022.02.013**.

Strojniški vestnik - Journal of Mechanical Engineering 70(2024)3-4, 141-158
DOI:10.5545/sv-jme.2023.691
Original Scientific Paper
Received for review: 2023-06-14
Received revised form: 2023-11-05
Accepted for publication: 2023-11-27

Transient Flow Characteristics of a Pressure Differential Valve with Different Valve Spool Damping Orifice Structures

Xu Zhang
Fluid Machinery Engineering Technology Research Centre of Jiangsu University, China

Lubrication system failure is a significant cause of in-flight shutdown incidents in aviation engines. The pressure differential valve, an essential component of a certain type of aviation engine lubrication system, is responsible for controlling the flow rate and pressure of the lubricating oil. Comprehending the transient flow characteristics of the pressure differential valve is of paramount importance for the secure operation of lubrication systems. This paper establishes a transient flow model of a pressure differential valve based on a transient computational fluid dynamics (CFD) method, and the experimental validation demonstrates the effectiveness of the computational model. The internal flow characteristics of the differential pressure valve at different stages during the opening process were studied. Additionally, four transient lubricating oil flow models with different valve spool damping orifice were established to analyse the impact of damping orifice structure on valve spool movement characteristics, pressure control characteristics, and flow field distribution. The results indicate that when the diameter of the valve spool damping orifice increases from 0.3 mm to 1.0 mm, the valve spool displacement and fluid force increase by 88 % and 20 %, respectively. Meanwhile, the peak valve spool velocity, peak oil supply pressure, and steady-state value decreased by 15 %, 29 %, and 34 %, respectively. As the length of the valve spool damping orifice increases from 0.894 mm to 4.0 mm, the growth rate of valve spool displacement and fluid force gradually decreases, with the peak valve spool velocity decreasing by 7 %. This study has potential significance for the structural optimization and application of pressure differential valve in lubrication systems.

Keywords: aviation engine lubrication system, pressure differential valve, flow impact, transient flow, valve spool damping orifice

Highlights

- *The spring force and fluid force jointly affect the pressure-regulating characteristics of the pressure differential valves.*
- *When the valve spool damping orifice structure is Φ0.3×0.894, the pressure regulation performance is poor.*
- *Increasing the diameter of the damping orifice can effectively reduce the maximum oil supply pressure, increasing the length of the damping hole has little effect on the oil supply pressure.*
- *The damping orifice structure of the pressure differential valve has little effect on the start time of the valve spool.*

0 INTRODUCTION

As one of the key systems of aviation engines, the lubrication system has a significant impact on the safe operation of the engine due to its lubrication performance [1]. According to relevant statistical data, in the engine shutdown accidents of the Chinese Air Force in 1985, lubrication system failures accounted for as much as 43 % of such cases. Similarly, a certain type of aviation engine in the US Air Force experienced 90 aviation accidents in just one year, of which 28 % were due to lubrication system failures [2]. The lubrication system undertakes the task of providing sufficient lubricating oil for aviation engines, as well as lubricating and cooling the supporting bearings and transmission components, reducing friction and temperature between each component, alleviating the ultra-high heat generated by mechanical friction, and preventing important parts from clogging and corrosion during operation [3] to [5]. Currently, the lubrication oil supply subsystem of foreign military aviation engines (such as the F110 military engine from GE in the United States and the АЛ-31Ф engine from Russia) commonly uses a fixed pressure valve to control the lubrication system flow. However, a certain type of domestically developed fighter jet in China uses a pressure differential valve to control the circulation of the lubrication oil supply system [6]. Compared with the traditional fixed-pressure oil supply method, the pressure differential valve pays more attention to the stability of the oil supply under high-speed and high-pressure conditions, making the aircraft more adaptable and providing certain excellent guarantees for the safe operation of aviation engines [7] and [8]. However, at present, there is relatively limited theoretical and experimental research data on this valve, especially regarding the transient flow of high-pressure lubricating oil inside the pressure differential valve, and relevant data is relatively scarce. Therefore, an in-depth exploration of the pressure-regulating valve has significant practical significance.

With the development of the industrial field, especially in the aerospace industry, the requirements for the pressure-regulating characteristics of valves are gradually increasing. Therefore, research on the

*Corr. Author's Address: Fluid Machinery Engineering Technology Research Centre of Jiangsu University, China, 18993458481@163.com

transient opening process of pressure differential valves is becoming increasingly important. Lai et al. [9] used unsteady computational fluid dynamics (CFD) methods to investigate the transient characteristics and internal flow distribution of dual disc check valve, and verified the reliability of CFD results through experiments, providing an approximate value of disc rotation characteristics. Afshari et al. [10] conducted research on some key parameters that have a significant impact on the dynamic response of direct-acting hydraulic pressure-reducing valves using bond graph simulation technology and proposed an analytical solution applicable to nonlinear complex systems with multiple energy domain interactions. Cui et al. [11] utilized the user-defined function UDF technology and mobile grid technology to conduct unsteady research on the opening and closing process of a ball valve. The results showed that due to the fluid lag and changes in the relative opening, there were significant differences in the transient performance and flow field of the ball valve during the opening and closing process. Sibilla et al. [12] studied the internal flow characteristics of the check valve based on the transient CFD model and dynamic mesh technology. In addition, the influencing factors of flow characteristics during valve opening and closing are also studied. Beune et al. [13] designed CFD software to analyse the opening characteristics of high-pressure safety valves, and studied the relationship between disk lift, flow force and mass flow rate versus time.

Chattopadhyay et al. [14] studied the internal flow structure of the spool-type pressure regulating valve at different openings and different pressure drops and found that the standard $k-\varepsilon$ turbulence model can predict higher levels of turbulent kinetic energy. In addition, it was found that the two-dimensional axisymmetric formula can capture the total flow parameters well. Han et al. [15] studied the variation of flow rate and pressure difference with time during the opening and closing process of the ball valve by using dynamic mesh technology and variable inlet and outlet boundary conditions. Saha et al. [16] studied the transient flow characteristics inside the shut-off valve and found that the higher the friction coefficient between the valve spool and the valve body, the faster the stability of the spool. Ray [17] established a nonlinear dynamic model of the relief valve and studied its transient response. It was found that the valve opening time was linearly related to the dimensionless parameters given by the ratio of the orifice length to its radius. Dasgupta [18] studied the dynamic characteristics of the pilot relief valve based on bond graph technique, and determined some key design parameters that have a significant impact on the dynamic response of the valve through simulation research. Zhang et al. [19] studied the full transient opening dynamic characteristics of the 3D power-operated pressure relief valve and obtained the pressure field and velocity field, including small-scale flow characteristics. Sun et al. [20] analysed the transient flow mechanism during the opening of the integrated valve and the variation of the transient characteristic parameters of the valve-induced pressure with the operating temperature, the initial flow rate of the fluid and the opening time of the valve. Yang et al. [21] studied the opening and closing process of a steam pressure relief valve in a nuclear power plant by using CFD technology combining the domain decomposition method (DDM) and the grid pre-deformation method (GPM) methods and found that reducing spring stiffness can effectively reduce the reseating pressure.

In addition, in order to adapt to the requirements of various industries and improve the working efficiency and voltage regulation characteristics of the valve, much research has been done on its structural design. Abdallah et al. [22] studied the relationship between different inlet pressures and pressure oscillation and proposed four solutions to reduce the pressure oscillation of the deflection jet servo valve by structural optimization. Zang et al. [23] studied the influence of different inlet diameters on the dynamic characteristics of the pilot valve by using dynamic mesh technology. The results show that increasing the inlet diameter can significantly shorten the opening time of the valve, but also increase the fluid force and velocity of the valve spool during the opening process. Liu et al. [24] used AMESim to study the effects of spring stiffness and preload on the dynamic characteristics of a three-way proportional reducing valve, and the experimental results were consistent with the simulation results. In addition, it was found that using closed-loop control of valve lift can effectively improve the dynamic characteristics. Combined with numerical calculation and experimental verification, Simic et al. [25] studied all geometric parameters of the valve to optimize the valve geometry. The results show that the axial component of the flow force can be significantly reduced, and the dynamic characteristics of the valve can be improved only by modifying the geometry of the spool and the valve shell. Liu et al. [26] proposed a structure for compensating the hydrodynamic force of the cartridge cone valve, and studied several parameters that may affect the hydrodynamic characteristics. The results show that the hydrodynamic compensation effect

of the valve core increases with the increase of the opening degree under the optimal size. Ye et al. [27] established a CFD model of a high-pressure hydrogen needle valve and studied the influence of valve spool shape on the performance and flow characteristics of the valve. The results show that changing the shape of the valve spool to make it have a larger flow area at a small opening can make the high-pressure hydrogen valve have a better flow field distribution. In addition, Ye et al. [28] studied the influence of spool head angle on spool motion performance and flow field characteristics. The results show that the acceleration, velocity, and kinetic energy of the valve spool increase with the increase of the valve spool head angle, which enhances the impact effect of the valve spool. Yang et al. [29] established the simulation model of the relief valve and analysed the influence of valve seat flow path diameter and valve seat chamfering depth on valve flow field performance. The results show that increasing the diameter of the flow path helps to suppress the negative pressure, and increasing the chamfering depth of the valve seat can reduce the flow rate and the maximum negative pressure of the throat. Han et al. [30] has proposed a novel fast-response water hydraulic proportional valve and developed an accurate nonlinear mathematical model to simulate its dynamic performance. Experimental results have demonstrated the valve's excellent static and dynamic control capabilities. Karanović et al. [31] conducted experimental research using a mechanically actuated 4/2 control valve to investigate the wear intensity of working elements under different levels of oil contamination by solid particles. Additionally, by measuring the pressure drop values during fluid flow through the valve, it was observed that oils with the lowest cleanliness level exhibited greater variability in the measured values. These results provide insights into the impact of working fluid cleanliness on potential defects and failures within hydraulic system components, thereby contributing to a better understanding of their reliability and durability.

The references show that there is less research on pressure differential valve under high-pressure lubricating oil flow conditions. Therefore, the main purpose of this paper is to explore the transient characteristics of pressure differential valve under the impact of high-pressure lubricating oil, quantify the movement and force of the valve spool, and summarize the influence of different valve spool damping orifice structures on the pressure regulating characteristics of the valve. It provides research accumulation for the structural optimization and application of pressure differential valve in aero-engine lubrication system. The specific research process is as follows. Firstly, the transient flow field characteristics during the opening process of the pressure differential valve are studied. Secondly, the variation of displacement, velocity, fluid force, oil supply pressure and other parameters during the transient opening process of pressure differential valve under different valve spool damping orifice structures are analysed. Finally, the movement law and pressure regulation characteristics of the valve spool under the impact of high-pressure lubricating oil are quantitatively analysed.

1 TRANSIENT CFD MODEL PRESSURE DIFFERENTIAL VALVE

1.1 Geometry of Pressure Differential Valve and 3D Model

Fig. 1 is a functional diagram of pressure differential valve. The valve spool can move back and forth under the combined action of spring force, inlet pressure, oil supply pressure, middle cavity pressure, hydraulic force, etc., thereby changing the opening size of the overflow orifice and ensuring that the pressure difference before and after each lubricating nozzle is stable within the specified range. The excess lubricating oil at the outlet of the lubricating oil pump is returned to the oil tank through the overflow pipeline to adjust the oil supply of the lubrication system.

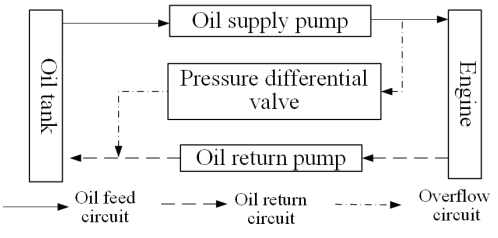

Fig. 1. *Functional diagram of pressure differential valve*

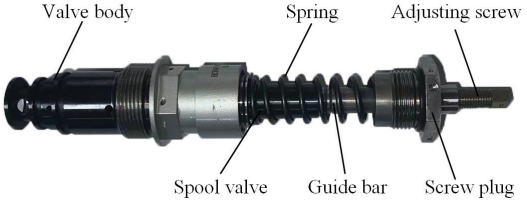

Fig. 2. *Physical diagram of pressure differential valve*

Fig. 2 is a physical diagram of pressure differential valve, which is widely applied in the lubrication system of aviation engines. It is installed on the lubrication oil pump to control the oil supply and pressure of the lubrication system and has a

certain impact on the stability of the aviation engine lubrication system.

Fig. 3 shows a 3D half section view of pressure differential valve, the valve is composed of a valve enclosure, valve body, valve spool, guide rod, screw plug, adjusting screw, and spring. Lubricating oil flows into the valve through the left inlet port. From the inlet of the valve, the overflow orifices, oil supply pressure inlet orifices, and middle cavity pressure orifices are located in succession from left to right. There are four orifices for each passage. Among them, the diameters are 6 mm, 2 mm, and 3 mm respectively, and the four orifices in each part are evenly distributed in the circumferential direction. The maximum outer diameter of the inner chamber of the valve is 22 mm, and the valve spool inside is a hollow structure with a damping orifice. After measurement, the mass of the valve spool is 50 g, the maximum stroke is 9 mm, the spring stiffness coefficient is 4900 N/m, and the preload is 69.8 N. There are two valve limits on the valve body to limit the displacement of the valve spool. When the pressure differential valve is opened, the valve spool stops moving when the end face of the valve spool contacts with the limit surface.

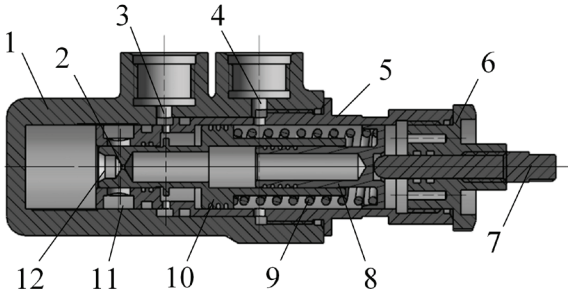

Fig. 3. *Half sectional view of pressure differential valve; 1 valve enclosure, 2 damping orifice, 3 oil supply pressure inlet, 4 medium cavity pressure inlet, 5 valve body, 6 screw plug, 7 adjusting screw, 8 guide rod, 9 spring, 10 valve spool, 11 overflow orifice, 12 valve inlet*

The internal structure of the valve spool is a cavity with a damping orifice, the diameter of which is 1mm and the length is 0.894 mm. The valve can set the initial opening pressure by adjusting the preload of the spring through the adjusting screw. At this time, due to the compression of the spring, the valve spool is located at a displacement of 0 under the action of the spring force, and the overflow orifices are closed. After the lubrication system starts to work, the lubricating oil enters the valve and the oil supply chamber under the action of the lubrication oil pump. The valve spool begins to move under the combined effect of the inlet pressure, oil supply pressure, middle cavity pressure, spring force, valve spool internal cavity pressure, hydraulic force, etc. As the displacement increases, the overflow orifices are opened, thereby regulating the average oil supply pressure and fluctuation amplitude.

1.2 Numerical Theory of Valve Spool Dynamic Balance

Fig. 4 is the simplified physical model of pressure differential valve. The pressure differential valve controls the oil supply pressure through the movement state of the valve spool; displacement determines the valve opening size. In the process of pressure regulation, the force of the valve spool in the lubricating oil is complex and changeable. In order to correctly build a simulation model to understand the transient flow characteristics of the high-pressure lubricating oil inside the pressure differential valve, it is particularly important to analyse the force of the valve spool. Many non-linear factors exist in the mathematical model for valve dynamic characteristics, such as hydraulic power, pipeline dynamic transmission characteristics, etc. At the same time, the work process has a number of interfering factors. Hence, factors like hydraulic pressure, viscous friction force, the spring force, the steady-state hydrodynamic force, and the transient hydrodynamic force must be fully considered in the development of the mathematical model.

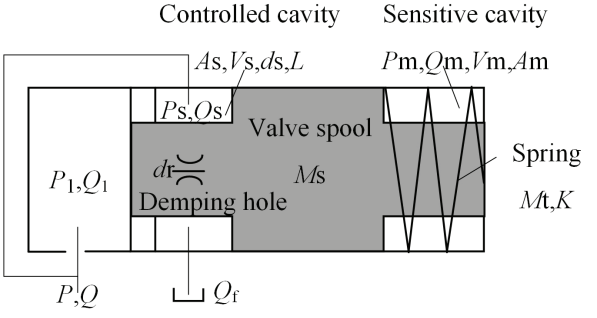

Fig. 4. *Physical model of pressure differential valve*

Valve spool force balance equation, Eq. (1):

$$P_1A_1 - P_2A_2 + P_sA_s - P_mA_m + F_{stf} + F_{trf}$$

$$-K(X_{s0} + X_s) \mp F_f = (M_s + \tfrac{1}{3}M_t)\frac{d^2X_s}{dt^2} + B_s\frac{dX_s}{dt}, \quad (1)$$

where $A_1 = A_2$, A_1 is the force area of the inlet end of the valve, A_2 is the force area of the rear cavity of the damping orifice, A_s is the force area of the oil supply cavity, and A_m is the force area of the middle cavity. P_1 is the inlet pressure of pressure differential valve, and P_2 is the cavity pressure behind damping orifice.

P_s is the pressure of the oil supply cavity, and P_m is the pressure of the middle cavity. M_s is the mass of the valve spool, M_t is the mass of the spring, K is spring stiffness, X_{s0} is the pre-compression of the spring, and X_s is the displacement of the valve spool.

Valve spool motion damping coefficient B_s:

$$B_s = \frac{\pi \eta l d}{(D-d)}, \tag{2}$$

where D and d are the diameter of the valve cavity and the diameter of the valve spool respectively, and l is the damping length.

F_{stf} and F_{trf} are steady-state hydrodynamic force and transient hydrodynamic force, respectively. The expressions are as follows:

$$F_{stf} = -K_s X_s P_s, \tag{3}$$

$$F_{trf} = K_L \frac{dX_s}{dt}, \tag{4}$$

where K_s is the steady-state hydrodynamic coefficient, and K_L is the transient hydrodynamic viscous damping coefficient.

1.3 Control Equations

Numerical solutions in CFD utilize fundamental equations including the continuity equation, momentum equation, and energy equation. In this study, the CFD simulation of pressure differential valve does not consider energy transfer; therefore, the energy equation is not considered. Additionally, CFD also includes component mass conservation equations for various chemical components and equations of state for gases with density variations. Different equations need to be introduced to describe different problems. The fundamental equations of fluid mechanics are always closed, and the corresponding numerical solutions are obtained by discretizing these equation groups.

The continuity equation, also known as the mass conservation equation, states that any fluid flow must satisfy the law of mass conservation. The continuity equation can be expressed as:

$$\frac{\partial \rho}{\partial t} + div(\rho \vec{u}) = 0. \tag{5}$$

Written in the form of divergence, it can be expressed as:

$$\frac{\partial \rho}{\partial t} + \frac{\partial (\rho u)}{\partial x} + \frac{\partial (\rho v)}{\partial y} + \frac{\partial (\rho w)}{\partial z} = 0, \tag{6}$$

where ρ represents the density of the fluid; u, v and w represent the velocity components of the fluid element in the X, Y, and Z directions; t represents time.

Momentum equation:

To solve any fluid flow problem, it is necessary to satisfy the momentum equation, which is a fundamental equation. For incompressible Newtonian fluids, the conservation equation of momentum for a viscous, incompressible flow can be represented by the following form of the Navier-Stokes (N-S) equation:

$$\begin{aligned}
&\rho\left(\frac{\partial u}{\partial t} + u\frac{\partial u}{\partial x} + v\frac{\partial u}{\partial y} + w\frac{\partial u}{\partial z}\right) = \\
&\rho F_x - \frac{\partial p}{\partial x} + \mu\left(\frac{\partial^2 u}{\partial x^2} + \frac{\partial^2 u}{\partial y^2} + \frac{\partial^2 u}{\partial z^2}\right), \\
&\rho\left(\frac{\partial v}{\partial t} + u\frac{\partial v}{\partial x} + v\frac{\partial v}{\partial y} + w\frac{\partial v}{\partial z}\right) \\
&= \rho F_y - \frac{\partial p}{\partial y} + \mu\left(\frac{\partial^2 v}{\partial x^2} + \frac{\partial^2 v}{\partial y^2} + \frac{\partial^2 v}{\partial z^2}\right), \\
&\rho\left(\frac{\partial w}{\partial t} + u\frac{\partial w}{\partial x} + v\frac{\partial w}{\partial y} + w\frac{\partial w}{\partial z}\right) \\
&= \rho F_z - \frac{\partial p}{\partial z} + \mu\left(\frac{\partial^2 w}{\partial x^2} + \frac{\partial^2 w}{\partial y^2} + \frac{\partial^2 w}{\partial z^2}\right),
\end{aligned} \tag{7}$$

where ρ represents the density of the fluid; μ represents the dynamic viscosity of the fluid; u, v and w represent the velocity components of the fluid element in the X, Y, and Z directions, respectively; p represents the pressure on the fluid element; t represents time; F_x, F_y, and F_z represent the components of external forces in the X, Y, and Z directions.

The Navier-Stokes equations consist of 3 fractional equations, plus the continuity equation, resulting in a total of 4 equations with 4 unknowns: u, v, w and p. The equation group is closed, and with proper initial and boundary conditions, the equations can be solved.

1.4 Computational Fluid Domain and Grid Independence Verification

In order to analyse the real transient flow inside the valve, the lubricating oil pump and pressure differential valve are connected through the pipeline for joint simulation. The fluid domain is shown in Fig. 5, and the fluid domain of the lubricating oil pump and pressure differential valve is shown in Fig. 6. In the actual lubrication process, the lubricating oil is sprayed to each lubrication point through the nozzle,

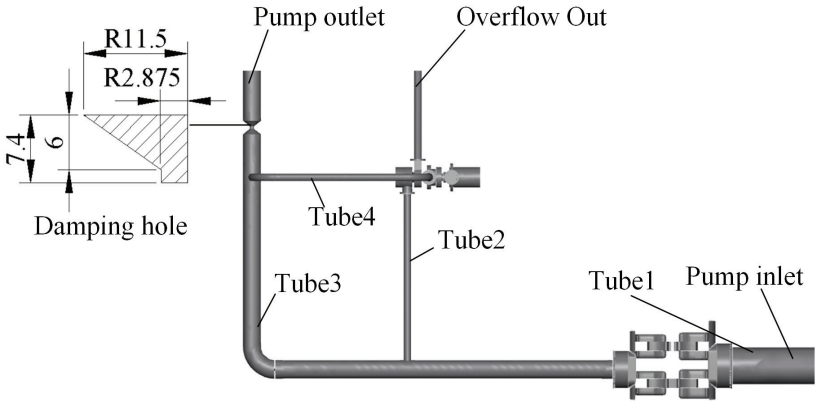

Fig. 5. *Schematic diagram of pump and valve fluid domain*

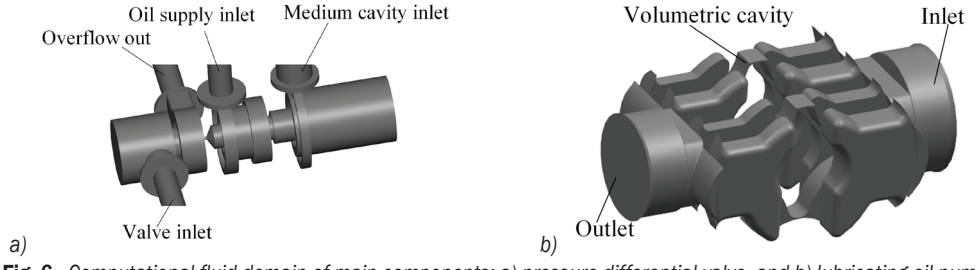

Fig. 6. *Computational fluid domain of main components; a) pressure differential valve, and b) lubricating oil pump*

and the damping orifice is designed to make the simulation closer to the test. The size of each part of the pipeline is shown in Table 1.

Table 1. *Pipeline parameters*

Name	Diameter [mm]	Length [mm]
Tube1	40	400
Tube2	8	180
Tube3	20	650
Tube4	12	280

Table 2. *Rotation centre coordinates*

Coordinate	rotor pair 1		rotor pair 2	
	internal rotor	external rotor	internal rotor	external rotor
X [mm]	294	294	294	294
Y [mm]	0	-4.5	0	-4.5
Z [mm]	207	207	247	247

Pumplinx software has a dedicated meshing template for internal gear pumps and a slide valve meshing template. First, the rotor template mesher module is used to divide the intermeshing region of the lubricating oil pump rotor. The internal rotor has 4 teeth, and the external rotor has 5 teeth. The rotation axis is the Z axis. The rotation centre is set as shown in Table 2, and the rotor mesh size is set to a high-quality mesh.

When the valve spool moves, pressure differential valve has a volume chamber that is stretched and compressed. Therefore, the valve template mesh module is used to divide the corresponding fluid domain, and the moving surface, cylindrical surface and end surface of the volume cavity are set. The direction of motion is X-axis, the minimum gap is 0.1 mm, and the maximum stroke is 9 mm. Because the valve spool is a moving part, the valve spool is also meshed by valve template mesh module. The rest parts, such as connecting pipelines and lubricating oil pump inlet and outlet, are divided into grids by general mesher module.

Table 3. *Number of grids*

Scheme	Number of grids [$\times 10^4$]	Pump outlet flow rate [m³/h]	Overflow rate [m³/h]
a	39	2.77	1.54
b	70	2.57	1.41
c	138	2.55	1.40
d	263	2.54	1.40

The number of grids is shown in Table 3. The pump outlet flow rate and valve overflow flow rate under each scheme are shown in Fig 7. Comparison

shows that scheme a has a significant difference from the other three schemes, with a much smaller number of meshes, which seriously affects the calculation results. Considering comprehensively, scheme b is finally selected as the number of grids calculated in this paper. The grids of pressure differential valve and lubricating oil pump are shown in Fig. 8.

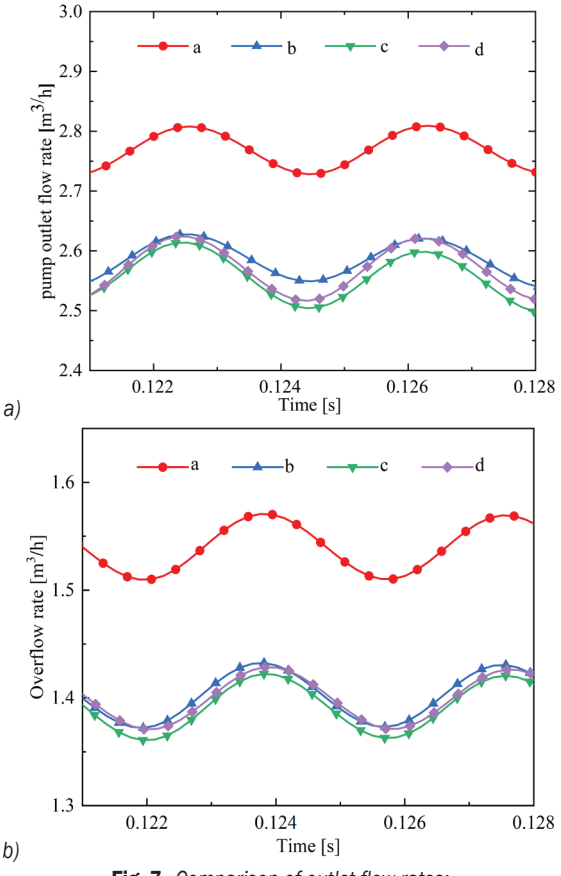

Fig. 7. *Comparison of outlet flow rates; a) pump outlet flow rate, and b) overflow rate*

The valve template mesh module is used to process the corresponding fluid domain mesh. The motion surface, cylindrical surface, and termination end surface of the volume chamber are set, and the motion direction is *X*-axis. The minimum gap is 0.1 mm and the maximum stroke is 9 mm. Since the valve spool belongs to the moving parts, the valve template mesh module is also used for mesh division. Other parts such as connecting pipes and sliding oil pump inlet and outlet are meshed using the general mesher module.

The domain of computing fluids is meshed by using the pumplinx professional pump and valve model. The lubricating oil pump rotor is meshed using the rotor template mesh module. The size of the rotor mesh is adjusted to fine. There are traction and compressed volume chambers in the direction of movement of the valve spool valve. Consequently, the valve template mesh is used for grid processing, and the other parts are mesh using the general mesh module. The fluid domain grid for joint simulation calculation is shown in Fig. 6. After grid partition, each grid is connected by connect selected boundaries via moving grid interface (MGI) and grid interaction surface is added to form a complete grid connecting the fluid fields of the pump-valve joint simulation calculation.

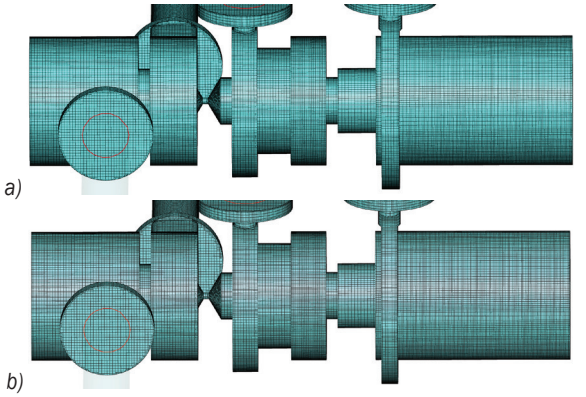

Fig. 8. *Grid division of a) pressure differential valve, and b) lubricating oil pump*

1.5 Initial and Boundary Conditions

4050 aviation lubricating oil is used as the fluid medium. Its service temperature is –40 ℃ to 200 ℃, and it can withstand temperatures up to 220 ℃ for a short time. It has excellent high and low temperature use ability. The equation of density changing with temperature is:

$$\rho_t = \rho_{20} - \beta(t-20), \tag{8}$$

where ρ_t, ρ_{20} are the density at temperature t 20 ℃ in [g/cm³]; the coefficient of β is different with different lubricating oil, β is 0.000035.

Lubricating oil kinematic viscosity and temperature calculation equation:

$$\ln\ln(v+A) = B - C\ln T, \tag{9}$$

where A, B, C are coefficients related to fuel. By looking up the relevant information, A = 0.6, B = 21.52, C = 3.54. The density of 4050 lubricating oil at 25 ℃ ρ = 0.972025 g/cm³, dynamic viscosity μ = 0.045844198 Pa·s.

The gerotor model, valve model, turbulence model, cavitation model, translation 1~DOF model

and flow model are added to the model window. First, select the reference pump in the extended model and set the speed to 2500 rpm and the rotation axis to the *Z* axis. In advanced mode, the translation 1~DOF module is set up, the specific parameters are shown in Table 4.

Table 4. *Translation 1~DOF model parameters*

Valve spool mass [kg]	Spring stiffness [N/m]	Spring preload [N]	Initial displacement [m]	Initial velocity [m/s]	Minimum gap [mm]	Maximum gap [mm]
0.05	4900	69.8	0	0	0.1	9.0

By comparing three turbulence models, namely Standard k–ε, renormalization group (RNG) k–ε, and realizable $k-\varepsilon$, it is found that the RNG $k-\varepsilon$ model has higher credibility and accuracy in analysing a wider range of flow characteristics compared to the Standard $k-\varepsilon$ model. The realizable $k-\varepsilon$ model performs well in predicting moderate-intensity swirling flow. Since this paper does not involve swirling flow issues, the RNG $k-\varepsilon$ turbulence model is ultimately chosen for numerical calculations.

Table 5. *Computational setup of pump model*

Boundary conditions	Boundary type
Location	
Inlet of model pump	Total Pressure(one-atmosphere)
Outlet of model pump	Total Pressure(one-atmosphere)
Physical wall surfaces	No-slip wall
Interfaces on both side of impeller	
Transient state	Transient rotor-stator

Table 6. *Computational setup of valve model*

Boundary conditions	Boundary type
Location	
Inlet of the middle cavity	Total Pressure(one-atmosphere)
outlet of the overflow cavity	Total Pressure(one-atmosphere)
Moving wall surfaces	Slip wall
Translation 1~DOF	Dynamic BC
Velocity	trans_1d.velocity, 0 m/s, 0 m/s
Remaining physical wall surfaces	No-slip wall
Control for transient simulation	
Time step	3.3×10^{-5} s
Total time	0.24 s
Convergence criterion	10^{-4}

During the work process, the internal and external rotors of the lubricating oil pump are constantly meshed and separated, and cavitation occurs during numerical calculations. The full cavitation model includes the N-S equation and the commonly used turbulence model. The phase change rate equation is obtained by improving the Rayleigh-Plesset bubble dynamics equation, so the full cavitation model is selected for calculation.

After the basic setting of the model is completed, the solution parameter settings of the lubricating oil pump and pressure differential valve are shown in Tables 5 and 6, respectively.

1.6 Parameters for the Calculation Schemes

This paper mainly studies the transient flow characteristics of the differential pressure valve with different valve spool damping orifice structures. By changing the diameter and length of the damping orifice, this paper designs five kinds of valve spools with different structures. When the structure of the damping orifice changes, its mass will also change. Fig. 10 shows the 3D structure of the valve spool. Table 7 shows the specific parameters of damping orifice under different structures.

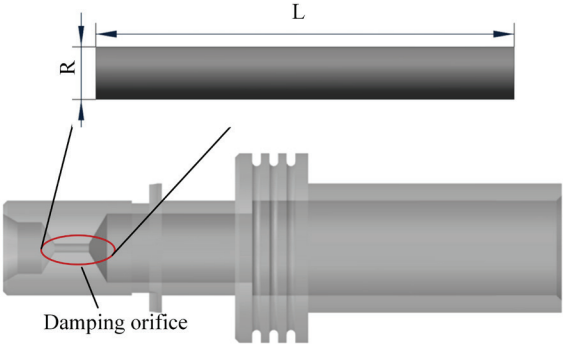

Fig. 9. *The 3D model with valve spool*

Table 7. *Specific parameter of damping orifice in different structures*

Scheme	Diameter [mm]	Length [mm]	Mass [g]
a	0.3	0.894	50.17
b	0.6	0.894	50.10
c	1.0	0.894	50.00
d	1.0	2.0	50.44
e	1.0	4.0	51.24

2 EXPERIMENTAL SETUP AND MEASUREMENT

Fig. 10 is the diagram of the transient flow characteristics test bench for pressure differential valve. The valve working system test bench includes oil tank, lubricating oil pump, servo motor, vortex flowmeter, pressure differential valve, pressure pulsation sensor, electric valve, and valve pipeline.

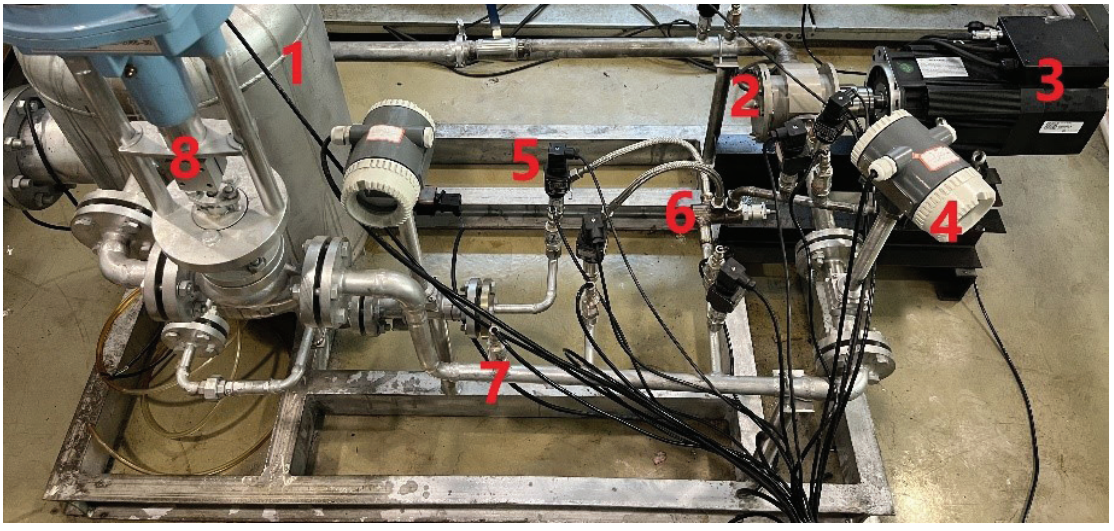

Fig. 10. *Pressure differential valve working system test bench; 1 oil tank, 2 lubricating oil pump, 3 servo motor, 4 vortex flowmeter, 5 temperature sensor, 6 pressure differential valve, 7 pressure pulsation sensor, 8 electric valve*

Table 8. *Main test equipment specifications*

Instrument	Model	Performance index
Pressure sensor	SCYG410 0 MPa to 0.5 MPa / 2.0 MPa	±0.1% FS
Turbine meter	LUGB-DN15/DN25	1.5 MPa to 1.6 MPa
Electric control valve	PHLZ-206S-30	1.6 MPa
Servo motor	VA-XX-4T5.5G	3.7 kw

The valve pipeline includes closed loop circuit, valve inlet pipeline, valve oil supply pipeline, valve overflow pipeline and valve intermediate bearing cavity inlet pipeline.

In this paper, 4050 aviation lubricating oil is used as the test medium. During the test, the ball valve is first opened, the servo motor is turned on to adjust the speed to 2500 rpm and the electric control valve is used to adjust the working pressure of the system between 0.3 MPa to 0.6 MPa. The data acquisition box is used to transfer the signal of the pressure sensor to the computer, and the pressure change is displayed in real time. The sampling frequency is 10240 Hz. Table 8 is the main test equipment and test component specifications of the test bench.

3 RESULT AND DISCUSSION

3.1 Experimental Test of Pressure Differential Valve

In this paper, pressure differential valve with damping orifice structure of Φ 1 mm × 0.894 mm is taken as an example (Method c in Table 7) for experimental verification. Figs. 11a and b respectively show the comparison of the inlet pressure pulsation and oil supply frequency spectra of pressure differential valve between the simulation results and the experimental results. It can be seen from the diagram that the main frequency of the inlet pressure pulsation and the oil supply pressure pulsation is within 5 % of the experimental value. Fig. 12 shows the comparison between the simulation and test results of pump outlet flow rate and valve overflow flowrate. It can be seen from the figure that the error between the simulation value and the test value is within 10 %. The comparison results show that the simulation model and simulation method have certain reliability.

3.2 Transient high-pressure lubricating oil flow behaviour in pressure differential valve

Taking pressure differential valve with damping orifice structure of Φ 1 mm × 0.894 mm as an example, the flow characteristics of transient high pressure lubricating oil inside the valve are studied. Fig. 13 shows the change of valve spool velocity and displacement with opening time. It can be seen that the valve spool begins to move at 0.02 s. With the increase of opening time, the valve spool displacement gradually increases. At 0.2 s, the valve

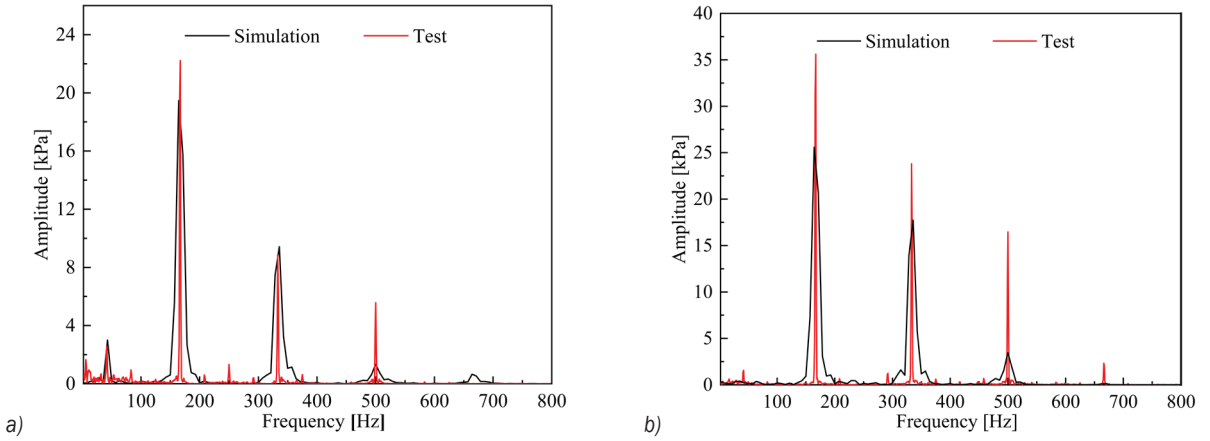

Fig. 11. *Comparison of pressure pulsation spectra; a) inlet valve pressure pulsation, and b) oil supply pressure pulsation*

spool displacement gradually stabilizes, and the displacement is 8.87 mm. At 0.02 s to 0.035 s, the velocity of the valve spool increases rapidly, reaches the maximum value of 0.236 m/s at 0.035 s, and then begins to decline to about 0 m/s.

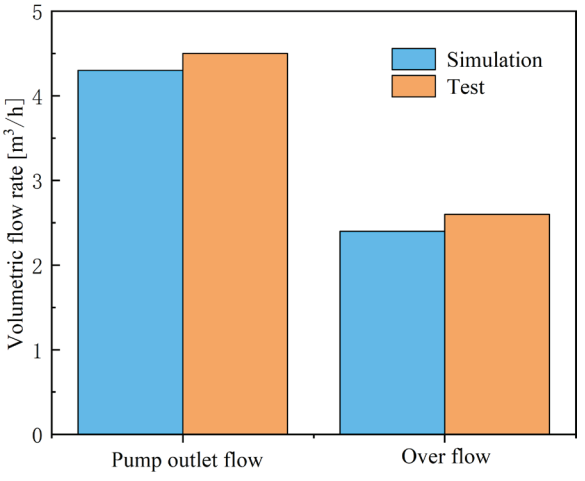

Fig. 12. *Comparison of outlet flow rate*

Fig. 14 shows the relationship between fluid force and spring force with valve spool displacement. The results show that the fluid force and spring force increase with the increase of valve spool displacement. In the range of 0 mm to 0.64 mm, the displacement of the valve spool is small, and the pressure increases rapidly due to the accumulation of lubricating oil at the entrance of the valve. The fluid force is greater than the spring force and the gap increases with the increase of the displacement. Then, as the displacement of the valve spool increases, the overflow orifice is opened, and the lubricating oil returns to the oil tank through the bypass pipeline and the overflow pipeline. In the whole opening process, the gap between the fluid force and the spring force is small, so the two play a leading role in the opening process of pressure differential valve.

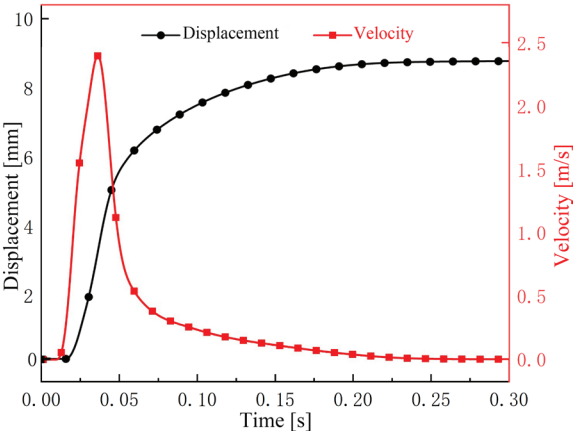

Fig. 13. *The relationship between both the valve spool displacement and velocity with the opening time*

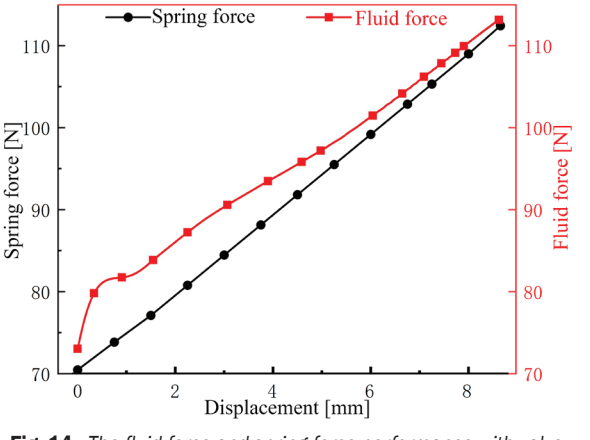

Fig. 14. *The fluid force and spring force performance with valve spool displacement*

Due to the limiting effect of the adjusting screw, the maximum displacement of the valve spool is 9 mm. It can be seen from Fig. 13 that during the opening process of pressure differential valve, the maximum displacement of the valve spool is less than 9 mm, and the movement velocity is very small when the valve spool reaches the maximum displacement, so the valve spool will not produce large kinetic energy to impact the adjustment screw to damage the valve component.

Fig. 15 shows the flow characteristics of high-pressure lubricating oil in pressure differential valve at 0.02 s, 0.035 s, 0.05 s and 0.065 s. Figs. 15a and b are the pressure and velocity contours of the central section of the valve, respectively. It can be found that during the opening process, the inlet pressure of the valve gradually increases, and the thrust acting on the gradually increasing head of the valve spool so that the valve spool begins to move. When the valve spool moves to the right and the overflow orifice is opened, the internal pressure of the valve finally reaches a stable state due to the overflow effect of the valve.

At 0.02 s, the oil supply pressure is about 349 kPa, the inlet pressure of the valve spool head is about 391 kPa. The valve spool head is subjected to a large thrust, and the valve spool begins to move. The maximum velocity projection in the X direction appears at the damping orifice, which is approximately 16.68 m/s. The high-pressure lubricating oil enters the inner chamber of the valve spool through the damping orifice. At this time, the volume chamber is not fully filled, the chamber pressure is about 92 kPa, and a large pressure gradient appears at the damping orifice.

At 0.035 s, the oil supply pressure is about 1219 kPa, and the inlet pressure of the valve spool head is about 1257 kPa, and the valve overflow orifice begins to be opened. At this time, the displacement of the valve spool increases rapidly, the volume of the inner chamber decreases rapidly, and the internal lubricating oil pressure reaches 3000 kPa. The maximum velocity projection in the X direction appears at the damping orifice at about -41.14 m/s, and the lubricating oil flows from the inner chamber to the valve inlet.

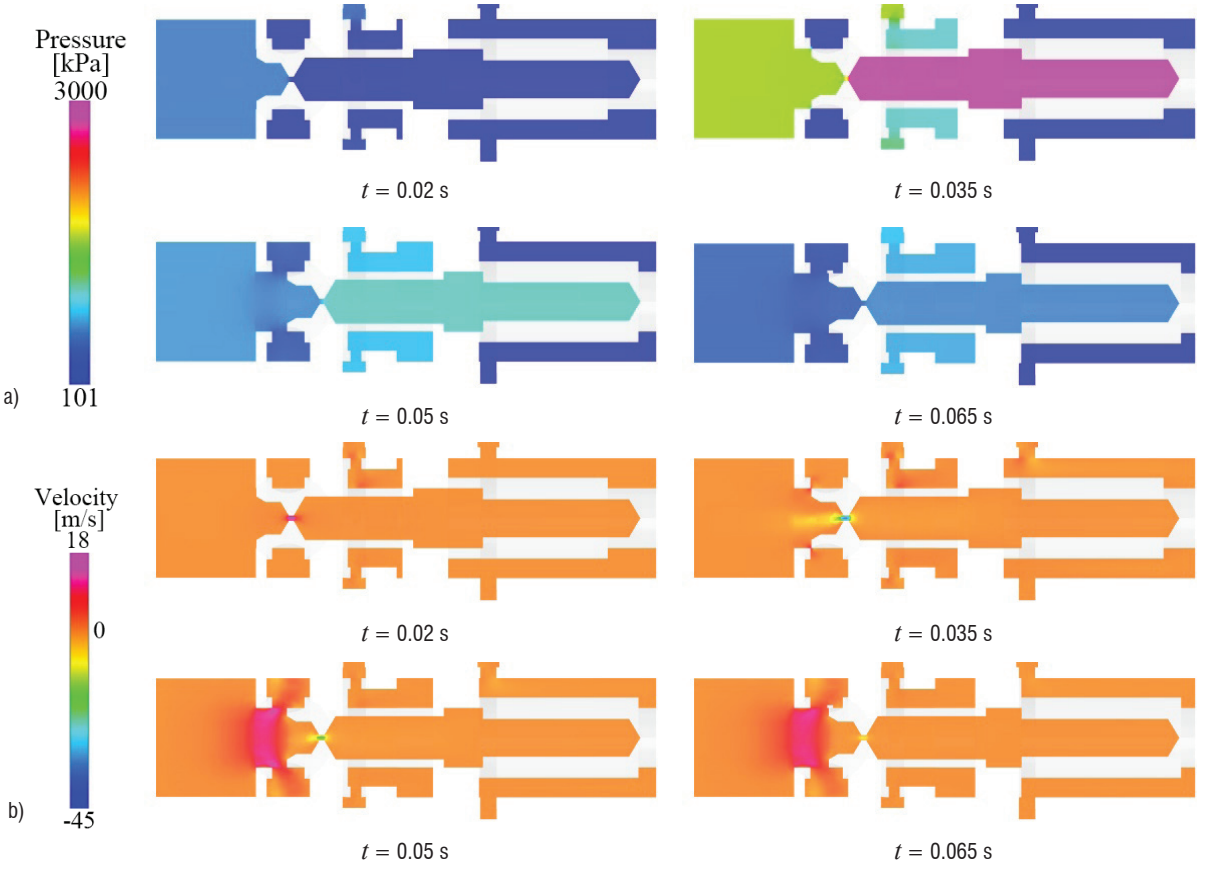

Fig. 15. *Pressure and velocity distributions in pressure differential valve at different moments: a) pressure distributions, and b) velocity distributions*

At 0.05 s, the movement velocity of the valve spool decreases, the movement displacement continues to increase, and the pressure drop characteristics of pressure differential valve increase with the increase of the valve opening. The oil supply pressure is reduced to 683 kPa, the inlet pressure of the valve spool head is 570 kPa, and the pressure in the inner chamber is about 1050 kPa. The maximum flow velocity projection in the X direction appears at the valve inlet area of about 12.05 m/s. The flow velocity of high-pressure lubricating oil at the damping orifice is reduced by about -23 m/s, and the valve opening is about 2.75 mm.

At 0.065 s, the pressure regulating characteristics of the valve begin to stabilize. With the slow increase of the valve spool displacement, the valve spool velocity decreases to 0.042 m/s. the valve opening continues to increase. The oil supply pressure is about 565 kPa, the inlet pressure of the valve spool head is about 460 kPa, and the pressure in the chamber of the valve spool gradually decreases to about 500 kPa. The pressure difference before and after the damping orifice is small, which makes the flow rate continue to decrease to about –0.9 m/s. The maximum velocity projection in the X direction appears in the valve inlet area about 12.05 m/s, and the valve opening is about 3.52 mm.

With the increase of opening time, the displacement and velocity of the valve spool are finally stabilized at about 8.87 mm and 0 m/s, respectively. The high-pressure difference before and after the valve spool damping orifice gradually disappears. The flow state of high-pressure lubricating oil inside the valve is relatively stable. The valve opening is maintained at about 5.8 mm, and the excess lubricating oil returns to the oil tank through the overflow pipeline and the bypass pipeline.

Fig. 16 shows the relationship between the valve inlet pressure and the oil supply pressure with the opening time. From the diagram, it can be seen that in the initial stage, the lubricating oil pump has not reached the specified speed, the oil supply quantity is less, and the valve oil supply pipeline is longer, so the valve inlet pressure is prior to the oil supply pressure response. At about 0.012 s, the oil supply pressure begins to rise. At 0.035 s, the two branch pressures of the valve reach the maximum value. After that, the overflow orifice begins to open with the increase of the displacement of the valve spool, and the valve opening gradually increases, which makes the two branch pressures gradually smaller. Finally, the oil supply pressure is stable at 521.7 kPa, and the valve inlet pressure is stable at 422.6 kPa.

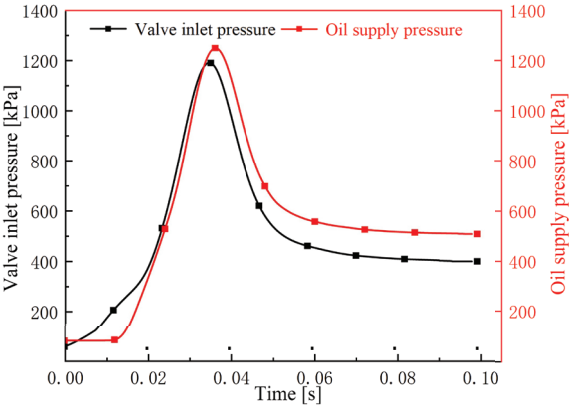

Fig. 16. *The relationship between both inlet pressure and oil supply pressure with the opening time*

3.3 Movement Performance of the Valve Spool with Different Damping Orifice Structures

Fig. 17 shows the relationship between valve spool displacement and opening time under different valve spool damping orifice structures. It can be seen that at 0.019 s, the valve spool structure of Φ 1 mm × 4 mm first begins to move, and at 0.02 s, the other four valve spool structures begin to move. As the diameter of the damping orifice gradually increases, the maximum motion displacement of the valve spool gradually increases, and the time required to reach a steady state gradually decreases. When the length of the damping orifice gradually increases, the influence on the maximum motion displacement of the valve spool is relatively small, but the time required to reach a steady state gradually increases. Under different valve spool structures, the first valve spool structure to reach a stable state is Φ 1 mm × 0.894 mm.

Fig. 18 shows the variation of valve spool velocity with displacement under different valve spool damping orifice structures. It can be seen that under different damping orifice structures of the valve spool, the shapes of the five velocity curves are relatively similar. At the beginning of the movement of the valve spool, the movement velocity of the valve spool rapidly increases and reaches its maximum value at a displacement of about 0.15 mm. Afterwards, it gradually decreases to around 0 m/s as the displacement increases. As the diameter or length of the damping orifice gradually increases, the maximum velocity of the valve spool gradually decreases. When the valve spool structures are respectively Φ 0.3 mm × 0.894 mm, Φ 0.6 mm × 0.894 mm, Φ 1 mm × 0.894 mm, Φ 1 mm × 2 mm and Φ 1 mm × 4 mm, the maximum motion velocity is 0.226 m/s, 0.209 m/s, 0.191 m/s, 0.183 m/s and 0.174 m/s, respectively. The

smaller the diameter or length of the damping orifice, the greater the maximum velocity of the valve spool.

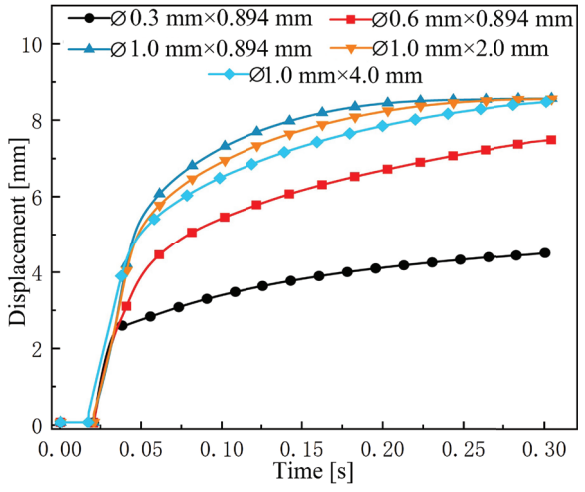

Fig. 17. *The relationship between the valve spool displacement and opening time for different damping orifice structures*

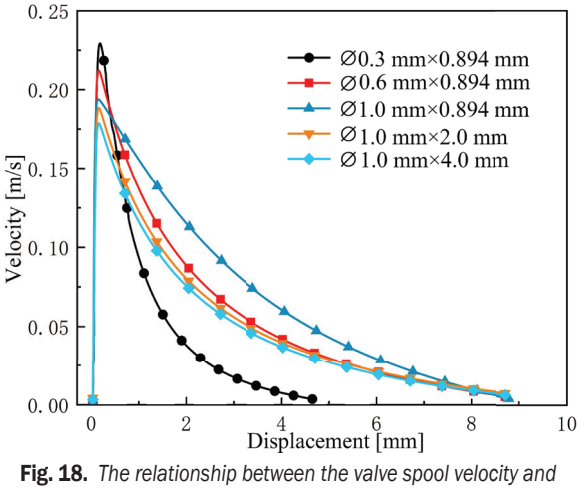

Fig. 18. *The relationship between the valve spool velocity and displacement for different damping orifice structures*

Fig. 19 shows the variation of fluid force with opening time under different valve spool damping orifice structures. Before 0.0087 s, due to the initial rotation of the lubricating oil pump, the system pressure is generally low, the valve inlet pressure and the oil supply pressure are relatively small, so the fluid force acting on the valve spool is almost zero. At 0.0087 s to 0.027 s, the valve spool is in the initial motion state, the motion displacement is very small, the overflow orifice has not been opened, and the diameter of the pipe outlet is small, which makes the pressure of the whole system increase, the lubricating oil gathers at the entrance of the valve, and the fluid force increases rapidly. The fluid force is 80.06 N at 0.027 s. After that, the fluid force continues to increase slowly and reaches a steady state at 0.275 s. As the diameter of the valve spool damping orifice increases, the fluid force gradually increases when it reaches a stable state. When the length of the valve spool damping orifice increases, the influence of the fluid force is very small. In the steady state, when the valve spool structures are respectively Φ 0.3 mm × 0.894 mm, Φ 0.6 mm × 0.894 mm, Φ 1 mm × 0.894 mm, Φ 1 mm × 2 mm and Φ 1 mm × 4 mm, the fluid force is 92.08 N, 106.91 N, 112.43 N, 112.34 N and 111.85 N, respectively.

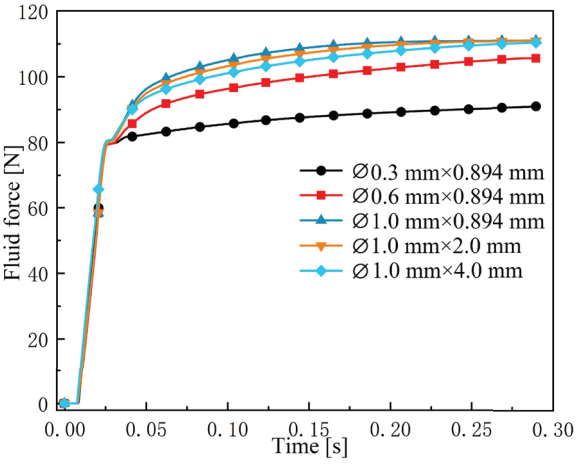

Fig. 19. *The relationship between the fluid force and opening time for different damping orifice structures*

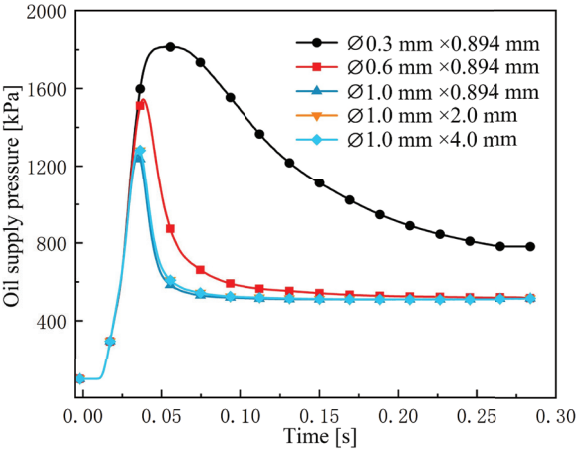

Fig. 20. *The relationship between the oil supply pressure and opening time for different damping orifice structures*

Fig. 20 shows the variation of oil supply pressure with opening time under different valve spool damping orifice structures. At the beginning, the lubricating oil has not yet entered the supply pipeline, and the change in supply pressure is minimal. At 0.02 s, the supply pressure begins to increase. As the

diameter of the valve spool damping orifice increases, the time required to reach the maximum oil supply pressure gradually decreases, and the maximum pressure also gradually decreases. When the length of the damping orifice in the valve spool increases, the impact on the oil supply pressure is minimal, and the pressure curve almost overlaps. When the damping orifice structures of the valve spool are respectively Φ 0.3 mm × 0.894 mm, Φ 0.6 mm × 0.894 mm, Φ 1 mm × 0.894 mm, Φ 1 mm × 2 mm and Φ 1 mm × 4 mm, the peak oil supply pressure is 1855 kPa, 1568 kPa, 1562 kPa, 1545 kPa and 1549 kPa, respectively. When the valve spool structure is Φ 0.3 mm × 0.894 mm, the peak pressure of the oil supply pressure is extremely high and the high-pressure state lasts longer, and the pressure drop is slower, which to some extent will affect the safe use of the valve.

In order to better understand the influence of different valve spool damping orifice structures on the opening process of pressure differential valve, Fig. 21 shows the pressure and velocity contours of the central section inside the valve when the oil supply

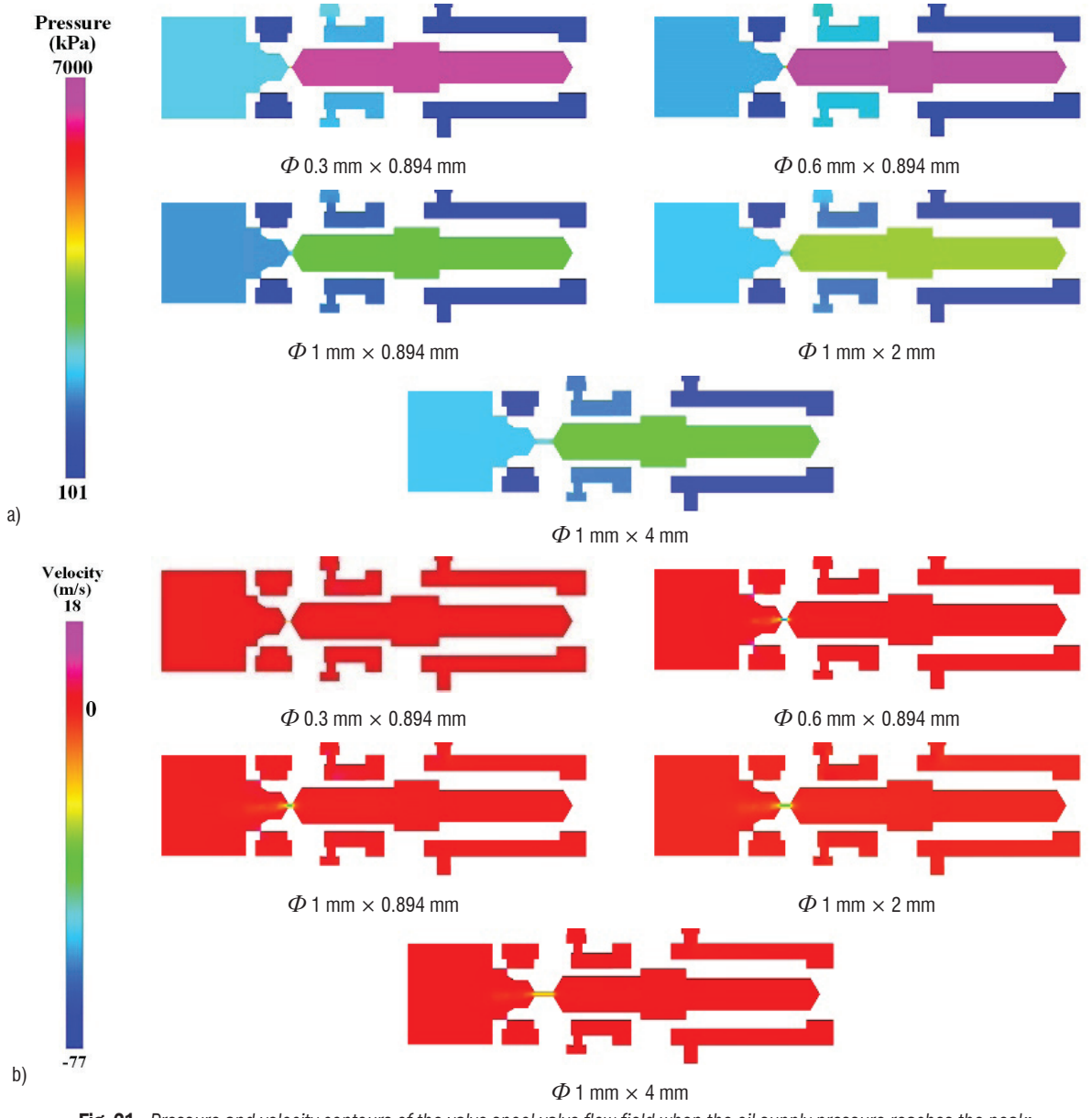

Fig. 21. *Pressure and velocity contours of the valve spool valve flow field when the oil supply pressure reaches the peak; a) static pressure contours for 5 damping orifice structures; and b) velocity contours for 5 damping orifice structures*

pressure reaches the maximum. It can be seen from Figs. 17 to 19 that when the valve spool displacement is 3 mm, the valve opening is in a critical state, and the overflow orifice is about to open. When it is greater than 3 mm, the valve opening increases gradually, the oil supply pressure decreases gradually, and the increase rate of fluid force decreases rapidly. As the displacement increases, the fluid force remains relatively stable. When the oil supply pressure reaches the maximum value, the damping orifice structures of the valve spool are respectively Φ 0.3 mm × 0.894 mm, Φ 0.6 mm × 0.894 mm, Φ 1 mm × 0.894 mm, Φ 1 mm × 2 mm and Φ 1 mm × 4 mm, and the valve spool displacement is 3.02 mm, 3.11 mm, 3.15 mm, 3.22 mm, and 3.32 mm, respectively. The velocity of the valve spool is 0.01667 m/s, 0.05071 m/s, 0.07653 m/s, 0.04829 m/s and 0.04226 m/s, respectively. The fluid force is 83.91 N, 86.09 N, 86.24 N, 85.78 N and 86.58 N, respectively.

When the oil supply pressure reaches the peak value, the valve opening is relatively small, and the rapidly increasing fluid force causes the lubricating oil

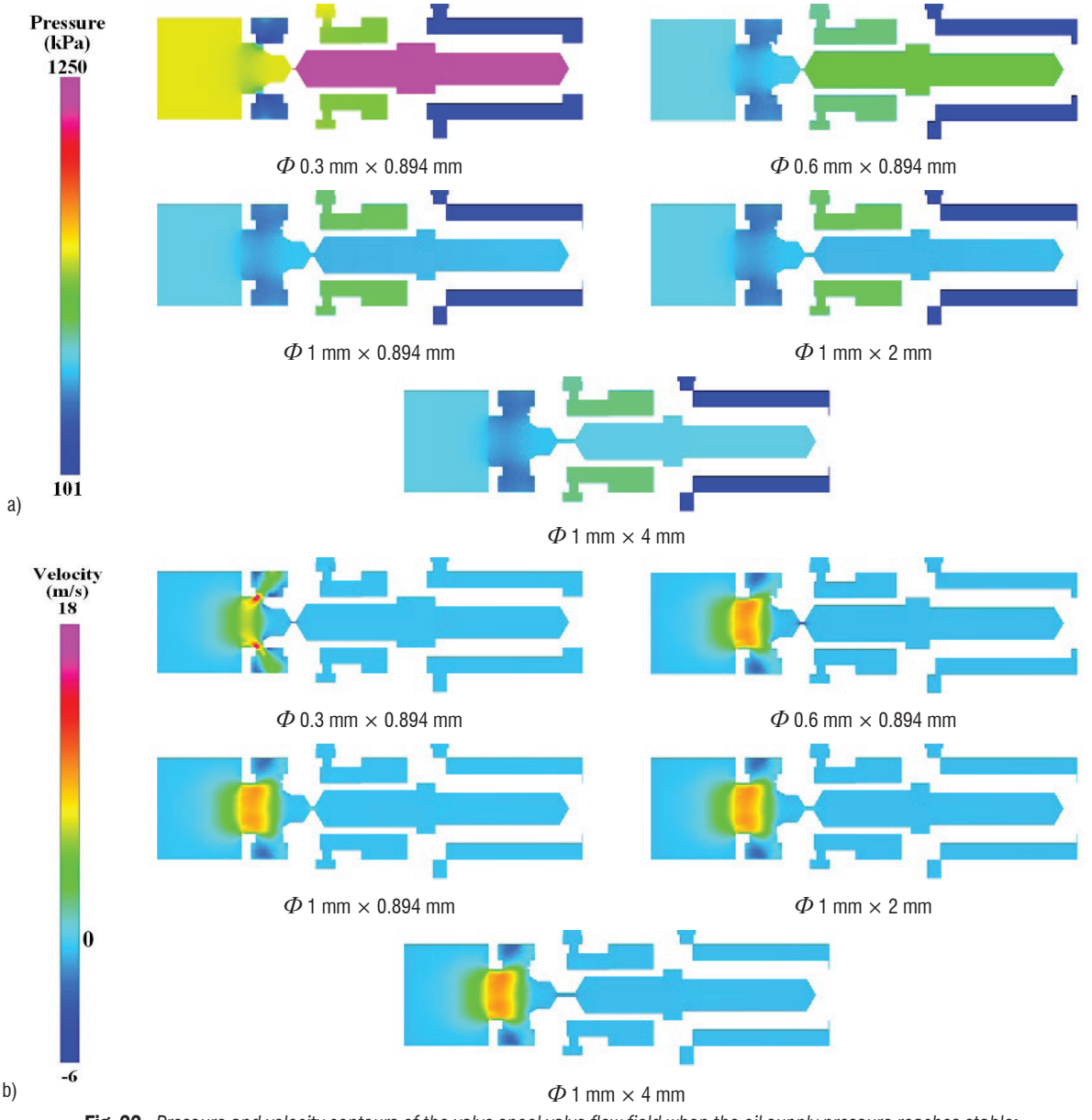

Fig. 22. *Pressure and velocity contours of the valve spool valve flow field when the oil supply pressure reaches stable; a) static pressure contours for 5 damping orifice structures, and b) velocity contours for 5 damping orifice structureses*

in the inner chamber to be squeezed, and the pressure increases rapidly. As shown in Fig. 21, with the increase of the diameter of the damping orifice, when the structure of the valve spool damping orifice is Φ 0.6 mm × 0.894 mm, the internal chamber pressure reaches the highest due to the relatively high inlet pressure and oil supply pressure of the valve. At the same time, the pressure gradient reaches the highest before and after the damping orifice, and the flow velocity of the lubricating oil reaches the maximum, as shown in Fig. 21b, which is about –76.22 m/s. With the increase of the length of the damping orifice, the influence on the pressure and velocity contours of pressure differential valve is relatively small. The pressure in the inner chamber of the valve spool is basically about 3000 kPa, and the velocity gradient at the damping orifice is relatively small.

Fig. 22 shows the pressure and velocity contours of the central section of pressure differential valve when the oil supply pressure is stable. From Figs. 17, to 19, it can be seen that in the steady state, the damping orifice structure of the valve spool is Φ 0.3 mm × 0.894 mm, Φ 0.6 mm × 0.894 mm, Φ 1 mm × 0.894 mm, Φ 1 mm × 2 mm and Φ 1 mm × 4 mm, the valve spool displacement is 4.66 mm, 7.79 mm, 8.87 mm, 8.87 mm, and 8.86 mm, respectively. The velocity of the valve spool is basically fluctuating around 0 m/s. The fluid force is 92.08 N, 106.9 N, 112.43 N, 112.34 N and 111.85 N, respectively.

As shown in Fig. 22a, the oil supply pressure is stable at this time. When the valve spool structure is Φ 0.3 mm × 0.894 mm, the diameter is very small, the internal high-pressure lubricating oil flows to the valve inlet through the damping orifice, the resistance along the way is very large, and the decompression process is relatively slow. The pressure in the inner chamber of the valve spool is significantly higher than that of the other four structures. As the diameter of the damping orifice increases, the pressure in the chamber of the valve spool and the pressure gradient at the damping orifice gradually decrease. As shown in Fig. 22b, as the valve spool diameter increases, the valve opening gradually increases, the flow area of the overflow orifice increases, and the velocity gradient of the high-pressure lubricating oil at the valve spool inlet decreases. With the increase of the length of the valve spool damping orifice, the influence on the pressure and velocity contours of pressure differential valve is very small.

4 CONCLUSIONS

In this paper, a transient high pressure lubricating oil flow model of pressure differential valve is established. Through the joint simulation of the two-stage internal gear pump and pressure differential valve, the flow characteristics of the high-pressure lubricating oil in the valve during the opening of pressure differential valve are analysed. In addition, the influence of the structure of the valve spool damping orifice on the pressure regulation characteristics of pressure differential valve is also compared and analysed.

The following conclusions can be made. The opening time of the differential pressure valve in the lubricating oil supply subsystem is very fast, and the time for the valve spool to reach the maximum stroke is less than 0.3 s. During the valve opening process, the valve inlet pressure and the oil supply pressure increase rapidly with time. The larger pressure makes the valve spool begin to move, the overflow orifice gradually opens, the pressure regulation of the valve is gradually significant, and the inlet pressure and oil supply pressure of the valve gradually decrease and reach stability. The fluid force increases rapidly at first, and the growth rate of the fluid force is obviously reduced due to the overflow effect, and finally reaches a stable state. The difference between the spring force and the fluid force is relatively small. During the valve opening process, the two together affect the pressure regulation characteristics of pressure differential valve. The velocity of the valve spool increases rapidly with the increase of displacement at the beginning, and then decreases gradually due to the overflow effect. When the displacement of the valve spool reaches stability, the velocity fluctuates around 0 m/s.

The pressure regulation characteristics of pressure differential valve during opening process are quantified. When the inlet pressure and outlet pressure are both 101 kPa, the minimum fluid force of the valve spool is 92.08 N, the maximum velocity is 0.226 m/s, the maximum oil supply pressure is 1855 kPa, and the maximum oil supply pressure is 800 kPa when it reaches a steady state. When the damping orifice structure of the valve spool is Φ 0.3 mm × 0.894 mm, the pressure regulation performance is poor, and the oil supply pressure reaches the maximum value for a long time and the pressure drops slowly, which has a great influence on the lubrication function of the lubrication system, and even causes damage to other components such as the engine.

The influence of valve spool damping orifice structure on the transient flow characteristics and

valve spool motion characteristics during the opening process of pressure differential valve. When the diameter of the damping orifice increases from 0.3 mm to 1.0 mm, the maximum displacement of the valve spool increases from 4.66 mm to 8.87 mm, the maximum velocity of the valve spool decreases from 0.226 m/s to 0.191 m/s, and the maximum oil supply pressure decreases from 1855 kPa to 1288 kPa. When the valve spool displacement reaches the maximum, the fluid force increases from 83.91 N to 86.24 N, and the oil supply pressure decreases from 800 kPa to 521 kPa. When the length of the valve spool damping orifice increases from 0.894 mm to 4.0 mm, the maximum displacement of the valve spool is about 8.85mm, the maximum velocity of the valve spool decreases from 0.191 m/s to 0.174 m/s, and the maximum oil supply pressure is about 1500 kPa. When the displacement of the valve spool valve reaches the maximum, the fluid force is about 112 N, and the oil supply pressure is about 521 kPa.

The internal and external mechanisms are as follows. The damping orifice structure of pressure differential valve has little effect on the start time of the valve spool. With the increase of the diameter of the damping orifice, the resistance of the valve spool throat decreases, and the pressure gradient between the inner cavity and the valve core head decreases. The high-pressure lubricating oil in the chamber is easier to flow back to the head of the valve spool through the damping orifice, and the high pressure in the inner chamber drops faster, and the maximum displacement of the valve spool also increases. At the same time, the fluid force during the movement of the valve spool also increases, and the moving velocity of the valve spool decreases. The increase of the displacement means that the opening of the valve gradually increases, and the pressure reduction characteristics of pressure differential valve gradually become obvious. The large flow area of the overflow orifice enables the high-pressure lubricating oil to quickly return to the tank through the overflow pipeline and the bypass pipeline. The inlet pressure and oil supply pressure of the valve decrease rapidly, and the oil supply pressure is more in line with the allowable requirements of the lubricating oil system. When the length of the damping orifice increases, it has little effect on the pressure regulation characteristics of pressure differential valve and the motion state of the valve spool.

5 REFERENCES

[1] Li, A., Zhang, S., Shi, H., Zhang, W.L. (2012). Simulation study for lubrication oil supply system for an aero-engine. *Journal of Shenyang Aerospace University*, vol. 29, p. 21-24, **DOI:10.3969/j.issn.2095-1248.2012.03.005**. (in Chinese)

[2] Li, Q. H., Zhang, J. (1991). *Aeroengine Reliability Engineer Qualification Training Course Textbook: Chapter 12 Aeroengine Condition Monitoring and Fault Diagnosis*. Beijing University of Aeronautics and Astronautics, Beijing.(in Chinese)

[3] Dumachenko, H.T., Kravitz, A.C. (1978). *Gas Turbine Engine*. National Defense Industry Press, Moscow (in Russian).

[4] Li, Y. (2010). *The Fault Diagnosis Analysis on a Model of the Air Engine Lubrication System*, PhD Thesis, Wuhan University of Technology, Wuhan. (in Chinese)

[5] Aeroengine Design Manual Editorial Board (2002). *Aeroengine Design Manual, Volume 12: Transmission and Lubrication Systems*. Aerospace Industry Press, Beijing. (in Chinese)

[6] Li, G.Q. (2011). Present and future aeroengine oil system. *Aeroengine*, vol. 37, no. 6, p. 49-52. (in Chinese)

[7] Wei, X.D. (2019). The present situation and future development of aero-engine lubricating oil system are analyzed. *Internal Combustion Engines and Accessories*, vol. 12, p. 63-64. (in Chinese)

[8] Li, G.Q. (2008). Analysis of altitude performance of aeroengine oil pump. *Aeroengine*, vol. 34, p. 46-47.

[9] Lai, Z.N., Karney, B., Yang, S., Wu, D., Zhang, F.X. (2017). Transient performance of a dual disc check valve during the opening period. *Annals of Nuclear Energy*, vol. 101, p. 15-22, **DOI:10.1016/j.anucene.2016.10.010**.

[10] Afshari, H.H., Zanj, A., Novinzadeh, A.B. (2010). Dynamic analysis of a nonlinear pressure regulator using bondgraph simulation technique. *Simulation Modelling Practice and Theory*, vol. 18, no. 2, p. 240-252, **DOI:10.1016/j.simpat.2009.11.001**.

[11] Cui, B.L., Lin, Z., Zhu, Z.C., Wang, H.J., Ma, G.F. (2017). Influence of opening and closing process of ball valve on external performance and internal flow characteristics. *Experimental Thermal and Fluid Science*, vol. 80, p. 193-202, **DOI:10.1016/j.expthermflusci.2016.08.022**.

[12] Sibilla, S., Gallati, M. (2008). Hydrodynamic characterization of a nozzle check valve by numerical simulation. *ASME Journal of Fluids Engineering*, vol. 130, no. 12, p. 1211011-12110112, **DOI:10.1115/1.3001065**.

[13] Beune, A., Kuerten, J.G.M., van Heumen, M.P.C. (2012). CFD analysis with fluid-structure interaction of opening high-pressure safety valves. *Computers & Fluids*, vol. 64, p. 108-116, **DOI:10.1016/j.compfluid.2012.05.010**.

[14] Chattopadhyay, H., Kundu, A., Saha, B.K., Gangopadhyay, T. (2012). Analysis of flow structure inside a spool type pressure regulating valve. *Energy Conversion and Management*, vol. 53, no. 1, p. 196-204, **DOI:10.1016/j.enconman.2011.08.021**.

[15] Han, Y., Zhou, L., Bai, L., Xue, P., Lv, W.N., Shi, W.D., Huang, G.Y. (2022). Transient simulation and experiment validation on the opening and closing process of a ball valve. *Nuclear Engineering and Technology*, vol. 54, no. 5, p. 1674-1685, **DOI:10.1016/j.net.2021.10.035**.

[16] Saha, B.K., Chattopadhyay, H., Mandal, P.B., Gangopadhyay, T. (2014). Dynamic simulation of a pressure regulating and shut-off valve. *Computers & Fluids*, vol. 101, p. 233-240, **DOI:10.1016/j.compfluid.2014.06.011**.

[17] Ray, A. (1978). Dynamic modeling and simulation of a relief valve. *Simulation*, vol. 31, no. 5, p. 167-172, **DOI:10.1177/003754977803100504**.

[18] Dasgupta, K., Karmakar, R. (2002). Dynamic analysis of pilot operated pressure relief valve. *Simulation Modelling Practice and Theory*, vol. 10, no. 1-2, p. 35-49, **DOI:10.1016/S1569-190X(02)00061-8**.

[19] Zhang, Z.H., Jia, L., Yang, L.X. (2019). Numerical simulation study on the opening process of the atmospheric relief valve. *Nuclear Engineering and Design*, vol. 351, p. 106-115, **DOI:10.1016/j.nucengdes.2019.05.034**.

[20] Sun, X.M., Qin, B.K., Bo, H.L., Xu, X.X. (2017). Transient flow analysis of integrated valve opening process. *Nuclear Engineering and Design*, vol. 313, p. 296-305, **DOI:10.1016/j.nucengdes.2016.12.014**.

[21] Yang, L., Wang, Z.J., Dempster, W., Yu, X.H., Tu, S.-T. (2017). Experiments and transient simulation on spring-loaded pressure relief valve under high temperature and high pressure steam conditions. *Journal of Loss Prevention in the Process Industries*, vol. 45, p. 133-146, **DOI:10.1016/j.jlp.2016.11.019**.

[22] Abdallah, H.K., Peng, J.H., Li, S.J. (2023). Analysis of pressure oscillation and structural parameters on the performance of deflector jet servo valve. *Alexandria Engineering Journal*, 63, p. 675-692, **DOI:10.1016/j.aej.2022.11.021**.

[23] Zang, J.-L., Yao, H.-Y., Zhang, F.-H., Liu, Z.-Y., Meng, J., Zhu, J.-M., Wang, Z.-M., Qian, J.-Y. (2022). Dynamic characteristics analysis of pilot valves with different inlet diameters installed on the main steam valve set. *Case Studies in Thermal Engineering*, vol. 34, art. ID 102004, **DOI:10.1016/j.csite.2022.102004**.

[24] Liu, J.-R., Jin, B., Xie, Y.-J., Chen, Y.,Weng, Z. T. (2009). Research on the electro-hydraulic variable valve actuation system based on a three-way proportional reducing valve. *International Journal of Automotive Technology*, vol. 10, p. 27-36, **DOI:10.1007/s12239-009-0004-6**.

[25] Simic, M., Herakovic, N. (2015). Reduction of the flow forces in a small hydraulic seat valve as alternative approach to improve the valve characteristics. *Energy Conversion and Management*, vol. 89, p. 708-718, **DOI:10.1016/j.enconman.2014.10.037**.

[26] Liu, J.L., Li, R.C., Ding, X.K., Liu, Q. (2022). Flow force research and structure improvement of cartridge valve core based on CFD method. *Heliyon*, vol. 8, no. 11, art. ID e11700, **DOI:10.1016/j.heliyon.2022.e11700**.

[27] Ye, J.J., Cui, J.X., Hua, Z.L., Xie, J.L., Peng, W.Z., Wang, W. (2023). Study on the high-pressure hydrogen gas flow characteristics of the needle valve with different spool shapes. *International Journal of Hydrogen Energy*, vol. 48, no. 30, p. 11370-11381, **DOI:10.1016/j.ijhydene.2022.04.073**.

[28] Ye, J.J., Zhao, Z.H., Cui, J.X., Hua, Z.L., Peng, W.Z., Jiang, P.C. (2022). Transient flow behaviors of the check valve with different spool-head angle in high-pressure hydrogen storage systems. *Journal of Energy Storage*, vol. 46, art. ID 103761, **DOI:10.1016/j.est.2021.103761**.

[29] Yang, X., Li, S.Z., Yang, B.B., Feng, Y.B. (2018). Influence of valve core and seat structure of overflow valve on flow field performance and optimization design. *Earth and Environmental Science*, vol. 170, art. ID 0221122, **DOI:10.1088/1755-1315/170/2/022112**.

[30] Han, M., Liu, Y., Liao, Y., Wang, S. (2021). Investigation on the modeling and dynamic characteristics of a novel hydraulic proportional valve driven by a voice coil motor. *Strojniški vestnik – Journal of Mechanical Engineering*, vol. 67, no. 5, p. 223-234, **DOI:10.5545/sv-jme.2021.7089**.

[31] Karanović, V., Jocanović, M., Baloš, S., Knežević, D., Mačužić, I. (2019). Impact of contaminated fluid on the working performances of hydraulic directional control valves. *Strojniški vestnik – Journal of Mechanical Engineering*, vol. 65, no. 3, p. 139-147, **DOI:10.5545/sv-jme.2018.5856**.

Strojniški vestnik - Journal of Mechanical Engineering 70(2024)3-4, 159-169
DOI:10.5545/sv-jme.2023.739
Original Scientific Paper
Received for review: 2023-07-25
Received revised form: 2023-11-12
Accepted for publication: 2024-01-25

An Eigenfrequency-Constrained Topology Optimization Method with Design Variable Reduction

Wenchang Liu – Chaohua Wu* – Xingan Chen
Wuhan University of Technology, School of Mechanical and Electronic Engineering, China

The dynamic response of structures heavily relies on eigenfrequency, so the optimization of eigenfrequency is valuable in various working conditions. The bi-directional evolutionary structural optimization (BESO) method has been widely applied due to its ability to eliminate grayscale elements. Based upon BESO, this paper introduces a topology optimization method that incorporates eigenfrequency constraints and reduces the number of design variables. In this method, the optimization objective was to minimize compliance. The Lagrange multiplier was used to introduce eigenfrequency constraints, allowing for coordinated control of compliance and eigenfrequency. To prevent oscillation during the optimization process, the sensitivity was normalized. Additionally, to achieve faster convergence, the variables were reduced after meeting volume constraints. The numerical examples demonstrate the effectiveness of this method in increasing the eigenfrequency of the structure and avoiding resonance.

Keywords: Eigenfrequency constraint, topology optimization, bi-directional evolutionary structural optimization, design variable reduction; Lagrange multiplier method

Highlights

- *The eigenfrequency constraint was introduced through the Lagrange multiplier method.*
- *To obtain faster convergence, the variables were reduced after meeting volume constraints.*
- *The first-order natural frequency was increased by 42 % and 26.7 % in 2D numerical examples and 3D numerical examples respectively.*

0 INTRODUCTION

Topology optimization is an optimization algorithm for material distribution. Compared with the traditional optimization methods, sufficient freedom is the biggest advantage of topology optimization, which provides a reliable and convenient solution for developing high-performance structures and obtaining the best material layouts [1] to [3].

After more than decades of research and development, the practicality of topology optimization has been fully proven. At present, continuum topology optimization methods mainly include Solid Isotropic Material with Penalization Method (SIMP), Level Eet Method (LSM), Evolutionary Structural Optimization (ESO), Bi-directional Evolutionary Structural Optimization (BESO), etc. [4] and [5].

The SIMP method was proposed by Bendsøe and Kikuchi [6], which based on the ideal of discretizing the design domain and relating the density and materials. This means that there is no material, or it is a solid material when the density value is 0 or 1. The variation of element density values between 0 and 1 leads to the presenceof intermediate density elements, which is irrelevant in practical engineering. To address this issue, Rozvany et al. [7] proposed a density penalty scheme, which can update the element density towards 0 and 1 to obtain an approximate 0-1 structure. Sigmund [8] proposed a sensitivity filtering method to eliminate the checkerboard pattern and mesh dependency, which makes SIMP more stable. Osher and Sethian [9] proposed the concept of a level set function, Sethian and Wiegmann [10] first to apply this method to topology optimization; it updates the structure through the continuous evolution of the level set function and obtains clear and smooth boundaries. The method has a slow convergence speed, and it is not easy to obtain hole structures. The ESO method was proposed by Xie and Steven [11], which based on the ideal of gradually removing less efficient materials until the material requirements are met; its update concept is simple and clear, completely different from traditional mathematical programming algorithms. However, due to the possibility of mistakenly deleting elements during the optimization process to obtain local optima, Huang and Xie [12] improved this method to BESO. In this method, the sensitivity information of each element needs to be calculated and then sorted. The threshold is determined based on the volume fraction of each step. The elements with sensitivity numbers greater than the threshold are retained as solid elements, while elements with sensitivity numbers less than the threshold are deleted. Even if an element becomes a void element by deletion, its sensitivity information is still preserved and can be reinstated as a solid element in subsequent

*Corr. Author's Address: Wuhan University of Technology, School of Mechanical and Electronic Engineering, China, wuchaohua@whut.edu.cn

iterations, ensuring that the optimization result is the optimal solution.

Topology optimization has also been widely applied to avoid structural resonance. Munk et al. [13] studied the problem of frequency topology optimization under dynamic loads, and proposed a topology optimization method that can enhance the selected frequency and the reduce gap between frequencies. Li et al. [14] proposed a modified frequency band-constrained Heaviside function, which is continuously differentiable and beneficial for sensitivity analysis. The numerical examples demonstrate that this method can maximize the eigenfrequency of the structure. Du et al. [15] carried out research on fault safety topology optimization based on independent continuous mapping (ICM) and expanded it to the realm of frequency optimization. Kang, et al. [16] proposed a topology optimization method for large-scale frequency constraints. Li, et al. [17] proposed a topology optimization method for frequency optimization with periodic structures and reduced the amount of calculation in the process of frequency optimization by utilizing dimension reduction technology. Leader, et al. [18] considered both stress and frequency constraints and utilized the Jacobi-Davidson eigenvalue solving method to solve the natural frequency problem. Wang et al. [19] established a dynamic topology optimization model for long-span continuum, effectively improving the first-order frequency. Xu et al. [20] proposed a frequency optimization problem with casting constraints, which can effectively obtain convergent solutions when dealing with frequency maximization problems. Su and Liu [21] studied the topology optimization of a coupled stress continuum to maximize the eigenfrequency, and also demonstrated the influence of eigen length on the results of eigenfrequency optimization. Ferrari et al. [22] proposed a frequency optimization method linked to a multi-mesh eigenvalue solver, greatly saving computational costs. Guan, et al. [23] proposed a multi-constraint topology optimization method with stress, displacement, and frequency constraints. Kim et al. [24] applied the topology optimization method to increase the frequency and reduce the noise of the steel wheel. Duan et al. [25] proposed a topology optimization method that can increase the frequency in a limited way while meeting the manufacturing constraints. Oh et al. [26] proposed a topology optimization method to maximize the operating frequency range of hyperbolic elastic meta-material and explained the mechanical knowledge of the model in detail. Vicente et al. [27] proposed a parallel topology optimization method for frequency optimization to find the optimal layout of materials from both macro- and micro-perspectives.

In addition, how to reduce the number of iteration steps and accelerate the convergence process are also a problem that need to be solved in topology optimization. Zheng et al. [28] introduced a freedom reduction mechanism in topology optimization, effectively accelerating the convergence process and saving the calculation cost. Jia et al. [29] combined ESO with LSM, which can reduce the number of iteration steps by automatically generating holes in the low-strain energy region near the node. Lian et al. [30] added a hierarchical mesh refinement algorithm into the moving morphable component (MMC) algorithm to improve convergence speed. Joo and Jang [31] proposed a deep neural network topology optimization algorithm, which can improve the convergence speed by obtaining the history of intermediate designs. Li and Zhang [32] used high noise and unbiased random gradients to update design variables and expedite the convergence process. Du et al. [33] shared a set of efficient topology optimization Matlab codes, which resulted in faster convergence speeds by removing the freedom not belonging to the transmission path in the finite element analysis. Yang et al. [34] proposed an adaptive step size strategy that multiplies the speeds of different nodes by different step sizes, which can accelerate convergence and also reduce mesh dependency. According to the characteristics of the BESO algorithm, Lin et al. [35] proposed a dynamic evolution strategy to accelerate convergence in topology optimization. Ren, et al. [36] used faster model reduction methods to enhance convergence speed.

In this paper, an eigenfrequency-constrained topology optimization method with design variable reduction is proposed, which can rapidly converge while increasing the eigenfrequency. Numerical examples demonstrate the effectiveness of this method.

1 TOPOLOGY OPTIMIZATION WITH EIGENFREQUENCY CONSTRAINTS

1.1 Problem Statement

When topology optimization is applied to structural design, volume is usually taken as the constraint, and the minimum compliance is taken as the optimization objective. This reflects the fact that stiffness is an extremely important objective in traditional structural design concepts. However, the topology optimization model will be multi-objective, multi-constraint and

include other related conditions to meet engineering requirements and address complex working conditions.

In recent years, constraints other than volume introduced in topology optimization can be broadly divided into two categories. One type is related to manufacturing, including maximum and minimum size constraints, connectivity constraints, hole size constraints, hole number constraints, inclination angle constraints, and self-supporting constraints; The other type of constraint is functionality, such as displacement constraints, stress-strain constraints, fatigue constraints, and damage constraints.

As is well known, avoiding resonance is one of the important design objectives in structural design; it can be avoided by increasing the eigenfrequency of the structure. BESO is widely applied due to its simple concept and clear boundaries. The BESO topology optimization model with eigenfrequency constraints can be described mathematically as follows,

$$\begin{cases} \text{find} & \mathbf{X}=\left(x_{11},x_{12},x_{13},\cdots x_{ij}\right) \\ & i=1,2,...,m; \quad j=1,2,...,n; \\ \min & C\left(\mathbf{X}\right)=\dfrac{1}{2}\mathbf{U}^{T}\mathbf{K}\mathbf{U} \\ \text{s.t.} & \mathbf{K}\mathbf{U}=\mathbf{F} \\ & \left(\mathbf{K}-\omega_n^2\mathbf{M}\right)\mathbf{u}_n=0 \\ & V=qV_0 \\ & x_{ij}=x_{\min} \text{ or } 1 \\ & WY<\omega_n \end{cases}, \tag{1}$$

where the $\mathbf{X}$ is the design variable, x_{ij} is the ij^{th} elemental density with a value of either 1 for solid or $x_{\min}$ (0.001 in this paper) for void, compliance $C(\mathbf{X})$ is an objective function, $\mathbf{K}$ is the global stiffness matrix, $\mathbf{U}$ is the global displacement vector, $\mathbf{F}$ is the force vector, $\mathbf{M}$ is the global mass matrix, $\mathbf{u}_n$ is the eigenvector corresponding to ω_n, V_0 is the initial volume of structure, q is reserved volume ratio, V is the final structural volume, ω_n is n^{th} natural frequency, WY is frequency constraint value.

The following Rayleigh quotient indicate the relationship between ω_n and $\mathbf{u}_n$, as follows (Eq. (2)),

$$\omega_n^2=\frac{\mathbf{u}_n^T\mathbf{K}\mathbf{u}_n}{\mathbf{u}_n^T\mathbf{M}\mathbf{u}_n}. \tag{2}$$

1.2 Material Interpolation Scheme

The material interpolation scheme applied in calculating compliance is expressed as follows, Eqs. (3) and (4):

$$E_{ij}=E_0x_{ij}^{penal}, \tag{3}$$

$$\mathbf{K}_{ij}=\mathbf{K}_0x_{ij}^{penal}, \tag{4}$$

where the E_{ij} is the ij^{th} elemental Young's modulus, E_0 is the Young's modulus of the solid element, *penal* (*penal*=3 in this paper) is a value used for the density penalty. When *penal*≤2, there is a large amount of porous material, and the optimized structure cannot be manufactured. When *penal*≥3.5, there is no significant change in the final topology result. When *penal*≥4, it will make the calculation very slowly. Therefore, *penal*=3 in this paper. $\mathbf{K}_{ij}$ is the stiffness matrix of the ij^{th} element, $\mathbf{K}_0$ is the stiffness matrix of the solid element.

To avoid local vibration modes during finite element analysis and the solution of frequencies, the material interpolation scheme is defined as follows, in Eqs. (5) and (6):

$$\rho\left(x_{ij}\right)=x_{ij}\rho_0, \tag{5}$$

$$E\left(x_{ij}\right)=\left[\frac{x_{\min}-x_{\min}^{penal}}{1-x_{\min}^{penal}}\left(1-x_{ij}^{penal}\right)+x_{ij}^{penal}\right]E_0, \tag{6}$$

where ρ_0 and $\rho(x_{ij})$ denote respectively the material density of the solid and ij^{th}.

1.3 Sensitivity Analysis

1.3.1 Lagrange Multiplier Method

In BESO topology optimization, constraints other than volume can be added with Lagrange multiplier method; the objective function is expressed as follows, Eq. (7):

$$f=C+\lambda\left(WY-\omega_n\right), \quad \lambda\geq 0, \tag{7}$$

where λ is the Lagrangian multiplier.

In the BESO method, the Lagrange multiplier method has been widely applied to solve multi-constraint problems. For instance, Huang and Xie [37] utilized this method to address displacement constraints, while Fan et al. [38] employed it to tackle stress constraints. The Lagrange multiplier method is suitable for obtaining optimal solutions under multiple constraints. It is easy to perform the sensitivity analysis by introducing a Lagrange multiplier to incorporate inequality constraints.

1.3.2 Sensitivity Number

In the BESO method, it is necessary to sort the sensitivity of each element and then update the

variables by determining a threshold based on volume constraints. According to Eq. (7), objective function sensitivity can be obtained as follows, Eq. (8):

$$\frac{\partial f}{\partial x_e} = \frac{\partial C}{\partial x_e} + \lambda \frac{\partial \omega_n}{\partial x_e}. \tag{8}$$

According to Eqs. (1), (3) and (4), compliance sensitivity can be obtained, as follows, Eq. (9):

$$\frac{\partial C}{\partial x_e} = -\frac{1}{2} penal\ x_e^{penal-1} \mathbf{U}_e^T \mathbf{K}_0 \mathbf{U}_e, \tag{9}$$

where $\mathbf{U}_e$ is the displacement vector of e^{th}. According to Eqs. (5) and (6), Eqs. (10) and (11) can be obtained by the derivation calculus, as follows:

$$\frac{\partial \mathbf{M}}{\partial x_{ij}} = \mathbf{M}_0, \tag{10}$$

$$\frac{\partial \mathbf{K}}{\partial x_{ij}} = \frac{1-x_{\min}}{1-x_{\min}^{penal}} penal\ x_{ij}^{penal-1} \mathbf{K}_0, \tag{11}$$

where $\mathbf{M}_0$ is the mass matrix of the solid element. Frequency sensitivity can obtained based on Eqs. (10) and (11), as follows, Eq. (12):

$$\frac{\partial \omega_n}{\partial x_e} = \frac{1}{2\omega_n} \mathbf{u}_n^T \left(\frac{1-x_{\min}}{1-x_{\min}^{penal}} penal\ x_e^{penal-1} \mathbf{K}_0 - \omega_n^2 \mathbf{M}_0 \right) \mathbf{u}_n. \tag{12}$$

According to Eqs. (8), (9) and (12), complete objective function sensitivity can obtained, as follows, Eq. (13):

$$\frac{\partial f}{\partial x_e} = -\frac{1}{2} penal\ x_e^{penal-1} \mathbf{U}_e^T \mathbf{K}_0 \mathbf{U}_e - \lambda \frac{1}{2\omega_n} \mathbf{u}_n^T \left(\frac{1-x_{\min}}{1-x_{\min}^{penal}} penalx_e^{penal-1} \mathbf{K}_0 - \omega_n^2 \mathbf{M}_0 \right) \mathbf{u}_n. \tag{13}$$

Finally, the sensitivity number can be obtained based on the sensitivity analysis, as follows, Eq. (14):

$$\alpha_e = -\frac{1}{penal} \frac{\partial f}{\partial x_e}, \tag{14}$$

where α_e is the sensitivity number of e^{th}.

1.3.3 Variable Update Principle

The filtering scheme can be used to avoid checkerboard patterns and mesh-dependency, as follows, Eq. (15):

$$\begin{cases} \Delta_{ij,lk} = \sqrt{(l-i)^2 + (k-j)^2} \\ \mu_{e,lk} = max\left\{0, r_{min} - \Delta_{e,lk}\right\}, \\ \alpha_e^{\ t} = \dfrac{\sum_{l=1}^{m}\sum_{k=1}^{n} \mu_{e,lk}\alpha_{lk}}{\sum_{l=1}^{m}\sum_{k=1}^{n} \mu_{e,lk}} \end{cases} \tag{15}$$

where $\Delta_{ij,lk}$ is the distance between the centers of elements lk and ij; $\mu_{e,lk}$ is a weight factor, $r_{\min}$ is a filter radius, t is current iteration steps. It is effective to ensure a smoother optimization process and improve the stability of the optimization model by averaging three historical sensitivity number for averaging, as follows, Eq. (16):

$$\alpha_e^{\ t} = \alpha_e^{\ t} + \alpha_e^{\ t-1} + \alpha_e^{\ t-2}, \tag{16}$$

where λ is 0 when frequency constraints are met. The objective function aims to minimize compliances, which is equivalent to the original model. λ can be updated a value that satisfies the constraints can be updated until the constraint is satisfied.

The update method for the Lagrange multiplier is expressed as follows, Eqs. (17) and (18):

$$s_{t+1} = 0.5\left(s_{\min} + s_t\right), \tag{17}$$

$$\lambda_{t+1} = \frac{1-s_{t+1}}{s_{t+1}}, \tag{18}$$

where s_t is a constant with a value range of $s_{\min}$ to 1, $s_{\min}$ is a very small positive number; s_{t+1} and λ_{t+1} can be updated to 1 and 0, respectively, when the constraint is met.

An appropriate Lagrange multiplier updating strategy is of great importance for achieving speed and accuracy. Lagrange multiplier updating strategies may vary in different constraint problems, which requires specific analysis according to the individual problems. It is particularly associated with the sensitivity to Lagrange multipliers and the nonlinearity of the optimization model. The oscillation is normal when using the Lagrange multiplier updating strategy optimization process. However, convergence becomes difficult when faced with numerous and large oscillations.

Therefore, the normalization strategy needs to be adopted to avoid oscillation, as follows, Eq. (19):

$$\alpha_e^{\ t} = \frac{\alpha_e^{\ t} - \alpha_{\min}^{\ t}}{\alpha_{\max}^{\ t} - \alpha_{\min}^{\ t}}, \tag{19}$$

where $\alpha_{min}{}^t$ and $\alpha_{max}{}^t$ is the minimum and maximum sensitivity value in the t^{th} iteration step, respectively.

During the optimization process, the variation pattern of volume is expressed, as follows, Eq. (20):

$$V^t = \max\left\{V, V^{t-1}\left(1-ER\right)\right\}, \tag{20}$$

where V^t is volume value in the t^{th} iteration step, ER is the volume evolution rate.

The convergence condition is the value of five relative changes in compliance less than 0.01, as follows, Eq. (21):

$$\nabla f = \frac{\left|\sum_{t-4}^{t} c_t - \sum_{t-9}^{t-5} c_t\right|}{\sum_{t-4}^{t} c_t} < 0.01, \tag{21}$$

where ∇f is the value of 5 relative changes in compliance, c_t is the compliance in the t^{th} iteration step.

2 2D NUMERICAL EXAMPLES

As shown in Fig. 1, the design domain is a 180:90 rectangular region for a prescribed volume fraction of V = 50 %. The beam is simply supported at both ends and vertically loaded (P = 10 N) in the middle of its lower edge. The rectangular design domain is divided into 180×90 four-node plane stress elements. Young's modulus E = 1 MPa, the volume evolution rate ER=0.01, filter radius r_{min} is twice the length of the element side, Poisson's ratio v=0.3 and mass density ρ=0.001 kg/m³. The optimization objective is to minimize the compliance while satisfying the constraint on the first-order eigenfrequency.

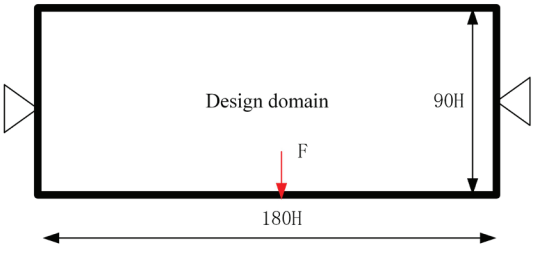

Fig. 1. *The design domain of 2D numerical example*

The optimization results can be obtained by setting different optimization parameters, as shown in Fig. 2.

The optimal topology without any eigenfrequency constraint is shown in Fig. 2a for comparison. When ω_1 is constrained to be 150 rad/s, 155 rad/s, 170 rad/s, 178 rad/s, 188 rad/s, the resulting topologies are shown in Fig. 2b to f. Their compliances are 547.9578, 681.4366, 812.0577, 710.2652, 1096.7411. Their first-order eigenfrequency are 150.8144 rad/s, 155.5822 rad/s, 175.5030 rad/s, 184.1129 rad/s, 188.7140 rad/s.

From Fig. 2b to f, it can be seen that the first-order eigenfrequency increases gradually after the eigenfrequency constraint is introduced, which can meet the constraint conditions. When the first-order eigenfrequency increases gradually, the compliance also increases gradually. It can be seen that the stiffness is sacrificed while satisfying the eigenfrequency constraint.

Without introducing eigenfrequency constraints, the optimization process is shown in Fig. 3a, When the eigenfrequency constraint is WY = 178 rad/s, the optimization process is shown in Fig. 3b.

From Fig. 3a, it can be seen that the compliance C continuously increased without eigenfrequency constraints as the material is continuously removed. When the volume constraint is satisfied, the compliance C reaches its maximum value, and finally tend to be stable. The first-order eigenfrequency will initially increase and then decrease. During the entire optimization process, ω_1 will fluctuate obviously, but it will eventually stabilize. C is stable growth, and there are no noticeable oscillations throughout the entire optimization process.

It can be seen from Fig. 3b that the topology optimization in the direction of satisfying the eigenfrequency constraint is carried out firstly when the eigenfrequency constraint is WY=178 rad/s. Then the topology optimization is then performed in the direction of minimum compliance once the structure satisfies the eigenfrequency constraint. The entire optimization process involves a coordinated optimization of eigenfrequency constraints and minimum compliance. The Lagrange multiplier plays a coordinating role. In the continuous coordination, the local optimal solution satisfying the eigenfrequency constraint and the minimum compliance is finally obtained. During the mid-term stage of the optimization process, there will be a large oscillation. With the removal of the material, fluctuates near WY=178 rad/s and eventually satisfies the constraints. At this time, the compliance is also converging.

In this example, ω_1=132.1478 rad/s can be increased to ω_1=188.7140 rad/s. The ω_1 is increased by 42 %. In practical engineering applications, the value of 42 % eigenfrequency increase is undoubtedly huge, which can effectively avoid structural resonance. When the design domain, material parameters and constraint conditions vary, the effect of frequency enhancement will be significantly different. However,

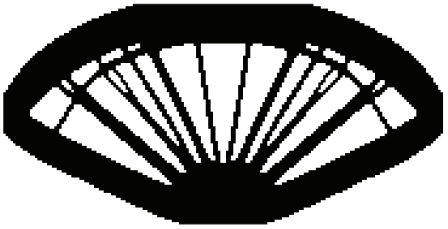

a) WY = 0 rad/s; ω_1 =132.1478 rad/s; C = 521.2869

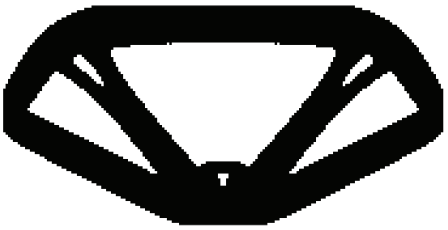

b) WY = 150 rad/s; ω_1 =150.8144 rad/s; C = 547.9578

c) WY = 155 rad/s; ω_1 =155.5822 rad/s; =681.4366

d) WY = 170 rad/s; ω_1 =175.5030 rad/s; C = 812.0577

e) WY = 178 rad/s; ω_1 =184.1129 rad/s; C = 710.2652

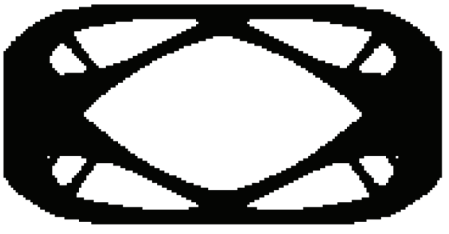

f) WY = 188 rad/s; ω_1 =188.7140 rad/s; C = 1096.7411

Fig. 2. *The optimization results of 2D numerical examples*

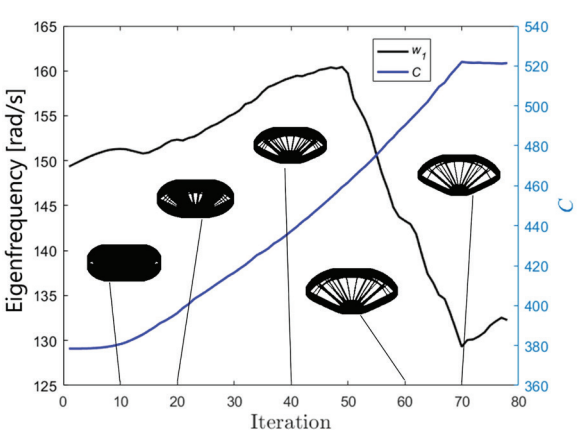

a)

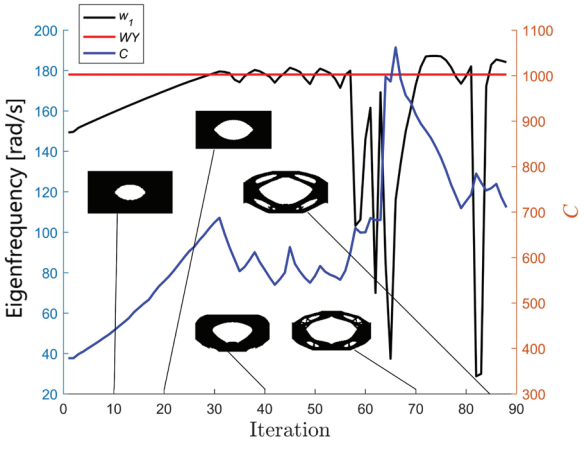

b)

Fig. 3. *The optimization process of 2D numerical examples*

this method is undoubtedly a solution and can provide a reference for related designs.

3 DESIGN VARIABLE REDUCTION

In topology optimization, the large number of variables necessitates extensive calculations and results in a high degree of freedom. In topology optimization,

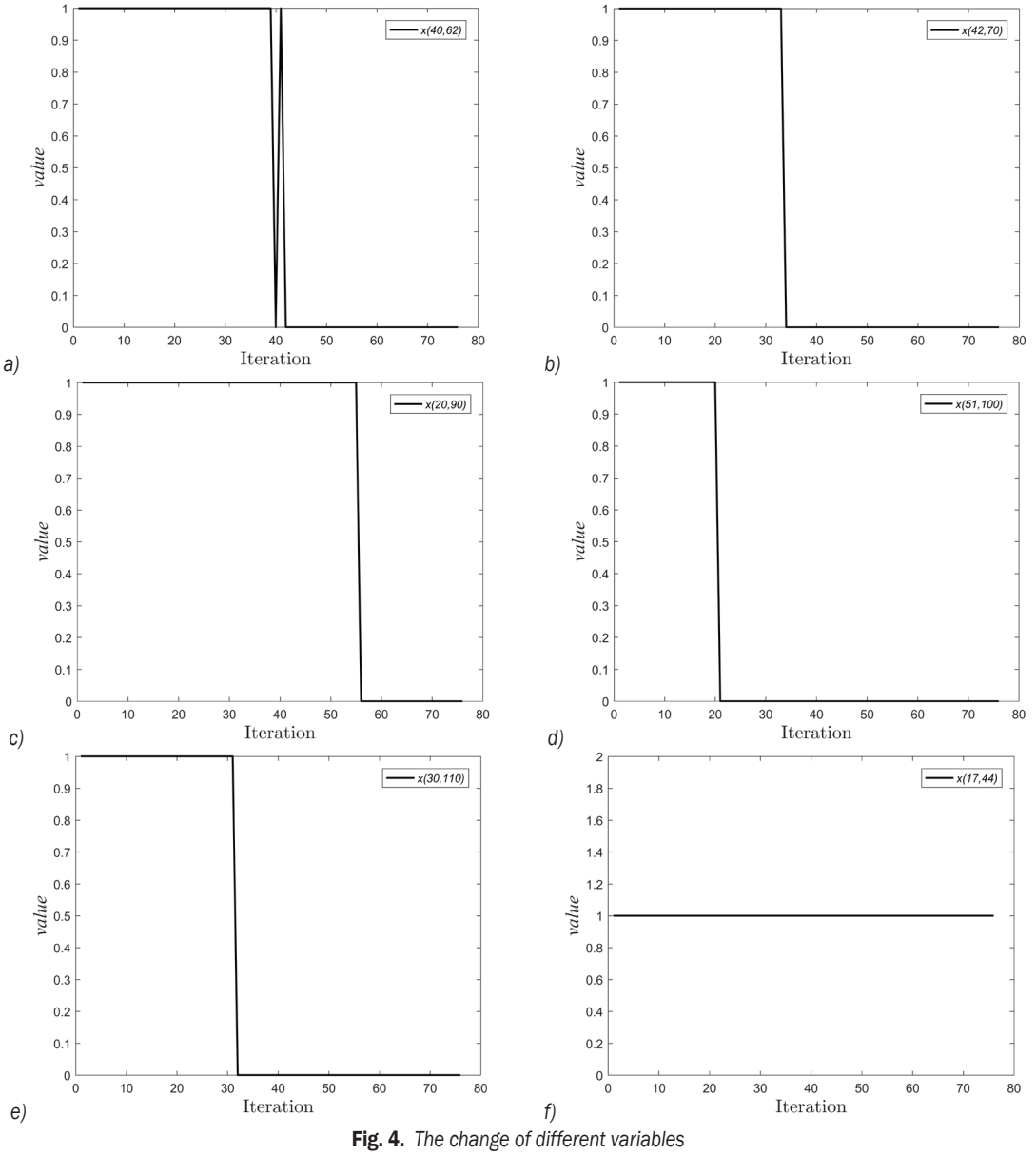

Fig. 4. *The change of different variables*

certain variables converge early and reach a stable state. Similarly, taking the simply supported beam in Section 2 as an example, when the eigenfrequency constraint is not introduced, the changes in some variables are shown in Fig. 4. Where the $X(i,j)$ is the ij^{th} elemental density.

It can be seen from Fig. 4 that different variables converge at different times: some converge early, and some converge later. This paper defines that when the value of the continuous 5-step variable does not change (that is, when Eq. (22) is satisfied), the variable is a stable variable, and the variable that does not satisfy Eq. (22) is a free variable.

$$x_{ij}^{\ t} + x_{ij}^{\ t-1} + x_{ij}^{\ t-2} + x_{ij}^{\ t-3} + x_{ij}^{\ t-4} = 5 \text{ or } 5x_{\min}. \quad (22)$$

When the topology optimization satisfies the volume constraint, the number of design variables can be reduced. This means that the stable variables remain unchanged and no longer participate in the variable update. The algorithm flowchart is shown in Fig. 5. For comparison, the simply supported beam in Section 3 is also utilized as an example. When

the eigenfrequency constraint is WY=178 rad/s, the optimization process is shown in Fig. 6 using the algorithm depicted in Fig. 5.

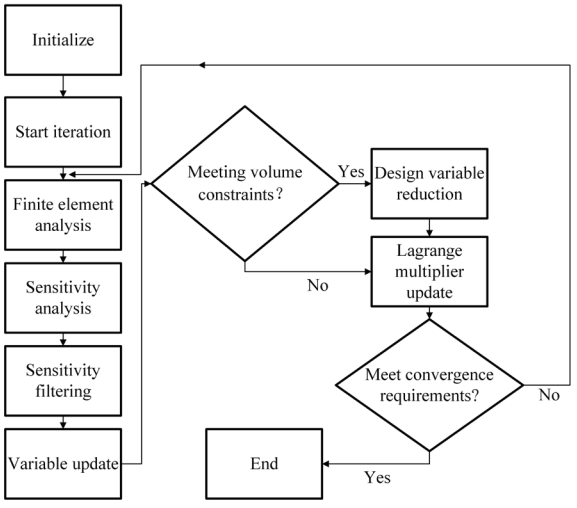

Fig. 5. *The algorithm flow chart*

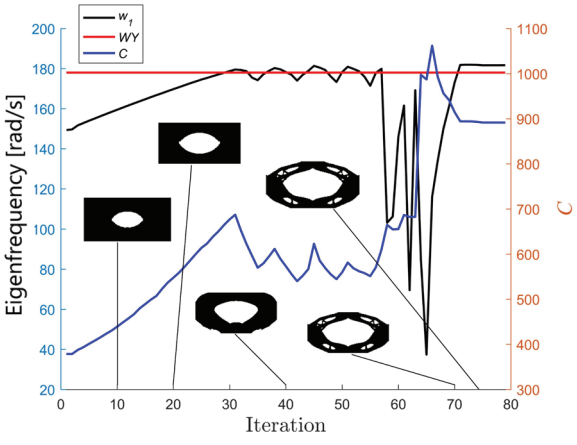

Fig. 6. *The optimization process by using the algorithm shown in Fig. 5*

It can be seen from Fig. 6 that when the design variable reduction mechanism is introduced, the entire optimization process can still obtain the results that meet the constraints, and the number of oscillations is significantly reduced.

This paper conducts a large number of numerical examples to compare the iterations required for convergence without the introduction of design variable reduction mechanism and with the introduction of design variable reduction mechanism. The comparison results are shown in Table 1 and Fig. 7.

It can be observed from Table 1 and Fig. 7 that the change trend of the number of iterations required for convergence in both methods is essentially the same. However, there is a significant reduction in the number of iterations after the design variable is decreased. It has been proven that reducing the design variables can effectively decrease the number of iterations and speed up convergence.

Table 1. *Iterations required for convergence*

Eigenfrequen constraint [rad/s]	Iterations without variable reduction	Iterations with variable reduction
WY = 150	82	75
WY = 155	83	79
WY = 170	78	75
WY = 178	88	79
WY = 188	81	77

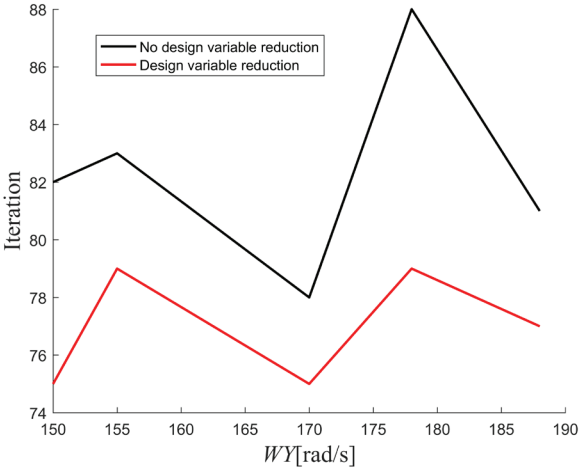

Fig. 7. *The comparison diagram of iterations*

4 3D NUMERICAL EXAMPLES

In the 2D example, the effectiveness of the eigenfrequency constrained topology optimization method with design variable reduction has been fully proved. Next, a 3D example is used for simple verification.

As shown in Fig. 8, the design domain is a 30 : 20 : 10 cube region in which the degree of freedom of the intermediate nodes on both sides is restricted, and a concentrated load of 1 N is applied to the midpoint of the bottom surface.

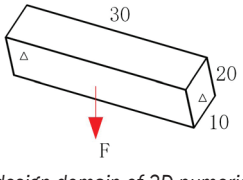

Fig. 8. *The design domain of 3D numerical examples*

The prescribed volume fraction is $V=15$ %. The cube design domain is divided into 30×20×10 four node plane stress elements. Young's modulus $E=1$ MPa, volume evolution rate $ER=0.01$, filter radius $r_{\min}$ is 1.5 times the element side length, Poisson's ratio $v=0.3$ and mass density $\rho=1$ kg/m^3. The optimization objective is to minimize the compliance with the first-order eigenfrequency constrained. The number of iterations is abbreviated as *it*. The optimization results of the 3D numerical examples are shown in Fig. 9.

The optimal topology without any eigenfrequency constraint is shown in Fig. 9a for comparison. When ω_1 is constrained to be 285 rad/s, 290 rad/s, 295 rad/s, 300 rad/s, 330 rad/s, the resulting topologies are shown in Figs. 9b to f. Their compliances are 4.0722, 4.0208, 4.0060, 4.1454, 5.1104. Their first-order eigenfrequency are 299.4611 rad/s, 303.2690 rad/s, 306.1478 rad/s, 311.2603 rad/s, 339.2250 rad/s. Their iterations are 132, 129, 129, 138, 139.

It can be seen from Fig. 9 that the first-order eigenfrequency can be improved by introducing eigenfrequency constraints. In this example, $\omega_1=267.6767$ rad/s can be increased to $\omega_1=339.2250$ rad/s. The ω_1 is increased by 26.7 %. The number of iterations is within 140 steps, and the convergence speed is faster.

5 CONCLUSIONS

In this paper, an eigenfrequency constrained topology optimization method with design variable reduction is proposed. Based on BESO, the eigenfrequency constraint is introduced using the Lagrange multiplier, and the topology optimization is performed with the objective of minimizing compliance. After satisfying the volume constraint, the design variable is reduced, which can significantly decrease the number of iterations and expedite convergence. The first-order eigenfrequency can be increased by 42 % and 26.7

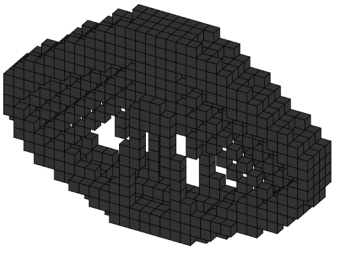

a) $WY = 0$ rad/s; $\omega_1 = 267.6767$ rad/s; $C = 3.6387$; $it = 200$

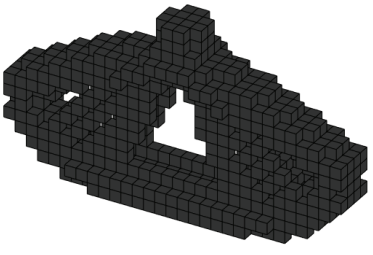

b) $WY = 285$ rad/s; $\omega_1 = 299.4611$ rad/s; $C = 4.0722$; $it = 197$

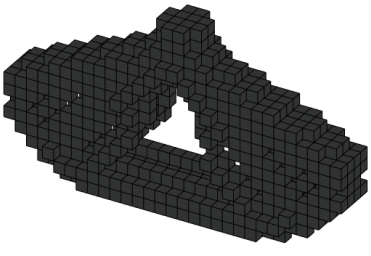

c) $WY = 290$ rad/s; $\omega_1 = 303.2690$ rad/s; $C = 4.0208$; $it = 198$

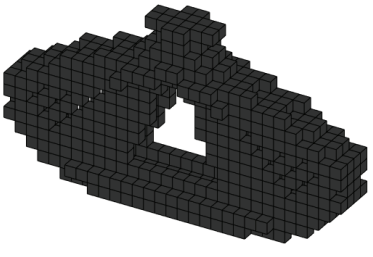

d) $WY = 295$ rad/s; $\omega_1 = 306.1478$ rad/s; $C = 4.0060$; $it = 200$

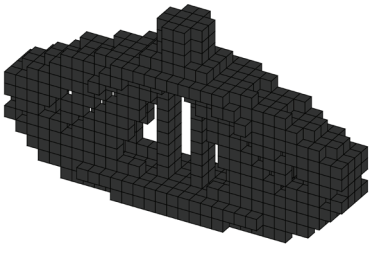

e) $WY = 300$ rad/s; $\omega_1 = 311.2603$ rad/s; $C = 4.1454$; $it = 201$

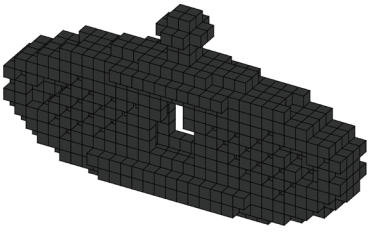

f) $WY = 330$ rad/s; $\omega_1 = 339.2250$ rad/s; $C = 5.1104$; $it = 203$

Fig. 9. *The optimization results of 3D numerical examples*

% in 2D numerical examples and in 3D numerical examples,respectively.

6 ACKNOWLEDGMENTS

This work was supported by Fundamental Research Funds for the Central Universities (2019III138cG).

7 REFERENCES

[1] Rosen, D.W. (2016). A review of synthesis methods for additive manufacturing. *Virtual and Physical Prototyping*, vol. 11, no. 4, p. 305-317, **DOI:10.1080/17452759.2016.1240208**.

[2] Liu, J., Gaynor, A.T., Chen, S., Kang, Z., Suresh, K., Takezawa, A., Li, L., Kato, J., Tang, J., Wang, C.C.L., Cheng, L., Liang, X., To, A.C. (2018). Current and future trends in topology optimization for additive manufacturing. *Structural and Multidisciplinary Optimization*, vol. 57, no. 6, p. 2457-2483, **DOI:10.1007/s00158-018-1994-3**.

[3] Meng, L., Zhang, W., Quan, D., Shi, G., Tang, L., Hou, Y., Piotr, B., Zhu, J., Gao, T. (2019). From topology optimization design to additive manufacturing: Today's success and tomorrow's roadmap. *Archives of ComputationalMethods in Engineering*, vol. 27, p. 805-830, **DOI:10.1007/s11831-019-09331-1**.

[4] Dilgen, C.B., Dilgen, S.B., Aage, N., Jensen, J.S.. (2019). Topology optimization of acoustic mechanical interaction problems: a comparative review. *Structural and Multidisciplinary Optimization*, vol. 60, no. 2, p. 779-801, **DOI:10.1007/s00158-019-02236-4**.

[5] Deaton, J.D., Grandhi, R.V. (2014). A survey of structural and multidisciplinary continuum topology optimization: post 2000. *Structural and Multidisciplinary Optimization*, vol. 49, no. 1, p. 1-38, **DOI:10.1007/s00158-013-0956-z**.

[6] Bendsøe, M.P., Kikuchi, N. (1988). Generating optimal topologies in structural design using a homogenization method. *Computer Methods in Applied Mechanics and Engineering*, vol. 71, no. 2, p. 197-224, **DOI:10.1016/0045-7825(88)90086-2**.

[7] Rozvany, G.I., Zhou, M., Birker, T. (1992). Generalized shape optimization without homogenization. *Structural Optimization*, vol. 4, p. 250-252, **DOI:10.1007/BF01742754**.

[8] Sigmund, O. (2001). A 99 line topology optimization code written in Matlab. Structural and Multidisciplinary Optimization, vol. 21, p. 120-127, **DOI:10.1007/s001580050176**.

[9] Osher, S., Sethian, J.A. (1988). Fronts propagating with curvature-dependent speed: Algorithms based on Hamilton-Jacobi formulations. *Journal of Computational Physics*, vol. 79, no. 1, p. 12-49, **DOI:10.1016/0021-9991(88)90002-2**.

[10] Sethian, J.A., Wiegmann, A. (2000). Structural boundary design via level set and immersed interface methods. *Journal of Computational Physics*, vol. 163, no. 2, p. 489-528, **DOI:10.1006/jcph.2000.6581**.

[11] Xie, Y.M., Steven, G.P. (1993). A simple evolutionary procedure for structural optimization. *Computers & Structures*, vol. 49, no. 5, p. 885-896, **DOI:10.1016/0045-7949(93)90035-C**.

[12] Huang, X., Xie, Y.M. (2007). Convergent and mesh-independent solutions for the bi-directional evolutionary structural optimization method. *Finite Elements in Analysis and Design*, vol. 43, no. 14, p. 1039-1049, **DOI:10.1016/j.finel.2007.06.006**.

[13] Munk, D.J., Vio, G.A., Steven, G.P. (2017). Novel moving isosurface threshold technique for optimization of structures under dynamic loading. *AIAA Journal*, vol. 55, no. 2, p. 638-651, **DOI:10.2514/1.J054692**.

[14] Li, Q., Wu, Q., Liu, J., He, J., Liu, S. (2021), Topology optimization of vibrating structures with frequency band constraints. *Structural and Multidisciplinary Optimization*, vol. 63, p. 1203-1218, **DOI:10.1007/s00158-020-02753-7**.

[15] Du, J.Z., Meng, F.W., Guo, Y.H., Sui, Y.K. (2020). Fail-safe topology optimization of continuum structures with fundamental frequency constraints based on the ICM method, *Acta Mechanica Sinica*, vol. 36, p. 1065-1077, **DOI:10.1007/s10409-020-00988-7**.

[16] Kang, Z., He, J., Shi, L., Miao, Z. (2020), A method using successive iteration of analysis and design for large-scale topology optimization considering eigenfrequencies. *Computer Methods in Applied Mechanics and Engineering*, no. 362, p. 112847, **DOI:10.1016/j.cma.2020.112847**.

[17] Li, M., Cheng, Z., Jia, G., Shi, Z. (2019), Dimension reduction and surrogate based topology optimization of periodic structures. *Composite Structures*, no. 229, p. 111385, **DOI:10.1016/j.compstruct.2019.111385**.

[18] Leader, M.K., Chin, T.W., Kennedy, G.J. (2019). High-resolution topology optimization with stress and natural frequency constraints. *AIAA Journa*l, vol. 57, no. 8, p. 3562-3578, **DOI:10.2514/1.J057777**.

[19] Wang, Y., Qin, D., Wang, R., Zhao, H. (2021). Dynamic topology optimization of long-span continuum structures. *Shock and Vibration*, no. 2021, p. 1-9, **DOI:10.1155/2021/4421298**.

[20] Xu, B., Han, Y.S., Zhao, L., Xie. Y.M. (2019). Topology optimization of continuum structures for natural frequencies considering casting constraints. *Engineering Optimization*, vol. 51, no. 6, p. 941-960, **DOI:10.1080/0305215X.2018.1506771**.

[21] Su, W., Liu, S. (2016). Topology design for maximization of fundamental frequency of couple-stress continuum, *Structural and Multidisciplinary Optimization*, no. 53, p. 395-408, **DOI:10.1007/s00158-015-1316-y**.

[22] Ferrari, F., Lazarov, B.S., Sigmund. O. (2018). Eigenvalue topology optimization via efficient multilevel solution of the frequency response. *International Journal for Numerical Methods in Engineering*, vol, 115, no. 7, p. 872-892, **DOI:10.1002/nme.5829**.

[23] Guan, H., Chen, Y.J., Loo, Y.C., Xie, Y.M. (2003). Bridge topology optimisation with stress, displacement and frequency constraints. *Computers & Structures*, vol. 81, no. 3, p. 131-145, **DOI:10.1016/S0045-7949(02)00440-6**.

[24] Kim, J., Kim, J.J., Jang, I.G. (2022). Integrated topology and shape optimization of the five-spoke steel wheel to improve the natural frequency. *Structural and Multidisciplinary Optimization*, vol. 65, no. 3, p. 78, **DOI:10.1007/s00158-022-03183-3**.

[25] Duan, Z., Yan, J., Lee, I., Lund, E., Wang, G. (2019), Discrete material selection and structural topology optimization of composite frames for maximum fundamental frequency with manufacturing constraints. *Structural and Multidisciplinary*

Optimization, no. 60, p. 1741-1758, **DOI:10.1007/s00158-019-02397-2**.

[26] Oh, J.H., Ahn, Y.K., Kim, Y.Y. (2015). Maximization of operating frequency ranges of hyperbolic elastic metamaterials by topology optimization. *Structural and Multidisciplinary Optimization*, no. 52, p. 1023-1040, **DOI:10.1007/s00158-015-1288-y**.

[27] Vicente, W.M., Zuo, Z.H., Pavanello. R., Calixto, T.K.L., Picelli., R., Xie, Y.M. (2016). Concurrent topology optimization for minimizing frequency responses of two-level hierarchical structures. *Computer Methods in Applied Mechanics and Engineering*, no. 301, p. 116-136, **DOI:10.1016/j.cma.2015.12.012**.

[28] Zheng, W., Wang, Y., Zheng, Y., Da, D. (2020). Efficient topology optimization based on DOF reduction and convergence acceleration methods. *Advances in Engineering Software*, no. 149, p. 102890, **DOI:10.1016/j.advengsoft.2020.102890**.

[29] Jia, H., Beom, H.G., Wang, Y., Lin, S., Liu, B. (2011). Evolutionary level set method for structural topology optimization. *Computers & Structures*, vol. 89, no. 5-6, p. 445-454, **DOI:10.1016/j.compstruc.2010.11.003**.

[30] Lian, R., Jing, S., He, Z., Shi, Z., Song, G. (2020). An accelerating convergence rate method for moving morphable components. *Mathematical Problems in Engineering*, vol. 2020, p. 1-15, **DOI:10.1155/2020/2478292**.

[31] Joo, Y., Yu, Y., Jang, I.G. (2021). Unit module-based convergence acceleration for topology optimization using the spatiotemporal deep neural network. *IEEE Access*, no. 9, p. 149766-149779, **DOI:10.1109/ACCESS.2021.3125014**.

[32] Li, W., Zhang, X.S. (2021). Momentum-based accelerated mirror descent stochastic approximation for robust topology optimization under stochastic loads. *International Journal for Numerical Methods in Engineering*, vol. 122, no. 17, p. 4431-4457, **DOI:10.1002/nme.6672**.

[33] Du, Z., Cui, T., Liu, C., Zhang, W., Guo, Y., Guo X. (2022). An efficient and easy-to-extend Matlab code of the Moving Morphable Component (MMC) method for three-dimensional topology optimization. *Structural and Multidisciplinary Optimization*, vol. 65, no. 5, p. 158, **DOI:10.1007/s00158-022-03239-4**.

[34] Yang, C.D., Feng, J.H., Shen, Y.D. (2022). Step-size adaptive parametric level set method for structural topology optimization, Journal of Mechanical Science and Technology, no. 36, p. 5153-5164, **DOI:10.1007/s12206-022-0928-6**.

[35] Lin, H., Xu, A., Misra, A., Zhao, R. (2020). An ANSYS APDL code for topology optimization of structures with multi-constraints using the BESO method with dynamic evolution rate (DER-BESO). Structural and Multidisciplinary Optimization, no. 62, p. 2229-2254, **DOI:10.1007/s00158-020-02588-2**.

[36] Ren, C., Min, H., Ma, T., Wang F. (2020). Efficient structure crash topology optimization strategy using a model order reduction method combined with equivalent static loads, *Proceedings of the Institution of Mechanical Engineers, Part D: Journal of Automobile Engineering*, vol. 234, no. 7, p. 1897-1911, **DOI:10.1177/0954407019893841**.

[37] Huang, X., Xie, Y.M. (2010). Evolutionary topology optimization of continuum structures with an additional displacement constraint. *Structural and Multidisciplinary Optimization*, vol. 40, no. 1-6, p. 409-416, **DOI:10.1007/s00158-009-0382-4**.

[38] Fan, Z., Xia, L., Lai, W., Xia, Q., Shi, T. (2019). Evolutionary topology optimization of continuum structures with stress constraints. *Structural and Multidisciplinary Optimization*, no. 59, p. 647-658, **DOI:10.1007/s00158-018-2090-4**.

Strojniški vestnik - Journal of Mechanical Engineering 70(2024)3-4, 170-180
DOI:10.5545/sv-jme.2023.852
Original Scientific Paper
Received for review: 2023-11-07
Received revised form: 2024-01-09
Accepted for publication: 2024-02-26

Forced Vibration of Time-Varying Elevator Traction System

Jie Sun[1] – Peng Xu[2,3] – Mingli Chen[1] – Jianghong Xue[1,*]
[1]Jinan University, School of Mechanics and Construction Engineering, MOE Key Laboratory of Disaster Forecast and Control in Engineering, China
[2]Qingdao Xinghua Intelligent Equipment Co., China
[3]South China University of Technology, School of Civil Engineering & Transportation, China

This paper proposes a theoretical model for the forced vibration of time-varying elevator traction systems caused by eccentric excitation of the traction machine. Based on the Hamilton principle and a variational principle with variable boundaries, the equations of motion and the complex boundary condition of a time-varying elevator traction system are established. A quantitative formula between the angular velocity of the traction machine, the diameter of the traction wheel, the elevator running distance and the running time is put forward. It is found that when the maximum values of acceleration and deceleration exceed 1.5 m/s², the elevator traction system may undergo resonance.
Keywords: elevator traction system, vibration, time-varying, dynamics, numerical analysis

Highlights
- *The equation of motion and the corresponding boundary condition for forced vibration of a time-varying elevator traction system is derived based on the Hamilton principle and a variational principle with variable boundaries.*
- *A quantitative formula is proposed to describe the relationship between the angular velocity of the traction machine and the diameter of the traction wheel, the running distance, and the running time of the elevator.*
- *It is found that the greater the running acceleration of the elevator, the higher the vibration amplitude and frequency of the elevator traction system.*
- *To prevent the occurrence of resonance, the maximum value of acceleration and deceleration should not exceed 1.5 m/s².*

0 INTRODUCTION

With the continuous emergence of high-rise and super-high-rise buildings, the demand for high-speed elevators continues to grow. Traction elevators are widely used in high-rise buildings due to their advantages, such as low energy consumption and simple structure [1]. Fig. 1 illustrates an elevator traction system.

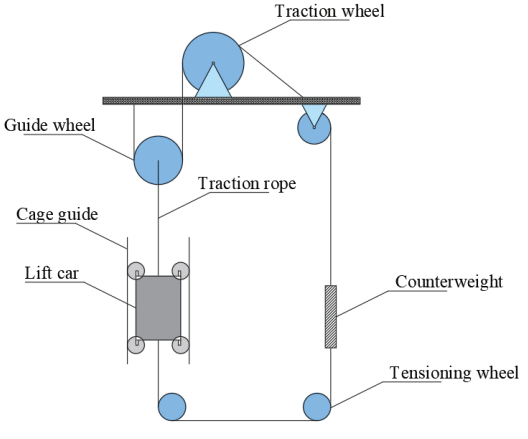

Fig. 1. *Traction system structure*

However, due to the increase in lifting height and operating speed, it is much more difficult to maintain the dynamic stability of the elevator traction system, and the elevators are more sensitive to external interferences and are more prone to undergo abnormal vibrations [2]. These abnormal vibrations may not only affect the working performance of the elevator but also accelerate the wear and fatigue of transmission components, shorten the service life of the elevator, and eventually lead to the occurrence of safety accidents.

Many scholars concentrate on the investigation of the mechanical properties of wire rope. Meng et al. [3] brought forward a theoretical approach to examine the influence of inter-wire contact on the mechanical performances of wire rope strands subjected to tension and torsion loads based on the thin rod and the elastic contact theories. Zhang et al. [4] proposed a theoretical model to investigate the dynamic torsional characteristics of the hoisting rope and its internal spiral components under tension. The variational trend of the twist angle of the wire rope, the lay angle, and the lay length of the spiral strand with the lifting time were discussed. By considering the double-helix structure in multi-strand configuration, Xiang et al. [5] introduced a new method to compute the local deformation of the curvatures and the twist of each wire. It was found that different friction states between adjacent wires can lead to a significantly different

*Corr. Author's Address: Jinan University,GuangDong,China, txue@jnu.edu.cn

distribution of local bending and torsion deformation of double-helix wire. The elastic-plastic deformation of metallic strands and wire ropes under axial–torsional loads were analysed by Xiang et al. [6] based on the thin rod theory of Love and the frictionless assumption of Foti et al. [7], using analytical and 3D finite element methods. For wire ropes with different strand shapes, Stanova et al. [8] developed a 3D solid model by using ABAQUS software and compared the predicted responses for the strands with different shapes and constructions.

The wire ropes of the elevators are flexible with low damping, so they are prone to vibrations [9]. Peng et al. [10] studied the free vibration of elevators in the vertical direction under normal operating conditions theoretically and experimentally. They established a centralized mass discretization model and obtained the theoretical solution. Xu et al. [11] proposed a theoretical model for analysing the tension-torsion coupling vibration of an elevator traction system. According to the Hamiltonian principle, the equation of motion of the elevator traction system with tension-torsional coupling effect is derived and is solved using the Newmark-β method. Based on Bayesian network theory, Zhang et al. [12] put forward a multi-state Bayesian network model for the horizontal vibration of an elevator. Their result can provide quantitative evaluation for the reliability of the multi-state horizontal vibration of the elevator. Much research has been done to investigate the vibrations of the ropes in the elevator system.

Nevertheless, many external interferences, such as the unevenness of the guide rail, the eccentricity of the traction wheel, the airflow disturbance in the lift well and the systematic intrinsic frequency, impact the vibration of the elevator traction system, which would significantly affect riding comfortability and safety. Such a situation is dire for elevators used in ultra-high buildings where the lifting height and the length of wire rope are increased significantly [13] to [15]. By employing the Hamiltonian principle, Bao et al. [16] conducted theoretical analysis for the nonlinear transverse vibration of a flexible hoisting rope with time-varying length and discussed resonance occurring in a passage of the hoisting system due to certain periodic external excitation. Based on the parameters of a typical double-drum Blair multi-rope (BMR) winding plant, Kaczmarczyk [17] proposed a non-linear model to investigate the non-linear dynamic phenomena of a hoisting cable system. The forced vibration of the mine hoisting cables induced by the periodic excitation resulting from the crossover cable motion on the winder drum is analysed. Zhang et al. [18] analysed the sensitivity of random parameters of transverse and horizontal vibration of high-speed elevator lifting systems based on the random perturbation method and analysed the influence of parameters, such as guide length, weight per unit length and bending stiffness, on the dynamic characteristics of a guide. Cao et al. [19] established a trackway-car coupled vibration model via numerical analysis to explore the influence of guide parameters on the lateral vibration of the elevator. The results show that the structural parameters of the guide have a significant influence on the vibration of the elevator system. Zhang et al. [20] studied the horizontal vibration in elevator vertical motion caused by uneven (or non-uniform) elevator guide rails. As the elevator traction systems are installed inside buildings, the swaying of the builds will lead to the vibration of the elevator traction system. Thus, the vibration response of the elevator traction systems is not only dependent on their structural parameters but also affected by the operating environment and building excitation [21] to [23]. Except for the vibration response of the elevator traction system, several researchers focused on the vibration control of the elevator in order to reduce the adverse impact of vibration on the safety performance of the elevator traction system. Nguyen et al. [24] studied the vibration of high-rise elevator ropes under earthquake excitation and verified the effectiveness of the elevator rope vibration suppression controller through numerical simulation. Knezevic et al. [25] proposed a synergistic solution based on the jerk control and the upgrade of the speed controller with a band-stop filter to solve the vibration problem in the process of elevator operation. Zhang et al. [26] developed a model of a cable conveyor system with arbitrarily variable lengths. The Hamiltonian principle was applied to derive the governing equations of motion. The approximate numerical solution of the governing equation was obtained by using the assumed mode method. Based on the precise integration method and Latin hypercube sampling method, Qiu et al. [27] proposed a design parameter optimization method for reducing the horizontal vibration of high-speed elevators.

The above-mentioned literature mainly focused on the free vibration caused by traction acceleration, the transverse vibration due to uneven guide rail, and the vibration control and shock absorption design. However, studies regarding the longitudinal vibration induced by the eccentric excitation of traction wheels are quite limited. In fact, during the operation of the elevator, with the increase of the angular speed of the traction wheel, the acceleration of the traction system

will increase, leading to the improvement of the eccentric excitation. When the angular speed of the traction wheel reaches a certain value, the frequency of the longitudinal vibration generated by the eccentric excitation of the traction wheel will be close to the natural frequency of the system itself, resulting in the occurrence of resonance phenomenon, which greatly affects the safety of the elevator operation. Such a phenomenon has not been discussed in the existing literature. In this paper, the longitudinal vibration of elevator traction systems with and without external excitation is investigated by considering the time-varying characteristics of elevator traction systems. An analytical model is employed to analyse the vibration performance of the elevator traction system subjected to the eccentric excitation of traction wheels. The relationship between the acceleration of the elevator traction system and the angular velocity of the traction wheel is proposed, and the influence of elevator operating acceleration on the resonance of the elevator is discussed. A safe range of acceleration is proposed in order to prevent the resonance of the elevator. The results from this study provide a reference for improving elevator safety and seismic design.

1 METHOD

1.1 Time-Varying Elevator Traction System

An elevator traction system mainly consists of a traction wheel, a lifting car, and a wire rope. The wire rope is simplified as a variable-length cord moving along the axis; the lifting car is simplified as a rigid body suspended at the lower end of the cord with a mass of m. Fig. 2 is an analytical model for the longitudinal vibration of time-varying elevator traction systems. A coordinate system is established with the origin located at the tangent point of the wire rope and pulley, and the positive direction is chosen as the downward direction, as shown in Fig. 2. During the movement, the longitudinal displacement at a spatial position x(t) on the wire rope is described as u(x(t), t). The elevator traction system has an acceleration a(t) and an axial velocity v(t) corresponding to a wire rope length x(t). The analytical model for the longitudinal vibration of a time-varying elevator traction system is based on the following assumptions. The elevator traction system only undergoes longitudinal vibration. During operation, the wire rope is always in tension and complies with Hooke's Law, and its elastic modulus remains constant along the whole length.

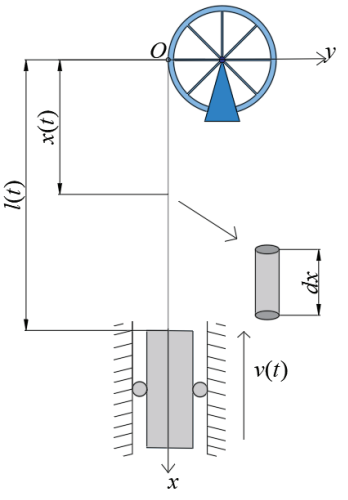

Fig. 2. *Time-varying longitudinal vibration model of elevator traction system*

According to the finite deformation theory of continuum mechanics, the displacement of the wire rope at time t at a spatial position $x(t)$ is

$$l = \left[x(t) + u\left(x\left(t\right), t\right) \right]. \tag{1}$$

The total velocity V at the spatial position $x(t)$ of the wire rope is the summation of the axial velocity $v(t)$ of the elevator and the vibration velocity at $x(t)$ and is expressed as:

$$V = \frac{dl}{dt} = \left[v\left(t\right) + \left(u_t\left(t\right) + v \cdot u_x\left(t\right)\right) \right]. \tag{2}$$

where the subscript of x or t denoted the partial differentiation with respect to x or t.

The kinetic energy of the elevator traction system is expressed as follows.

$$E_k = 0.5 m v_c^2 \Big|_{x=l(t)} + 0.5\rho \int_0^{l(t)} V^2 dx, \tag{3}$$

where the first term is the kinetic energy of the lifting car, and the second term is the kinetic energy of the wire rope.

Since the lifting car is considered to be a rigid body, the elastic strain energy of the elevator traction system is that of the wire rope, which is formulated as follows:

$$E_s = \int_0^{l(t)} (P u_x + 0.5 E A u_x^2) dx, \tag{4}$$

where E and A are Young's modulus and the nominal cross-section area of the wire rope, respectively. P is the quasi-static tension measured at the spatial position $x(t)$ on the wire rope and is expressed by:

$$P=\left[m+\rho\left(l\left(t\right)-x\right)\right]g. \tag{5}$$

In Eq. (4), the first term in the bracket denotes the static strain energy, and the second term represents the dynamic strain energy. The gravitational potential energy of the elevator traction system is:

$$E_g=-\int_0^{l(t)}\rho gudx-mgu\big|_{x=l(t)}. \tag{6}$$

1.2 Dynamic Model Without External Interference

The elevator starts to run when an acceleration a(t) is provided by a lift machine. Furthermore, vibration is also generated in the elevator traction system. According to the Hamiltonian principle, the movement trajectory of the elevator in any time interval makes the time integral of the total energy stationary, that is:

$$I=\int_{t_1}^{t_2}\left[\delta E_k-\delta E_s-\delta E_g\right]dt=0. \tag{7}$$

The boundary conditions of the elevator traction are:

$$\delta u\left(0,t\right)=\delta u\left(x,t_1\right)=\delta u\left(x,t_2\right)=0,$$
$$u\left(0,t\right)=0. \tag{8}$$

Using integral by parts with a variable upper boundary, the expression of δE_k, δE_g and δE_s are further reformed as follows:

$$\begin{aligned}\int_{t_1}^{t_2}\delta E_k dt=&-\int_{t_1}^{t_2}\left\{m\frac{\partial}{\partial t}\left(v+u_t+vu_x\right)\right.\\&\left.+m\frac{\partial}{\partial x}\left[v\left(v+u_t+vu_x\right)\right]\right\}\delta u\big|_{x=l(t)}dt\\&-\int_{t_1}^{t_2}\left\{\rho\int_0^{l(t)}\frac{\partial}{\partial t}\left(v+u_t+vu_x\right)\delta udx\right.\\&\left.-\int_0^{l(t)}\left[\rho v\int_0^{l(t)}\frac{\partial}{\partial x}\left(v+u_t+vu_x\right)\right]\right\}dt,\end{aligned} \tag{9}$$

$$\int_{t_1}^{t_2}\delta E_g dt=-\int_{t_1}^{t_2}\left(mgu\big|_{x=l(t)}+\int_0^{l(t)}\rho gudx\right)\delta dt, \tag{10}$$

$$\begin{aligned}\int_{t_1}^{t_2}\delta E_s dt=&\int_{t_1}^{t_2}\left[\left(P\delta u+EAu_x\delta u\right)\big|_{x=l(t)}\right.\\&\left.-\int_0^{l(t)}\left(P_x\delta u-EAu_{xx}\right)\delta udx\right]dt.\end{aligned} \tag{11}$$

Substitute Eqs. (9) to (11) into Eq. (7). By applying Leibniz's formula and considering the arbitrary property of δu, the following equations are derived:

$$\rho\left(u_{tt}+2vu_{xt}+au_x+v^2u_{xx}+a\right)=EAu_{xx},$$
$$0<x<l\left(t\right), \tag{12}$$

$$m\left(u_{tt}+2vu_{xt}+au_x+v^2u_{xx}+a\right)+EAu_x=0,\ x=l\left(t\right). \tag{13}$$

Eq. (12) is the equation of motion for the longitudinal vibration of the time-varying elevator traction system and Eq. (13) is the corresponding boundary conditions of the elevator traction system.

1.3 Dynamic Model with External Interference

As one of the external interferences, the eccentricity of the traction wheel will produce an eccentric force during the operation of the elevator, which leads to the force vibration of the elevator traction system. Due to the limitations of the manufacturing technology, errors from the manufacture and installation cause a deviation of the central axis of the traction wheel from the rotating axis, resulting in the eccentricity of the traction wheel. The boundary condition in this situation is formulated as:

$$u\left(0,t\right)=e,\quad u\left(l,t\right)=0, \tag{14}$$

where e is the eccentric excitation displacement dependent on time. Note that the boundary conditions in Eq. (14) are nonhomogeneous. To solve the governing Eq. (12) by satisfying the boundary conditions in Eq. (14), the displacement function $u(x,t)$ is decomposed into two parts:

$$u\left(x,t\right)=u_1\left(x,t\right)+u_2\left(x,t\right), \tag{15}$$

where $u_1(x,t)$ satisfies the homogeneous boundary conditions, and $u_2(x,t)$ satisfies the nonhomogeneous boundary conditions in Eq. (14). Since this paper studies the vibration of the time-varying elevator traction system under the influence of periodic forces, the expression $u_2(x,t)$ is obtained according to the stress-strain relationship as follows:

$$u_2\left(x,t\right)=e-\frac{e}{l}x. \tag{16}$$

Substituting Eq. (16) into (15) and then the acquired Eqs. (12) and (13), the equation of motion and the corresponding boundary condition for the forced longitudinal vibration of the time-varying elevator traction system are obtained as follows:

$$\begin{aligned}\mathfrak{D}\left(u(x,t)\right)=&\rho\left(u_{1,tt}+2vu_{1,xt}+au_{1,x}+v^2u_{1,xx}+a\right)\\&-EAu_{1,xx}-\rho\left\{2v\left(\frac{le_t-ve}{l^2}\right)+\frac{ae}{l}\right.\\&\left.+\left[\frac{e_{tt}}{l}-\frac{ae}{l^2}-\frac{2ve_t}{l^2}+\frac{2v^2e}{l^3}\right]x\right\}=0,\\&0<x<l\left(t\right),\end{aligned} \tag{17}$$

$$\mathfrak{B}\left(u(x,t)\right)=m\left(u_{1,tt}+2vu_{1,xt}+au_{1,x}+v^2u_{1,xx}+a\right)+EAu_{1,x}-\frac{EAe}{l}+m\left\{2v\frac{ve-le_t}{l^2}-\frac{ae}{l}+\left[-\frac{e_{tt}}{l}+\frac{2ve_t}{l^2}+\frac{ae}{l^2}-\frac{2v^2e}{l^3}\right]x\right\}=0,\quad x=l(t). \tag{18}$$

1.4 Discretization Process

Since the equation of motion, Eq. (17), for the longitudinal vibration of the time-varying elevator system is a complex partial differential equation with infinite degrees of freedom and time-varying parameters, it is almost impossible to obtain accurate solutions. In this paper, the Galerkin method is used to discretize the equation of motion so that the equation of motion is converted into a set of ordinary differential equations. Following this work, the Newmark-β method is applied to obtain the numerical solution. The Newmark-β method is a numerical calculation method that linearizes and averages the generalized acceleration in the equation of motion for a dynamic problem. It is one of the most commonly used numerical methods in finite element analysis for dynamic problems and can ensure stable numerical solutions [28]. The solution of u1 is assumed in the form:

$$u_1(x,t)=\sum_{i=1}^{n}\varphi_i(x)\,p_i(t), \tag{19}$$

where $p_i(t)$ is the generalized coordinate, and n is the number of included modulus, $\varphi_i(x)$ is the trial function. Since the wire rope is considered as a cantilever beam, the trial function $\varphi_i(x)$ is taken as the following form:

$$\varphi_i(x)=\sqrt{2}\sin\left(\frac{2i-1}{2l}\pi x\right). \tag{20}$$

Although Eq. (20) satisfies the boundary condition in Eq. (8) at $x = 0$, it cannot satisfy the boundary condition in Eq. (18) at $x = l(t)$. To eliminate the residuals generated by the trial function in the domain of x and at the boundary of x, the method of weighted residuals is adopted, which requires the total residual of the trial function in the domain of x and that at the boundary of x vanish:

$$\int_0^{l(t)}\mathfrak{D}_j(u,\varphi)\varphi_i(x)dx+\mathfrak{B}_j(u,\varphi)\varphi_i(x)|_{x=l(t)}=0,\quad (i,j=1,2,\cdots,n). \tag{21}$$

For the convenience of analysis, a new variable $\xi = x/l(t)$ is defined to normalize the variable x, and the time-varying domain $[0, l(t)]$ related to x is transformed into a fixed domain [0, 1] of ξ. Replace $x = \xi\, l(t)$. After some calculus calculation, the equations of motion are transformed into the following form of the matrix:

$$M\ddot{p}+C\dot{p}+Kp=F, \tag{22}$$

where

$$\begin{aligned}
M_{ji}&=\rho\delta_{ij}+\frac{m}{l(t)}\phi_i(1)\phi_j(1),\\
C_{ji}&=\frac{2\rho v(t)}{l(t)}\int_0^1(1-\xi)\phi_i'(\xi)\phi_j(\xi)d\xi,\\
K_{ji}&=\frac{\rho v^2(t)}{l^2(t)}\int_0^1(1-\xi)^2\varphi_i''(\xi)\varphi_j(\xi)d\xi-\frac{EA}{l^2}\int_0^1\varphi_i''(\xi)\varphi_j(\xi)d\xi+\frac{a\rho}{l}\int_0^1(1-\xi)\varphi_i'(\xi)\varphi_j(\xi)d\xi-\frac{2v^2\rho}{l^2}\int_0^1(1-\xi)\varphi_i'(\xi)\varphi_j(\xi)d\xi+\frac{EA}{l^2}\varphi_i'(1)\varphi_j(1)\\
F_j&=-\rho\int_0^1\left[2v\left(e_t-\frac{ve}{l}\right)+ae+\xi\left(e_{tt}l-ae-2ve_t+\frac{2v^2e}{l}\right)\right]\varphi_j(\xi)d\xi-\rho a\int_0^1\varphi_j(\xi)d\xi-\frac{ma}{l}\varphi_j(1)-\left(me_{tt}+\frac{EAe}{l}\right)\varphi_j(1),
\end{aligned} \tag{23}$$

and δ_{ij} is the delta function. Eqs. (22) and (23) are solved by using Newmark-β method. Fig. 3 is a flow chart to solve Eqs. (22) and (23) by developing a MATLAB program.

2 MODELLING OF THE RUNNING STATUS OF THE ELEVATOR TRACTION SYSTEM

A complete running cycle of the elevator includes at least seven stages: acceleration increasing $(0, t_1)$, uniform acceleration (t_1, t_2), the acceleration decreasing to zero (t_2, t_3), uniform motion (t_3, t_4), deceleration increasing to the maximum (t_4, t_5), uniform deceleration (t_5, t_6), and deceleration decreasing to zero (t_6, t_7). The hoisting jerk $j_i(t)$ (the change of the acceleration per unit time) of the elevator at Stage I is taken as a quadratic function of time as follows:

$$j_i(t)=60\eta_0^i(t-t_{i-1})^2+24\eta_1^i(t-t_{i-1})+6\eta_2^i. \tag{24}$$

Assuming that the maximum acceleration, the maximum speed, and the maximum jerk are a_m, v_m, j_m, respectively, the jerk $j_i(t)$, hoisting acceleration

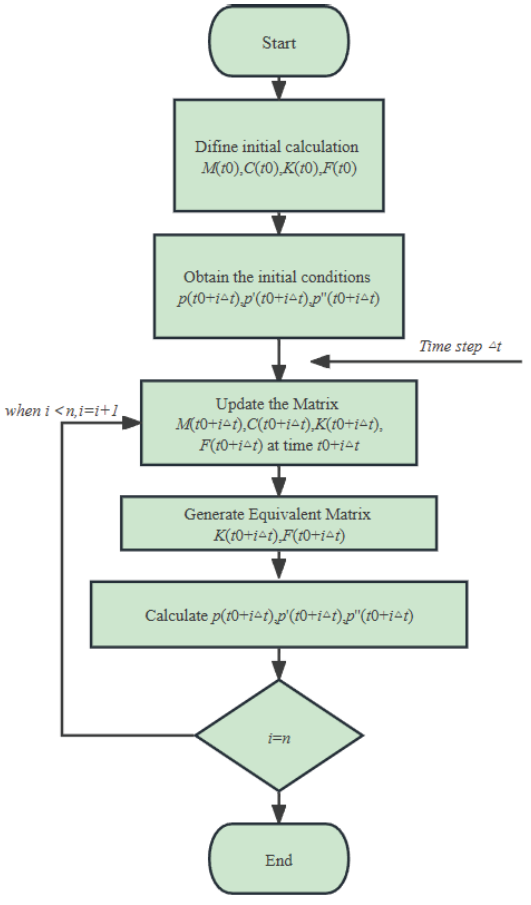

Fig. 3. *A flow chart to solve Eqs. (22) and (23)*

$a_i(t)$, the hoisting speed $v_i(t)$ and the length $l_i(t)$ of the elevator at each stage are determined by integrating sequential and applying the continuity conditions. Fig. 4 shows typical running curves of an elevator when it goes up and down.

3 NUMERICAL RESULTS AND DISCUSSION

As an example, the typical parameters of the elevator traction system in a high-rise elevator are $\rho = 0.575$ kg/m, $m = 1000$ kg, $EA = 7.02\times10^7$ N. The length of the wire rope is $l_0 = 140$ m.

According to the Newmark method, the iteration equation for solving Eq. (22) in the given time domain is derived as follows:

$$\widehat{K}_{t+\Delta t}\, p_{t+\Delta t} = \widehat{F}_{t+\Delta t},$$

$$\dot{p}_{t+\Delta t} = \frac{\gamma}{\beta\Delta t}\left(p_{t+\Delta t} - p_t\right) + \left(1-\frac{\gamma}{\beta}\right)\dot{p}_t + \left(1-\frac{\gamma}{2\beta}\right)\ddot{p}_t\Delta t,$$

$$\ddot{p}_{t+\Delta t} = \frac{1}{\beta\Delta t^2}\left(p_{t+\Delta t} - p_t\right) - \frac{1}{\beta\Delta t}\dot{p}_t - \left(\frac{1}{2\beta}-1\right)\ddot{p}_t, \qquad (25)$$

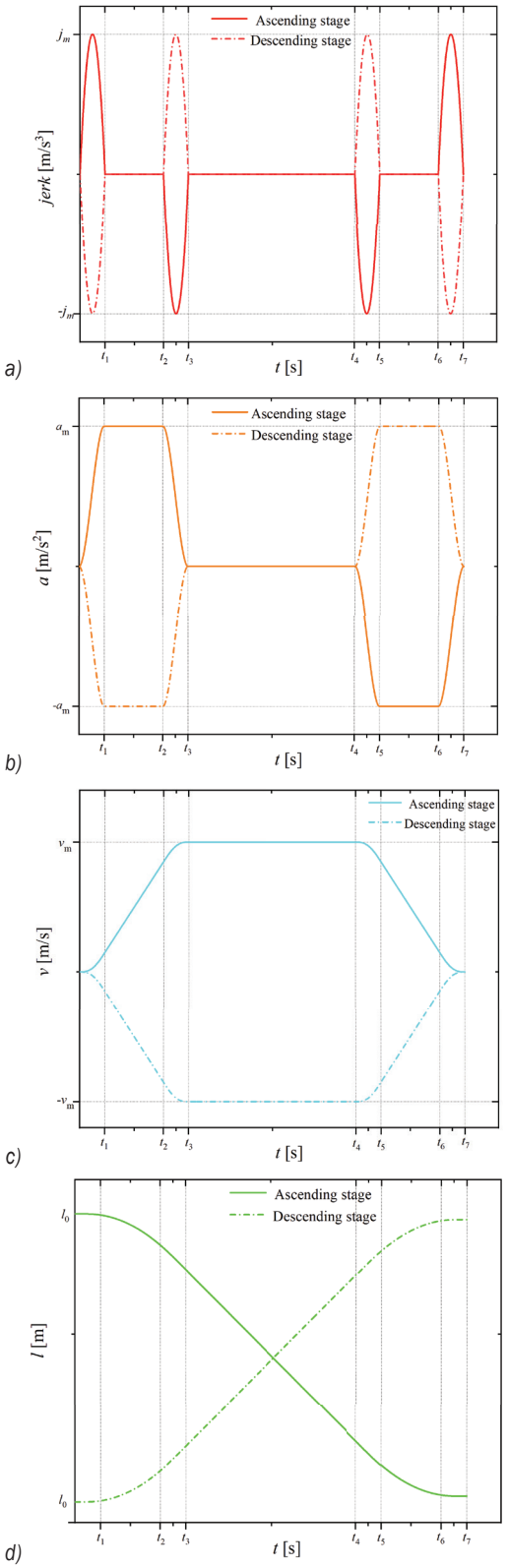

Fig. 4. *Typical running curves of an elevator: a) Increase of acceleration, b) acceleration of elevator, c) velocity of the elevator, d) length of wire rope*

where

$$\widehat{K} = K_{t+\Delta t} + \frac{1}{\beta \Delta t^2} M + \frac{\gamma}{\beta \Delta t} C,$$

$$\widehat{F} = F_{t+\Delta t} + M\left[\frac{1}{\beta \Delta t^2} p_t + \frac{1}{\beta \Delta t} \dot{p}_t + \left(\frac{1}{2\beta} - 1\right) \ddot{p}_t\right] + C\left[\frac{\gamma}{\beta \Delta t} p_t + \left(\frac{\gamma}{\beta} - 1\right) \dot{p}_t + \left(\frac{\gamma}{2\beta} - 1\right) \ddot{p}_t \Delta t\right], \quad (26)$$

γ and β are the calculation parameters from the algorithm of the Newmark-β method. In this paper, $\gamma = 1/2$ and $\beta = 1/4$.

At time $t = 0$, the elevator traction system is stationary. Thus, the initial values of the generalized coordinate and its velocity are zero, i.e., $[p_0] = 0$ and $[\dot{p}_0] = 0$. As to the initial value of the acceleration of $[\ddot{p}_0]$, it is obtained from Eq. (22) with the known values of $[p_0]$ and $[\dot{p}_0]$. In the following of this section, the influence of the running direction, the acceleration, and the mass of the lifting car on the vibration performance of the elevator traction system is under investigation.

3.1 Vibration Without the Eccentric Excitation

Table 1 lists the time interval of the seven stages in a complete running cycle of the elevator traction system. Fig. 5 plots the time history for the longitudinal vibration of the elevator traction system without the eccentric excitation when $v_m = 5$ m/s and $a_m = 1$ m/s².

It can be seen from Fig. 5 that regardless of whether the elevator is in the ascending or descending stages, aperiodic displacement occurs during the starting and braking stages. These aperiodic displacements are attributed to the inertial force from the acceleration or deceleration, indicating that the elevator deviates from the initial equilibrium position. Another observation from Fig. 5 is that the vibration amplitude and frequency of the elevator traction system decrease during the ascending stage and increase during the descending stage. The reason for such response is that the length of the steel wire rope is reduced during the ascending process, which causes the increasing of the stiffness of the elevator traction system, as a result of that, the amplitude and frequency of the longitudinal vibration decreases. The situation is reversed during the descending process.

Table 1. *Time interval of seven stages in a complete running cycle of the elevator traction system [s]*

t_1	t_2	t_3	t_4	t_5	t_6	t_7
1.5	5	6.5	16.5	18	21.5	23

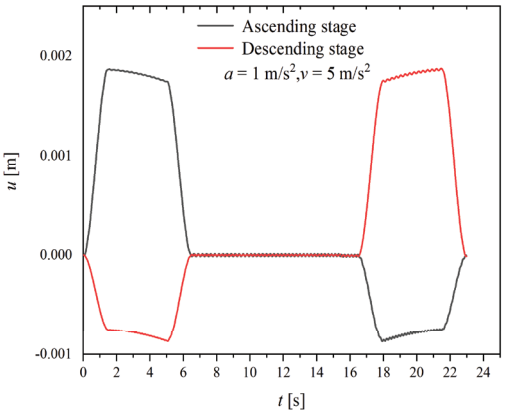

Fig. 5. *The time history of longitudinal vibration of the elevator traction system without external interference*

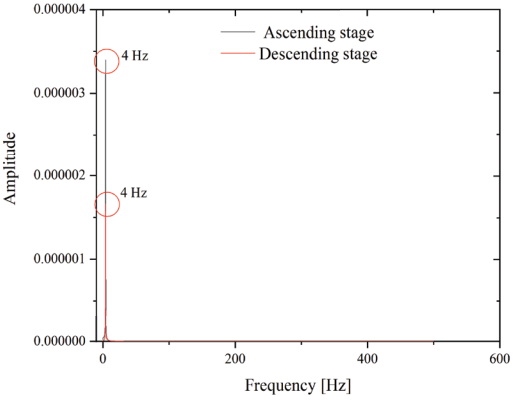

Fig. 6. *Extracted frequency spectrum of the elevator traction system without the eccentric excitation*

Fig. 6 shows the frequency spectrum of the elevator traction system obtained by Fourier transform of the time history of the longitudinal vibration during uniform motion in both ascending and descending processes without eccentric excitation. As shown in Fig. 6, the fundamental frequencies of the elevator traction system during uniform motion in both ascending and descending processes are 4 Hz.

3.2 Vibration Response with Eccentric Excitation

The eccentric excitation distance e is applied at the top of the rope and is expressed as:

$$e = 1 \times 10^{-4} \sin \omega_0 t \ \ [\mathrm{m}], \quad (27)$$

where ω_0 is the angular velocity of the lift machine and is closely related to the diameter d_0 of the traction wheel, the maximum hoisting speed v_m and the maximum acceleration a_m of the elevator traction system. In this paper, the angular velocity of the lift machine ω_0 is calculated by considering that the

distance travelled by the elevator per unit of time must equal that of the traction wheel and is estimated as follows:

$$\omega_0 = \frac{2l_T}{d_0 t_7}, \tag{28}$$

where l_T is the distance travelled by the elevator in a running cycle, and t_7 is the time period of a running cycle.

3.2.1 Influence of the Running Direction

In this subsection, the diameter of the traction wheel, the maximum hoisting speed and the maximum acceleration of the elevator traction system are chosen as d_0 = 0.4 m, v_m = 2.5 m/s, a_m = 0.5 m/s², and ω_0 = 3π. The time intervals of the seven stages are the same as those in Table 1 of Section 3.1. The time history of the longitudinal vibration of the elevator traction system in the process of ascending and descending is drawn in Fig. 7. It can be seen from Fig. 7 that the amplitude of the longitudinal vibration of the elevator traction system with external excitation gradually decreases during the ascending process and increases during the descending process, which is consistent to the response for the elevator traction system without eccentric excitation in Section 3.1. Nevertheless, the time histories shown in Fig. 7 for the elevator with eccentric excitation are quite different from those in Fig. 5 for the elevator without eccentric excitation.

To facilitate explain the reason for the difference, frequency spectra for the time history in Fig. 7 are extracted and plotted in Fig. 8. As shown in Fig. 8, the leading frequency is 1.5 Hz, which is the frequency of the lift machine. Furthermore, the fundamental frequency 4 Hz of the elevator traction system is also captured. The spectrum analysis indicates that the vibration response of the elevator with eccentric excitation is governed by eccentric excitation.

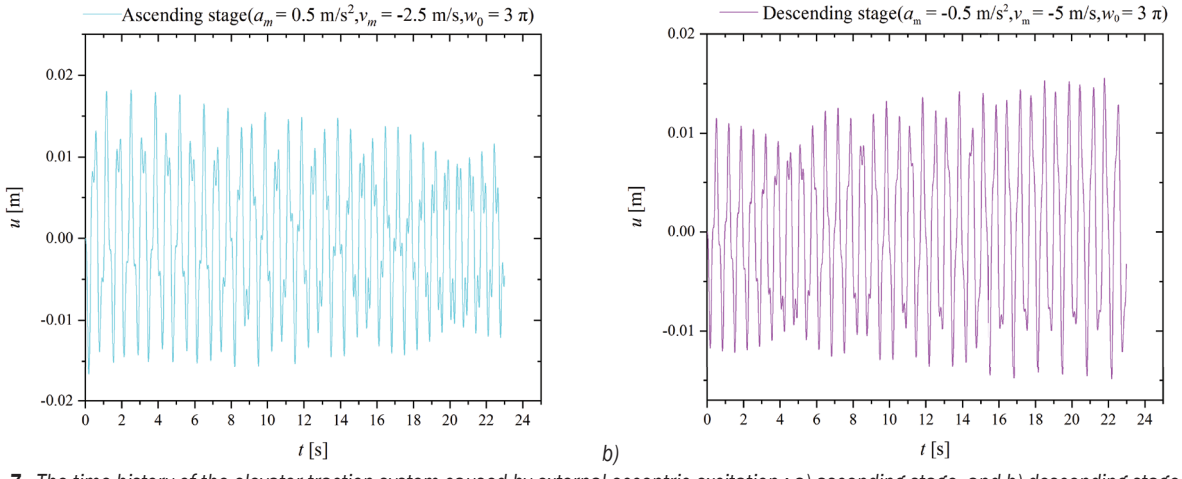

Fig. 7. *The time history of the elevator traction system caused by external eccentric excitation.; a) ascending stage, and b) descending stage*

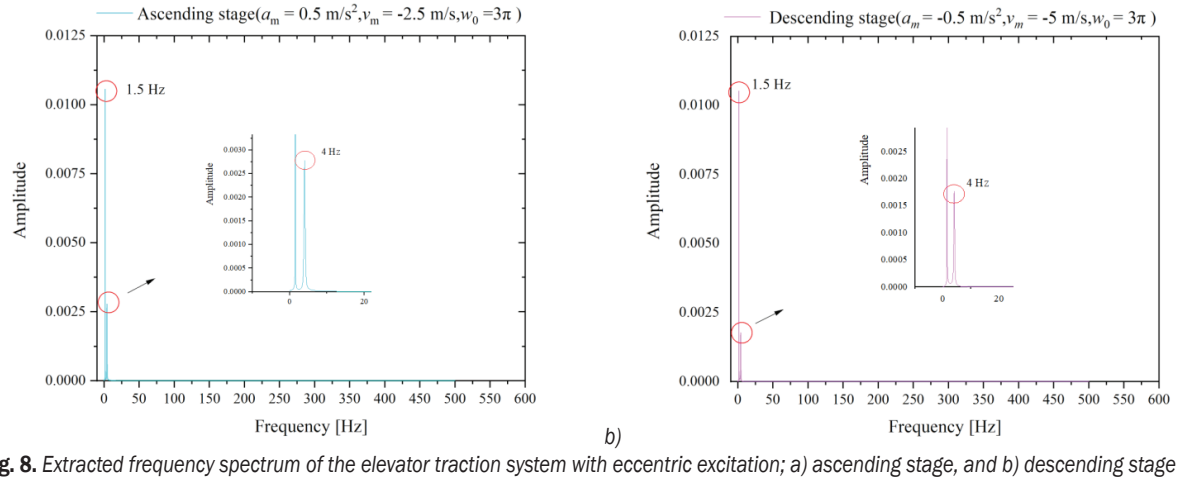

Fig. 8. *Extracted frequency spectrum of the elevator traction system with eccentric excitation; a) ascending stage, and b) descending stage*

3.2.2 *Influence of the Acceleration of the Elevator*

To clarify the influence of the acceleration of the elevator traction system on its vibration performance, the following three cases in which the elevator goes down are investigated:

Case I v_m = -3.75 m/s, a_m = -0.75 m/s2, $\omega_0 = 9/2\pi$;
Case II v_m = -5.0 m/s, a_m = -1.0 m/s2, $\omega_0 = 6\pi$;
Case III v_m = -7.5 m/s, a_m = -1.5 m/s2, $\omega_0 = 9\pi$.

Fig. 9 demonstrates the influence of the acceleration on the time history of the descending elevator traction system. It can be seen the vibration amplitude of the elevator traction system increases for all three cases during the descending process. Furthermore, the vibration amplitudes of the elevator for Case II are less than those for Case III but greater than those for Case I. In other words, the greater the values of vm and am, the larger the vibration amplitude of the elevator. However, Fig. 9c also shows that the amplitude of the elevator increases significantly at t = 13 s. Such a response indicates that the resonance occurs in the elevator traction system, as the frequency of the eccentric excitation of the traction machine is close to the fundamental frequency of the elevator traction system. Therefore, in order to prevent the occurrence of resonance and the maximum values of acceleration and deceleration should not exceed 1.5 m/s².

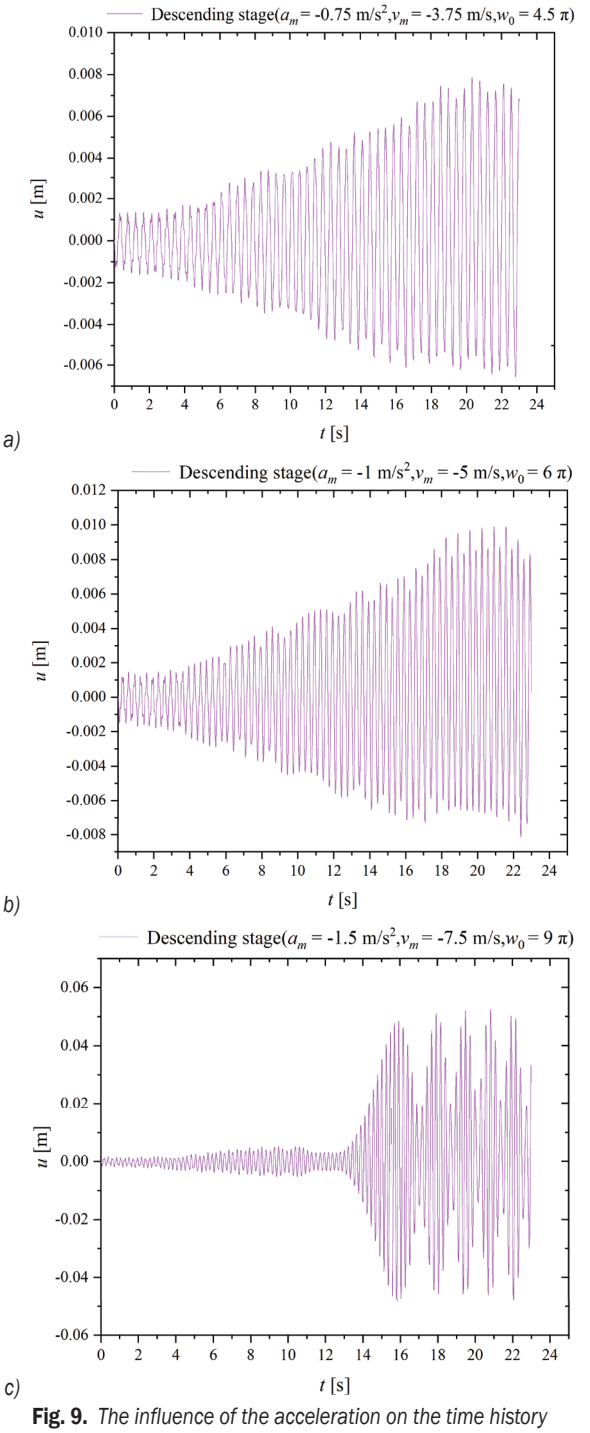

Fig. 9. *The influence of the acceleration on the time history of the descending elevator traction system; a) a_m = -0.75 m/s², b) a_m = -1 m/s², and c) a_m = -1.5 m/s²*

4 CONCLUSIONS

In this paper, the longitudinal vibration of the time-varying elevator traction system is studied by means of theoretical analysis and numerical simulation. The equation of motion and the corresponding boundary condition of the time-varying elevator traction system with and without external interference is derived based on the Hamiltonian principle and is solved by employing Galerkin's weighted residual method to take into consideration the boundary condition. As an application of the proposed analytical approach, the force vibration of the elevator traction system induced by the eccentric excitation of the traction wheel is analysed. Depending on the running status of the elevator, a mathematical formula is proposed to estimate the angular velocity of the traction wheel. A MATLAB program is developed to obtain the numerical solutions of the elevator traction system under different running statuses. The following conclusions can be drawn:

1. During the ascending stage, the equivalent stiffness of the elevator traction system increases with the decreasing length of the wire rope, resulting in a decrease in the vibration amplitude

and vibration frequency. The situation is reversed during the descending stage.

2. As far as the structural parameters of the elevator are determined, the vibration response of the elevator traction system is determined by its running state. In particular, the greater the running acceleration of the elevator, the larger the angular velocity of the traction wheel, and the higher the vibration amplitude and frequency of the elevator traction system.
3. When the acceleration reaches am = 1.5 m/s², the frequency of eccentric excitation of the traction machine is close to the fundamental frequency of the elevator traction system, which leads to the resonance of the elevator traction system. Therefore, in order to prevent the occurrence of resonance, the maximum value of acceleration and deceleration should not exceed 1.5 m/s².

In practical engineering applications, elevators are installed within buildings, so the vibration of elevators is affected by the vibration of buildings. Further experimental and theoretical studies can be conducted on the coupled vibration between the elevators and the buildings subjected to wind loads and earthquakes, which may provide a reference for seismic design of elevator traction system.

5 ACKNOWLEDGEMENTS

This work is supported by the Guangdong Natural Science Foundation (No. 2021A1515012037).

6 REFERENCES

[1] Cortés, P., Muñuzuri, J., Vázquez-Ledesma, L.A. (2021). Double deck elevator group control systems using evolutionary algorithms: Interfloor and lunchpeak traffic analysis. *Computers & Industrial Engineering*, vol. 155, art. ID 107190, **DOI:10.1016/j.cie.2021.107190**.

[2] Zhu, W.D., Teppo, L.J. (2003). Design and analysis of a scaled model of a high-rise, high-speed elevator. *Journal of Sound and Vibration*, vol. 264, no. 3, p. 707-731, **DOI:10.1016/S0022-460X(02)01218-X**.

[3] Meng, F., Chen, Y., Du, M., Gong, X. (2016). Study on effect of inter-wire contact on mechanical performance of wire rope strand based on semi-analytical method. *International Journal of Mechanical Sciences*, vol. 115-116, p. 416-427, **DOI:10.1016/j.ijmecsci.2016.07.012**.

[4] Zhang, J., Wang, D.G., Zhang, D.K., Ge, S.R, Wang, D.A. (2017). Dynamic torsional characteristics of mine hoisting rope and its internal spiral components. *Tribology International*, vol. 109, p. 182-191, **DOI:10.1016/j.triboint.2016.12.037**.

[5] Xiang, L., Wang, H.Y., Chen, Y., Guan, Y.J., Wang, Y.L., Dai, L.H. (2015). Modeling of multi-strand wire ropes subjected to axial tension and torsion loads. *International Journal of Solids and Structures*, vol. 58, p. 233-246, DOI:10.1016/j.ijsolstr.2015.01.007.

[6] Xiang, L., Wang, H.Y., Chen, Y., Guan, Y.J., Dai, L.H. (2017). Elastic-plastic modeling of metallic strands and wire ropes under axial tension and torsion loads. *International Journal of Solids and Structures*, vol. 129, p. 103-118, **DOI:10.1016/j.ijsolstr.2017.09.008**.

[7] Foti, F., de Luca di Roseto A. (2016). Analytical and finite element modelling of the elastic-plastic behaviour of metallic strands under axial-torsional loads. *International Journal of Mechanical Sciences*, vol. 115-116, p. 202-214, **DOI:10.1016/j.ijmecsci.2016.06.016**.

[8] Stanova, E., Fedorko, G., Kmet, S., Molnar, V., Fabian, M. (2015). Finite element analysis of spiral strands with different shapes subjected to axial loads. *Advances in Engineering Software*, vol. 83, p. 45-58, **DOI:10.1016/j.advengsoft.2015.01.004**.

[9] Wang, J.J., Cao, G.H., Zhu, Z.C., Wang, Y.D., Peng, W.H. (2015). Lateral response of cable-guided hoisting system with time-varying length: Theoretical model and dynamics simulation verification. *Proceedings of the Institution of Mechanical Engineers, Part C: Journal of Mechanical Engineering Science*, vol. 229, no. 16, p. 2908-2920, **DOI:10.1177/0954406214566032**.

[10] Peng, Q.F., Jiang, A.H., Yuan, H., Huang, G.J., He, S., Li, S.Q. (2020). Study on theoretical model and test method of vertical vibration of elevator traction system. *Mathematical Problems in Engineering*, vol. 2020, art. ID 851802, **DOI:10.1155/2020/8518024**.

[11] Xu, P., Peng, Q.F., Jin, F.S., Xue, J.H., Yuan, H. (2023). Theoretical and experimental study on tension-torsion coupling vibration for time-varying elevator traction system. *Acta Mechanica Solida Sinica*, vol. 36, p. 899-913, **DOI:10.1007/s10338-023-00429-5**.

[12] Zhang, R.J., Yang, W.W., Wang, X.W. (2014). The reliability analysis of horizontal vibration of elevator based on multi-state fuzzy Bayesian network. *Jordan Journal of Mechanical and Industrial Engineering*, vol. 8, no. 1, p. 43-49.

[13] Wang, J., Pi, Y., Krstic, M. (2018). Balancing and suppression of oscillations of tension and cage in dual-cable mining elevators. *Automatica*, vol. 98, p. 223-238, **DOI:10.1016/j.automatica.2018.09.027**.

[14] Trąbka, A. (2014). Dynamics of telescopic cranes with flexible structural components. *International Journal of Mechanical Sciences*, vol. 88, p. 162-174, **DOI:10.1016/j.ijmecsci.2014.07.009**.

[15] Zhang,Y., Zhang, Q., Peng, Y.X., Wang, C., Chang, X.D., Chen, G.A. (2022). Tribological behavior of octadecylamine functionalized graphene oxide modified oil for wire rope in mine hoist. *Wear*, p. 494-495, art. ID 204273, **DOI:10.1016/j.wear.2022.204273**.

[16] Bao, J.H., Zhang, P., Zhu, C.M. (2014). Transverse vibration of flexible hoisting rope with time-varying length. *Journal of Mechanical Science and Technology*, vol. 28, p. 457-466, **DOI:10.1007/s12206-013-1110-y**.

[17] Kaczmarczyk, S., Ostachowicz, W. (2003). Transient vibration phenomena in deep mine hoisting cables. Part 2: Numerical simulation of the dynamic response. *Journal of Sound and*

Vibration, vol. 262, no. 2, p. 245-289, **DOI:10.1016/S0022-460X(02)01148-3**.

[18] Zhang, R.J., Wang, C., Zhang, Q., Liu, J. (2019). Response analysis of non-linear compound random vibration of a high-speed elevator. *Journal of Mechanical Science and Technology*, vol. 33, p. 51-63, **DOI:10.1007/s12206-018-1206-5**.

[19] Cao, S.X., Zhang, R.J., Zhang, S.H., Qiao, S., Cong, D.S., Dong, M.X. (2019). Roller-rail parameters on the transverse vibration characteristics of super-high-speed elevators. *Transactions of the Canadian Society for Mechanical Engineering*, vol. 43, no. 4, p. 535-543, **DOI:10.1139/tcsme-2018-0083**.

[20] Zhang, R.J., Wang, C., Zhang, Q. (2018). Response analysis of the composite random vibration of a high-speed elevator considering the nonlinearity of guide shoe. *Journal of the Brazilian Society of Mechanical Sciences and Engineering*, vol. 40, art. ID 190, **DOI:10.1007/s40430-017-0936-0**.

[21] Gaiko, N.V., van Horssen, W.T. (2018). Resonances and vibrations in an elevator cable system due to boundary sway. *Journal of Sound and Vibration*, vol. 424, p. 272-292, **DOI:10.1016/j.jsv.2017.11.054**.

[22] Yang, D.H., Kim, K.Y., Kwak, M.K., Lee, S. (2017). Dynamic modeling and experiments on the coup-led vibrations of building and elevator ropes. *Journal of Sound and Vibration*, vol. 390, p. 164-191, **DOI:10.1016/j.jsv.2016.10.045**.

[23] Crespo, R.S., Kaczmarczyk, S., Picton, P., Su, H. (2018). Modelling and simulation of a stationary high-rise elevator system to predict the dynamic interactions between its components. *International Journal of Mechanical Sciences*, vol. 137, p. 24-45, **DOI:10.1016/j.ijmecsci.2018.01.011**.

[24] Nguyen, T.X., Miura, N., Sone, A. (2019). Analysis and control of vibration of ropes in a high-rise elevator under earthquake excitation. *Earthquake Engineering and Engineering Vibration*, vol. 18, p. 447-460, **DOI:10.1007/s11803-019-0514-9**.

[25] Knezevic, B.Z., Blanusa, B., Marcetic, D.P. (2017). A synergistic method for vibration suppression of an elevator mechatronic system. *Journal of Sound and Vibration*, vol. 406, p. 29-50, **DOI:10.1016/j.jsv.2017.06.006**.

[26] Zhang, Y.H., Agrawal, S.K., Hagedorn, P. (2005). Longitudinal vibration modelling and control of a flexible transporter system with arbitrarily varying cable lengths. *Journal of Vibration and Control*, vol. 11, no. 1, no. 3, p. 431-456, **DOI:10.1177/1077546305047988**.

[27] Qiu, L.M., Wang, Z., Zhang, S., Zhang, L., Chen, J.A. (2020). Vibration-related design parameter optimization method for high-speed elevator horizontal vibration reduction. *Shock and Vibration*, vol. 2020, art. ID 1269170, **DOI:10.1155/2020/1269170**.

[28] Yavuz, Ş., Malgaca, L., Karagülle, H. (2016). Analysis of active vibration control of multi-degree-of-freedom flexible systems by Newmark method. *Simulation Modelling Practice and Theory*, vol. 69, p. 136-148, **DOI:10.1016/j.simpat.2016.06.004**.

Strojniški vestnik - Journal of Mechanical Engineering 70(2024)3-4, 181-193
DOI:10.5545/sv-jme.2023.825
Original Scientific Paper
Received for review: 2023-10-09
Received revised form: 2023-12-19
Accepted for publication: 2023-12-23

Nonlinear Free Vibration Analysis of Functionally Graded Porous Conical Shells Reinforced with Graphene Nanoplatelets

Xiaolin Huang – Nengguo Wei – Chengzhe Wang – Xuejing Zhang*
Guilin University of Electronic Technology, School of Architecture and Transportation Engineering, China

The nonlinear vibration analysis of functionally graded reinforced with graphene platelet (FG-GRC) porous truncated conical shells surrounded by the Winkler-Pasternak elastic foundation is presented in this paper. An improved model for evaluating the material properties of porous composites is proposed. Three types of porous distribution and three patterns of graphene nanoplatelets (GPLs) dispersion are estimated. Coupled with the effect of the Winkler-Pasternak elastic foundation, the nonlinear governing equations are developed by using the Hamilton principle. The Galerkin integrated technique is employed to obtain the linear and nonlinear frequencies of the shells. After the present method is validated, the effects of the pores, GPLs, the Winkler-Pasternak foundation, and the semi-vertex are investigated in detail. The results show that the linear frequency can be raised by increasing the values of the mass volume of the GPL and foundation parameters. In contrast, the ratio of nonlinear to linear frequency declines as the mass volume of the GPLs and foundation parameters rises. Furthermore, it is found that the minimum ratio of nonlinear to linear frequency can be obtained as the semi-vertex angle is about 55°, and the effect of porosity distribution on the linear and linear frequencies might be neglected.

Keywords: nonlinear vibration, truncated conical shell, graphene nanoplatelet, porous materials, elastic foundation

Highlights

- *A new model for estimating the material properties of FG-GRCs is presented.*
- *The nonlinear vibrational equations for FG-GRCs conical shells are built.*
- *The formulations for the linear and nonlinear frequency of FG-GRCs conical shells are presented.*

0 INTRODUCTION

Because the nonlinear dynamic behaviour of structures inevitably appears in engineering applications, the nonlinear characteristics of the structures have attracted the attention of many researchers. For example, Lu et al. **[1]** and **[2]** and Hao et al. **[3]** developed a novel model to analyse the nonlinear vibration of isolation systems with a high-static-low-dynamic stiffness. They validated the analytical results by using direct time integration and experiments. The inherent vulnerability of nonlinear vehicle platoons was studied by Wang et al. **[4]**. They proposed a vibration-theoretic approach to compute the platoon's resonance frequency. Zhou et al. **[5]** presented a high-order nonlinear friction model to investigate the nonlinear hysteresis characteristics of metal rubbers. They found that the nonlinear friction hysteresis dynamic model has a high prediction accuracy and signal-to-noise ratio. Yang and Kai **[6]** built the nonlinear coupled Schrodinger equation in fibre gratings, and the periodic solution was presented. For porous composite plates reinforced with graphene platelets, Huang et al. **[7]** presented a two-step perturbation technique to analyse the nonlinear vibration of the plates. In their studies, the effects of the pores, graphene platelets, and elastic foundations on the nonlinear to linear frequency ratio were discussed in detail.

Due to the advantages of withstanding severe high temperatures while maintaining structural integrity, functionally graded materials (FGMs) are widely used in engineering fields such as aerospace, nuclear, mechanical, and civil engineering. The nonlinear static and dynamic characteristics of FGM shell structures have gained much attention. Chan et al. **[8]** to **[10]** studied the nonlinear buckling and vibration of FGM truncated conical shells, and Duc et al. **[11]** and Vuong et al. **[12]** investigated the nonlinear stability of FGM toroidal shells.

Applying the concept of FGMs, a new type of functionally graded nanocomposites, in which the carbonaceous nanofilters such as graphene platelets (GPLs) and carbon nanotubes (CNTs), are gradually distributed in the thickness direction of the polymeric matrix, has been developed. Because nanocomposites are one of the most promising materials in composite structures, research work has been devoted to examining the linear vibration of functionally graded truncated conical shells reinforced by GPLs and CNTs. Wang et al. **[13]** studied the free vibration of the composite conical shells reinforced with GPLs. They found that the fundamental frequency is greatly affected by the distribution patterns of GPLs. Afshari **[14]** and **[15]** examined the vibration characteristics

*Corr. Author's Address: Guilin University of Electronic Technology, Jinji Road 1#, Guilin, China,pingguotree4426@163.com

of truncated conical shells reinforced with graphene nanoplatelets and discussed the influences of the boundary conditions and constant angular velocity on the natural frequencies. For the joined conical-conical shells made of epoxy-enriched with graphene nanoplatelets, Damercheloo et al. [16] studied free vibration and examined the influences of the boundary conditions, the length-to-small radius ratio, and semi-vertex angle in two shell segments. Using the finite element method in conjunction with a higher-order shear deformation theory, Singha et al. [17] investigated the free vibration behaviour of rotating pre-twisted sandwich conical shell panels with functionally graded graphene-reinforced composite face sheets and homogenous cores in a uniform thermal environment. In their studies, the influence of graphene distribution patterns on the fundamental frequencies is discussed with an emphasis on triggering parameters like pre-twist angle, cone length-to-thickness ratio, core-to-face sheets thickness ratio, and dimensionless rotational speed. Adab et al. [18] and [19] presented a vibrational analysis on truncated conical sandwich microshells. For the vibration behaviour of the composite conical shell reinforced with CNTs, Yousef et al. [20] and [21] investigated the effect of CNTs agglomeration on the vibration characteristics of three-phase CNT/polymer/fibre laminated truncated conical shells. The results show that the subjoining of CNTs leads to a remarkable rise in the natural frequency. Employing the first-order shear deformation theory and the Eshelby-Mori-Tanaka scheme along with the rule of mixture, Afshari and Amirabadi [22] conducted the free vibration analysis of rotating truncated conical shells reinforced with CNTs and the effects of different parameters on the forward and backward frequencies of the shells are investigated. Moreover, the aeroelastic stability of polymeric truncated conical shells reinforced with CNTs and under supersonic fluid flow was studied by Afshari et al. [23]. However, the published literature on the nonlinear vibrations of functionally graded graphene-reinforced composite (FG-GRC) plates and conical shells is limited. Using the 2-D differential quadrature method, arc-length continuation technique, and harmonic balance technique, Jamalabadi et al. [24] studied the nonlinear vibration of FG-GRC truncated conical shells and investigated the effects of the mass volume and distribution of the GPLs, semi-vertex, and foundation parameters on the ratio of linear to nonlinear frequency. They found that the rising valve of the GPL mass volume can raise the linear frequency. In contrast, the ratio of the nonlinear to linear frequency declines. Using the variational differential quadrature and finite element method, Ansari et al. [25] investigated the nonlinear vibration characteristics of FG-GRC conical panels with arbitrary-shaped cutouts. The results show that the natural frequency rises as the weight fraction of the GPLs increases. Yang et al. [26] employed the Galerkin and harmonic balance methods to obtain the nonlinear frequencies of FG-GRC conical shells and studied the periodic and chaotic motions. To investigate the nonlinear dynamic characteristics of FG-GRC conical shells, Wang et al. [27] employed the Galerkin method and fourth-order Runge-Kutta technique to obtain the frequency response. They found that both the mass volume and distribution of GPLs significantly affect the resonance response of the shells. Ding and She [28] obtained the nonlinear dynamic response of FG-GRC truncated conical shells and discussed the effects of the mass fraction of the GPLs, geometrical parameters, and the position of the external load on the response. Additionally, Bidgoli and Arefi [29] presented the nonlinear vibration analysis of sandwich plates with graphene nanoplatelet-reinforced face sheets. They found that the nonlinear to linear frequency ratio can be affected by the weight fraction and geometric parameters of graphene nanoplatelets.

In the literature above, the conical shells were regarded as the perfect structures without pores. However, internal pores may appear inside composite materials [30]. Thus, it is necessary to investigate the effect of internal pores on the dynamic behaviour of porous structures. Some researchers studied the vibration characteristics of porous isotropic [31] and [32], sandwich [33] and [34]. For the functionally graded porous (FGP) truncated conical panels with piezoelectric actuators in thermal environments, Chan et al. [35] investigated the nonlinear dynamic response and free vibration. In their studies, the effect of the porosity distribution on the natural frequency and the deflection amplitudes were discussed. Considering the two types of porosity distribution, the buckling and vibration of sigmoid functionally graded material shells were studied by Huang et al. [36]. The results show both the porosity volume fraction and distribution have significant effects on the buckling pressures and lowest frequency. Nevertheless, little work has been done for the porous truncated conical shells reinforced by nano filters [37]. Bahhadini et al. [38] and Yan et al. [39] studied the linear vibration of porous FG-GRC nanocomposite sandwich conical shells and found that the natural frequencies were increased with the rising material length-scale parameter and porosity coefficient. The

vibration behaviour of porous sandwich truncated conical shells with FG face sheets and a saturated FGP core was studied by Rahmani et al. [40] and Esfahani et al. [41]. The effect of internal pores on the natural frequency was also discussed in detail. Applying the isogeometric analysis, Le et al. [42] obtained the three-dimensional solution of the free vibration and buckling for functionally graded porous-cellular conical shells. Sobhani et al. [43] studied the vibrational behaviour of porous nanocomposite joined hemispherical-cylindrical-conical shells and examined the effects of the porosity distributions and geometric properties. The results revealed that the natural frequency inclines with the increase of the porosity factor. Additionally, the free vibration of FG-joined conical-cylindrical shells reinforced with graphene nanoplatelets was investigated by Kiarasi et al. [44]. It was found that the volume fraction and distributions of the internal pores have an insignificant impact on the natural frequencies of FG-GRC porous conical shells.

Unlike the Winkler elastic foundation model, the Winkler-Pasternak model incorporates the shear interaction between structures and foundations and has been widely used to examine the dynamic behaviour of FGM-truncated conical shells [45] to [47]. However, the model was used less to investigate the vibration of FG-GRC conical shells. Safarpour et al. [48] studied the free vibration of perfect and imperfect FG-GRC conical shells resting on Pasternak foundations. Their results show that the effect of the elastic foundation becomes more dominant as the foundation parameters increase. Eyvazian et al. [49] computed the natural frequencies and the corresponding mode shapes of FG-GRC conical panels and discussed the influences of boundary conditions, GPLs volume fraction, and foundation parameters. Furthermore, the frequency responses of rotating two-directional FG-GPLs conical shells on elastic foundations were presented by Amirabadi et al. [50]. They found that the increasing value of the GPL mass fraction can raise the natural frequency. The pattern of GPLs scattering near the inner surface has a higher effect on the frequency.

As reviewed above, the published literature on the free vibration of FG-GRC porous truncated conical shells remains limited. Most of the open literature focused on the case of the linear problem. The model used for evaluating the material properties of porous nanocomposites was based on the three assumptions about Young's elastic modulus, shear modulus, and mass density, which is too complicated. Hence, the present work attempts to solve these problems, that is, to propose an improved model for estimating the material properties and present the analytical solution for the nonlinear free vibration of FG-GRC porous truncated shells. Also, the effects of the internal pores, GPL, and elastic foundation on the linear and nonlinear frequencies are investigated.

1 A POROUS FG-GPLS TRUNCATED CONICAL SHELL

As shown in Fig. 1, a porous FG-GPLs truncated conical shell surrounded by Winkler-Pasternak elastic medium is considered. The curvilinear coordinate system (x, θ, z) is located on the middle surface of the shell. s_1 and s_2 are the distances from the vertex to the small and large ends, respectively. L, h and α denote the length, thickness, and semi-vertex of the shell.

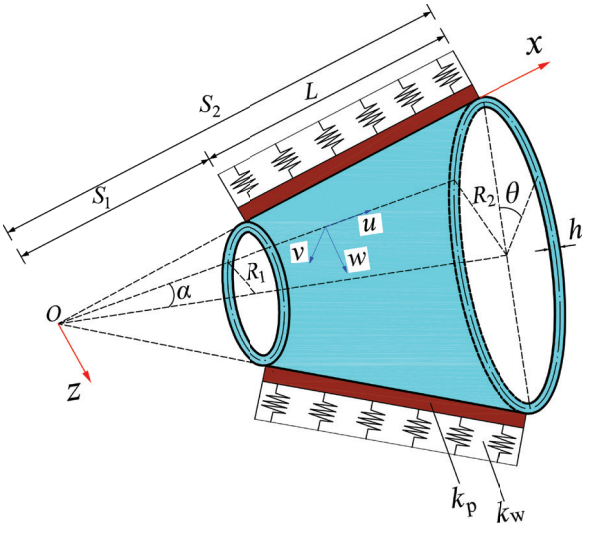

Fig. 1. *A FG-GPLs truncated conical shell surrounded by a Winkler-Pasternak elastic foundation*

Three types of porous distribution in the thickness direction, denoted by P-1, P-2, and P-3, are taken into account, as depicted in Fig. 2.

It is assumed all the internal pores are tiny and the total volume fraction of the pores is small. Unlike other models for evaluating the material properties [30] and [39], in which Young's modulus, shear modulus, and mass density need to be assumed, the present model is based on the following assumption about the volume fraction $V_P(z)$ of the internal pores:

$$V_P(z) = e_0 \cos\left(\frac{\pi z}{h}\right), \quad (\mathrm{P}-1)$$

$$V_P(z) = e_0 \cos\left(\frac{\pi z}{2h} + \frac{\pi}{4}\right), \quad (\mathrm{P}-2)$$

$$V_P(z) = e_0, \quad (\mathrm{P}-3) \qquad (1)$$

here, e_0 denotes the porosity coefficient. Young's elastic modulus $E(z)$ and mass density $\rho(z)$ for various porosity distributions can be expressed as [39].

$$E(z) = E_1\left(1 - V_P(z)\right),$$
$$\rho(z) = \rho_1\left(1 - \frac{e_m}{e_0}V_P(z)\right), \quad (2)$$

where E_1 and ρ_1 denote the maximum values of Young's modulus and mass density, and e_m is the mass coefficients. Furthermore, the coefficients e_0, e_m and the Poisson ratio $\mu(z)$ are calculated as follows [39]:

$$e_m = \frac{1.121e_0[1-\sqrt[2,3]{1-V_P(z)}]}{V_P(z)},$$
$$\mu(z) = 0.221p + \mu_1(0.342p^2 - 1.21p + 1.0),$$
$$p = 1.121(1-\sqrt[2,3]{1-V_P(z)}), \quad (3)$$

in which μ_1 is the Poisson ratio of the composite without pores, and p is the coefficient of the Poisson ratio.

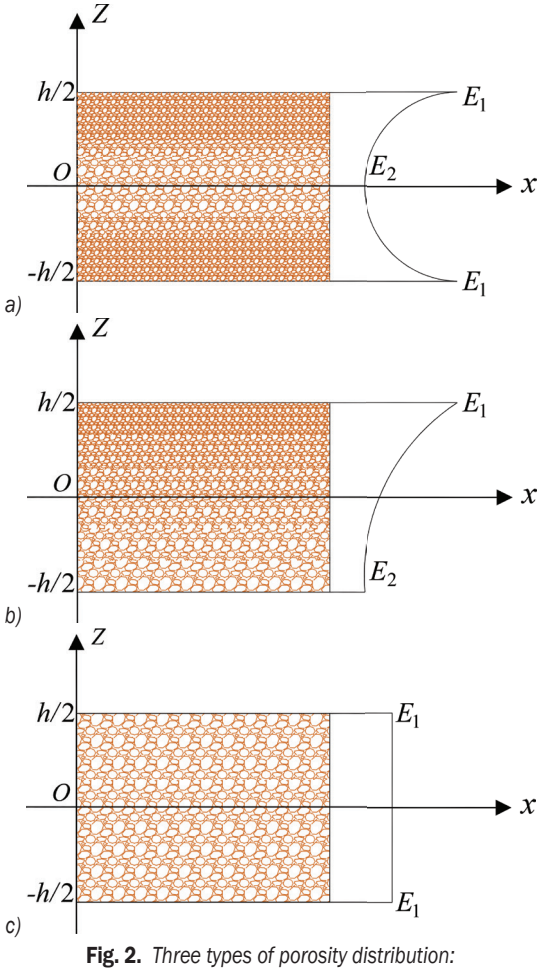

Fig. 2. *Three types of porosity distribution: a) symmetric distribution (P-1), b) asymmetric distribution (P-2), and c) even distribution (P-3)*

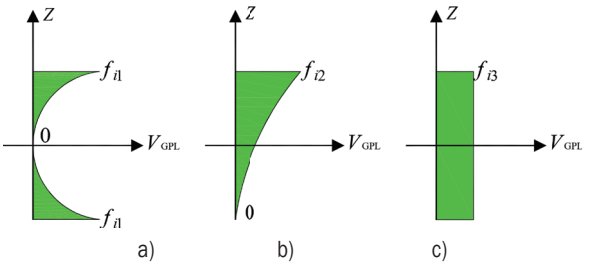

Fig. 3. *Three patterns of GPLs dispersion: a) symmetric distribution (G-1), b) asymmetric distribution (G-2), and c) even distribution (G-3)*

It is noted that the present model in Eqs. (1) to (3) can be used not only for FG-GRCs but also for other composites in which the foam metal is the matrix.

In the present study, three patterns of GPL dispersion, denoted by G-1, G-2, and G-3, are considered, as shown in Fig. 3. The volume fractions $V_{GPL}(z)$ for the three patterns are expressed as follows [43]:

$$V_{GPL}(z) = f_{i1}\left[1 - \cos\left(\frac{\pi z}{h}\right)\right], \quad (G-1)$$
$$V_{GPL}(z) = f_{i2}\left[1 - \cos\left(\frac{\pi z}{2h} + \frac{\pi}{4}\right)\right], \quad (G-2)$$
$$V_{GPL}(z) = f_{i3}, \quad (G-3) \quad (4)$$

where f_{i1}, f_{i2} and f_{i3} are the maximum values of various GPL distributions, calculated by [39]:

$$\frac{W_{GPL}}{W_{GPL} + (\rho_{GPL}/\rho_m)(1-W_{GPL})}\int_{-h/2}^{h/2}\left[1 - \frac{e_m}{e_0}V_P(z)\right]dz$$
$$= \int_{-h/2}^{h/2} V_{GPL}(z)\left[1 - \frac{e_m}{e_0}V_P(z)\right]dz. \quad (5)$$

In Eqs. (2) and (3), E_1, ρ_1, and μ_1 can be determined by using the Halpin-Tsai micromechanics model and the rule of the mixture as follows [39]:

$$E_1 = \frac{3}{8}\left(\frac{1+\xi_a\eta_a V_{GPL}}{1-\eta_a V_{GPL}}\right)E_m + \frac{3}{8}\left(\frac{1+\xi_b\eta_b V_{GPL}}{1-\eta_b V_{GPL}}\right)E_m, \quad (6)$$
$$\rho_1(z) = V_{GPL}(z)\rho_{GPL} + \left[1 - V_{GPL}(z)\right]\rho_m, \quad (7)$$
$$\mu_1(z) = V_{GPL}(z)\mu_{GPL} + \left[1 - V_{GPL}(z)\right]\mu_m, \quad (8)$$

in which the geometric parameters of GPL ξ_a , ξ_b, η_a and η_b can be stated as

$$\xi_a = \frac{2a_{GPL}}{h_{GPL}}, \qquad \xi_b = \frac{2b_{GPL}}{h_{GPL}},$$
$$\eta_a = \frac{E_{GPL}/E_m - 1}{E_{GPL}/E_m + \xi_a}, \quad \eta_b = \frac{E_{GPL}/E_m - 1}{E_{GPL}/E_m + \xi_b}, \quad (9)$$

here, E_{GPL}, ρ_{GPL} and μ_{GPL} denote the Young's modulus, mass density and Poisson ratio of GPL, and E_m, ρ_m and μ_m are the corresponding values of the matrix. a_{GPL}, b_{GPL} and h_{GPL} are the length, width, and thickness of the GPL.

2 FORMULATIONS

2.1 Governing Equations

It is assumed that the shell is thin and has a large deformation. According to the classic shell theory with the geometrical nonlinearity, the normal strains (ε_1, ε_2) and shear strain γ_{12} can be expressed as [51]

$$\varepsilon_1 = \varepsilon_1^0 + z\kappa_1, \quad \varepsilon_2 = \varepsilon_2^0 + z\kappa_2, \quad \gamma_{12} = \gamma_{12}^0 + 2z\kappa_{12}, \tag{10}$$

in which the strains $\left(\varepsilon_1^0, \varepsilon_2^0, \gamma_{12}^0\right)$, curvatures (κ_1, κ_2) and twist κ_{12} in the middle surface are defined by [51]

$$\begin{aligned}
\varepsilon_1^0 &= \frac{\partial u}{\partial x} + \frac{1}{2}\left(\frac{\partial u}{\partial x}\right)^2, \\
\varepsilon_2^0 &= \frac{1}{x\sin\alpha}\frac{\partial v}{\partial \theta} + \frac{u}{x} + \frac{w}{x}\cot\alpha + \frac{1}{2x^2\sin^2\alpha}\left(\frac{\partial w}{\partial \theta}\right)^2, \\
\gamma_{12}^0 &= \frac{1}{x\sin\alpha}\frac{\partial u}{\partial \theta} - \frac{v}{x} + \frac{v}{x}\cot\alpha + \frac{1}{x\sin\alpha}\frac{\partial w}{\partial x}\frac{\partial w}{\partial \theta}, \\
\kappa_1 &= -\frac{\partial^2 w}{\partial x^2}, \qquad \kappa_2 = -\frac{1}{x^2\sin^2\alpha}\frac{\partial^2 w}{\partial \theta^2} - \frac{1}{x}\frac{\partial w}{\partial x}, \\
\kappa_{12} &= -\frac{1}{x\sin\alpha}\frac{\partial^2 w}{\partial x \partial \theta} + \frac{1}{x^2}\frac{\partial w}{\partial \theta},
\end{aligned} \tag{11}$$

where u, v and w are the displacements along the directions of x, θ and z axes, respectively.

According to Hooke's law, the normal stresses σ_1 and σ_2, and the shear stress σ_{12} can be stated as [51]

$$\begin{pmatrix} \sigma_1 \\ \sigma_2 \\ \sigma_{12} \end{pmatrix} = \begin{bmatrix} Q_{11} & Q_{12} & 0 \\ Q_{12} & Q_{22} & 0 \\ 0 & 0 & Q_{66} \end{bmatrix} \begin{bmatrix} \varepsilon_1 \\ \varepsilon_2 \\ \gamma_{12} \end{bmatrix}. \tag{12}$$

Here, Q_{ij} $(i,j = 1,2,6)$ are the reduced stiffness coefficients, defined by [51]

$$\begin{aligned}
Q_{11} &= Q_{22} = \frac{E(z)}{1-\mu^2(z)}, \quad Q_{12} = \frac{\mu(z)E(z)}{1-\mu^2(z)}, \\
Q_{66} &= \frac{E(z)}{2\left(1+\mu(z)\right)}.
\end{aligned} \tag{13}$$

The membrane forces (N_1, N_2, N_{12}) and moments (M_1, M_2, M_{12}) are expressed as [55]

$$\begin{aligned}
&\left[\left(N_1, N_2, N_{12}\right), \left(M_1, M_2, M_{12}\right)\right] \\
&= \int_{-h/2}^{h/2} \left[1, z\right]\left(\sigma_1, \sigma_2, \sigma_{12}\right) dz.
\end{aligned} \tag{14}$$

Substituting Eq. (12) into (14), the following equations can be obtained [51]:

$$\begin{aligned}
N_1 &= A_{11}\varepsilon_1^0 + A_{12}\varepsilon_2^0 + B_{11}\kappa_1 + B_{12}\kappa_2, \\
N_2 &= A_{12}\varepsilon_1^0 + A_{22}\varepsilon_2^0 + B_{12}\kappa_1 + B_{22}\kappa_2, \\
N_{12} &= A_{66}\gamma_{12}^0 + 2B_{66}\kappa_{12}, \\
M_1 &= B_{11}\varepsilon_1^0 + B_{12}\varepsilon_2^0 + D_{11}\kappa_1 + D_{12}\kappa_2, \\
M_2 &= B_{12}\varepsilon_1^0 + B_{22}\varepsilon_2^0 + D_{12}\kappa_1 + D_{22}\kappa_2, \\
M_{12} &= B_{66}\gamma_{12}^0 + 2D_{66}\kappa_{12}.
\end{aligned} \tag{15}$$

The stiffness constants A_{ij}, B_{ij}, and D_{ij}, can be calculated by [51]

$$\left(A_{ij}, B_{ij}, D_{ij}\right) = \int_{-h/2}^{h/2} Q_{ij}\left(1, z, z^2\right) dz. \tag{16}$$

The interaction force between the Winkler-Pasternak medium and shell is assumed to be $F = k_w w - k_p \nabla^2 w$, in which k_w and k_p are the parameters of Winkler and Pasternak foundation, and ∇^2 is the Laplace operator. Using the Hamilton principle, the nonlinear dynamic Equilibrium equations of the conical shell surrounded by the Winkler-Pasternak medium can be derived as [51]:

$$\begin{aligned}
&x\frac{\partial N_1}{\partial x} + \frac{1}{\sin\alpha}\frac{\partial N_{12}}{\partial \theta} + N_1 - N_2 = \rho_t \frac{\partial^2 u}{\partial t^2}, \\
&\frac{1}{\sin\alpha}\frac{\partial N_2}{\partial \theta} + x\frac{\partial N_{12}}{\partial x} + 2N_{12} = \rho_t \frac{\partial^2 v}{\partial t^2}, \\
&x\frac{\partial^2 M_1}{\partial x^2} + 2\frac{\partial^2 M_1}{\partial x} + \frac{2}{\sin\alpha}\left(\frac{\partial^2 M_{12}}{\partial x \partial \theta} + \frac{1}{x}\frac{\partial M_{12}}{\partial \theta}\right) \\
&\quad + \frac{1}{x\sin^2\alpha}\frac{\partial^2 w}{\partial \theta^2} - \frac{\partial M_2}{\partial x} - N_2\cot\alpha \\
&\quad + \left(xN_1\frac{\partial w}{\partial x} + \frac{1}{\sin\alpha}N_{12}\frac{\partial w}{\partial \theta}\right)_{,x} \\
&\quad + \frac{1}{\sin\alpha}\left(xN_1\frac{\partial w}{\partial x} + \frac{1}{\sin\alpha}N_{12}\frac{\partial w}{\partial \theta}\right)_{,\theta} \\
&\quad - xk_w w - xk_p \nabla^2 w = x\rho_t \frac{\partial^2 w}{\partial t^2},
\end{aligned} \tag{17}$$

where the mass inertia is $\rho_t = \int_{-0.5h}^{0.5h} \rho(z) dz$.

Substituting Eqs. (11) and (15) into (17), the nonlinear vibrational equations of the shell can be derived as follows [51]:

$$L_{11}(u) + L_{12}(v) + L_{13}(w) + L_{14}(w) = \rho_t \frac{\partial^2 u}{\partial t^2}, \tag{18}$$

$$L_{21}(u) + L_{22}(v) + L_{23}(w) + L_{24}(w) = \rho_t \frac{\partial^2 v}{\partial t^2}, \tag{19}$$

$$L_{31}(u)+L_{32}(v)+L_{33}(w)+L_{34}(u,v,w)=x\rho_t\frac{\partial^2 w}{\partial t^2}, \quad (20)$$

where the linear operators L_{ij} $(i,j=1,2,3)$ have been given by Duc et al. [51]. The nonlinear operators L_{i4} $(i,j=1,2,3)$ are listed in Appendix. According to Volmir's assumption [26], the inertia forces $\rho_t\frac{\partial^2 u}{\partial t^2}$ and $\rho_t\frac{\partial^2 v}{\partial t^2}$ can be neglected.

2.2 The Solution of the Governing Equations

In this study, simply supported boundaries are considered. The boundary conditions are written as

$$v=w=0,\ N_1=0,\ M_1=M_{12}=0,\ \text{at } x=s_1,s_2. \quad (21)$$

In the present case, the asymmetric solution is taken into account. The solution satisfying the boundary conditions is assumed to be [51]

$$\begin{aligned} u&=u_{mn}(t)\cos\frac{m\pi(x-s_1)}{L}\sin\left(\frac{n\theta}{2}\right),\\ v&=v_{mn}(t)\sin\frac{m\pi(x-s_1)}{L}\cos\left(\frac{n\theta}{2}\right),\\ w&=w_{mn}(t)\sin\frac{m\pi(x-s_1)}{L}\sin\left(\frac{n\theta}{2}\right), \end{aligned} \quad (22)$$

where m and n are the numbers of half-waves along the generator and parallel circle, respectively.

In Eq. (22), if the terms of $\sin(n\theta/2)$ and $\cos(n\theta/2)$ are eliminated, the asymmetric solution is transformed into the corresponding symmetric solution.

For the sake of convenience in integration, multiplying Eqs. (18) and (19) by x and Eq. (20) by x^2, then applying the Galerkin method for the resulting equations, Eq. (18) to (20) can be developed as follows [51]:

$$\begin{aligned} &\int_{s_1}^{s_2}\int_0^{2\pi}\Delta_1\cos\frac{m\pi(x-s_1)}{L}\sin\frac{n\theta}{2}x\sin\alpha\,dxd\theta=0,\\ &\int_{s_1}^{s_2}\int_0^{2\pi}\Delta_2\sin\frac{m\pi(x-s_1)}{L}\cos\frac{n\theta}{2}x\sin\alpha\,dxd\theta=0,\\ &\int_{s_1}^{s_2}\int_0^{2\pi}\Delta_3\sin\frac{m\pi(x-s_1)}{L}\sin\frac{n\theta}{2}x\sin\alpha\,dxd\theta\\ &=\int_{s_1}^{s_2}\int_0^{2\pi}\rho_t\frac{\partial^2 w}{\partial t^2}\sin\frac{m\pi(x-s_1)}{L}\sin\frac{n\theta}{2}x^3\sin\alpha\,dxd\theta, \end{aligned} \quad (23)$$

in which

$$\begin{aligned} \Delta_1&=x\left[L_{11}(u)+L_{12}(v)+L_{13}(w)+L_{14}(w)\right],\\ \Delta_2&=x\left[L_{21}(u)+L_{22}(v)+L_{23}(w)+L_{24}(w)\right],\\ \Delta_3&=x^2\left[L_{31}(u)+L_{32}(v)+L_{33}(w)+L_{34}(w)\right]. \end{aligned} \quad (24)$$

Substituting Eqs. (22) and (24) into Eq. (23), the following ordinary differential equations can be derived:

$$a_1\frac{d^2 w_{mn}}{dt^2}+a_2 w_{mn}+a_3 w_{mn}^2+a_4 w_{mn}^3=0, \quad (25)$$

where a_i $(i,j=1,2,3,4)$ are integral coefficients.

According to Eq. (25), the linear frequency is obtained as $\omega_L=\sqrt{a_2/a_1}$, and the nonlinear frequency can be derived as [52]:

$$\omega_{NL}=\omega_L\sqrt{1+\frac{9a_4a_2-10a_3^2}{12a_2^2}A^2}. \quad (26)$$

Here, the dimensionless vibrational amplitude A is $w_{\max}/h$, in which $w_{\max}$ is the maximum dynamic deflection.

3 RESULTS AND DISCUSSION

3.1 Comparison Studies

In this subsection, two examples are given to validate the accuracy of the present method.

Example 1. In Fig. 4, the curves of the dimensionless linear frequency λ versus the porosity coefficient e_0 for a porous FG-GRC truncated conical shell are depicted. The material properties of the matrix are $E_m=130$ GPa, $\rho_m=8960$ kg/m³ and $\mu_m=0.34$. The pattern of GPL dispersion is G–1. The material and geometrical parameters are $E_{GPL}=1.01$ TPa, $\rho_{GPL}=1062.5$ kg/m³, $\mu_{GPL}=0.86$, $a_{GPL}=2.5$ μm, $b_{GPL}=1.5$ μm, and $h_{GPL}=1.5$ nm. The geometrical parameters of the shell are $R_2/h=200\cos\alpha$, $L=s_1$ and $\alpha=10°$. The dimensionless linear frequency is $\lambda=\omega[\rho_t h^2L^2/D_1]^{0.5}$. The figure reveals that the present results are in good agreement with those given by Bahaadini et al. [38]. It is noted the natural frequency decreases with the rising porous coefficient e_0. Although both the stiffness and mass density decline with the increase of the coefficient, the decreasing speeds are different. As the decreasing speed of the mass density is higher than that of stiffness, the natural frequency reduces. In the opposite case, the natural frequency increases.

Example 2. The fundamental linear and nonlinear frequencies for an isotropic truncated conical shell surrounded by a Winkler-Pasternak foundation are calculated and listed in Table 1. The geometrical parameters of the shell are $R_1/h=300$, $L=2R_1$, $\gamma=30°$. The vibrational amplitude is $A=3$. The dimensionless frequencies are $\Omega_L=\omega_L R_2\sqrt{(1-\mu^2)\rho/E}$, $\Omega_{NL}=\omega_{NL}R_2\sqrt{(1-\mu^2)\rho/E}$.

It is seen that the present results agree well with those given by Najafov and Sofiyev [53].

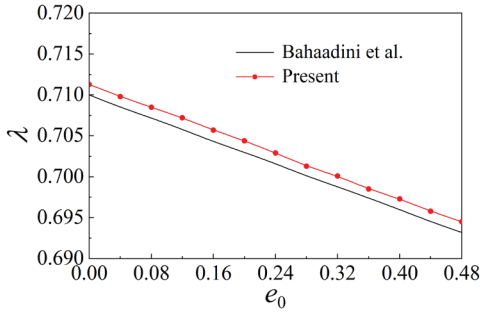

Fig. 4. *Comparison of the fundamental frequency for a porous FG truncated conical shell*

3.2 Parametric Studies

After the present method is validated, the effects of GPL, pore, and semi-vertex angle on the dimensionless linear and nonlinear frequencies for porous FG-GRC truncated conical shells surrounded by Winkler-Pasternak elastic foundations are investigated in this subsection. The material parameters of the GPL are the same as those given in Example 1. The material properties of the matrix are E_m=3.0 GPa, ρ_m=1200 kg/m³ and ν_m=0.34 and the geometrical parameters of the shell are R_1/h=100, $L=R_1$ and α=30°. The dimensionless linear frequency $\varpi_L=\omega_L R_2\sqrt{\rho_m/E_m}$. Unless specially stated, the type of the porosity distribution is P–1, and the pattern of GPL dispersion is G–1.

Table 1. *Dimensionless linear and nonlinear fundamental frequencies for an isotropic truncated conical shell rested on an elastic foundation*

k_w [N/m³]	k_p [N/m]	Ω_L		Ω_{NL}	
		Ref. [53]	Present	Ref. [53]	Present
10^5	0	0.101	0.102	0.119	0.120
	2.5×10^4	0.106	0.106	0.123	0.125
	5.0×10^4	0.110	0.111	0.126	0.128
	7.5×10^4	0.115	0.113	0.129	0.130
5.0×10^4	0	0.119	0.117	0.132	0.134
	2.5×10^4	0.123	0.123	0.138	0.140
	5.0×10^4	0.131	0.129	0.140	0.141
	7.5×10^4	0.134	0.131	0.143	0.145

The variation of the linear frequency ϖ_L with the generatrix half-wave number m and circumferential half-wave number n is shown in Fig. 5. As demonstrated by other literature [37] to [39], the number m has a different impact on the frequency with that of the genetrix number n. The frequency is raised with the rising value of m. If $n<13$, the frequency is monotonously decreased. However, if $n>13$, the frequency is increased. This is because the mass density declines more significantly than the stiffness when $n<13$. In contrast, the mass density declines more slowly than the stiffness when $n>13$. Hence, the fundamental frequency can be obtained when $m\approx1$, $n\approx13$. The following linear and nonlinear frequencies are calculated at the vibration mode (1,13).

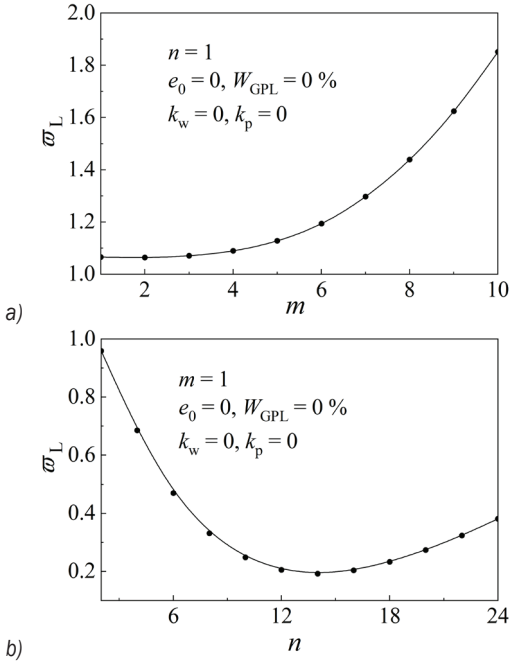

Fig. 5. *Variation of the linear frequency with a) the generatrix half-wave number m and b) the circumferential half-wave number n*

Tables 2 to 4 list the dimensionless linear frequencies ϖ_L of the shell with the different parameters of pores, GPL, and elastic foundations. Because the Winkler-Pasternak foundation can raise the effective stiffness of the conical shell, the frequency inclines with the increases of foundation parameters k_w and k_p. Furthermore, the effect of this is more significant than that of the parameter because it can enhance the effective stiffness more significantly k_w. The three tables show that the frequency increases with the increasing mass fraction of the GPLs, which is due to the fact that the elastic modulus of the GPL is higher than that of the matrix. Also, the tables reveal that the effect of the porosity coefficient e_0 is related to the parameters of the elastic foundation. If the values of k_w and k_p are not zero, the frequency reduces with the increasing value of the porosity coefficient e_0. In contrast, if the values of k_w and k_p are zero

Table 2. *Dimensionless linear frequencies ϖ_L for a porous FG-GRC conical shell distributed with G-1 GPLs and rested on an elastic foundation*

	k_w 10^6 [N/m³]	k_p 10^4 [N/m]	$e_0 = 0.0$	P-1		P-2		P-3	
				$e_0 = 0.2$	$e_0 = 0.4$	$e_0 = 0.2$	$e_0 = 0.4$	$e_0 = 0.2$	$e_0 = 0.4$
$W_{GPL} = 0.0$ %	0	0	0.192	0.188	0.184	0.185	0.178	0.196	0.192
		2.5	0.337	0.342	0.350	0.341	0.347	0.337	0.338
		5.0	0.436	0.446	0.460	0.445	0.457	0.436	0.437
	1.0	0	0.413	0.421	0.434	0.421	0.431	0.413	0.414
		2.5	0.497	0.510	0.526	0.509	0.524	0.497	0.499
		5.0	0.568	0.584	0.605	0.584	0.604	0.568	0.569
$W_{GPL} = 0.1$ %	0	0	0.231	0.226	0.221	0.223	0.213	0.231	0.230
		2.5	0.360	0.365	0.372	0.363	0.366	0.360	0.361
		5.0	0.454	0.463	0.476	0.462	0.472	0.454	0.455
	1.0	0	0.432	0.440	0.452	0.439	0.474	0.432	0.434
		2.5	0.513	0.525	0.541	0.524	0.537	0.513	0.515
		5.0	0.583	0.598	0.617	0.597	0.614	0.583	0.586
$W_{GPL} = 0.3$ %	0	0	0.294	0.289	0.283	0.284	0.271	0.294	0.293
		2.5	0.403	0.406	0.411	0.403	0.403	0.403	0.404
		5.0	0.489	0.497	0.508	0.494	0.501	0.489	0.490
	1.0	0	0.469	0.475	0.485	0.472	0.477	0.469	0.471
		2.5	0.544	0.555	0.569	0.552	0.563	0.544	0.546
		5.0	0.610	0.627	0.642	0.622	0.637	0.610	0.613

Table 3. *Dimensionless linear frequencies ϖ_L of a porous FG-GRC conical shell distributed with G-2 GPLs and rested on an elastic foundation*

	k_w 10^6 [N/m³]	k_p 10^4 [N/m]	$e_0 = 0.0$	P-1		P-2		P-3	
				$e_0 = 0.2$	$e_0 = 0.4$	$e_0 = 0.2$	$e_0 = 0.4$	$e_0 = 0.2$	$e_0 = 0.4$
$W_{GPL} = 0.1$ %	0	0	0.220	0.215	0.210	0.212	0.202	0.220	0.219
		2.5	0.353	0.358	0.364	0.356	0.360	0.353	0.354
		5.0	0.484	0.458	0.471	0.456	0.467	0.448	0.449
	1.0	0	0.426	0.434	0.446	0.433	0.442	0.426	0.426
		2.5	0.508	0.520	0.536	0.519	0.533	0.508	0.510
		5.0	0.578	0.594	0.613	0.592	0.611	0.578	0.579
$W_{GPL} = 0.3$ %	0	0	0.259	0.253	0.247	0.250	0.238	0.259	0.258
		2.5	0.379	0.382	0.387	0.380	0.382	0.379	0.380
		5.0	0.469	0.477	0.488	0.475	0.484	0.469	0.471
	1.0	0	0.480	0.455	0.465	0.453	0.460	0.448	0.449
		2.5	0.526	0.537	0.552	0.536	0.548	0.526	0.528
		5.0	0.595	0.609	0.627	0.607	0.624	0.595	0.597

Table 4. *Dimensionless linear frequencies ϖ_L of a porous FG-GPLs conical shell distributed with G-3 GPLs and rested on an elastic foundation*

	k_w 10^6 [N/m³]	k_p 10^4 [N/m]	$e_0 = 0.0$	P-1		P-2		P-3	
				$e_0 = 0.2$	$e_0 = 0.4$	$e_0 = 0.2$	$e_0 = 0.4$	$e_0 = 0.2$	$e_0 = 0.4$
$W_{GPL} = 0.1$ %	0	0	0.222	0.218	0.214	0.214	0.205	0.224	0.220
		2.5	0.369	0.374	0.382	0.372	0.377	0.368	0.370
		5.0	0.471	0.482	0.496	0.481	0.403	0.470	0.473
	1.0	0	0.427	0.436	0.448	0.434	0.444	0.426	0.429
		2.5	0.519	0.532	0.548	0.530	0.545	0.518	0.521
		5.0	0.569	0.612	0.633	0.611	0.630	0.595	0.599
$W_{GPL} = 0.3$ %	0	0	0.268	0.263	0.258	0.259	0.247	0.269	0.267
		2.5	0.398	0.402	0.409	0.399	0.402	0.397	0.399
		5.0	0.495	0.504	0.517	0.502	0.512	0.494	0.496
	1.0	0	0.453	0.460	0.471	0.458	0.465	0.452	0.454
		2.5	0.540	0.551	0.567	0.550	0.562	0.538	0.540
		5.0	0.615	0.630	0.650	0.628	0.645	0.613	0.616

(k_w=0, k_p=0), the frequency rises. Additionally, it can be observed that the effects of the pattern of GPL dispersion and the type of porosity distribution on the linear frequency can be neglected.

The influences of the type of GPL dispersion and mass fraction of the GPL on the ratio of nonlinear to linear frequency ϖ_{NL}/ϖ_L are shown in Fig. 6. Among the three patterns of GPL dispersion, the ratio for G–2 is slightly larger than those for G–3 and G–1. That is because the nonlinear frequency for G–2 increases faster than that for G–3 and G–1. Moreover, the mass fraction of the GPLs W_{GPL} rises with the increase of the ratio. For instance, when W_{GPL} changes from 0 % to 0.5 %, the ratio increases by about 9 % at A=5.

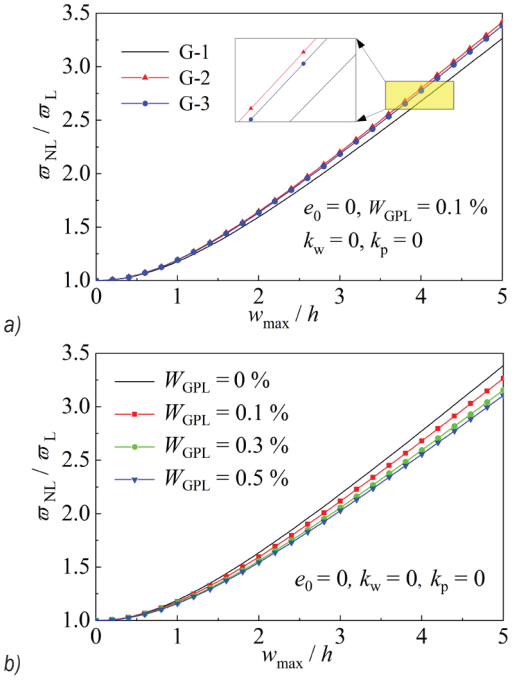

Fig. 6. *Influence of the GPLs on the frequency ratio; a) the pattern of GPL dispersion, and b) the mass fraction of the GPLs*

The influences of the porosity distribution and porosity coefficient on the frequency ratio ϖ_{NL}/ϖ_L are shown in Fig. 7. It is found that the porosity distribution has an insignificant effect on the ratio. When A = 5, the ratio for P–1 is only higher by 1.5 % than that for P–3. Also, it is found that the ratio can be raised by increasing the porosity coefficient.

Fig. 8 shows the effects of parameters k_w and k_p on the frequency ratio ϖ_{NL}/ϖ_L. It is seen that the effects are very significant. For example, when the parameter k_p changes from 0 kN/m to 75 kN/m, the ratio declines by 98.9 %.

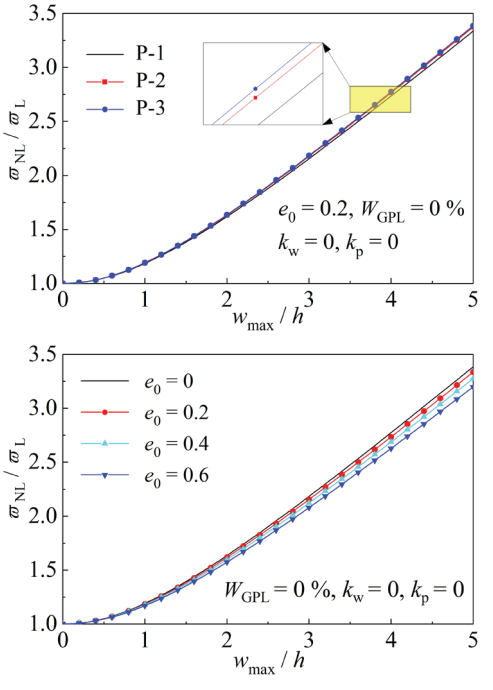

Fig. 7. *Influence of pores on the frequency ratio; a) porosity distribution, and b) porosity coefficient*

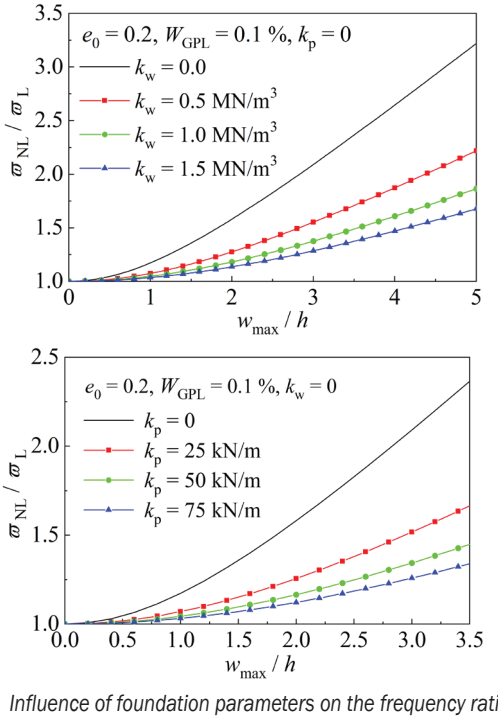

Fig. 8. *Influence of foundation parameters on the frequency ratio; a) Winkler parameter, and b) Pasternak parameter*

Finally, the effects of the semi-vertex angle α on the linear frequency ϖ_L and the ratio of linear to nonlinear frequency ϖ_{NL}/ϖ_L are shown in Fig. 9. It is shown that the linear frequency declines when the

semi-vertex angle increases. This is because the effective stiffness is raised with the increase of the semi-vertex angle. The figure also shows that the ratio reduces as the angle increases from 15º to 55º. In contrast, it is increased as the angle changes from 55º to 75º. Thus, the minimum value of frequency ratios can be obtained at $\alpha \approx 55º$.

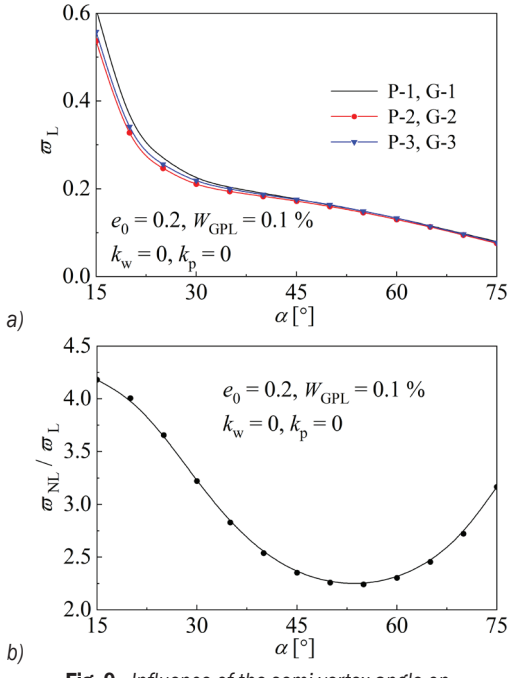

Fig. 9. *Influence of the semi-vertex angle on a) the linear frequency and b) the frequency ratio*

4 CONCLUSIONS

In this study, an improved method for evaluating the material properties of porous FG-GRCs was proposed. An analytical method to investigate the nonlinear vibration of composite such as FGM, FG-GRC, and FG-CNT porous truncated conical shells was presented. The effects of the pore, GPL, elastic foundation, and semi-vertex angle on the linear frequency and the ratio of nonlinear to linear frequency were discussed. Compared with other methods for investigating the nonlinear vibration behaviour of FG-GRC porous conical shells, the present method is simpler and briefer. However, it is not more accurate because the inertia forces $\rho_t \frac{\partial^2 u}{\partial t^2}$ and $\rho_t \frac{\partial^2 v}{\partial t^2}$ are neglected. Moreover, some interesting conclusions can be drawn from the parametric studies as follows:

1. As the values of the mass fraction of the GPLs is raised. In contrast, the frequency ratio reduces. Among the three patterns of GPLs dispersion, the frequency ratio for G-1 is the lowest, and that for G-2 is the highest.
2. The natural frequency is not monotonously varied with the rise of the porous coefficient e_0. If the mass density decreases faster than the stiffness, the natural frequency increases. In contrast, the natural frequency declines.
3. The frequency ratio can be decreased by increasing the porosity coefficient. However, the effect of porosity distribution on the frequency ratio might be negligible.
4. The linear frequency reduces if the semi-vertex angle increases. The minimum value of the frequency ratio can be obtained as the semi-vertex angle is approximately 55º.
5. Both the Winkler and Pasternak foundation parameters can significantly raise the natural frequency. However, they lower the ratio of nonlinear to linear frequency.

5 ACKNOWLEDGEMENTS

The authors thank for the financial support of the Natural Science Foundation of Guangxi [No.2021GXNSFAA220087] and the National Natural Science Foundation of China [No.12162010].

6 REFERENCES

[1] Lu, Z.Q., Yang, T.J., Brennan, M.J., Liu, Z.G., Chen, L.Q. (2017). Experimental investigation of a two-stage nonlinear vibration isolation system with high-static-low-dynamic stiffness. *Journal of Applied Mechanics*, vol. 84, no. 2, art. ID 021001, **DOI:10.1115/1.4034989**.

[2] Lu, Z.Q., Gu, D.H., Ding, H., Lacarbonara W., Chen, L.Q. (2020). Nonlinear vibration isolation via a circular ring. Mechanical Systems and Signal Processing, vol. 136, art. ID 106490, **DOI:10.1016/j.ymssp.2019.106490**.

[3] Hao, R.B., Lu, Z.Q., Ding, H., Chen, L.Q. (2022). A nonlinear vibration isolator supported on a flexible plate: analysis and experiment. *Nonlinear Dynamics*, vol. 108, p. 941-958, **DOI:10.1007/s11071-022-07243-7**.

[4] Wang, P.C., Wu, X.K., He, X.Z. (2023). Vibration-theoretic approach to vulnerability analysis of Nonlinear vehicle platoons. *IEEE Transactions on Intelligent Transportation Systems*, vol. 24, no. 10, p. 11334-11344, **DOI:10.1109/TITS.2023.3278574**.

[5] Zhou, C.H., Ren, Z.Y., Lin, Y.X., Huang, Z.H., Shi, L.W., Yang, Y., Mo, J.L. (2023). Hysteresis dynamic model of metal rubber based on higher-order nonlinear friction (HNF). *Mechanical Systems and Signal Processing*, vol. 189, art. ID 110117, **DOI:10.1016/j.ymssp.2023.110117**.

[6] Yang, Y., Kai, Y. (2023). Dynamical properties, modulation instability analysis and chaotic behaviors to the nonlinear

coupled Schrödinger equation in fiber Bragg gratings. *Modern Physics Letters B*, vol. 38, no. 6, art. ID 2350239, **DOI:10.1142/S0217984923502391**.

[7] Huang, X.L., Wang, C.Z., Wang, J.H., Wei, N.G. (2022). Nonlinear vibration analysis of functionally graded porous plates reinforced by graphene platelets on nonlinear elastic foundations. *Strojniški vestnik - Journal of Mechanical Engineering*, vol. 68, no. 9, p. 571-582, **DOI:10.5545/sv-jme.2022.274**.

[8] Chan, D.Q., Long, V.D., Duc, N.D. (2019). Nonlinear buckling and post-buckling of FGM shear-deformable truncated conical shells reinforced by FGM stiffeners. *Mechanics of Composite Materials*, vol. 54, p. 745-764, **DOI:10.1007/s11029-019-9780-x**.

[9] Chan, D.Q., Quan, T.Q., Kim, S.E., Duc, N.D. (2019). Nonlinear dynamic response and vibration of shear deformable piezoelectric functionally graded truncated conical panel in thermal environments. *European Journal of Mechanics / A Solids*, vol. 77, art. ID 103795, **DOI:10.1016/j.euromechsol.2019.103795**.

[10] Chan, D.Q., Anh, V.T.T., Duc, N.D. (2019). Vibration and nonlinear dynamic response of eccentrically stiffened functionally graded composite truncated conical shells surrounded by an elastic medium in thermal environments. *Acta Mechanics*, vol. 230, p. 157-178, **DOI:10.1007/s00707-018-2282-4**.

[11] Duc, N.D., Anh, V.T.T., Cong, P.H. (2014). Nonlinear axisymmetric response of FGM shallow spherical shells on elastic foundations under uniform external pressure and temperature. *European Journal of Mechanics A/Solids*, vol. 45, p. 80-89, **DOI:10.1016/j.euromechsol.2013.11.008**.

[12] Vuong, P.M., Duc, N.D. (2020). Nonlinear static and dynamic stability of functionally graded toroidal shell segments under axial compression. *Thin-Walled Structures*, vol. 155, art. ID 106973, **DOI:10.1016/j.tws.2020.106973**.

[13] Wang, Y.A., Sheng, Y.P., Jiang, P.C. (2019). Free vibration of graphene reinforced composite truncated conical shell. *International Journal of Mechanics Research*, vol. 8, p. 101-108, **DOI:10.12677/ijm.2019.82012**. (in Chinese)

[14] Afshari, H. (2022). Free vibration analysis of GNP-reinforced truncated conical shells with different boundary conditions. *Australian Journal of Mechanical Engineering*, vol. 20, no. 5, p. 1363-1378, **DOI:10.1080/14484846.2020.1797340**.

[15] Afshari, H. (2020). Effect of graphene nanoplatelet reinforcements on the dynamics of rotating truncated conical shells. *Journal of the Brazilian Society of Mechanical Sciences and Engineering*, vol. 42, art. ID 519, **DOI:10.1007/s40430-020-02599-6**.

[16] Damercheloo, R.A., Khorshidvand, R.A., Khorsandijou, M.S., Jabbari, M. (2021). Free vibrational characteristics of GNP-reinforced joined conical-conical shells with different boundary conditions. *Thin-Walled Structures*, vol. 169, art. ID 108287, **DOI:10.1016/j.tws.2021.108287**.

[17] Singha, D.T., Rout, M., Bandyopadhyay, T., Karmakar, A. (2021). Free vibration of rotating pretwisted FG-GRC sandwich conical shells in thermal environment using HSDT. *Composite Structures*, vol. 257, art. ID 113144, **DOI:10.1016/j.compstruct.2020.113144**.

[18] Adab, N., Arefi, M., Amabili, M. (2022). A comprehensive vibration analysis of rotating truncated sandwich conical microshells including porous core and GPL-reinforced face-sheets. *Composite Structures*, vol. 279, art. ID 114761, **DOI:10.1016/j.compstruct.2021.114761**.

[19] Adab, N., Arefi, M. (2023). Vibrational behavior of truncated conical porous GPL-reinforced sandwich micro/nano-shells. *Engineering with Computers*, vol. 39, p. 419-443, **DOI:10.1007/s00366-021-01580-8**.

[20] Yousefi, A.H., Memarzadeh, P., Afshari, H., Hosseini, J.S. (2020). Agglomeration effects on free vibration characteristics of three-phase CNT/polymer/fiber laminated truncated conical shells. *Thin-Walled Structures*, vol. 157, art. ID 107077, **DOI:10.1016/j.tws.2020.107077**.

[21] Yousefi, A.H., Memarzadeh, P., Afshari, H., Hosseini, J.S. (2023). Optimization of CNT/polymer/fiber laminated truncated conical panels for maximum fundamental frequency and minimum cost. *Mechanics Based Design of Structures and Machines*, vol. 51, no. 5, p. 3922-3944, **DOI:10.1080/15397734.2021.1945932**.

[22] Afshari, H., Amirabadi, H. (2022). Vibration characteristics of rotating truncated conical shells reinforced with agglomerated carbon nanotubes. *Journal of Vibration and Control*, vol. 28, no. 15-16, p. 1894-1914, **DOI:10.1177/10775463211000499**.

[23] Afshari, H., Ariaseresht, Y., Koloor, S.S.R., Amirabadi, H., Amirabadi, H., Bidgoli, M.O. (2022). Supersonic flutter behavior of a polymeric truncated conical shell reinforced with agglomerated CNTs. *Waves of Random Complex Media*, p. 1-25, **DOI:10.1080/17455030.2022.2082581**.

[24] Jamalabadi, M.Y.A., Borji, P., Habibi, M., Pelalak, R. (2021). Nonlinear vibration analysis of functionally graded GPL-GRC conical panels resting on elastic medium. *Thin-Walled Structures*, vol. 160, art. ID 107370, **DOI:10.1016/j.tws.2020.107370**.

[25] Ansari, R., Hassani, R., Hasrati, E., Rouhi, H. (2022). Studying nonlinear vibrations of composite conical panels with arbitrary-shaped cutout reinforced with graphene nanoplatelets based on higher-order shear deformation theory. *Journal of Vibration and Control*, vol. 28, no. 21-22, p. 3019-3041, **DOI:10.1177/10775463211024847**.

[26] Yang, S.W., Hao, Y.X., Zhang, W., Yang, L., Liu, L.T. (2021). Nonlinear vibration of functionally graded graphene platelet reinforced composite truncated conical shell using first-order shear deformation theory. *Applied Mathematics and Mechanics (English Edition)*, vol. 42, p. 981-998, **DOI:10.1007/s10483-021-2747-9**.

[27] Wang, A.W., Pang, Y.Q., Zhang, W., Jiang, P.C. (2019). Nonlinear dynamic analysis of functionally graded graphene reinforced composite truncated conical shells. *International Journal of Bifurcation and Chaos*, vol. 29, no. 11, p. 12244-12252, **DOI:10.1142/S0218127419501487**.

[28] Ding, H.X., She, G.L. (2023). Nonlinear primary resonance behavior of graphene platelet reinforced metal foams conical shells under axial motion. *Nonlinear Dynamics*, vol. 111, p. 13723-13752, **DOI:10.1007/s11071-023-08564-x**.

[29] Bidgoli, E.M.R., Arefi, M. (2023). Nonlinear vibration analysis of sandwich plates with honeycomb core and graphene nanoplatelet-reinforced face-sheets. *Archives of Civil and*

Mechanical Engineering, vol. 23, art. ID. 56, **DOI:10.1007/s43452-022-00589-0**.

[30] Wu, H.L., Yang, J., Kitipornchai, S. (2020). Mechanical analysis of functionally graded porous structures: A review. *International Journal of Structural Stability and Dynamics*, vol. 20, no. 13, art. ID 2041015, **DOI:10.1142/S0219455420410151**.

[31] Li, H., Hao, Y.X., Zhang, W., Liu, L.T., Yang, S.W., Wang, D.M. (2021). Vibration analysis of porous metal foam truncated conical shells with general boundary conditions using GDQ. *Composite Structures*, vol. 269, art. ID 114036, **DOI:10.1016/j.compstruct.2021.114036**.

[32] Amirabadi, H., Afshari, H., Afjaei, M.A., Sarafeaz, M. (2022). Effect of variable thickness on the aeroelastic stability boundaries of truncated conical shells. *Waves of Random Complex Media*, **DOI:10.1080/17455030.2022.2157517**.

[33] Mohammadrezazadeh, S., Jafari, A.A. (2022). The study of the nonlinear vibration of S-S and C-C laminated composite conical shells on elastic foundations through an approximate method. *Proceedings of the Institution of Mechanical Engineers, Part C: Journal of Mechanical Engineering Science*, vol. 236, no. 3, p. 1377-1390, **DOI:10.1177/09544062211021439**.

[34] Hao, X.Y., Li, H., Zhang, W., Ge, X.S., Yang, W.S., Cao, Y.T. (2022). Active vibration control of smart porous conical shell with elastic boundary under impact loadings using GDQM and IQM. *Thin-Walled Structures*, vol. 175, art. ID 109232, **DOI:10.1016/j.tws.2022.109232**.

[35] Chan, D.Q., Thanh, N.T., Khoa, N.K., Duc, N.D. (2020). Nonlinear dynamic analysis of piezoelectric functionally graded porous truncated conical panel in thermal environments. *Thin-Walled Structures*, vol. 154, art. ID 106837, **DOI:10.1016/j.tws.2020.106837**.

[36] Huang, X.L., Wang, J.H. Wei, N.G., Wang, C.Z., Bin, M. (2023). Buckling and vibration of porous sigmoid functionally graded conical shells. *Journal of Theoretical and Applied Mechanics*, vol. 61, p. 559-570, **DOI:10.15632/jtam-pl/168072**.

[37] Kiarasi, F., Babaei, B., Sarvi, P., Asemi, K., Hosseini, M., Bidgol, M.O. (2021). A review on functionally graded porous structures reinforced by graphene platelets. *Journal of Computational Applied Mechanics*, vol. 52, no. 4, p. 731-750, **DOI:10.22059/jcamech.2021.335739.675.**

[38] Bahhadini, R., Saidi, A.R., Arabjamaloei, Z., Chanbari-Nejad-Parizi, A. (2019). Vibration analysis of functionally graded graphene reinforced porous nanocomposite shells. *International Journal of Applied Mechanics*, vol. 11, no. 7, art. ID 1950068, **DOI:10.1142/S1758825119500686**.

[39] Yan, K., Zhang, Y., Cai, H., Tahouneh, V. (2020). Vibrational characteristic of FG porous conical shells using Donnell's shell theory. *Steel and Composite Structures*, vol. 35, no. 2, p. 249-260, **DOI:10.12989/scs.2020.35.2.249**.

[40] Rahmani, M., Mohammadi, Y., Kakavand, F. (2019). Vibration analysis of sandwich truncated conical shells with porous FG face sheets in various thermal surroundings. *Steel and Composite Structures*, vol. 32, no. 2, p. 239-252, **DOI:10.12989/scs.2019.32.2.239**.

[41] Esfahani, M.N., Hashemian, M., Aghadavoudi, F. (2022). The vibration study of a sandwich conical shell with a saturated FGP core. *Scientific Reports*, vol. 12, art. ID 4950, **DOI:10.1038/S41598-022-09043-W**.

[42] Cuong-Le T., Nguyen, K.D., Nguyen-Trong, N., Khatir, S., Nguyen-Xuan, H., Abdel-Wahab, M. (2021). A three-dimensional solution for free vibration and buckling of annular plate, conical, cylinder and cylindrical shell of FG porous-cellular materials using IGA. *Composite Structures*, vol. 259, art. ID 113216, **DOI:10.1016/j.compstruct.2020.113216**.

[43] Sobhani, E., Arbabian, A., Civalek, Ö., Avcar, M. (2022). The free vibration analysis of hybrid porous nanocomposite joined hemispherical-cylindrical-conical shells. *Engineering with Computers*, vol. 38, p. 3125-3152, **DOI:10.1007/s00366-021-01453-0**.

[44] Kiarasi, F., Babaei, M., Mollaei, S., Mohammadi, M., Asemi, K. (2021). Free vibration analysis of porous FG joined truncated conical-cylindrical shell reinforced by graphene nanoplatelets. *Advances in Nano Research*, vol. 11, no. 4, p. 361-380, **DOI:10.12989/anr.2021.11.4.361**.

[45] Sofieyev, A.H., Kuruoglu, N. (2011). Natural frequency of laminated orthotropic shells with different boundary conditions and resting on the Pasternak type elastic foundation. *Composites Part B: Engineering*, vol. 42, no. 6, p. 1562-1570, **DOI:10.1016/j.compositesb.2011.04.015**.

[46] Fu, T., Wu, X., Xiao, Z.M., Chen, A.B., Li, B. (2021). Analysis of vibration characteristics of FGM sandwich joined conical-conical shells surrounded by elastic foundations. *Thin-Walled Structures*, vol. 165, art. ID 107979, **DOI:10.1016/j.tws.2021.107979**.

[47] Deniz, A., Zerin, Z., Karaca, Z. (2016). Winkler-Pasternak foundation effect on the frequency parameter of FGM truncated conical shells in the framework of shear deformation theory. *Composites Part B: Engineering*, vol. 104, p. 57-70, **DOI:10.1016/j.compositesb.2016.08.006**.

[48] Safarpour, M., Rahimi, A.R., Alibeigloo, A. (2020). Static and free vibration analysis of graphene nanoplatelets reinforced composite truncated conical shell, cylindrical shell, and annular plate using theory of elasticity and DQM. *Mechanics Based Design of Structures and Machines*, vol. 48, no. 4, p. 496-524, **DOI:10.1080/15397734.2019.1646137**.

[49] Eyvazian, A., Musharavati, F., Tarlochan, F., Pasharavesh, A., Rajak, D.K., Husain, M.B., Tran, T.N. (2020). Free vibration of FG-GPLRC conical panel on elastic foundation. *Structural Engineering and Mechanics*, vol. 75, no. 1, p. 1-18, **DOI:10.12989/sem.2020.75.1.001**.

[50] Amirabadi, H., Farhatnia, F., Civalek, O. (2021). Frequency response of rotating two-directional functionally graded GPL-reinforced conical shells on elastic foundation. *Journal of the Brazilian Society of Mechanical Sciences and Engineering*, vol. 43, art. ID 349, **DOI:10.1007/s40430-021-03058-6**.

[51] Duc, N.D., Cong, P.H., Tuan, N.D., Tran, P., Thanh, N.V. (2017). Thermal and mechanical stability of functionally graded carbon nanotubes (FG CNT)-reinforced composite truncated conical shells surrounded by the elastic foundations. *Thin-Walled Structures*, vol. 115, p. 300-310, **DOI:10.1016/j.tws.2017.02.016**.

[52] Huang, X.L., Shen, H.S. (2004). Nonlinear vibration and dynamic response of functionally graded plates in thermal environments. *International Journal of Solids and Structures*, vol. 41, no. 9-10, p. 2403-2427, **DOI:10.1016/j.ijsolstr.2003.11.012**.

[53] Najafov, A.M., Sofiyev, A.H. (2013). The non-linear dynamics of FGM truncated conical shells surrounded by an elastic medium. *International Journal of Mechanical Sciences*, vol. 66, p. 33-44, **DOI:10.1016/j.ijmecsci.2012.10.006.**

7 APPENDIX

$$L_{14}(w)=A_{11}x\frac{\partial w}{\partial x}\frac{\partial^2 w}{\partial x^2}-\frac{A_{12}+A_{22}}{2x^2\sin^2\alpha}\left(\frac{\partial w}{\partial\theta}\right)^2+\frac{A_{12}+A_{66}}{x\sin^2\alpha}\frac{\partial w}{\partial\theta}\frac{\partial^2 w}{\partial x\partial\theta}+A_{66}\frac{1}{x\sin^2\alpha}\frac{\partial w}{\partial x}\frac{\partial^2 w}{\partial\theta^2}+\frac{1}{2}\left(A_{11}-A_{22}\right)\left(\frac{\partial w}{\partial x}\right)^2,$$

$$L_{24}(w)=\left(A_{12}+A_{66}\right)\frac{1}{\sin\alpha}\frac{\partial w}{\partial x}\frac{\partial^2 w}{\partial x\partial\theta}+A_{22}\frac{1}{x^2\sin^3\alpha}\frac{\partial w}{\partial\theta}\frac{\partial^2 w}{\partial\theta^2}+A_{66}\frac{1}{x\sin\alpha}\frac{\partial w}{\partial x}\frac{\partial w}{\partial\theta}+A_{66}\frac{1}{\sin\alpha}\frac{\partial^2 w}{\partial x^2}\frac{\partial w}{\partial\theta},$$

$$\begin{aligned}L_{34}(u,v,w)=&\left(B_{11}-3B_{12}\right)\frac{\partial w}{\partial x}\frac{\partial^2 w}{\partial x^2}+\left(B_{12}-B_{22}+2B_{66}\right)\frac{1}{x^2\sin^2\alpha}\frac{\partial w}{\partial x}\frac{\partial^2 w}{\partial\theta^2}+\left(A_{12}-\frac{1}{2}A_{22}\right)\cot\alpha\left(\frac{\partial w}{\partial x}\right)^2+A_{12}\cot\alpha\, w\frac{\partial^2 w}{\partial x^2}\\&+2\left(B_{66}-B_{12}\right)\frac{1}{x\sin^2\alpha}\frac{\partial^2 w}{\partial x^2}\frac{\partial^2 w}{\partial\theta^2}+2\left(4B_{66}-B_{12}\right)\frac{1}{x^2\sin^2\alpha}\frac{\partial w}{\partial\theta}\frac{\partial^2 w}{\partial x\partial\theta}+B_{12}\frac{1}{x\sin^2\alpha}\frac{\partial w}{\partial\theta}\frac{\partial^3 w}{\partial x^2\partial\theta}\\&+\left(B_{12}+B_{22}-4B_{66}-\frac{1}{2}A_{22}x\cot\alpha\right)\frac{1}{x^3\sin^2\alpha}\left(\frac{\partial w}{\partial\theta}\right)^2+A_{22}\cot\alpha\frac{1}{x^2\sin^2\alpha}w\frac{\partial^2 w}{\partial\theta^2}+B_{22}\frac{1}{x^3\sin^4\alpha}\frac{\partial w}{\partial\theta}\frac{\partial^3 w}{\partial\theta^3}\\&-2B_{66}\frac{1}{x^2\sin^3\alpha}\frac{\partial w}{\partial\theta}\frac{\partial^3 w}{\partial x\partial\theta^2}-A_{12}\frac{1}{x^2\sin^2\alpha}\frac{\partial w}{\partial x}\left(\frac{\partial w}{\partial\theta}\right)^2+A_{12}\frac{1}{x\sin^2\alpha}\frac{\partial w}{\partial x}\frac{\partial w}{\partial\theta}\frac{\partial^2 w}{\partial x\partial\theta}+\frac{1}{2}A_{11}x\frac{\partial^2 w}{\partial x^2}\left(\frac{\partial w}{\partial x}\right)^2\\&+\frac{1}{2}A_{12}\frac{1}{x\sin^2\alpha}\frac{\partial^2 w}{\partial x^2}\left(\frac{\partial w}{\partial\theta}\right)^2-A_{66}\frac{1}{x^2\sin^2\alpha}\frac{\partial w}{\partial x}\left(\frac{\partial w}{\partial\theta}\right)^2+A_{66}\frac{1}{x\sin^2\alpha}\frac{\partial^2 w}{\partial x^2}\left(\frac{\partial w}{\partial\theta}\right)^2+4A_{66}\frac{1}{x\sin^2\alpha}\frac{\partial w}{\partial\theta}\frac{\partial w}{\partial x}\frac{\partial^2 w}{\partial x\partial\theta}\\&+A_{66}\frac{1}{x\sin^2\alpha}\frac{\partial^2 w}{\partial\theta^2}\left(\frac{\partial w}{\partial x}\right)^2+A_{66}\frac{1}{x^2\sin^3\alpha}\frac{\partial^2 w}{\partial x\partial\theta}\left(\frac{\partial w}{\partial\theta}\right)^2+A_{66}\frac{1}{x\sin^3\alpha}\frac{\partial w}{\partial x}\frac{\partial w}{\partial\theta}\frac{\partial^2 w}{\partial\theta^2}+\frac{1}{2}A_{12}\frac{1}{x\sin^2\alpha}\frac{\partial^2 w}{\partial\theta^2}\left(\frac{\partial w}{\partial x}\right)^2\\&+\frac{1}{2}A_{22}\frac{1}{x^3\sin^4\alpha}\frac{\partial^2 w}{\partial\theta^2}\left(\frac{\partial w}{\partial\theta}\right)^2+A_{11}\frac{\partial w}{\partial x}\frac{\partial u}{\partial x}+A_{11}x\frac{\partial w}{\partial x}\frac{\partial^2 u}{\partial x^2}+A_{12}\frac{1}{\sin\alpha}\frac{\partial w}{\partial x}\frac{\partial^2 v}{\partial x\partial\theta}+A_{12}\frac{\partial w}{\partial x}\frac{\partial u}{\partial x}+A_{11}x\frac{\partial^2 w}{\partial x^2}\frac{\partial u}{\partial x}\\&+A_{12}\frac{1}{\sin\alpha}\frac{\partial^2 w}{\partial x^2}\frac{\partial v}{\partial\theta}+A_{12}u\frac{\partial^2 w}{\partial x^2}-A_{66}\frac{1}{\sin\alpha}\frac{\partial w}{\partial\theta}\frac{\partial u}{\partial\theta}+A_{66}\frac{1}{x\sin^2\alpha}\frac{\partial w}{\partial\theta}\frac{\partial^2 u}{\partial x\partial\theta}+A_{66}\frac{1}{x^2\sin\alpha}\frac{\partial w}{\partial\theta}v-A_{66}\frac{1}{x\sin\alpha}\frac{\partial w}{\partial\theta}\frac{\partial v}{\partial x}\\&+A_{66}\frac{1}{\sin\alpha}\frac{\partial w}{\partial\theta}\frac{\partial^2 v}{\partial x^2}+A_{66}\frac{1}{x\sin^2\alpha}\frac{\partial^2 w}{\partial x\partial\theta}\frac{\partial u}{\partial\theta}-A_{66}\frac{1}{x\sin\alpha}v\frac{\partial^2 w}{\partial x\partial\theta}+A_{66}\frac{1}{\sin\alpha}\frac{\partial^2 w}{\partial x\partial\theta}\frac{\partial v}{\partial x}+A_{66}\frac{1}{x\sin^2\alpha}\frac{\partial w}{\partial x}\frac{\partial^2 u}{\partial\theta^2}\\&-A_{66}\frac{1}{x\sin\alpha}\frac{\partial w}{\partial x}\frac{\partial v}{\partial\theta}+A_{66}\frac{1}{\sin\alpha}\frac{\partial w}{\partial x}\frac{\partial^2 v}{\partial x\partial\theta}+A_{66}\frac{1}{x\sin^2\alpha}\frac{\partial^2 w}{\partial x\partial\theta}\frac{\partial u}{\partial\theta}-A_{66}\frac{1}{x\sin\alpha}\frac{\partial^2 w}{\partial x\partial\theta}v+A_{66}\frac{1}{\sin\alpha}\frac{\partial^2 w}{\partial x\partial\theta}\frac{\partial v}{\partial x}\\&+A_{66}\frac{1}{x^2\sin^3\alpha}\frac{\partial w}{\partial\theta}\frac{\partial^2 u}{\partial\theta^2}-A_{66}\frac{1}{x^2\sin^2\alpha}\frac{\partial w}{\partial\theta}\frac{\partial v}{\partial\theta}+A_{66}\frac{1}{x\sin^2\alpha}\frac{\partial^2 v}{\partial x\partial\theta}\frac{\partial w}{\partial\theta}+A_{12}\frac{1}{x\sin^2\alpha}\frac{\partial^2 w}{\partial\theta^2}\frac{\partial u}{\partial x}\\&+A_{22}\frac{1}{x^2\sin^3\alpha}\frac{\partial^2 w}{\partial\theta^2}\frac{\partial v}{\partial\theta}+A_{22}\frac{1}{x^2\sin^2\alpha}\frac{\partial^2 w}{\partial\theta^2}u.\end{aligned}$$

Strojniški vestnik - Journal of Mechanical Engineering 70(2024)3-4, 194-208
DOI:10.5545/sv-jme.2023.768
Original Scientific Paper
Received for review: 2023-08-21
Received revised form: 2023-12-04
Accepted for publication: 2024-01-25

Design Optimization of Mechanical Valves in Dishwashers Based on the Minimization of Pressure Losses

Furkan Kılavuz[1,2] – Binnur Gören Kıral[3,*]

[1] Dokuz Eylul University, The Graduate School of Natural and Applied Sciences, Turkey
[2] Arçelik A.Ş., Turkey
[3] Dokuz Eylul University, Department of Mechanical Engineering, Turkey

Energy savings, albeit very small, are of great importance for devices whose use has become indispensable. In this study, an optimization based on sustainability and energy saving was aimed at designing the valve used in a white goods company's mass production of dishwashers. One significant factor that affects the overall efficiency of a dishwasher is pressure loss within the mechanical valve system. By optimizing the system, it is possible to minimize pressure loss and increase overall efficiency. To this end, 4th-order Bézier curves, which are used to model the blades of the impeller, were obtained using MATLAB R2023a software. Using Bézier curves, solid models of impellers with different blade profiles and numbers were created with SOLIDWORKS 2021 software. Fifty different models with six different blade numbers and five different materials were considered. In the numerical analyses, pressure losses were determined using ANSYS Fluent 2023R2 software. In addition to numerical analysis, blades were produced using the additive manufacturing method, and outlet pressures were measured experimentally. The experimental results were compared with the computational fluid dynamics analysis findings to evaluate the performance of different impeller designs. To determine the optimal design, the design of experiments and response optimizer approaches are applied, which enables the systematic evaluation of different design parameters. Furthermore, using numerical results, an artificial neural network model was created, and efficiency was predicted for the optimum parameters. Experimental and numerical results show that the optimum blade design enables the least pressure loss.

Keywords: dishwasher, energy-saving, impeller blade design optimization, statistical analysis, artificial neural network

Highlights

- *The experimental setup for a bottom-up investigation of effect of impeller design in dishwasher was built.*
- *Design optimization of the mechanical valve impeller in dishwashers was made using Bezier curves.*
- *Both experimental setup and computational fluid dynamics analysis were performed to validate the design optimization.*
- *This paper studies the effect of parameters such as minimum pressure loss, maximum outlet pressure, and maximum efficiency for mechanical valve impellers used in dishwashers.*
- *The results of ANOVA, DOE, and regression analysis show that blade angles and the number of blades have significantly affect on the impeller design in the mechanical valve system.*

0 INTRODUCTION

Dishwashers have become indispensable appliances in modern households, providing convenience and efficiency in the cleaning of dishes and utensils. The effectiveness of a dishwasher relies on various components, and the mechanical valve is a critical element responsible for directing and controlling the flow of water during the washing process. Pressure loss is the reduction in pressure experienced by water as it flows through the valve. Excessive pressure loss can result in decreased water flow rates, increased energy consumption, and compromised cleaning effectiveness. The design of the mechanical valve plays a crucial role in determining the pressure loss within the dishwasher system. By optimizing the design parameters, such as the number of blades and materials used in the gear mechanism, it is possible to minimize pressure loss and improve the overall efficiency of the dishwasher. This study aims to investigate the impact of the mechanical valve design on pressure loss within dishwasher systems. The focus will be on modifying the number of blades and exploring different materials for the gear within the mechanical valve. By systematically varying these design parameters, the goal of the study is to determine the optimal configuration that minimizes pressure loss and maximizes water flow efficiency.

Although there is no study in the literature on the optimization of the blade design of the mechanical valve of dishwashers, some studies on the optimization of the blades and air foil have been done. Lu et al. [1] carried out the two multi-objective optimization designs of the rotor blade for an axial transonic compressor. Rengma et al. [2] developed a new method for creating wing shapes using a Bezier curve with six control points. Zhong et al. [3] proposed a unified formulation for the material optimization

*Corr. Author's Address: Dokuz Eylul University, Department of Mechanical Engineering, Izmir, Turkey, binnur.goren@deu.edu.tr

and modelling of rotating in-plane functionally graded (IFG) thin-shell blades with variable thickness. Tang et al. [4] investigated a multivariate optimization design approach for the rotorcraft wing structure using computational fluid dynamics, neural networks, and evolutionary algorithms to improve the Mars rover's driving path. Using a supervised learning model approach, Luo et al. [5] investigated the aerodynamic design optimization of a transonic fan rotor by blade sweeping. Lu et al. [6] optimized the geometry of S-shaped blades used in Savonius turbines using genetic algorithms (GA) and numerical simulation of computational fluid dynamics (CFD). Fazil and Jayakumar [7] focused on leveraging the camber profile's control point to create an air foil profile using CATIA software. Fincham and Friswell [8] created an optimization technique for morphing aerofoils that took into consideration a known potential morphing system while still maintaining the aerodynamic optimization process. For wind turbine applications, Hansen [9] created and evaluated an air foil optimization technique that reduces performance loss from leading-edge contamination. To provide greater lift than the original air foil shape produces, Jeong and Kim [10] researched the optimization of the air foil shape.

Among the most relevant studies to the present study, Salimi et al. [11] emphasized the optimization of a regenerative pump with an S- shaped impeller using response surface methodology. They aimed to design and optimized a new S-shaped impeller. In their study, the design of experiments (DOE), the response surface methodology, and the box Behnken design (BBD) were utilized for optimization. Satjaritanun et al. [12] have researched that a pitched-blade, contra-rotating impeller, baffle-free tank with opposing inward flow is optimized using various designs of mixers derived from the Taguchi method. Mixing efficiency and torque were used to find the optimal design for the different specific gravities of solid particles employed in both experiments and CFD simulations. Mohammed et al. [13] have optimized the rotary blades for a wind-powered water pumping system. They investigated the blade parameters such as chord distribution length, angle of twist, tip speed ratio, power coefficient of the blade and attack angle.

The scope of this study is to find the optimal impeller design that minimizes outlet pressure drop while maximizing performance. This study employs a multifaceted approach to determine the optimal impeller design for mechanical valves in dishwashers. The combination of experimental testing, computational fluid dynamic (CFD) analysis, statistical analysis, and artificial neural network for a comprehensive assessment of the impeller performance and to identify the most effective design was used. By optimizing the number of blades and exploring different materials for the impeller, the study seeks to minimize the pressure loss and improve the water flow efficiency. The findings will contribute to the development of more efficient and environmentally friendly dishwasher designs, ultimately enhancing the overall performance and user experience of these essential household appliances. The findings of this study will provide valuable insights into the optimization of mechanical valve design for dishwashers. By minimizing pressure loss, manufacturers can enhance the performance and energy efficiency of dishwasher systems, contributing to sustainable water and energy consumption. Additionally, a better understanding of the fluid dynamics within the mechanical valve system can have wider implications for other applications involving flow control mechanisms.

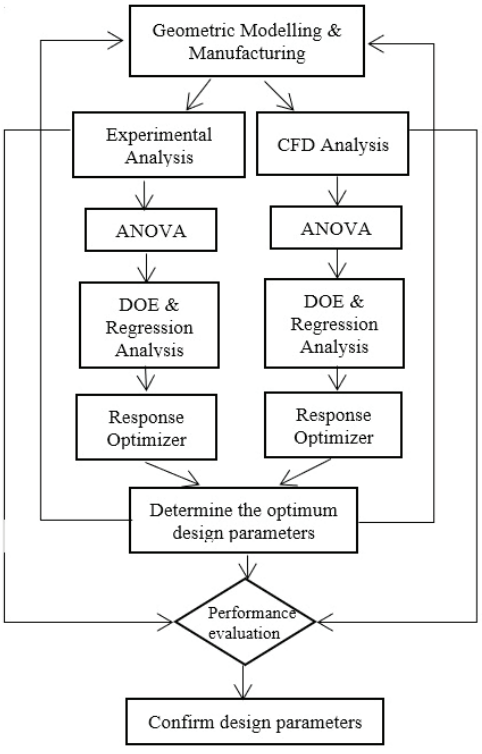

Fig. 1. *Optimization procedure of the impeller*

1 MATERIALS AND METHODOLOGY

This research focuses on determining the optimal impeller design for the mechanical valve in

dishwashers using a comprehensive approach that integrates experimental testing, CFD analysis, statistical analysis, and artificial neural network analysis. In this study, the design of the impeller is based on Bézier curves, which are utilized to generate the blade profiles. 3D solid models of these designs are then created, printed with three-dimensional (3D) printers and tested in a special experimental setup. Fig. 1 shows a flowchart of the optimization studies carried out to determine the design parameters of the impeller to minimize pressure losses.

1.1 Creation of Blade Profiles Using Bézier Curve with MATLAB

The aim of this study is to design the surface of the blade profile of a centrifugal impeller, which provides a high performance to the impeller. Parametric examination studies have started to be carried out using Beziér curves used in the modelling of blade profiles. The Bézier's technique is one of the most prominent in computer-aided geometric design. The fundamental aim is to determine curves that approach the given points rather than passing through them like a specific spline. Bézier curves have a useful convex formation that restricts the curve to never leave the bounding polygon of the control points. A Bézier curve of order n is defined by the Bernstein polynomials $B_{n,i}$:

$$P(u)=\sum_{i=0}^{n}B_{n,i}(u)P_i, \tag{1}$$

where the Bézier coefficients, are determined as follows:

$$B_{n,i}(u)=\frac{n!}{i!(n-i)!}u^i(1-u)^{n-i}, \tag{2}$$

and the point that corresponds to u on the Bézier curve is the "weighted" average of all control points, where the weights are the coefficients, $B_{n,i}$. The line segments, P_0P_1, P_1P_2, …, $P_{n\text{-}1}$, P_n are called "control segments" [14] to [16]. A code was developed to obtain the control points using MATLAB R2023a software [17]. The blade profile was generated using 251 points obtained using MATLAB software; then a 3D solid model of the blade was created using SOLIDWORKS 2021 software [18].

The curvature of the blade profile to be optimized has been determined by a 4th degree of Bézier curve. The basic dimensions of the impeller are defined as the inner diameter is 5.53 mm and the outer diameter is 22 mm as given in Fig. 2. Fig. 3 shows the fundamental parameters, which are the control points and installation angles to draw the blade profile. This figure also shows the wave form of the blade which has been determined by MATLAB software. As shown in the Fig. 3, points P_2 and P_3 are located at the midpoints between P_0 to P_5 and P_4 to P_5, respectively. These points were used to define the equations of the Bézier curve.

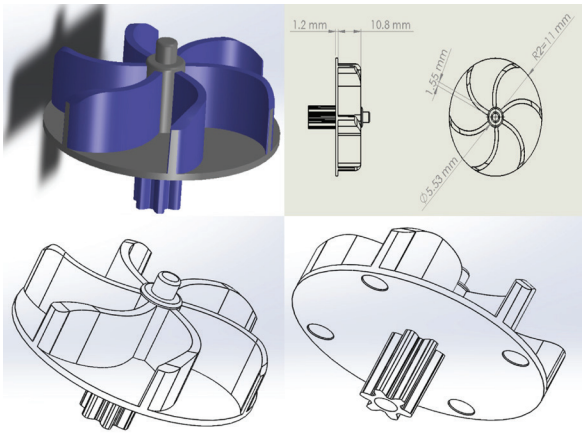

Fig. 2. *Basic dimensions and solid model of the impeller*

Angles β_1 and β_2 that are the fundamental parameters for modelling the blade shown in Fig. 3, are the impeller inlet and outlet installation angles. Blade profiles are selected in the range of β_1 =10° to 30° and β_2 = 10° to 40° increasing 5° after the constraints in the modelling and studies in the literature are examined.

After the impeller blade profiles were created, three-dimensional solid models were generated by using SOLIDWORKS 2021 software. Fig. 4 shows the images of the solid models and graphs of the mass and mass moment of inertia values of the impellers for blade profiles of β_1 = 10° and β_2 = 30° exemplary. As seen from Fig. 4b, as the number of blades increases, the mass and mass moment of inertia of the blades increase slightly. The average power consumption is obtained by:

$$P=\frac{1}{T}\int_T M(t)\cdot\omega(t)dt, \tag{3}$$

where T is the time period, $M(t)$ is the torque [N·m] and $\omega(t)$ is the angular velocity of the impeller [rad/s] [19]. Under steady conditions, there is no torque imbalance meaning that the torque and angular acceleration are zero [20]. The required torque during the transient stage is calculated as follows:

$$M=I\cdot\frac{d\omega}{dt}, \tag{4}$$

where I is the mass moment of inertia with respect to shaft axis [kg·m²] and is the angular acceleration [rad/s²]. The mechanical valve in this system is activated by pressurized water. Since the mass moment of inertia of the impeller is much smaller than the moment of pressurized water relative to the shaft axis, the required torque is exceeded in a short time, and the system starts to operate in a regular regime at a constant angular velocity. It has been seen from the literature that the rotational speed has more effect on the efficiency [19] and [20].

1.2 Materials

The material used in the mass production of the impeller examined in this study is polyoxymethylene (POM).

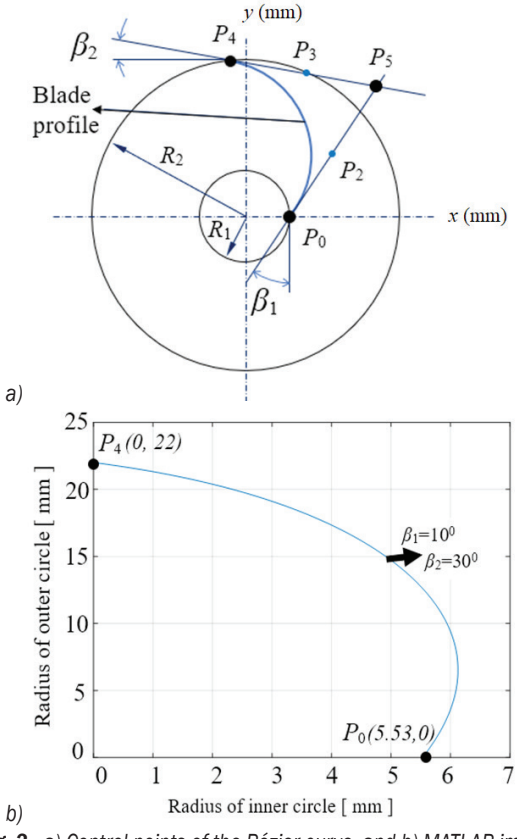

Fig. 3. *a) Control points of the Bézier curve, and b) MATLAB image sample of the blade profile for β_1 =10° & β_2 =30°*

In this study, in addition to this material, impellers from polylactic acid (PLA), pure resin, resin reinforced with boron and graphene by the 0.1 % weight-ratio produced with a three-dimensional printer using fused deposition modelling (FDM) and stereolithography (SLA technologies were also produced. PLA, which is the material of the impeller produced by FDM technology in this study, is a thermoplastic monomer obtained in the organic region such as polylactic acid, corn cab or sugar cane. Pure resin, which is the material of the impellers produced with SLA, is selected as a biocompatible resin that is safe in contact with food and not harmful to human health. Boron nitride and graphene particle additives were used to increase the strength of impellers produced with SLA and to reduce friction and, accordingly, pressure losses. Also noteworthy is the possibility of using graphene in the field of biomedicine, both in diagnostic and therapeutic areas. As a carrier of medicine, graphene oxide is characterized by high biocompatibility and excellent solubility. This allows for precise dosing of anti-inflammatory and anti-cancer agents as well as enzymes and mineral substances. Boron, which is among the most valuable natural resources in Turkey, provides a significant contribution to human health Boron is needed in low amounts in the human body; it is a mineral taken from the outside by food and water [21] and [22].

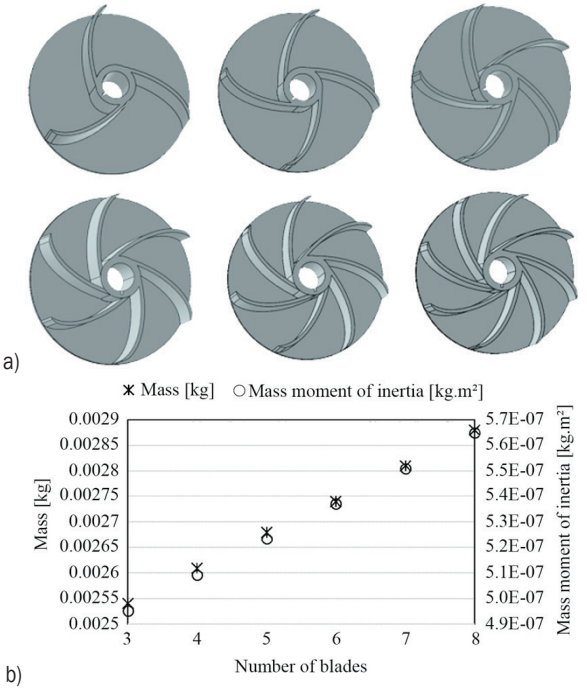

Fig. 4. *a) Solid models; and b) mass and mass moment of inertia values of the impellers for blade profiles of β_1 = 10° and β_2 = 30°.*

Table 1 presents the material properties and dimensions of the reinforced particles used in this study. The resin used in the SLA process is biocompatible. The resin with methacrylate-based

Table 1. *Material properties of impellers*

Material	Modulus of Elasticity [MPa]	Tensile strength [MPa]	Elongation [%]
Resin with methacrylate-based compounds methacrylate [23]	1933.322	52.402	5.378
POM [24]	3150	48.5	25
PLA [25]	3500	50	7

Particle	Size [nm]	Purity [%]
Graphene nanoplatelet [26]	6	99.9
Boron nitride [27]	450	99.55

compounds methacrylate is also used for the fixation of monomer resin, dental materials, and prosthetic devices in orthopaedic surgery [23].

Fig. 5 shows examples of mechanical valve impellers produced in real dimensions with SLA and FDM technologies, using different materials for pressure measurements over the dishwasher. As an example, the assembly of the impeller produced by the SLA method using resin reinforced by graphene and original impeller made of POM used in the mass production to the mechanical valve is shown in Fig. 6.

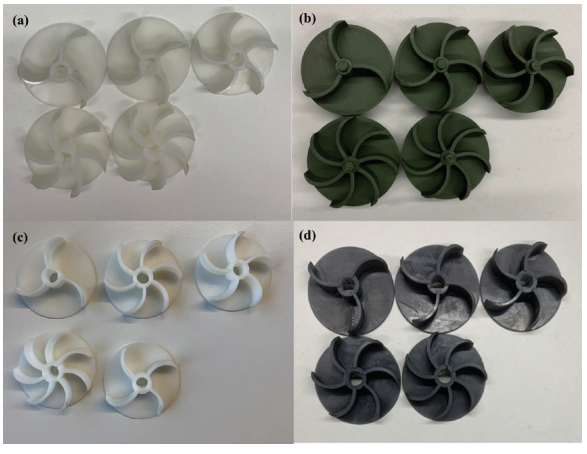

Fig. 5. *Impellers produced using: a) pure resin, b) PLA, c) resin reinforced by boron, and d) resin reinforced by graphene by the additive manufacturing technology*

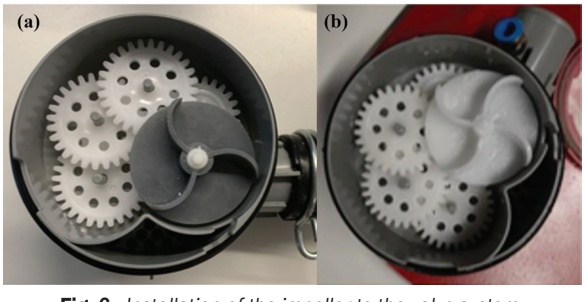

Fig. 6. *Installation of the impeller to the valve system; a) impeller made of resin reinforced by graphene, and b) impeller made of POM*

To determine whether the roughness of the surfaces would affect the flow, images of the blade surfaces of the propellers were taken with an optical microscope. Fig. 7 shows the images of the blades made of materials used in this study. The most roughness is seen on the blade surface made of PLA using FDM, as expected. However, considering the scale, it is calculated that the maximum value of the distance between the bottom surface and the top point can be approximately 70 μm. Images were obtained at many different magnification values, and only images magnified five times are presented in this study. Zhou et al. stated that the effect of surface roughness on pressure drop was negligible at low speeds, while pressure drop decreases with surface roughness at higher speeds in their study [28]. As a result, it was concluded that the geometric parameters of the blade are more dominant than the roughness on the pressure drop.

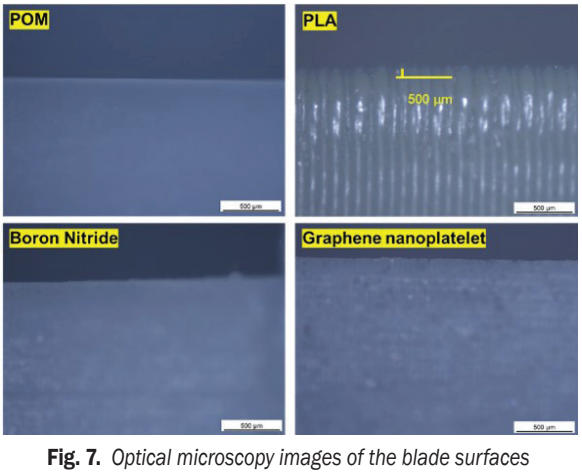

Fig. 7. *Optical microscopy images of the blade surfaces*

2 EXPERIMENTAL WORK

In this study, a specialized experimental setup was designed to measure the outlet pressure from the mechanical valve. Water from the dishwasher reservoir was passed through the mechanical valve, utilizing the

blade and gear systems. Pressure measurements were taken at the valve's outlet using a calibrated nozzle.

Experimental studies were conducted under two different fixed input pressures (300 mbar and 350 mbar). Previous studies have explored dishwasher water distribution systems and various valve designs. Electric motor-driven valves are commonly used due to their precise control capabilities, but their high cost and complexity have prompted research into alternative mechanical valves.

Fig. 8 exhibits the experimental methods in this study. The experimental setup consists of a water tank (#1), circulation pump (#2), pressure adjustment valve (#3), flow meter (EMFM HFD3000 electromagnetic flow meter, #4), dishwasher body (#5), sump group mounted on this body and mechanical valve within the chamber group (#6), pressure transmitter to measure the inlet pressure of the water before the mechanical valve (#7), pressure transmitter to measure the pressure in the outlet impeller (#8), and digital pressure gage (WIKA, #9). WIKA cph 6200 model having 0.2 % accuracy with calibration certificate was used in the measurements of the outlet pressure.

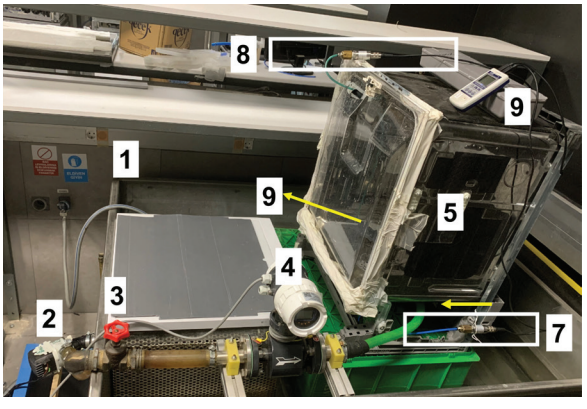

Fig. 8. *Experimental setup*

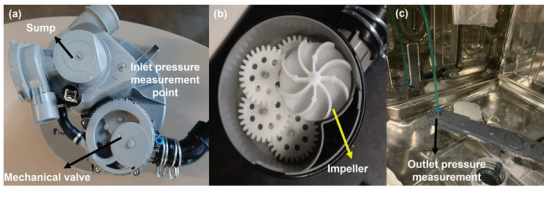

Fig. 9. *a) Sump group with mechanical valve and inlet pressure measurement point, b) mechanical valve inside with impeller, and c) outlet pressure measurement point at lower spray arm*

In the test system, water comes from the tap to the tank via the circulation pump. The circulation pump sucks the water from the tank and sends the water to the valve in the experimental setup. The pressure adjustment valve provides adjusting the water pressure at the inlet pressure. In addition, before water is not entering the system, the flow meter is measured using an electromagnetic flow meter (EMFM). An inlet pressure transmitter in the system provides to adjust inlet water pressure at the mechanical valve entering. The outlet pressure transmitter provides a reading of the outlet water pressure at the lower spray arm; 300 mbar and 350 mbar water inlet pressure have been applied for experiment studies. The sump group with a mechanical valve was assembled into the dishwasher body. The sump group, mechanical valve system, and inlet/outlet pressure measurement points are shown in Fig. 9.

2.1 Numerical Examinations (CFD Analyses, Optimization and Artificial Neural Networks)

In this study, the modeling of the impeller was carried out using SOLIDWORKS software. To obtain the outlet pressure, the outlet velocity and forces acting on the blade were obtained by performing the CFD analyses by ANSYS Fluent 2023R2 [29].

The first stage of the numerical studies consists of determining the parameters of the blade by design of experiments (DOE) in Minitab® 21.1 statistical software [30]. The parameters were determined with the DOE method used to structure and organize an experiment using scientific methods and statistical techniques. DOE is a powerful research method used in scientific research, product and process improvement, quality control, and more. It contributes to the advancement of science and the solution of problems by helping to obtain efficient and accurate results. The purpose is to analyze the data obtained by carrying out experiments in a systematic and planned manner and to obtain accurate, reliable and statistically supported outcomes from the results. The main purpose of the DOE is to design and conduct experiments in a thoughtful and planned way rather than being random or unplanned. Therefore, it aids in using time and resources efficiently by collecting the less amount of data to obtain accurate results. DOE has been prepared for β_1, β_2 and blade number inputs, which affect the impeller design. The analysis range was determined for each parameter. The maximum and minimum states for all inputs are defined in the analysis. It is introduced to the system that these inputs yield the maximum pressure output, because the higher the output pressure, the lower the pressure loss will be. As the pressure loss decreases, the washing performance of the system will increase.

Table 2. *Case setup variables in design of experiments (DOE) which has the design angles (β_1, β_2) and number of blades*

β_1, inlet installation angle [deg]	β_2, outlet installation angle [deg]	Number of blades
10	30	4
30	30	4
10	40	4
30	40	4
10	30	8
30	30	8
10	40	8
30	40	8

As a result, all of the design cases in the above-mentioned DOE are created, and the DOE parameter details are mentioned in Table 2. Three-dimensional solid models of the impellers were created with SOLIDWORKS according to the parameters given in Table 2. Using these models, CFD analyses were performed with the help of ANSYS Fluent 2023R2 software. From these analyses, outlet pressure, outlet velocity, and force values acting on the blades were determined. The optimization phase was carried out using the output pressure findings, which is the most important performance indicator. Response optimizer approaches were exploited to determine the effects of the design parameters on valve performance.

In this study, an artificial neural network (ANN) is also used to predict the outlet pressure for various blade models and the optimum blade profile obtained by ANOVA analysis. For this purpose, the MATLAB neural network fitting application **[31]** and **[32]** was used to compare the experimental and numerical results. Several ANN analyses using different numbers of hidden layers, and dual and triple combinations of transfer functions such as logarithmic sigmoid, tangent sigmoid, linear algorithms, ratio of training, validation, and testing were carried out to obtain the best ANN architecture. The ANN parameters used in this study correspond to the values at which the minimum error is obtained. The following transfer functions and other parameters defined are the parameters obtained as a result of various analyses. In the network architecture, the Levenberg-Marquardt back-propagation algorithm was used because learning of the network with this algorithm is faster than the gradient descent algorithm for data fitting **[33]**. The multilayer artificial neural network receives three parameters, which are impeller inlet and outlet installation angles at five ranks as inputs and then yields the estimation of the outlet estimation through the activation function. The Levenberg-Marquardt back-propagation algorithm is then operated with the performance function, which is a function of the ANN-based weight and bias variables were adjusted according to the Levenberg-Marquardt method, and the back-propagation algorithm is used to calculate the Jacobian matrix of the performance function with respect to the weight and bias variables. With updated weights and biases, the ANN further estimates the output values such as outlet pressure and efficiency of the impeller. Using the outlet pressure data obtained via the CFD analyses, outlet pressure values for different impeller parameters were estimated with the help of the ANN method. The neural network consisting of an input layer, two hidden layers, and an output layer was used. In the training of neural networks, input and output values are frequently scaled to a range 0 to 1, which is called the normalisation process [31[and **[32]**, which process is done separately for all network input and output values. First, each value was subtracted from the smallest number in Table 5 and then divided by the difference between the largest and smallest number in the table. The hidden and output layers of the ANN were modelled using logarithmic sigmoid, tangent sigmoid and positive linear transfer functions, respectively. The ideal number of neurons in the hidden layers was obtained as 9. The learning process of the network model was completed in the 220-epoch based on the mean square error method. The program automatically generates the initial weights and biases of the network. A total of 40 data points were selected to evaluate the performance of the trained network model.

3 RESULTS AND DISCUSSION

3.1 Experimental Results

Experimental studies in this paper consist of two parts. In the first step, outlet pressure values were measured for the original blade design used in mass production using the different materials and six different number of blades. In the second step, outlet pressure was measured using an impeller having the optimal blade profile obtained with flow analyses in ANSYS Fluent and response optimizer analyses in ANOVA.

In the first stage, with the experimental setup shown in Fig. 8, the outlet pressure values were measured at 300 mbar and 350 mbar water inlet pressure to see only the effect of the number of blades and the raw material of the impeller. The goal was to determine how the impellers produced with different number of blades and different raw materials affect the outlet pressure taken from the lower spray arm of the

system and to keep the pressure loss to a minimum. In the experimental examinations, the point where the inlet pressure was adjusted at 300 mbar and 350 mbar is shown in Fig. 8a. The outlet pressure of the water entering the mechanical valve system after the mechanical valve is measured from the nozzle shown in Fig. 8c on the lower impeller. Experiments were repeated 20 times at both 300 mbar and 350 mbar inlet pressures to measure the output pressure and flow rate for each impeller type. In the numerical investigations, the pressure value on the blade was determined and a correlation was attempted between the numerical and experimental findings. Considering the pressure drop of the water during the operation of the dishwasher, experimental studies were carried out for two different constant inlet pressures of 300 mbar and 350 mbar. The nominal inlet pressure in the washing state of the dishwasher is 350 mbar. The first element of the mechanical valve to encounter water is the impeller and the current design of this part has eight blades. In the first stage of the experimental studies, the difference between inlet and outlet pressures was determined in the case of the existing impeller made of POM material having eight and four blades. Different designs for this material could not be examined comprehensively due to mold costs and the effect of the number of vanes was investigated with alternative materials used in the additive manufacturing method. In the later stages of the study, it was aimed to reduce pressure losses by examining the design parameters of the impeller geometry. Fig. 10 shows the variation of the outlet pressure with respect to the inlet pressure for the current impeller made of POM having eight blades used in mass production. Pressure loses differences in the system can be easily seen from the figure.

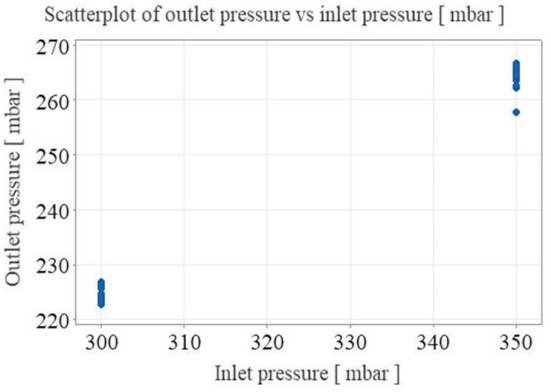

Fig. 10. *Comparison of outlet pressure with respect to the inlet pressure for current impeller with eight blades*

When 300 mbar inlet pressure is applied, the average outlet pressure is 224.44 mbar, while the average outlet pressure is 263.71 mbar when 350 mbar inlet pressure is applied. Under 300 mbar inlet pressure conditions, an average of 25.19 % pressure loss can occur, while under 350 mbar inlet pressure conditions, 24.65 % pressure loss can occur.

Within the scope of this study, impellers with the current blade design were also produced by the additive manufacturing method using different materials. The materials used in the additive manufacturing process are PLA in FDM, pure resin, and resin reinforced by both boron nitride and graphene nanoplatelet having nanosized in SLA. The

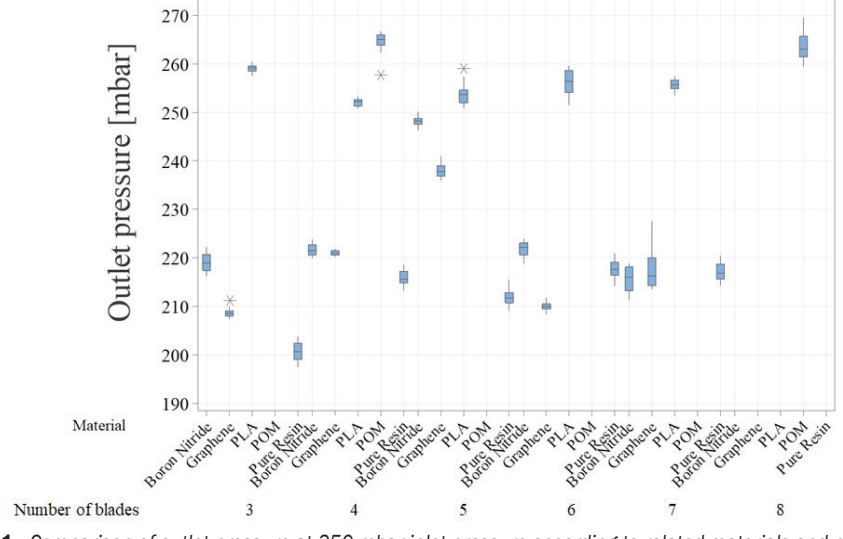

Fig. 11. *Comparison of outlet pressure at 350 mbar inlet pressure according to related materials and number of blades respect to the inlet pressure for current impeller with eight blades*

motivation for the use of boron and graphene was to reduce the friction coefficient of the blade surface and consequently reduce the inlet-outlet pressure differences. In addition to using different materials, 3-, 4-, 5-, 6-, 7- and 8-bladed impellers with existing blade profiles were produced to investigate the effect of the blade number at this stage of the study. Fig. 11 shows a comparison of the outlet pressure at 350 mbar inlet pressure according to related materials and the number of blades with respect to the inlet pressure for the current impeller with eight blades.

The regression equations for all impeller types obtained by ANOVA at 350 mbar pressure depending on the number of blades are shown in Fig. 12. As can be seen, while the outlet pressure has the lowest value for all blade numbers when the impeller produced using graphene nanoplatelet doped resin is used, the least pressure loss occurred when impellers made of PLA material were used.

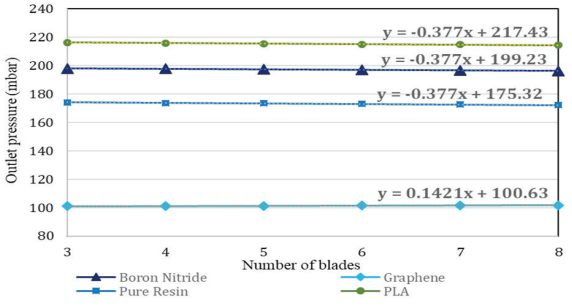

Fig. 12. *Regression equations expressing the outlet pressure depending on the number of blades*

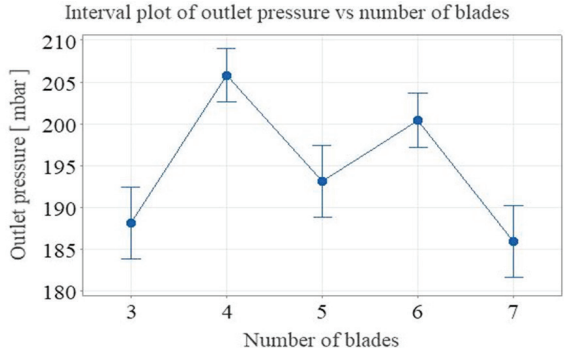

Fig. 13. *Number of blades-outlet pressure box plot graph for 350 mbar inlet pressure for PLA material*

Figs. 12 to 14 summarize the measurement results for outlet pressure performed at an inlet pressure of 350 mbar.

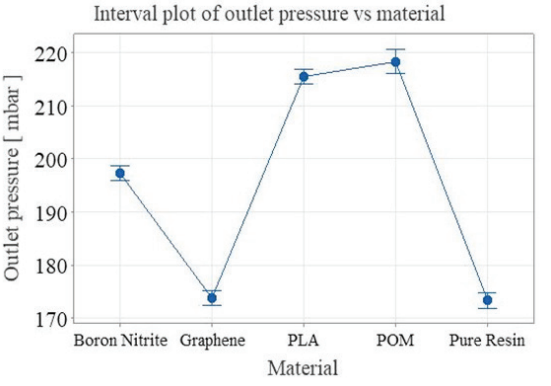

a)

b)

Model Summary

S	R-sq	R-sq(adj)	R-sq(pred)
7.32905	86.77 %	86.65 %	86.47 %

Fig. 14. *a) Material-Outlet pressure graph; and b) regression analysis R-sq(adj) values at 350 mbar inlet pressure*

3.2 Numerical Results

At this stage of the study, extensive analyses were carried out to determine the effect of the profile and number of blades on the pressure losses, outlet velocity, and force acting on the blade. As mentioned in Section 1, first, using Bezier curves, impellers with different blade profiles were modelled in three dimensions using SOLIDWORKS software. Flow analysis was performed with ANSYS Fluent CFD using the solid models obtained. Before solid models were created, design parameters were determined using the DOE tool in Minitab and models were created for these parameters. Then, using the data obtained from the flow analyses, the optimum design was determined using the ANOVA Response Optimizer tool. Flow analysis of this optimum design was also performed. Finally, this impeller, having the optimum design, was manufactured from PLA material with FDM technology, and the outlet pressure was measured experimentally.

3.2.1 Creation of Flow Volume and Definition of Boundary Conditions

Fig. 15 shows the boundary conditions of the impeller used in the CFD analyses. For the analyses, a cylindrical flow volume was first created with a porous jump to simulate pressure loss in the system and then an angular speed of 550 rpm was defined for the impeller around its shaft axis. Inlet flow rate and outlet pressure were defined as 0.675 kg/s and 0 Pa, respectively. Unlike experimental studies, since it is not possible to simulate the system exactly, the

Table 3. *Mesh parameters*

	Surface mesh size		Volume mesh size		Mesh metric					
	Min [mm]	Max [mm]	Max [mm]	Min [mm]	Max aspect ratio	Average aspect ratio	Minimum orthogonal quality	Average orthogonal quality	Max skewness	Average skewness
Mesh#1	0.2	12.8	6.4	0.8	76.3	6.36	0.15	0.88	0.85	0.12
Mesh#2	0.1	6.4	3.2	0.4	85.53	4.22	0.15	0.92	0.85	0.08

pressure value on the blade of the impeller was determined in numerical analysis, and explanations were attempted using these values. Exemplary, the minimum orthogonal mesh quality of the related six-bladed impeller is 0.153, the maximum aspect ratio is 58, and the maximum skewness is 0.64; the finite volume model of this impeller has 897,484 nodes and 282,049 computational cell numbers. In the flow analysis, an attempt was made to create a finite volume model with the same size volume for all the impeller models.

As the control parameter, the total pressure at the outlet condition and the total pressure at the inlet condition of the flow volume where the blades are located were taken and attempts were made to bring them to the maximum value. The function of "$f(x) = Total\ pressure_{outlet} - Total\ pressure_{inlet}$" was tried to be maximized.

To reduce the computational cost of the optimization problem, the analysis was carried out in a steady state, independent of time. The frame motion [mrf (multiple reference frame)] option suitable for this setting is given to the flow volume in the selected impellers. Inlet condition is mass flow inlet and normal to the boundary. The outlet condition is the pressure outlet with 0 Pa direction is normal to the boundary.

The viscous model and material have been selected as kω-shear stress transport (SST) turbulence model and the water-liquid whose density is 998.2 kg/m³, respectively. Rhie-Chow interpolation method has been used as the flux type method in CFD calculations. Standard initialization from inlet has been used. The run calculation method is pseudo-transient, and the number of calculations is 400. The temperature of the fluid is 20 °C.

In this study, mesh independence analysis was performed. Table 3 shows the surface mesh size, volume mesh size, maximum and average aspect ratio values, minimum and average orthogonal quality values, and maximum and average skewness values for two different mesh sizes taken into consideration.

Table 4. *Comparison of pressure results versus the mesh type*

	Pressure inlet [mbar]	Pressure outlet [mbar]	Pressure loss, Δp [mbar]
Mesh1	131.97	0.0342	131.94
Mesh2	129.39	0.0257	129.39

Table 4 presents the pressure difference between the inlet and outlet for the two mesh sizes. As seen,

Table 5. Results of flow analyses depending on the number of blades, β_1 and β_2 variables

	Number of blades	$\beta_1 = 10^\circ$ $\beta_2 = 30^\circ$	$\beta_1 = 10^\circ$ $\beta_2 = 40^\circ$	$\beta_1 = 20^\circ$ $\beta_2 = 30^\circ$	$\beta_1 = 20^\circ$ $\beta_2 = 40^\circ$	$\beta_1 = 25^\circ$ $\beta_2 = 30^\circ$	$\beta_1 = 25^\circ$ $\beta_2 = 40^\circ$	$\beta_1 = 30^\circ$ $\beta_2 = 30^\circ$	$\beta_1 = 30^\circ$ $\beta_2 = 40^\circ$
Total pressure loses ΔP [mbar]	3	132.58	132.55	132.55	132.54	132.64	132.55	132.64	132.56
	4	132.62	132.35	132.43	132.37	132.56	132.43	132.58	132.47
	5	132.50	132.25	132.35	132.33	132.50	132.30	132.54	132.34
	6	132.28	132.10	132.27	132.19	132.38	132.12	132.44	132.19
	7	132.18	132.01	132.29	132.08	132.39	132.11	132.47	132.16
	8	132.11	131.94	132.28	132.04	132.43	132.09	132.67	132.21
Efficiency of related impellers [%]	3	41.19	48.43	43.49	46.27	39.66	46.90	38.73	46.01
	4	54.65	63.44	58.30	60.59	51.04	60.15	50.61	57.85
	5	63.90	72.70	66.30	67.09	58.23	69.73	55.46	67.47
	6	71.37	80.14	71.73	75.47	66.18	78.24	62.38	75.84
	7	76.96	83.60	72.03	80.65	66.53	80.91	62.42	77.83
	8	80.40	86.57	72.91	82.95	65.39	81.24	55.43	76.31

there is a 1.95 % difference between two analyses. It is concluded from the analyses that mesh independence has been provided.

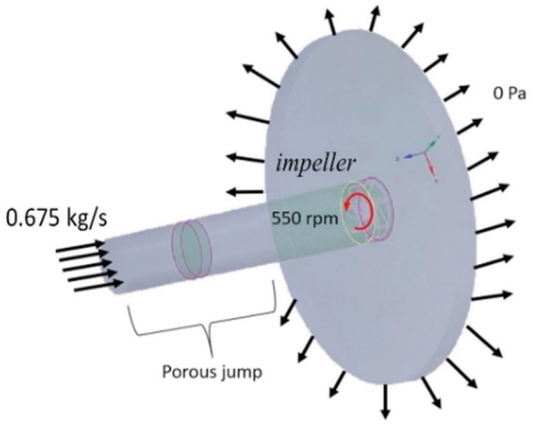

Fig. 15. *Boundary conditions*

Table 5 shows the results obtained from the CFD analysis for 48 different cases. These results will be evaluated with the statistical analyses performed by Minitab, and the optimum design will be selected. The analysis shows that the impeller with the optimum design should have 4.85 blades, which means approximately five blades according to the experimental results, in order to obtain the maximum outlet pressure shown in Figure 16. Among the raw materials that have been experimentally studied, PLA raw material can have the maximum effect on the outlet pressure.

Percent impeller efficiency is calculated by using Eq. (5) as follows:

$$\% \text{ efficiency} = \frac{P_{discharge} - P_{suction}}{P_{discharge}} \times 100. \tag{5}$$

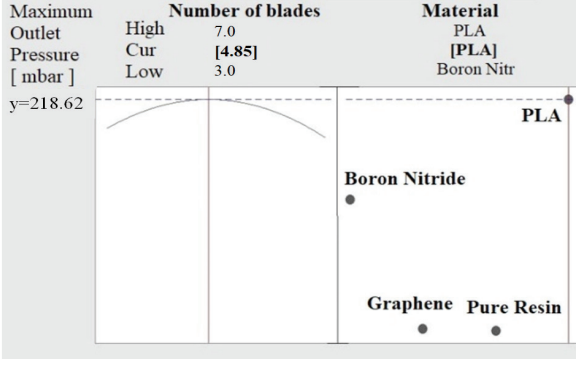

Fig. 16. *Response optimization of outlet pressure for experimental measurements versus the number of blades and material*

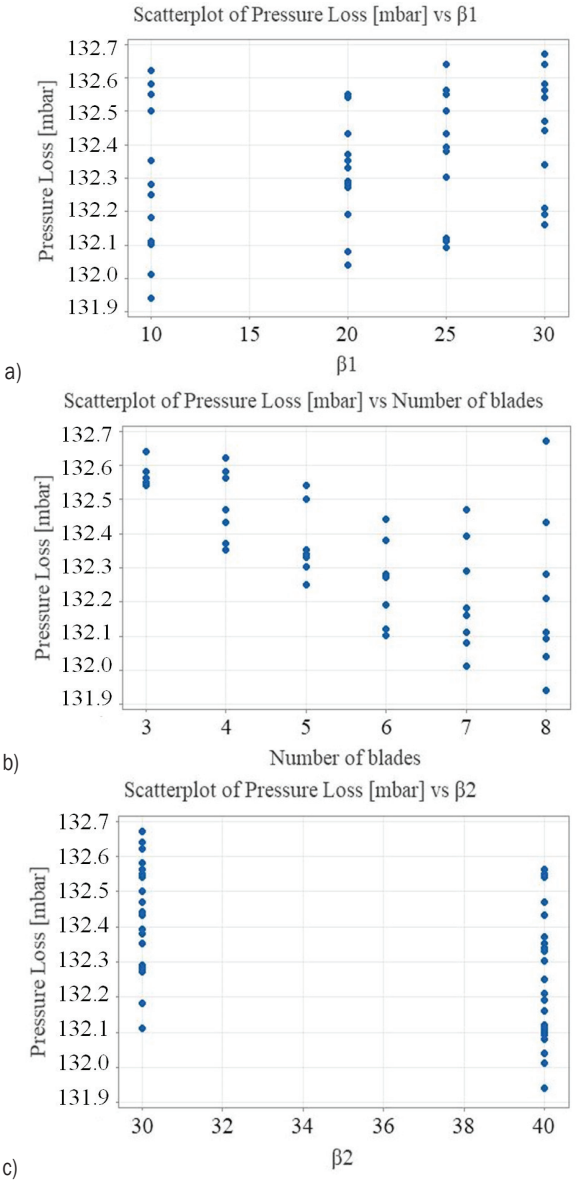

Fig. 17. *Pressure loss depending on: a) the number of blades, b) β_1, and c) β_2*

Fig. 17 shows the variation of the pressure loss and force acting on the blade depending on the number of blades, impeller inlet and outlet installation angles β_1 and β_2, respectively.

Fig. 18 shows the effect of the determined parameters on the pressure loss and efficiency of impeller. Results from both experimental measurements and CFD analyses show the significant influence of the number of blades. These evaluations show that pressure losses will be significantly reduced if six-, seven-, or eight-bladed impellers are used. It is possible to say that the experimental results and the CFD analyses results are consistent with each other.

Although the results indicate the minimum pressure loss when the impeller blade pieces are increased, the values for the impeller with six, seven and eight blades, which give values close to this, were also examined. As the β_1 angle of the blade increases, the pressure loss increases, and as the β_2 angle increases, the pressure loss decreases. It has been seen that the pressure loss decreases as the number of blades increases. Considering all the results, the number of blades of the wheel should be six, seven, or eight. Considering the impeller efficiency, which is calculated inversely to the pressure loss, the efficiency of the impeller increases as β_1 decreases, β_2 increases, and the number of blades increases. The optimum values of the number of blades, inlet mounting angle β_1 and outlet mounting angle β_2 will be decided after statistical analysis in Minitab.

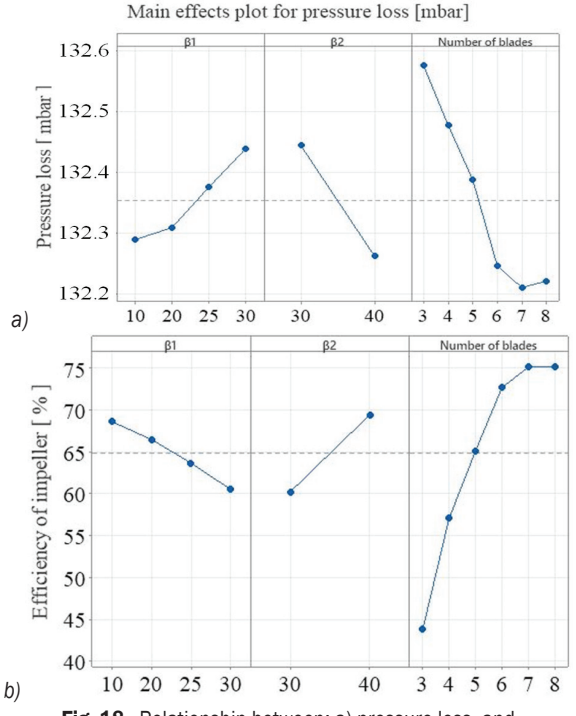

Fig. 18. Relationship between; a) pressure loss, and b) efficiency of impeller obtained by the CFD analyses and β_1, β_2 and number of blades

Fig. 19 shows the optimum values of the design parameters obtained after the regression analyses are performed. A new model was created using the parameters led by the regression analysis and CFD analyses were performed for this model. The response optimizer has been calculated according to the situation where the minimum pressure loss of the impeller efficiency is maximum. Fig. 20 shows the blade surface mesh image and total pressure distribution graph for the suction and discharge sides. These values belong to optimum design as the response optimizer suggestion in the regression analysis. In this design, the pressure loss is calculated as 131.94 mbar and pump efficiency was calculated as 86.57 % at CFD analyses. According to the regression response optimizer tool, pressure loss will be 131.98 mbar, and impeller efficiency will be 89.47 %. The calculated values are so similar to each other. Also, a DOE factorial response optimizer has been applied; pressure loss has been seen at 131.89 mbar, and impeller efficiency has been seen at 91.09 %. The two different methods' results have been seen as similar to each other.

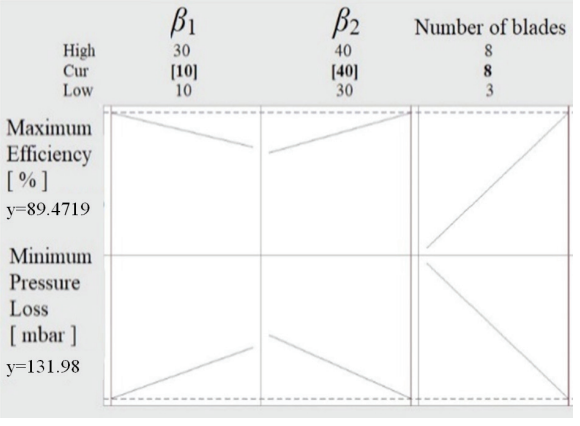

Fig. 19. *Results of regression response optimization analysis using the findings by CFD analyses*

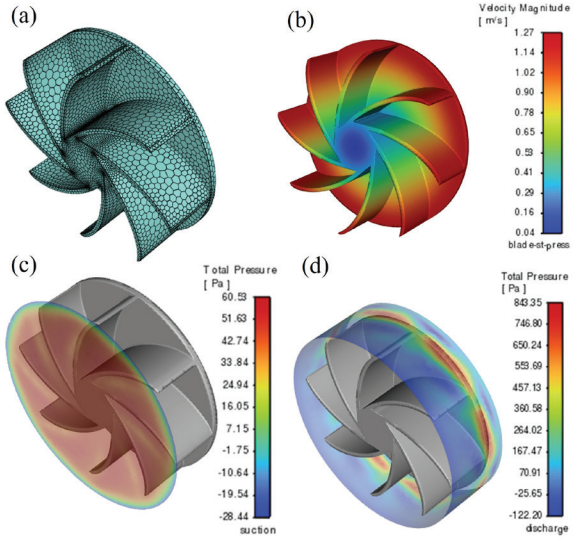

Fig. 20. *Optimum design at β_1=10 °, β_1=40 °, number of blades = 8; a) blade surface mesh image, b) total velocity distribution, c) total pressure distribution at suction side, and d) total pressure distribution at discharge side*

According to the response optimization of the results obtained in the experimental studies, as shown in Fig. 16, the optimum material should be PLA to keep maximum outlet pressure. Additionally, after all CFD analysis have been finished at 48 different designs, optimum design parameters obtained by the response optimizer analysis are determined as $\beta_1 = 10°$, $\beta_2 = 40°$, number of blades is 8. Fig. 19 shows these optimum design suggestions of response optimizer tool.

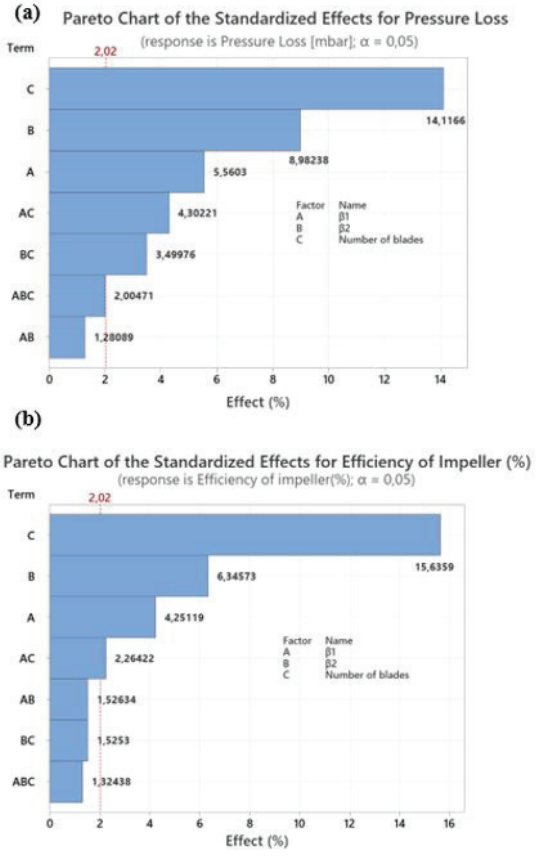

c)

Model Summary

S	R-sq	R-sq(adj)	R-sq(pred)
4.96912	87.73 %	85.64 %	79.82 %

Fig. 21. *Impact ratios of inputs for; a) pressure loss, b) efficiency of impeller, and c) factorial regression R-sq value*

Fig. 21 shows the impact ratios of the design parameters on pressure loss and efficiency of impeller. The maximum effect among the parameters to reach the minimum pressure loss belongs to number of blades with 14.11 % and to reach maximum efficiency of impeller belongs to number of blades with 15.63 %. Also, the *R-sq*(*adj*) value was also found to be 85.64 % in factorial regression analysis and the analysis is reliable since it is over 80 %.

Table 6 includes all results summary together. With the optimum design, approximately 6.5 % improvement in outlet pressure has been achieved compared to the design in conventional mass production. Impeller efficiency increased from 59.77 % to 86.57 %. With this optimization study, a design with minimum pressure loss and maximum impeller efficiency was obtained. As mentioned in the previous sections, while the pressure values by CFD analysis shows the pressures on the part, the outlet pressure in the experimental study shows the pressures taken from the lower spray arm nozzle after the impeller.

Table 6. *Comparison of conventional and optimized impellers*

	Efficiency of impeller [%]	Experimental outlet pressure [mbar]	Experimental pressure loss [mbar]	CFD analysis pressure loss [mbar]
Conventional design	59.77	220.5	130	132.5
Optimum design	86.57	234.8	116	131.94

Within the scope of this study, a model was created with ANN using CFD analysis studies, and efficiency was predicted for the optimum parameters obtained from the response optimizer analyses.

Fig. 22 shows the training and prediction performances of the neural network used in this study. As can be seen, the tested values and the predicted values are quite close to each other, so it can be said that the ANN model is well trained. When all the results regarding the prediction performance of the neural network are considered, a match between the predicted and actual values is detected. As seen from the figure, the correlation factor for training is greater than 0.99. The developed ANN model has good interpolation capability and can be used as an efficient predictive tool for the outlet pressure of the valve. After ensuring that the neural network was trained for the entire database to achieve the best prediction accuracy, the impeller efficiency prediction for the optimal parameters was calculated using this model. For $\beta_1 = 10°$, $\beta_2 = 40°$, number of blades is 8, impeller efficiency was predicted as 82.6217 % using this ANN model. This result agrees with the results obtained from CFD analysis and response optimizer analysis.

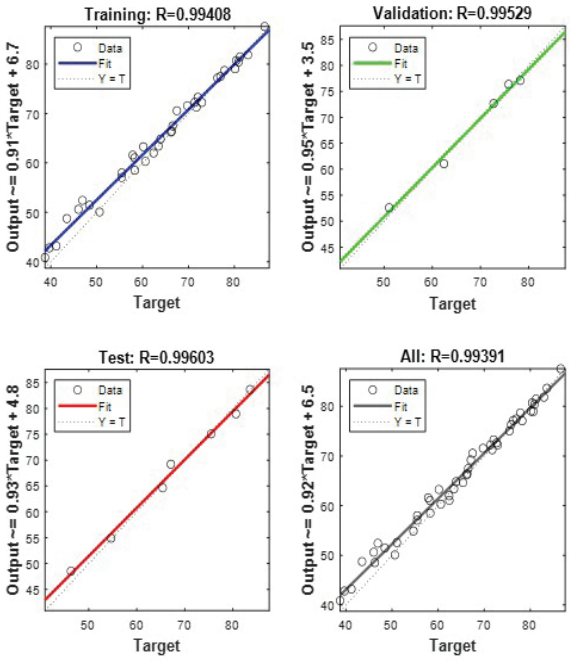

Fig. 22. *Neural network training, validation, and test results regression results*

4 CONCLUSIONS

This research investigates the effect of mechanical valve design on pressure loss in dishwasher systems. Within the scope of this study, a powerful methodology has been created for the design optimization of the impeller with the integration of experiments on real systems, CFD analysis, statistical analysis, and artificial neural network analysis. It has been concluded that the effectiveness of the impeller of the mechanical valve used in dishwashers depends on the blade profile's design and the number of blades. The results of this study also highlight the significance of material selection in the design and performance optimization of dishwasher mechanical valves. In this way, considering the findings obtained, it will contribute to the advancement of dishwasher technology by increasing the efficiency and effectiveness of the cleaning process, and saving energy. The research findings have practical implications for improving the performance of dishwashers and may contribute to the development of more efficient and reliable appliances in the future. The results of such research should be validated by practical tests in real-life dishwasher scenarios.

5 REFERENCES

[1] Lu, B., Teng, J., Zhu, M., Qiang, X. (2023). Design optimization of a transonic compressor blade with sweep and lean integrated with axial slot casing treatment. *Aerospace Science and Technology*, vol. 136, art. ID 108225, **DOI:10.1016/j.ast.2023.108225**.

[2] Rengma, T.S., Gupta, M.K., Subbarao, P.M.V. (2023). A novel method of optimizing the Savonius hydrokinetic turbine blades using Bezier curve. *Renewable Energy*, vol. 216, art. ID 119091, **DOI:10.1016/j.renene.2023.119091**.

[3] Zhong, S., Jin, G., Ye, T. (2023). Isogeometric vibration and material optimization of rotating in-plane functionally graded thin-shell blades with variable thickness. *Thin-Walled Structures*, vol. 185, art. ID 110593, **DOI:10.1016/j.tws.2023.110593**.

[4] Tang, D., Tang, B., Shen, W. Zhu, K., Quan, G.Deng, Z. (2023). On genetic algorithm and artificial neural network combined optimization for a Mars rotorcraft blade. *Acta Astronautica*, vol. 203, p. 78-87, **DOI:10.1016/j.actaastro.2022.11.032**.

[5] Luo, J., Fu, Z., Fu, W., Chen, J. (2023). Aerodynamic optimization of a transonic fan rotor by blade sweeping using adaptive Gaussian process. *Aerospace Science and Technology*, vol. 137, art. ID 108255, **DOI:10.1016/j.ast.2023.108255**.

[6] Lu, J., Zhang, F., Tao, R., Li, X., Zhu, D, Xiao, R. (2023). Optimization of runner and vane blade angle of an oscillating water column based on genetic algorithm and neural network. *Ocean Engineering*, vol. 284, art. ID115257, **DOI:10.1016/j.oceaneng.2023.115257**.

[7] Fazil, J., Jayakumar, V. (2011). Investigation of airfoil profile design using reverse engineering Bezier curve. *Journal of Engineering and Applied Sciences*, vol. 6, no. 7, p. 43-52.

[8] Fincham, J.H.S., Friswell, M.I. (2015). Aerodynamic optimisation of a camber morphing aerofoil. *Aerospace Science and Technology*, vol. 43, p. 245-255, **DOI:10.1016/j.ast.2015.02.023**.

[9] Hansen, T.H. (2018). Airfoil optimization for wind turbine application. *Wind Energy*, vol. 21, no. 7, p. 502-514, **DOI:10.1002/we.2174**.

[10] Jeong, J.H., Kim, S.H. (2018). Optimization of thick wind turbine airfoils using a genetic algorithm. *Journal of Mechanical Science and Technology*, vol. 32, no. 7, p. 3191-3199, **DOI:10.1007/s12206-018-0622-x**.

[11] Salimi, A., Rostami, H.H., Riasi, A., Nejadali, J. (2023). Multi-objective optimization of a regenerative pump with S-shaped impeller using response surface methodology. *International Communications in Heat and Mass Transfer*, vol. 143, no. 106734, **DOI:10.1016/j.icheatmasstransfer.2023.106734**.

[12] Satjaritanun, P., Regalbuto, J.R., Regalbuto, J.A., Tippayawong, N., Shimpalee, S. (2021). Mixing optimization with inward flow configuration contra-rotating impeller, baffle-free tank. *Alexandria Engineering Journal*, vol. 60, no. 4, p. 3759-3779, **DOI:10.1016/j.aej.2021.02.045**.

[13] Mohammed, A.; Lemu, H. G., Sirahbizu, B. (2021). Determining optimum rotary blade design for wind-powered water-pumping systems for local selected sites. *Strojniški vestnik - Journal of Mechanical Engineering*, vol. 67, no. 5, p. 214-222, **DOI:10.5545/sv-jme.2021.7104**.

[14] Zhang, H., Tang, L., Zhao, Y. (2020). Influence of blade profiles on plastic centrifugal pump performance. *Advances in Materials Science and Engineering*, vol. 2020, art. ID 6665520, **DOI:10.1155/2020/6665520**.

[15] Elhosenya, M., Tharwat, A., Hassaniene, A.E. (2018). Bezier curve based path planning in a dynamic field using modified genetic algorithm. *Journal of Computational Science*, vol. 25, p. 339-350, **DOI:10.1016/j.jocs.2017.08.004**.

[16] Wahba, W.A. (2001). *Design Optimization of Centrifugal Pump Impellers Using Parallel Genetic Algorithm*. PhD. Thesis, School of Mechanical Engineering, Department of Power, Propulsion and Aerospace Engineering, Cranfield University, Cranfield.

[17] Matlab R2022a. (2022). from *https://www.mathworks.com/*, accessed on 2022-09-01.

[18] Solidworks (2021). from *https://www.solidworks.com/*, accessed on 2022-07-07.

[19] Bao, Y., , Li T., Wang, D., Cai, Z., Gao, Z. (2020). Discrete element method study of effects of the impeller configuration and operating conditions on particle mixing in a cylindrical mixer. *Particuology*, vol. 49, p. 146-158, **DOI:10.1016/j.partic.2019.02.002**.

[20] Schmelzle, S., Leppert, S., Nirschl, H. (2015). Influence of impeller geometry in a vertical mixer described by DEM simulation and the dispersion model. Advanced Powder Technology, vol. 26, no. 5, p. 1473--1482, **DOI:10.1016/j.apt.2015.08.003**.

[21] Eti Maden. (2023). Welfare Provided by Boron, from *https://www.etimaden.gov.tr/en/health*, accessed on 2023-06-02.

[22] PCC Group. (2023). Graphene - what is it and what is it used for?, from *https://www.products.pcc.eu/en/blog/graphene-what-is-it-and-what-is-it-used-for*, accessed on 2023-07-05.

[23] Acar Yavuz, G., Gören Kıral, B. (2022). Effect of cross-head speed on mechanical properties of photosensitive resins used in three-dimensional printing of a stereolithographic elastomer. *Materials Testing*, vol. 64, no. 11, p. 1675-1686. **DOI:10.1515/mt-2022-0125**.

[24] Designer Data. POM (hom.) (2023). from *https://designerdata.nl/materials/plastics/thermo-plastics/polyoxymethylene-(hom.)*, accessed on 2023-06-04.

[25] Farah, S., Anderson, D.G., Langer, R. (2016). Physical and mechanical properties of PLA, and their functions in widespread applications - A comprehensive review. *Advanced Drug Delivery Reviews*, vol. 107, p. 367-392, **DOI:10.1016/j.addr.2016.06.012**.

[26] Nanografi (2023). Graphene, from *https://nanografi.com/graphene/*, accessed on 2023-06-04.

[27] Nanografi. Boron Nanoparticles (2023). from *https://nanografi.com/nanoparticles/element-alloys-nanoparticles/boron-nanoparticles/*, accessed on 2023-06-04.

[28] Zhou, F., Sun, G., Zhang, Y., Ci, H., Wei, Q. (2018). Experimental and CFD study on the effects of surface roughness on cyclone performance. *Separation and Purification Technology*, vol. 193, p. 175-183, **DOI:10.1016/j.seppur.2017.11.017**.

[29] ANSYS 2023R2. (2023). from *https://www.ansys.com*, accessed on 2023-07-24.

[30] Minitab® 21.1. (2023). from *https://www.minitab.com*, accessed on 2023-07-23.

[31] MathWorks. Deep Learning Toolbox, (2023). from *https://ww2.mathworks.cn/en/products/deep-learning.html*, accessed on 2023-05-05.

[32] MathWorks. Improve neural network generalization and avoid overfitting (2023). from *https://ww2.mathworks.cn/help/deeplearning/deep-learning-with-simulink.html*, accessed on 2023-05-05.

[33] Atilla, D., Sencan, C., Goren Kiral, B., Kiral, Z. (2020). Free vibration and buckling analyses of laminated composite plates with cutout. *Archive of Applied Mechanics*, vol. 90, p. 2433-2448, **DOI:10.1007/s00419-020-01730-2**.

Vsebina

Strojniški vestnik - Journal of Mechanical Engineering
letnik 70, (2024), številka 3-4
Ljubljana, marec-april 2024
ISSN 0039-2480

Izhaja dvomesečno

Razširjeni povzetki (extended abstracts)

Strojniški vestnik - Journal of Mechanical Engineering 70(2024)3-4, SI 13

Prejeto v recenzijo: 2023-09-07
Prejeto popravljeno: 2024-01-31
Odobreno za objavo: 2024-02-13

Eksperimentalni sistem za testiranje adsorpcijskega ogrevanja prostorov

Urška Mlakar[1,*] – Rok Koželj[1] – Alenka Ristić[2] – Uroš Stritih[1]
[1] Univerza v Ljubljani, Fakulteta za strojništvo, Slovenija
[2] Kemijski inštitut, Slovenija

Ko govorimo o zelenem prehodu, ne moremo mimo tehnologij shranjevanja energije. Tehnologije shranjevanja energije so ključne za povečano vključevanje obnovljivih virov energije v različne sektorje. Shranjevanje energije nam pomaga premostiti neujemanje med razpoložljivostjo virov energije in potrebo po energiji. Če želimo v prihodnjih generacijah izboljšati učinkovitost sistemov v stavbnem, industrijskem in prometnem sektorju, bo uporaba tehnologij shranjevanja toplote nujna. Toploto je mogoče shraniti v senzibilnih, latentnih in termokemijskih hranilnikih. V okviru prispevka smo se osredotočili na termokemijske hranilnike, natančneje na hranilnike, ki temeljijo na adsorpciji. Ta vrsta hranilnikov, glede na pretekle raziskave, kaže največji potencial na tem področju, saj jih med drugim odlikuje kompaktnost, visoka gostota shranjene energije in manjše izgube v primerjavi z ostalimi tehnologijami shranjevanja.

Glavni namen tega prispevka je pokazati eksperimentalno primerjavo dveh materialov – zeolitov za namen adsorpcijskega ogrevanja prostorov. Med obema uporabljenima materialoma (zeolit 13X in zeolit NaYBFK), je zeolit 13X eden izmed najpogosteje uporabljenih materialov na področju raziskav adsorpcijskega shranjevanja.

V okviru raziskav, ki so predstavljene v tem prispevku, sta bila izvedena dva eksperimenta procesa adsorpcije delovne tekočine na nasutje zeolita 13X in zeolita NaYBFK. V prvem eksperimentu je bil delovni medij vlažen zrak, kateremu smo dodali vodno paro iz ultrazvočnega vlažilnika, v drugem eksperimentu pa smo kot delovni medij uporabili vodno paro. Ko je bila zraku dodana vodna para, sta se ta dva toka pomešala, preden sta vstopila v nasutje. V nasutju zeolita so bile temperature izmerjene na različnih lokacijah ali višinah. Prva temperatura je bila izmerjena takoj za bombažno tkanino na dnu nasutja. Druga temperatura je bila izmerjena na srednji višini nasutja. Naslednji termočlen je bil nameščen na vrhu nasutja. Zadnji termočlen je meril temperaturo zraka za nasutjem. Eksperimentalna postavitev za drugi poskus je del eksperimentalne postavitve prvega poskusa. Razlika je v tem, da tokrat kot delovni medij uporabljamo samo vodno paro, s katerim smo odstranili problem mešanja zraka in vodne pare pred vstopom v nasutje. Tako kot v prvem poskusu smo tudi tokrat merili temperaturo vodne pare, masni pretok vodne pare in temperature v nasutju na različnih višinah. Za vsak poskus je bilo izvedenih več nizov meritev.

Rezultati so pokazali, da zeolit NaYBFK dosega nižjo maksimalno temperaturo nasutja, vendar ima boljšo adsorpcijo vode kot zeolit 13X, kadar se kot delovni medij uporablja vlažen zrak. Adsorpcijo vode na zeolit 13X je mogoče izboljšati z višjo vstopno temperaturo vodne pare, medtem ko je dosežena najvišja temperatura v nasutju v fazi adsorpcije nižja. Najvišja dosežena temperatura v nasutju med adsorpcijo se je za zeolit NaYBFK z uporabo vodne pare, kot medija povečala za 24 °C, adsorpcija vode pa se pri enaki vstopni temperaturi ni spremenila. Nižja vhodna temperatura in manjša količina NaYBFK dosežeta višjo maksimalno temperaturo v nasutju, medtem ko sproščena toplota adsorpcijske faze traja dlje, ko je bila kot medij uporabljena vodna para.

Ena od slabosti uporabe zeolitov v aplikacijah adsorpcijskega sharanjevanja toplote je visoka desorpcijska temperatura (200 °C do 300 °C), ki jo potrebujemo za regeneracijo snovi v fazi dehidracije. Če ne zagotovimo takih temperatur, ne moremo popolnoma izkoristiti potenciala shranjevanja. Predstavljena raziskava je pokazala, da zeolit NaYBFK pri uporabi vodne pare pri nižji vstopni temperaturi in manjši količini materiala omogoča doseganje višje maksimalne temperature v primerjavi z zeolitom 13X. V primeru uporabe vlažnega zraka z dodajanjem vodne pare zeolit NaYBFK pri enaki vstopni temeraturi in manjši količini materiala omogoča doseganje višje maksimalne temperature, pri večji količini materiala pa ima boljšo adsorcijo vode.

Ključne besede: adsorpcijsko shranjevanje toplote, ogrevanje prostorov, vodna para, vlažen zrak, zeolit 13X, zeolit NaYBFK

*Naslov avtorja za dopisovanje: Univerza v Ljubljani, Fakulteta za strojništvo, Aškerčeva 6, 1000 Ljubljana, Slovenija, urska.mlakar@fs.uni-lj.si

Strojniški vestnik - Journal of Mechanical Engineering 70(2024)3-4, SI 14

Prejeto v recenzijo: 2023-05-31
Prejeto popravljeno: 2023-10-31
Odobreno za objavo: 2023-11-20

Raziskava prilagodljivosti pakerjev za operacije lomljenja z integriranimi kolonami cevi v nahajališčih z nizko poroznostjo in permeabilnostjo

Zhiyong Wan[1,*] – Hao Yu[1] – Yong Xiao[2] – Zhaoyang Zhao[1] – Zhanghua Lian[1] – Fangxin Chen[1]

[1] Državni laboratorij za geologijo in izkoriščanje nahajališč nafte in plina, Jugozahodna univerza za naftno industrijo, Kitajska
[2] Chengdu North Petroleum Exploration and Development Technology Co, Ltd, Kitajska

Konvencionalne proizvodne operacije pri razvoju naftnih in plinskih polj danes pogosto vključujejo večkratno menjavo kolon cevi, kar pa je povezano z manjšo učinkovitostjo izgradnje, tveganjem poškodb nahajališč in večjimi tveganji pri nadzoru vrtin. Tovrstne prakse tudi ne izpolnjuje zahtev glede preizkušanja vrtin in stimulacije plinskih in naftnih vrtin s kislo tekočino.

Rešitev za omenjene izzive je integracija operacij perforacije, lomljenja in dokončanja vrtin v eni sami koloni cevi. Tak pristop lahko izboljša učinkovitost izgradnje, zniža stroške raziskovanja in razvoja polj, zmanjša tveganje sekundarnega onesnaženja formacij z izplako ter izpolnjuje zahteve glede zaščite okolja, lomljenja in učinkovite izgradnje. Operacije z integrirano kolono cevi lahko tudi odpravijo težave v zvezi z nadzorom glav vrtin pri montaži preprečevalcev izbruhov, s tem pa zmanjšajo tveganja v zvezi z nadzorom vrtin in izgradnjo ter obratovalne stroške. Pri konstruiranju integriranih kolon cevi pa je treba izpolniti tudi strožje zahteve. Paker kot ključna komponenta integrirane kolone cevi ima odločilno vlogo pri zatesnitvi kolone med procesi perforacije in tlačne stimulacije s kislino. Nujne so podrobne varnostne analize.

Na voljo sta dve izvedbi pakerjev – odstranljivi testni tlačni paker (Retrievable Test Treat Squeeze Packer – RTTS) in odstranljivi paker s hidravlično namestitvijo (Hydraulic-Set Retrievable Packer – RH). Za simulacijo temperatur in aksialnih sil kolone cevi vrtine med procesom perforacije in lomljenja je bil postavljen numerični model v ustreznem programskem paketu. Simulirani podatki, vključno s temperaturo in aksialno silo, so bili nato uporabljeni v programskem paketu za analize po MKE za preučitev uporabnosti ključnih komponent integrirane kolone cevi, kot je paker. Za tri vrste vrtin, ki so trenutno v razvoju, so bili opravljeni izračuni za analizo porazdelitve obremenitev pri pakerjih RTTS za različne obratovalne pogoje in tipe vrtin. Iz rezultatov sledi sklep, da lahko pakerji RTTS izpolnijo zahteve v zvezi z varnostjo proizvodnje na naftnih poljih. Pri pakerjih RH je bila ugotovljena pomanjkljiva zmogljivost tesnjenja, ki predstavlja varnostno tveganje. Za integrirane kolone cevi je zato priporočljiva uporaba pakerjev RTTS. Analiza pakerjev RTTS po metodi končnih elementov je razkrila, da se največje napetosti v zahtevnih pogojih proizvodnje pojavijo v osrednji cevi pakerja. Kontaktni tlak na gumijastem obroču doseže vrednost 30 MPa, odpoved tesnilnega kontakta pa ni bila ugotovljena. Zaradi vbrizgavanja kisle tekočine za lomljenje na sobni temperaturi med procesom tlačne stimulacije se v najzahtevnejših pogojih pojavlja toplotno raztezanje in krčenje kolone cevi in posledično aksialne natezne sile do 500 kN. Za zmanjšanje tveganja pojava aksialnih napetosti v opremi glave vrtine in preprečitev incidentov, kot je pogrezanje glave vrtine, je priporočljiva vgradnja dilatacijskih spojev v kolone cevi.

Vrtine na Srednjem vzhodu se zaradi značilne globine nahajališč prištevajo med navadne globoke vrtine, na Kitajskem pa trenutno poteka razvoj ultraglobokih vrtin, ki segajo do globin nad 11.000 metrov. Temperature v ultraglobokih vrtinah bodo presegle 200 °C, aksialne natezne sile pa bodo večje. Tehnologija integriranih kolon cevi mora zato izpolnjevati strožje zahteve, kar bo zahtevalo dodatne raziskave in analize. Predstavljeni model mehanskih obremenitev pakerja po metodi končnih elementov med procesom lomljenja s kislo tekočino omogoča simulacijo porazdelitve napetosti v vsaki komponenti pakerja po njegovi namestitvi pri različnih delovnih pogojih. Analiza prilagodljivosti pakerjev je zanesljiva teoretična podlaga za oceno njihove varnosti v kontekstu povečanja proizvodnje naftnih in plinskih polj.

Izračunani so bili temperatura, aksialna sila v ceveh in porazdelitev varnostnega faktorja za vsak del treh različnih vrtin na iraškem naftnem polju. Rezultati analize so teoretična podlaga za nadzor vrtin.

Ključne besede: nahajališča z nizko poroznostjo in permeabilnostjo, integrirana kolona cevi, gumijast obroč, lomljenje s kislino, simulacija po metodi končnih elementov

*Naslov avtorja za dopisovanje: Državni laboratorij za geologijo in izkoriščanje nahajališč nafte in plina, Jugozahodna univerza za naftno industrijo, Kitajska, 202122000793@stu.swpu.edu.cn

Strojniški vestnik - Journal of Mechanical Engineering 70(2024)3-4, SI 15

Prejeto v recenzijo: 2023-06-04
Prejeto popravljeno: 2023-10-17
Odobreno za objavo: 2023-11-23

Optimizacija zmogljivosti in eksperimentalna študija novega neokroglega planetarnega prenosnika tipa W-W

Changbin Dong[1,*] – Xudong Yang[1] – Dawei Li[1] – Gang Zhao[2] – Anran Wan[3] – Yongping Liu[1] – Junhai Guo[1]

[1] Tehniška univerza v Landžovu, Šola za strojništvo in elektrotehniko, Kitajska
[2] Državni laboratorij province Hubej za mehanske prenosnike in proizvodni inženiring, Znanstveno-tehniška univerza v Vuhanu, Kitajska
[3] Tehniški institut v Wuxiju, Šola za strojništvo, Kitajska

V članku sta predstavljeni dve novi kombinaciji neokroglih planetarnih prenosnikov (NCPGT) tipa W-W, ki odpravljata težave z vibracijami med delovanjem tradicionalnih prenosnikov tega tipa. Proučene so tudi napake med prenosom in izboljšanje zmogljivosti.

Po metodi inkrementalne ubirnice so bili postavljeni modeli napak prenosa za obe kombinaciji prenosnika in analiziran je bil vpliv ekscentričnosti na napako prenosa.

Uporabljena je bila metodologija zobniških prenosnikov, ubiranja zobnikov in inkrementalne ubirnice.

Novi prenosnik tipa W-W, ki ga sestavljajo neokrogli in cilindrični zobniki, ima boljšo zmogljivost prenosa. Eksperimentalno so bili določeni karakteristični diagrami pri različnih načinih ujemanja obremenitve in frekvence. Optimalna kombinacija je 20 kN in 20 Hz. S prilagajanjem frekvence motorja je bilo torej mogoče učinkovito doseči dinamično uravnoteženje obremenitev preizkusne črpalne enote.

Izboljšanje zmogljivosti prenosnikov NCPGT je težavna naloga. Obravnavani prenosniki so trenutno zaradi svoje točnosti primerni le za kmetijsko mehanizacijo, njihova uporaba v industrijskih aplikacijah in razvoj pa sta omejena zaradi težavnega izboljševanja natančnosti. Članek podaja primerjalno analizo dveh kombiniranih načinov novega prenosnika tipa W-W in njuno uporabo v obračalni napravi črpalne enote z bobnom. S poenostavljenim laboratorijskim preizkusom sta bili opredeljeni optimalna obremenitev in frekvenca motorja črpalne enote NCPGT.
Ključne besede: neokrogli planetarni prenosniki, obračalna naprava, metoda inkrementalne ubirnice, napaka prenosa, karakteristični diagram

*Naslov avtorja za dopisovanje: Tehniška univerza v Landžovu, Šola za strojništvo in elektrotehniko, Lanzhou, Kitajska, ldw969968604@163.com and lutdcb@126.com

Strojniški vestnik - Journal of Mechanical Engineering 70(2024)3-4, SI 16

Prejeto v recenzijo: 2023-06-14
Prejeto popravljeno: 2023-11-05
Odobreno za objavo: 2023-11-27

Lastnosti prehodnih tokov v tlačno-diferencialnem ventilu pri različnih izvedbah dušilne odprtine v krmilnem batu

Xu Zhang
Tehnološko raziskovalno središče za fluidno tehniko pri univerzi Jiangsu, Kitajska

V pregledu literature se je izkazalo, da je le malo raziskav na temo delovanja tlačno-diferencialnih ventilov v pogojih visokotlačnega mazanja z oljem. Glavni cilji članka so zato raziskati prehodne pojave v tlačno-diferencialnem ventilu pod vplivom visokotlačnega mazalnega olja, kvantificirati gibanje in silo krmilnega bata ventila ter določiti vpliv različnih izvedb dušilne odprtine v krmilnem batu na karakteristiko tlačne regulacije ventila.

Postavljeni so štirje modeli prehodnih tokov mazalnega olja pri različnih dušilnih odprtinah v krmilnem batu za analizo vpliva njihove izvedbe na karakteristiko gibanja krmilnega bata in regulacije tlaka ter porazdelitev pretočnega polja. Pridobljeno znanje bo uporabno za optimizacijo konstrukcije in za aplikacije tlačno-diferencialnih ventilov v sistemih za mazanje letalskih motorjev.

Za raziskovalno metodo je bila izbrana numerična simulacija v kombinaciji z eksperimentalno potrditvijo. Opravljena je bila raziskava prehodnih tokov v notranjosti omenjenega ventila z analizo vpliva dušilne odprtine na gibanje, karakteristiko regulacije tlaka in porazdelitev pretočnega polja na krmilnem batu ventila.

Na podlagi načela delovanja, zgradbe in zmogljivosti tlačno-diferencialnega ventila je bila opravljena podrobna analiza lastnosti prehodnih tokov v ventilu. Vpliv dušilne odprtine na lastnosti prehodnega toka je bil kvantitativno preučen s kombinacijo numerične simulacije in eksperimentalne potrditve.

Izvedba dušilne odprtine tlačno-diferencialnega ventila ima majhen vpliv na zagonski čas krmilnega bata ventila. S povečanjem premera dušilne odprtine se zmanjša upor na grlu krmilnega bata, prav tako pa se zmanjša tlačni gradient med notranjim prostorom in glavo jedra ventila. Visokotlačno mazalno olje v komori lažje odteče skozi dušilno odprtino nazaj v glavo krmilnega ventila, visok tlak v notranji komori hitreje upade, poveča pa se tudi največji odmik krmilnega bata ventila. Istočasno se poveča sila fluida med gibanjem krmilnega bata ventila, hitrost gibanja bata pa se zmanjša. Povečanje odmika povzroči postopno razširitev odprtine ventila in na ta način se oblikuje karakteristika znižanja tlaka v diferencialnem ventilu. Velika pretočna površina prelivne odprtine omogoča hitro vračanje visokotlačnega mazalnega olja v posodo skozi prelivno in obvodno cev. Vstopni tlak in dovodni tlak olja se hitro zmanjšata, dovodni tlak olja pa je bolje usklajen z zahtevami sistema za oljno mazanje. Podaljšanje dušilne odprtine le malo vpliva na karakteristiko regulacije tlaka in na gibanje krmilnega bata.

Ključne besede: sistem mazanja letalskih motorjev, tlačno-diferencialni ventil, vplivi na tok, prehodni tok, dušilna odprtina na krmilnem batu ventila

*Naslov avtorja za dopisovanje: Tehnološko raziskovalno središče za fluidno tehniko pri univerzi Jiangsu, Kitajska, 18993458481@163.com

Strojniški vestnik - Journal of Mechanical Engineering 70(2024)3-4, SI 17

Prejeto v recenzijo: 2023-07-25
Prejeto popravljeno: 2023-11-12
Odobreno za objavo: 2024-01-25

Metoda topološke optimizacije z omejevanjem lastnih frekvenc in redukcijo konstrukcijskih spremenljivk

Wenchang Liu – Chaohua Wu* – Xingan Chen
Tehniška univerza v Wuhanu, Šola za strojništvo in elektroniko, Kitajska

Dinamični odziv konstrukcij je v veliki meri odvisen od lastnih frekvenc, optimizacija le-teh v različnih obratovalnih pogojih pa je zato pomembna naloga. V članku je predstavljen predlog optimizacijske metode, ki omogoča povečanje lastne frekvence konstrukcij in preprečuje pojav resonance.

Omejitev pri topoloških optimizacijah v okviru projektiranja konstrukcij je običajno volumen, cilj optimizacije pa je minimalna podajnost. Togost je namreč izjemno pomemben kriterij pri tradicionalnem projektiranju konstrukcij. Model topološke optimizacije vključuje več ciljev, omejitev in drugih povezanih pogojev za izpolnjevanje tehničnih zahtev oz. za kompleksne obratovalne pogoje.

Metoda dvosmerne evolucijske optimizacije konstrukcij (BESO) je razširjena v praksi, ker odpravlja sive elemente. Predstavljena je metoda topološke optimizacije na podlagi pristopa BESO, ki vključuje omejitve lastne frekvence ter zmanjšano število konstrukcijskih spremenljivk. Cilj metode je minimalna podajnost. Omejitve lastne frekvence so bile vpeljane z Lagrangeovim multiplikatorjem za usklajen nadzor nad podajnostjo in lastno frekvenco. Občutljivost je bila normalizirana, da med procesom optimizacije ne bi prihajalo do oscilacij. Spremenljivke so bile po omejitvi volumna reducirane za hitrejšo konvergenco. Učinkovitost metode pri povečevanju lastne frekvence konstrukcij in preprečevanju resonance je ilustrirana z numeričnimi primeri.

Obravnavana raziskovalna področja vključujejo statiko, dinamiko konstrukcij ter analizo po metodi končnih elementov.

Po izpolnitvi omejitve volumna so bile reducirane konstrukcijske spremenljivke, kar lahko znatno zmanjša število iteracij in pospeši konvergenco. Lastna frekvenca prvega reda v 2D in 3D numeričnih primerih se lahko poveča za 42 % oz. 26,7 %.

Predstavljena raziskava obravnava samo lastno frekvenco prvega reda, ne pa tudi tistih višjega reda. Iz raznih objav je razvidno, da tudi lastne frekvence konstrukcij višjega reda ostajajo pomemben predmet zanimanja. Med optimizacijo se pojavljajo medsebojni vplivi lastnih frekvenc različnih redov, z višanjem reda lastne frekvence pa se povečuje kompleksnost optimizacijskega problema. Razvoj učinkovitega modela za optimizacijo lastnih frekvenc in uvajanje primernih strategij za izboljšanje stabilnosti optimizacijskega procesa bosta lahko temi prihodnjih raziskav.

Članek predstavlja omejitev lastne frekvence po metodi Lagrangeovega multiplikatorja za uspešno obvladovanje podajnosti in lastne frekvence konstrukcij. Metoda hitro konvergira po redukciji konstrukcijskih spremenljivk. Učinkovitost metode je ilustrirana z numeričnimi primeri.

Predstavljena teorija optimizacijskega modela temelji na metodi dvosmerne evolucijske optimizacije konstrukcij (BESO), ki je preprosto razumljiv koncept. Metoda Lagrangeovega multiplikatorja ima prednosti pri analizi občutljivosti in pri programiranju. Med iterativnim postopkom optimizacije je bilo ugotovljeno, da nekatere spremenljivke konvergirajo prej kot druge in na tej osnovi so bile opredeljene stabilne in proste spremenljivke. Po omejitvi volumna z optimizacijo konstrukcije je bila uporabljena strategija za reduciranje konstrukcijskih spremenljivk. To pomeni, da se vrednost stabilnih spremenljivk ne spreminja oz., da se spremenljivke ne posodabljajo več. Numerični primeri demonstrirajo, da lahko strategija za reduciranje konstrukcijskih spremenljivk učinkovito zmanjša število iteracij in pospeši konvergenco.

Pričujoča raziskava je multidisciplinarna, saj zajema znanja iz različnih področij, vključno z računalniško mehaniko, optimizacijo in projektiranjem konstrukcij ter analizo po metodi končnih elementov. Članek bo tako uporaben kot pomembno izhodišče pri optimizaciji konstrukcij.

Ključne besede: omejitev lastne frekvence; topološka optimizacija; BESO; redukcija konstrukcijskih spremenljivk; metoda Lagrangeovega multiplikatorja

*Naslov avtorja za dopisovanje: Tehniška univerza v Wuhanu, Šola za strojništvo in elektroniko, Kitajska, wuchaohua@whut.edu.cn

Strojniški vestnik - Journal of Mechanical Engineering 70(2024)3-4, SI 18

Prejeto v recenzijo: 2023-11-07
Prejeto popravljeno: 2024-01-09
Odobreno za objavo: 2024-02-26

Vsiljene vibracije časovno spremenljivih dvigalnih pogonskih sistemov

Jie Sun[1] – Peng Xu[2,3] – Mingli Chen[1] – Jianghong Xue[1,*]

[1] Univerza Jinan, Šola za mehaniko in gradbeništvo,
Državni laboratorij MOE za napovedovanje in obvladovanje nesreč v tehniki, Kitajska
[2] Qingdao Xinghua Intelligent Equipment Co., Kitajska
[3] Tehniška univerza Južne Kitajske, Šola za strojništvo in avtomobilsko tehniko, Kitajska

Za analizo vzdolžnih vibracij dvigalnih pogonskih sistemov pod vplivom zunanjega vzbujanja in posledičnega pojava resonance je v članku predstavljen predlog teoretične analize vsiljenih vibracij omenjenih sistemov, ki jih povzroča ekscentrično vzbujanje pogonskega stroja. Postavljen je bil analitični model vzdolžnih vibracij časovno spremenljivega dvigalnega pogonskega sistema. Na podlagi Hamiltonovega in variacijskega načela so bile izpeljane enačbe gibanja za vzdolžne vibracije časovno spremenljivega dvigalnega pogonskega sistema, kakor tudi ustrezni robni pogoji. Enačbe so bile diskretizirane po Galerkinovi metodi. Vibracije pri različnih smereh gibanja in pospeških so bile analizirane v paketu MATLAB, rezultati pa so bili preverjeni s primerjavo numeričnih in teoretičnih rešitev. Ugotovljeno je bilo naslednje:

Vibracijski odziv dvigalnega pogonskega sistema z opredeljenimi konstrukcijskimi parametri je določen s stanjem delovanja. Večji kot je vozni pospešek dvigala, večji je kotni pospešek pogonskega kolesa ter višji sta amplituda in frekvenca vibracij dvigalnega pogonskega sistema.

Ko pospešek a_m doseže vrednost 1,5 m/s², je frekvenca ekscentričnega vzbujanja pogonskega stroja blizu osnovni frekvenci dvigalnega pogonskega sistema, kar vodi do resonance le-tega. Največja vrednost pospeška in pojemka v izogib resonanci zato ne sme preseči 1,5 m/s².

Obstoječa literatura na temo vibracij dvigalnih pogonskih sistemov se osredotoča predvsem na proste vibracije med pospeševanjem, prečne vibracije zaradi neravnih vodil ter projektiranje rešitev za nadzor nad vibracijami in blaženje sunkov. Raziskave vzdolžnih vibracij zaradi ekscentričnega vzbujanja pogonskih koles so maloštevilne. Med delovanjem dvigala z rastjo kotne hitrosti pogonskega kolesa narašča tudi pospešek pogonskega sistema in s tem ekscentrično vzbujanje. Ko kotna hitrost pogonskega kolesa doseže določeno vrednost, je frekvenca vzdolžnih vibracij, ki jih ustvari ekscentrično vzbujanje pogonskega kolesa, blizu lastni frekvenci samega sistema in nastopi resonanca, ki močno vpliva na varnost delovanja dvigala. Ta pojav še ni bil obravnavan v literaturi. Novost v članku je predlog opisa odvisnosti med pospeškom dvigalnega pogonskega sistema in kotno hitrostjo pogonskih koles. Podrobno je opisan vpliv delovnega pospeška dvigala na resonanco dvigala, predlagano pa je tudi območje varnih pospeškov, ki preprečuje resonanco dvigala. Rezultati pričujoče študije bodo uporabni kot izhodišče za izboljševanje varnosti dvigal in protipotresno gradnjo. Članek ima tudi svoje omejitve: dvigala so vgrajena v stavbah, zato so vibracije dvigal odvisne od vibracij stavb. V prihodnje bo mogoče opraviti dodatne eksperimentalne in teoretične študije sklopitve vibracij dvigal in stavb, izpostavljenih vetrnim obremenitvam in potresom, ki bodo lahko izhodišče za protipotresno gradnjo dvigalnih pogonskih sistemov.

Ključne besede: dvigalni pogonski sistem, vibracije, časovna spremenljivost, dinamika, numerična analiza, pojav, Hamiltonovo načelo, Galerkinova metoda

*Naslov avtorja za dopisovanje: Jinan Univerza, GuangDong, Kitajska, txue@jnu.edu.cn

Strojniški vestnik - Journal of Mechanical Engineering 70(2024)3-4, SI 19

Prejeto v recenzijo: 2023-10-09
Prejeto popravljeno: 2023-12-19
Odobreno za objavo: 2023-12-23

Analiza nelinearnih prostih vibracij funkcionalno gradientnih poroznih koničnih lupin, ojačenih z grafenskimi nanoploščicami

Xiaolin Huang – Nengguo Wei – Chengzhe Wang – Xuejing Zhang*
Univerza za elektroniko v Guilinu, Šola za arhitekturo in transport, Kitajska

V članku je predstavljena analiza nelinearnih vibracij funkcionalno gradientnih poroznih koničnih lupin, ojačenih z grafenskimi nanoploščicami. Podan je predlog modela za ocenjevanje materialnih lastnosti poroznih nanokompozitov in metode za izračun nelinearnih frekvenc lupin.

Obravnavane so tri vrste porazdelitve poroznosti in trije vzorci disperzije GPL. Predstavljen je izboljšani model za ocenjevanje materialnih lastnosti nanokompozitov z različnimi porazdelitvami GPL in por na podlagi modela Halpin-Tsai. Po klasični teoriji tankih lupin z geometrijskimi nelinearnostmi so bile izpeljane enačbe nelinearnih vibracij poroznih prirezanih koničnih lupin, ki upoštevajo učinek Winkler-Pasternakovega elastičnega medija. Enačbe so bile razrešene po Galerkinovi metodi in Volmirjevi domnevi in nato so bile izračunane linearne in nelinearne frekvence.

Predstavljeni model in metoda sta bila v nadaljevanju numerično validirana. Podrobno so bili preučeni vplivi por, grafenskih ploščic, elastične osnove in geometrijskih parametrov na linearne in nelinearne frekvence poroznih koničnih lupin. Rezultati so pokazali osnovno frekvenco pri polovičnem valu vzdolž paralelnega kroga $n = 13$. Z rastjo masnega deleža GPL se povečuje lastna frekvenca in zmanjšuje frekvenčno razmerje. Najnižje frekvenčno razmerje med tremi vzorci disperzije GPL ima G–1, najvišje pa G–2. Frekvenčno razmerje je mogoče zmanjšati s povečanjem količnika poroznosti. Vpliv porazdelitve poroznosti na frekvenčno razmerje je zanemarljiv. Rezultati kažejo, da je minimalno frekvenčno razmerje doseženo pri polkotu približno 55°.

Rešitev enačb nelinearnih vibracij za porozne konične lupine bi bilo zelo težko izpeljati analitično in zato so bile prezrte vztrajnostne sile v ravnini. V prihodnjih raziskavah bomo upoštevali tudi njihov vpliv.

Predstavljen je model za vrednotenje materialnih lastnosti funkcionalno gradientnih poroznih kompozitov, ojačenih z grafenom. Podanih je več zanimivih ugotovitev v zvezi z vplivi por, GPL in Winkler-Pasternakove elastične podlage. Rezultati bodo lahko uporabni pri projektiranju podobnih konstrukcij v praksi.

Ključne besede: nelinearne vibracije, prirezana konična lupina, kompozit, grafenska nanoploščica, pore, elastična podlaga

*Naslov avtorja za dopisovanje: Univerza za elektroniko v Guilinu, Šola za arhitekturo in transport, Jinji Road 1#, Guilin, Kitajska, pingguotree4426@163.com

Strojniški vestnik - Journal of Mechanical Engineering 70(2024)3-4, SI 20

Prejeto v recenzijo: 2023-08-21
Prejeto popravljeno: 2023-12-04
Odobreno za objavo: 2024-01-25

Optimizacija konstrukcije mehanskega ventila za pomivalni stroj na podlagi minimizacije tlačnih izgub

Furkan Kılavuz[1,2] – Binnur Gören Kıral[3,*]

[1] Univerza Dokuz Eylul, Visoka šola za naravoslovne in uporabne vede, Turčija
[2] Arçelik A.Ş., Turčija; [3] Univerza Dokuz Eylul, Oddelek za strojništvo, Turčija

Cilj pričujoče študije je optimizacija konstrukcije ventila za pomivalni stroj, ki ga uporablja proizvajalec bele tehnike, za varčevanje z energijo in trajnostno delovanje. Tlačne izgube v sistemu mehanskega ventila so pomemben dejavnik celotne učinkovitosti pomivalnega stroja. Namen študije je poiskati optimalno konstrukcijo rotorja za minimalen tlačni padec na izhodni strani in največjo zmogljivost.

Najprej so bile v programskem paketu MATLAB R2023a modelirane lopatice rotorja z Bézierjevimi krivuljami 4. reda. β_1 in β_2 kot osnovna parametra za določitev omenjenih krivulj sta vgradni vstopni in izstopni kot rotorja. Po preučitvi omejitev pri modeliranju in literature so bili določeni profili lopatic v razponu β_1 = 10° do 30° in β_2 = 10° do 40° v korakih po 5°. Z Bézierjevimi krivuljami so bili nato v programski opremi SOLIDWORKS 2021 ustvarjeni tridimenzionalni polni modeli rotorjev z različnimi profili oz. števili lopatic. Obravnavanih je bilo 50 modelov s šestimi števili lopatic in petimi materiali. Za množično proizvodnjo rotorjev, ki so predmet te študije, se uporablja polioksimetilen (POM). S postopki ciljnega nalaganja (FDM) in stereolitografije (SLA) so bili izdelani tudi rotorji iz materiala PLA (polilaktična kislina), čiste smole in smole, ojačene z 0,1 ut. % borovega nitrida in grafena. Površina rotorskih lopatic je bila preiskana pod optičnim mikroskopom za opredelitev vpliva hrapavosti površin na tokovne razmere. Opravljena je bila tudi numerična analiza tokov s polnimi modeli v programskem paketu ANSYS CFD za določitev tlačnih izgub. Pred izdelavo polnih modelov so bili z orodjem Design of Experiment (DOE) v Minitabu določeni konstrukcijski parametri in nato so bili z njimi ustvarjeni modeli. V naslednjem koraku je bila na podlagi podatkov, pridobljenih v analizi tokov, z orodjem ANOVA Response Optimizer določena optimalna konstrukcija. Numerični analizi sta sledila izdelava lopatic po metodi 3D-tiska in eksperimentalna meritev tlakov na izstopu. Za meritev tlaka na izhodu mehanskega ventila je bil pripravljen poseben eksperiment. Na podlagi rezultatov numerične analize je bil ustvarjen model z umetno nevronsko mrežo in napovedana je bila učinkovitost pri optimalnih parametrih. Končno je bil izdelan rotor z optimalno konstrukcijo po postopku FDM in eksperimentalno je bil izmerjen tlak na izstopu.

Preiskava slik površine rotorskih lopatic je pokazala, da je najbolj hrapava lopatica iz materiala PLA. Največja razdalja med spodnjo površino in zgornjo točko je znašala približno 70 μm. Tako objavljeni članki kot rezultati pričujoče študije so pokazali, da imajo geometrijski parametri večji vpliv na tlačne izgube kot hrapavost.

V prvem koraku eksperimentalnih študij je bila izmerjena razlika med vstopnim in izstopnim tlakom obstoječega rotorja, ki je v množični proizvodnji. S postopki 3D-tiska so bili izdelani tudi rotorji iz materiala PLA, čiste smole ter smole, ojačene z borovim nitridom in grafenskimi nanoploščicami. Najnižji izstopni tlak za vsa števila lopatic je bil zabeležen pri rotorju iz smole, ojačene z grafenskimi nanoploščicami, medtem ko je bil najnižji tlačni padec zabeležen pri rotorjih iz materiala PLA. Rezultati eksperimentov in analize CFD nakazujejo pomembno vlogo števila lopatic.

V naslednjem koraku je bil preučen vpliv kotov, ki so osnovni parametri Bézierjevih krivulj. Izkoristek rotorja je obratno sorazmeren s tlačno izgubo, zato se izkoristek rotorja povečuje z zmanjševanjem kota β_1, povečevanjem kota β_2 in številom lopatic. Optimalne vrednosti za število lopatic, vstopni kot β_1 in izstopni kot β_2 so bile določene po statistični analizi v Minitabu. Optimalni konstrukcijski parametri po analizi CFD, pridobljeni z analizo optimizatorja odziva, so β_1 = 10°, β_2 = 40°, število lopatic je 8. Pri rotorju z optimalno konstrukcijo je bilo v primerjavi z rotorjem iz množične proizvodnje doseženo izboljšanje izstopnega tlaka za 6,5 %. Izkoristek rotorja se je povečal s 59,77 % na 86,57 %. Ko je bila nevronska mreža naučena na celotni podatkovni bazi za največjo točnost napovedi, je bila na podlagi modela izračunana napoved izkoristka rotorja pri optimalnih parametrih. Napoved izkoristka rotorja, za β_1 = 10°, β_2 = 40° in število lopatic je 8, po tem modelu ANN znaša 82,62 %. Rezultati se ujemajo z rezultati analize CFD in optimizatorja odgovora.

Sledi sklep, da je izkoristek rotorja mehanskega ventila pomivalnega stroja odvisen od profila in števila lopatic. Rezultati raziskav bodo uporabni za izboljšanje zmogljivosti pomivalnih strojev ter lahko prispevajo k razvoju učinkovitejših in zanesljivejših gospodinjskih aparatov. Rezultate bo mogoče potrditi s praktičnimi preizkusi v realnih scenarijih uporabe pomivalnih strojev.

Ključne besede: pomivalni stroj, varčevanje z energijo, optimizacije oblike lopatic rotorja, statistična analiza, umetna nevronska mreža

*Naslov avtorja za dopisovanje: Univerza Dokuz Eylul, Visoka šola za naravoslovne in uporabne vede, Turčija, binnur.goren@deu.edu.tr

Guide for Authors

All manuscripts must be in English. Pages should be numbered sequentially. The manuscript should be composed in accordance with the Article Template given above. The suggested length of contributions is 10 to 20 pages. Longer contributions will only be accepted if authors provide justification in a cover letter. For full instructions see the Information for Authors section on the journal's website: http://en.sv-jme.eu .

SUBMISSION:

Submission to SV-JME is made with the implicit understanding that neither the manuscript nor the essence of its content has been published previously either in whole or in part and that it is not being considered for publication elsewhere. All the listed authors should have agreed on the content and the corresponding (submitting) author is responsible for having ensured that this agreement has been reached. The acceptance of an article is based entirely on its scientific merit, as judged by peer review. Scientific articles comprising simulations only will not be accepted for publication; simulations must be accompanied by experimental results carried out to confirm or deny the accuracy of the simulation. Every manuscript submitted to the SV-JME undergoes a peer-review process.

The authors are kindly invited to submit the paper through our web site: http://ojs.sv-jme.eu. The Author is able to track the submission through the editorial process - as well as participate in the copyediting and proofreading of submissions accepted for publication - by logging in, and using the username and password provided.

SUBMISSION CONTENT:

The typical submission material consists of:

- A **manuscript** (A PDF file, with title, all authors with affiliations, abstract, keywords, highlights, inserted figures and tables and references),
- Supplementary files:
  - a **manuscript** in a WORD file format
  - a **cover letter** (please see instructions for composing the cover letter)
  - a ZIP file containing **figures** in high resolution in one of the graphical formats (please see instructions for preparing the figure files)
  - possible **appendicies** (optional), cover materials, video materials, etc.

Incomplete or improperly prepared submissions will be rejected with explanatory comments provided. In this case we will kindly ask the authors to carefully read the Information for Authors and to resubmit their manuscripts taking into consideration our comments.

COVER LETTER INSTRUCTIONS:

Please add a **cover letter** stating the following information about the submitted paper:

1. Paper **title**, list of **authors** and their **affiliations**. **One** corresponding author should be provided.
2. **Type of paper**: original scientific paper (1.01), review scientific paper (1.02) or short scientific paper (1.03).
3. A **declaration** that neither the manuscript nor the essence of its content has been published in whole or in part previously and that it is not being considered for publication elsewhere.
4. State the **value of the paper** or its practical, theoretical and scientific implications. What is new in the paper with respect to the state-of-the-art in the published papers? Do not repeat the content of your abstract for this purpose.
5. We kindly ask you to suggest at least two **reviewers** for your paper and give us their names, their full affiliation and contact information, and their scientific research interest. The suggested reviewers should have at least two relevant references (with an impact factor) to the scientific field concerned; they should not be from the same country as the authors and should have no close connection with the authors.
6. Please confirm that authors are willing/able to pay the Open Access **publication fee** as indicated in the Guide for Authors under Publication Fee, available at https://www.sv-jme.eu/guide-for-authors-online/.

FORMAT OF THE MANUSCRIPT:

The manuscript should be composed in accordance with the Article Template. The manuscript should be written in the following format:

- A **Title** that adequately describes the content of the manuscript.
- A list of **Authors** and their **affiliations**.
- An **Abstract** that should not exceed 250 words. The Abstract should state the principal objectives and the scope of the investigation, as well as the methodology employed. It should summarize the results and state the principal conclusions.
- 4 to 6 significant **key words** should follow the abstract to aid indexing.
- 4 to 6 **highlights;** a short collection of bullet points that convey the core findings and provide readers with a quick textual overview of the article. These four to six bullet points should describe the essence of the research (e.g. results or conclusions) and highlight what is distinctive about it.
- An **Introduction** that should provide a review of recent literature and sufficient background information to allow the results of the article to be understood and evaluated.
- A **Methods** section detailing the theoretical or experimental methods used.
- An **Experimental section** that should provide details of the experimental set-up and the methods used to obtain the results.
- A **Results** section that should clearly and concisely present the data, using figures and tables where appropriate.
- A **Discussion** section that should describe the relationships and generalizations shown by the results and discuss the significance of the results, making comparisons with previously published work. (It may be appropriate to combine the Results and Discussion sections into a single section to improve clarity.)
- A **Conclusions** section that should present one or more conclusions drawn from the results and subsequent discussion and should not duplicate the Abstract.
- **Acknowledgement** (optional) of collaboration or preparation assistance may be included. Please note the source of funding for the research.
- **Nomenclature** (optional). Papers with many symbols should have a nomenclature that defines all symbols with units, inserted above the references. If one is used, it must contain all the symbols used in the manuscript and the definitions should not be repeated in the text. In all cases, identify the symbols used if they are not widely recognized in the profession. Define acronyms in the text, not in the nomenclature.
- **References** must be cited consecutively in the text using square brackets [1] and collected together in a reference list at the end of the manuscript.
- **Appendix(-icies)** if any.

SPECIAL NOTES

Units: The SI system of units for nomenclature, symbols and abbreviations should be followed closely. Symbols for physical quantities in the text should be written in italics (e.g. *v*, *T*, *n*, etc.). Symbols for units that consist of letters should be in plain text (e.g. ms^{-1}, K, min, mm, etc.). Please also see: http://physics.nist.gov/cuu/pdf/sp811.pdf .

Abbreviations should be spelt out in full on first appearance followed by the abbreviation in parentheses, e.g. variable time geometry (VTG). The meaning of symbols and units belonging to symbols should be explained in each case or cited in a **nomenclature** section at the end of the manuscript before the References.

Figures (figures, graphs, illustrations digital images, photographs) must be cited in consecutive numerical order in the text and referred to in both the text and the captions as Fig. 1, Fig. 2, etc. Figures should be prepared without borders and on white grounding and should be sent separately in their original formats. If a figure is composed of several parts, please mark each part with a), b), c), etc. and provide an explanation for each part in Figure caption. The caption should be self-explanatory. Letters and numbers should be readable (Arial or Times New Roman, min 6 pt with equal sizes and fonts in all figures). Graphics (submitted as supplementary files) may be exported in resolution good enough for printing (min. 300 dpi) in any common format, e.g. TIFF, BMP or JPG, PDF and should be named Fig1.jpg, Fig2.tif, etc. However, graphs and line drawings should be prepared as vector images, e.g. CDR, AI. Multi-curve graphs should have individual curves marked with a symbol or otherwise provide distinguishing differences using, for example, different thicknesses or dashing.

Tables should carry separate titles and must be numbered in consecutive numerical order in the text and referred to in both the text and the captions as Table 1, Table 2, etc. In addition to the physical quantities, such as *t* (in italics), the units [s] (normal text) should be added in square brackets. Tables should not duplicate data found elsewhere in the manuscript. Tables should be prepared using a table editor and not inserted as a graphic.

REFERENCES:

A reference list must be included using the following information as a guide. Only cited text references are to be included. Each reference is to be referred to in the text by a number enclosed in a square bracket (i.e. [3] or [2] to [4] for more references; do not combine more than 3 references, explain each). No reference to the author is necessary.

References must be numbered and ordered according to where they are first mentioned in the paper, not alphabetically. All references must be complete and accurate. Please add DOI code when available. Examples follow.

Journal Papers:

Surname 1, Initials, Surname 2, Initials (year). Title. *Journal*, volume, number, pages, DOI code.

[1] Hackenschmidt, R., Alber-Laukant, B., Rieg, F. (2010). Simulating nonlinear materials under centrifugal forces by using intelligent cross-linked simulations. *Strojniški vestnik - Journal of Mechanical Engineering*, vol. 57, no. 7-8, p. 531-538, DOI:10.5545/sv-jme.2011.013.

Journal titles should not be abbreviated. Note that journal title is set in italics.

Books:

Surname 1, Initials, Surname 2, Initials (year). Title. Publisher, place of publication.

[2] Groover, M.P. (2007). *Fundamentals of Modern Manufacturing*. John Wiley & Sons, Hoboken.

Note that the title of the book is italicized.

Chapters in Books:

Surname 1, Initials, Surname 2, Initials (year). Chapter title. Editor(s) of book, book title. Publisher, place of publication, pages.

[3] Carbone, G., Ceccarelli, M. (2005). Legged robotic systems. Kordić, V., Lazinica, A., Merdan, M. (Eds.), Cutting Edge Robotics. Pro literatur Verlag, Mammendorf, p. 553-576.

Proceedings Papers:

Surname 1, Initials, Surname 2, Initials (year). Paper title. Proceedings title, pages.

[4] Štefanić, N., Martinčević-Mikić, S., Tošanović, N. (2009). Applied lean system in process industry. *MOTSP Conference Proceedings*, p. 422-427.

Standards:

Standard-Code (year). Title. Organisation. Place.

[5] ISO/DIS 16000-6.2:2002. *Indoor Air – Part 6: Determination of Volatile Organic Compounds in Indoor and Chamber Air by Active Sampling on TENAX TA Sorbent, Thermal Desorption and Gas Chromatography using MSD/FID.* International Organization for Standardization. Geneva.

WWW pages:

Surname, Initials or Company name. Title, from http://address, date of access.

[6] Rockwell Automation. Arena, from *http://www.arenasimulation.com*, accessed on 2009-09-07.

EXTENDED ABSTRACT:

When the paper is accepted for publishing, the authors will be requested to send an **extended abstract** (approx. one A4 page or 3500 to 4000 characters or approx. 600 words). The instruction for composing the extended abstract are published on-line: http://www.sv-jme.eu/information-for-authors/ .

COPYRIGHT:

Authors submitting a manuscript do so on the understanding that the work has not been published before, is not being considered for publication elsewhere and has been read and approved by all authors. The submission of the manuscript by the authors means that the authors automatically agree to publish the paper uder CC-BY 4.0 Int. or CC-BY-NC 4.0 Int. when the manuscript is accepted for publication. All accepted manuscripts must be accompanied by a Copyright Agreement, which should be sent to the editor. The work should be original work by the authors and not be published elsewhere in any language without the written consent of the publisher. The proof will be sent to the author showing the final layout of the article. Proof correction must be minimal and executed quickly. Thus it is essential that manuscripts are accurate when submitted. Authors can track the status of their accepted articles on https://en.sv-jme.eu/.

PUBLICATION FEE:

Authors will be asked to pay a publication fee for each article prior to the article appearing in the journal. However, this fee only needs to be paid after the article has been accepted for publishing. The fee is 380 EUR (for articles with maximum of 6 pages), 470 EUR (for articles with maximum of 10 pages), plus 50 EUR for each additional page. The additional cost for a color page is 90.00 EUR (only for a journal hard copy; optional upon author's request). These fees do not include tax.

Strojniški vestnik -Journal of Mechanical Engineering
Aškerčeva 6, 1000 Ljubljana, Slovenia, e-mail: info@sv-jme.eu

9 770039 248001
ISSN 0039-2480

http://www.sv-jme.eu

Contents

Papers